Phase equilibria in the Ni-Si-Mg system and fracture toughness of selected in-situ intermetallic composites

by

Young-Kyu Song

A thesis
presented to the University of Waterloo
in fulfilment of the
thesis requirement for the degree of
Doctor of Philosophy
in
Mechanical Engineering

Waterloo, Ontario, Canada, 2000

The University of Waterloo requires the signatures of all persons using or photocopying this thesis. Please sign below, and give address and date.

Abstract

The phase equilibria in the Ni-Si-Mg system and mechanical properties such as fracture toughness and yield strength of selected ternary and binary composites in the system have been studied.

The Ni-Si-Mg ternary phase diagram has been established after homogenization and slow cooling to room temperature. The isothermal section of the phase diagram at 900°C in the Ni-rich region was also established after isothermal annealing at the temperature followed by water quenching. The chemical compositions of the alloys and their phases were obtained using fully quantitative energy dispersive x-ray spectroscopy (EDS) with standard spectrum files created from intermetallic compounds Mg_2Ni and Ni_2Si. The following intermetallic phases have been observed: (a) four new ternary intermetallic phases, designated as ν, ω, μ, and τ, (b) a ternary intermediate phase, $Mg(Ni,Si)_2$ based on the binary $MgNi_2$ phase containing Si, (c) three ternary intermetallic phases, η, κ, and ζ, previously reported by the present authors [96Son, 98Son[1]], and (d) Mg_2SiNi_3 (Fe_2Tb type), previously reported by Noreus et al. [85Nor]. The $MgNi_6Si_6$ phase, which was also previously reported [81Buc] was not observed at the corresponding composition in the present work. However, the $MgNi_6Si_6$ phase reported as being of hexagonal symmetry (Cu_7Tb type) with the lattice parameters: a = 0.4948nm and c = 0.3738nm possibly corresponds to the μ phase ($Mg(Si_{0.48}Ni_{0.52})_7$) discovered in the present work. The lattice structure of the newly discovered ω phase ($(Mg_{0.52}Ni_{0.48})_7Si_4$) was determined with the help of the X-ray indexing program TREOR to be a hexagonal structure of the Ag_7Te_4-type with the lattice parameters, a = 1.3511nm and c = 0.8267nm.

The fracture behaviour and fracture toughness of binary and ternary intermetallic phases and composites using chevron-notched bend specimens (CNB) have been studied. Single or near single phase intermetallic alloys such as η, Ni_2Si, and $MgNi_2$ showed low average fracture toughness values such as ~2.0 $MPa.m^{1/2}$, ~3.0 $MPa.m^{1/2}$, and ~6.0 $MPa.m^{1/2}$, respectively. However, near Ni_3Si single phase alloy tested in air showed the average fracture toughness ~31.0 $MPa.m^{1/2}$. The composite rule-of-mixture-like relationship between fracture toughness

and volume fraction of toughening Ni_3Si, Ni_3Si+(Ni(Si)) and Ni(Si) phases showed that the fracture toughness values with increasing the volume fraction of the toughening phases seem to follow similar to the lower bound of the composite rule of mixtures.

Environmental effects on fracture toughness have been investigated for single or near-single phase alloys and selected intermetallic composites. No environmental effects were observed for near-single phase η, single phase Ni_2Si, and most of the selected in-situ composites. Fracture toughness of a single phase Ni_3Si also does not seem to be affected by the test environment. However, fracture toughness of a near-single phase Ni_3Si containing fine (Ni_3Si+Ni(Si)) mixture seems to be susceptible to test environment. This seems to be the effect of the susceptibility of the interfaces Ni_3Si/Ni(Si) in the mixture to moisture-generated hydrogen.

Indentation microcracking pattern and indentation fracture toughness of binary and ternary intermetallic phases in the Ni-Si-Mg system were studied. It is shown that the determination of the crack system as being either Palmqvist or halfpenny by simple polishing away of the indented surface is unreliable due to the existence of the core zone (crack-free zone) with compressive stresses. In general, the existence of the indentation core zone in the pseudo halfpenny cracks does not seem to change the crack length-load characteristic of the halfpenny cracks allowing the use of existing equations for the penny shaped crack system to calculate indentation fracture toughness. However, equally reasonable indentation fracture toughness values are also obtained by using Shetty et al. [85She[1]], based on the Palmqvist crack system, which is modified in the present work. Our modification takes into account the indentation size effect (ISE) and yields results of K_{IC} independent of indentation loads. Comparing the fracture toughness values obtained by indentation method (1.3-1.8MPa.$m^{1/2}$) with those obtained by bulk CNB specimens (1.7MPa.$m^{1/2}$) for the η phase, the indentation fracture toughness values are in a good agreement with those obtained on the bulk materials.

Acknowledgments

I would like to offer my sincere gratitude to my supervisor Prof. R.A. Varin for his advice and guidance during the PhD program.

I would also like to express my appreciation to the thesis examining committee members, Prof. A. Plumtree, Prof. G. Glinka and J. Corbett and to the external examiner, Prof. Sharvan K. Kumar for their concern and constructive advice.

Dedicated to

my mother and father

my wife, Mesook

my lovely daughters, Joanna and Susanna

Table of Contents

Nomenclature

Toughening mechanisms and fracture toughness calculations in composites

K_i: initiation fracture toughness

K_g: crack growth fracture toughness

σ_y^c: yield stress of composite

σ_y^d: yield stress of ductile phase (toughening phase)

V_m: volume fraction of matrix

V_d: volume fraction of ductile phase

σ_y^m: yield stress of matrix

$\bar{\varepsilon}_f$: effective fracture strain

$\bar{\varepsilon}_f^m$: effective fracture strain of matrix

$\bar{\varepsilon}_f^d$: effective fracture strain of ductile phase

$\bar{\varepsilon}_m$: effective strain of matrix

$\bar{\varepsilon}_c$: effective strain of composite

ε_y^c: yield strain of composite

ε_y^m: yield strain of matrix

n: strain hardening exponent

I_n: Integration component that depends on n

r: radial co-ordinate from the crack tip

α': dimensionless constant

E_m: Young's modulus of matrix

E_c: Young's modulus of composite

V_m: volume fraction of matrix

ε_{yy}: strain in y direction

ε_{xx}: strain in x direction

K_N: renucleation fracture toughness

θ: angular co-ordinate from the crack tip

σ_f^m : fracture stress of matrix

h_m: ductile phase layer thickness

K_p: fracture toughness of particle

s: distance from the centre of the reinforcing particle

R: particle radius

K(s): crack tip stress intensity factor

L: distance between particles

u*: crack opening displacement at the point when the ductile material fails

W: work of fracture

C: constant

σ_f^d : particle fracture stress

u_y: displacement at yielding

γ_ℓ : shear strain of ligament

γ_ℓ^* : critical shear strain of ligament

w: shear ligament width

L_s: process zone length

$\bar{\ell}$: average ligament length

D: average grain size

τ_ℓ : shear stress in the ligament

V_ℓ : volume fraction of shear ligament

ϕ: crack deflection angle

k_1: local tensile opening (Mode I) stress intensity factor

k_2: local sliding (Mode II) stress intensity factor

a*: half of the maximum acceptable crack in the component

CNB fracture toughness

K_{IC}: plane strain fracture toughness calculated from the test procedure in ASTM E399-90

P_{max}: maximum load

Y*: stress intensity factor coefficient for CNB fracture toughness calculations

B: specimen thickness

W: specimen width

a: depth to notch/crack front as defined in Fig. 2.9

a_0: depth to notch apex as defined in Fig. 2.9

a_1: maximum depth of notch front as defined in Fig. 2.9

α: dimensionless notch depth =a/W

α_0: dimensionless notch depth =a_0/W

α_1: dimensionless notch depth =a_1/W

Ymin: minimum stress intensity factor coefficient

K_{Iv}: plane strain fracture toughness determined by using chevron notched bar or rod specimens

K_{IvM}: plane strain fracture toughness determined based on the maximum load by using chevron notched bar or rod specimens

σ_{YS}: yield strength

N: notch width

R: notch root radius

θ: notch root angle

K_{Ivb}: fracture toughness determined by CNB specimen of advanced ceramics

S_1: outer support roller span

S_2: inner load roller span

$C_V(\alpha)$: compliance function of chevron-notched specimens

Y: stress intensity factor coefficient for fracture toughness calculations in ASTM E399-90

A_T: projected fracture area of the specimen

E: elastic modulus

ν: Poisson's ratio

Indentation fracture toughness

a: indentation half diagonal

l: length of cracks emanated from the indentation corners

c: crack length from the center of the indentation

W: Palmqvist crack resistance parameter

P: indentation load

H: mean contact pressure exerted by the Vickers indentation

H_V: Vickers hardness

D: median crack depth

$P_\perp$: indentation force normal to the median plane

Pc: critical indentation load to nucleate or propagate flaws

List of Tables

List of Figures

1. Introduction

There is an ever increasing need to develop low density materials that can maintain their high strength and stiffness properties at elevated temperatures. Intermetallics have long been investigated with this high temperature, strength/density characteristics in mind and have a number of properties that make them extremely attractive for structural applications, particularly at elevated temperatures [87Pam, 77Wes]. Intermetallic compounds are a unique class of metallic materials, which form a long-range ordered crystal structure below their critical ordering temperature, T_c. These ordered intermetallics usually exist in relatively narrow compositional ranges around simple stoichiometric ratios. The strong tendency for chemical ordering, strong bonding, and closer packing between atoms (atomic ordering produces a volume contraction of approximately 1.3 pct. for all the cubic ordered alloys [79Liu]) result in good stability of superlattice structure, reduced diffusion mobility, and thus increased resistance to plastic deformation at elevated temperatures [79Liu, 84Liu[1], 89Izu, 93Yoo].

In fact, for many intermetallic alloys such as Ni_3Al [70Tho, 84Liu[2]], Cu_3Au [76Kur], Fe_3Ga [84Sch], Ni_3Si [50Low, 90Tak[1]] etc., the yield strength shows an increase rather than a decrease with increasing temperature up to a certain temperature. In this regard, some intermetallics are likely good candidates for high temperature use to replace Ni-base superalloys in advanced gas turbine and aerospace applications [88Ant, 89Fle].

In spite of the above advantages, so far, there has been relatively limited success in developing useful intermetallic alloys for high temperature structural applications, mostly limited to Ni_3Al, and FeAl [96Dee, 97Geo, 97Wil]. The major difficulty with this class of alloys is their reported brittle fracture and low ductility, particularly at lower temperatures. This low fracture toughness can be related to three major factors [89Izu, 84Liu[2], 90Liu[1]].

i) Grain boundary embrittlement, caused by segregation of harmful impurities and /or intrinsic weakness of grain boundary due to its structural configuration.

ii) Environmental embrittlement leading to an intergranular or cleavage fracture in polycrystals, or cleavage fracture in single crystals.

iii) Low symmetry ordered crystal structures having a limited number of slip systems.

Severity of factors (i) and (ii) can to a certain extent be alleviated by doping with microalloying elements. For example, various dopants such as B, C, Ti, Ce, Ca, Mg, Si or Mn were added to Ni_3Al, and of these, boron is the most effective in improving ductility and fabricability of Ni_3Al [79Aok[1], 84Liu[1], 85Liu, 88Mas]. However, among the factors, the number of slip systems (factor (iii)) depends on crystal structures and high symmetry is required for satisfying the so-called von Mises' criterion in which more than five available slip systems are required if a polycrystal is to change its shape freely [89Izu]. Therefore, it is essential to change the crystal structure to a higher symmetry unit cell to overcome the factor (iii). To a certain extent, this problem has been rectified by controlling the ordered lattice structure through macroalloying processes. For example addition of third elements, such as Cu, Ni, Zn [65Ram[1]], Mn [89Mab], Fe [81Sei, 88Kum], or Pd [90Pow] to tetragonal $D0_{22}$ Al_3Ti, Fe [84Liu[2]] to tetragonal $D0_{22}$ Ni_3V, Ni, Cu, [65Ram[1]], V [66Ram], Zn [65Ram[2]], Fe, Cr [89Sch], or Mn and Cr [91Vir, 92Vir] to tetragonal $D0_{23}$ Al_3Zr, and Fe [84Liu[2]] to hexagonal $D0_{19}$ Co_3V produce $L1_2$ $(Al+third\ element)_3Ti$, $(Ni,Fe)_3V$, $(Al+third\ element)_3Zr$, and $(Co,Fe)_3V$ structures, respectively.

The aim of many investigations has been to design multiphase materials, including composites, whose microstructures are optimized for a combination of high temperature mechanical response, e.g. creep resistance, and room temperature fracture toughness [93Ebr]. Another method of toughening is based on the concept of so-called in-situ composite [93Ant]. In these composites, the toughening phase in the intermetallic matrix is incorporated in a 'natural' manner, based on the equilibrium phase diagram via solidification and subsequent thermomechanical treatments. In the in-situ intermetallic composites, macrostructural toughening usually involves the incorporation of a ductile second phase in a brittle intermetallic matrix. The purpose of the ductile phase is to interact with the progression of cracks through the matrix phase. The ductile second phase can take the form of isolated particles, interpenetrating networks or continuous phases such as lamellas or fibers. While the degree of toughening is generally dependent on the volume fraction and morphology of the second phase, the actual characteristics of the ductile phase that will generate optimum toughness have not yet been adequately established or modelled. Toughening mechanisms in the in-situ intermetallic composite will be discussed in Chapter 5.

2. Objective of the study

The present study consists of three major topics. The objective of each topic is as follows.

2.1 Phase equilibria in the Ni-Si-Mg system

The binary Ni-Si, Mg-Ni, and Mg-Si systems are well established [90Mas] and contain intermetallic phases of scientific and commercial importance (e.g., Ni_3Si, Mg_2Ni, and $MgNi_2$, etc.) as discussed in the following chapter. However, the Ni-Si-Mg ternary system was not systematically studied in the past. The existence of only two ternary intermetallic phases $MgNi_6Si_6$ [81Buc] and Mg_2SiNi_3 [85Nor] were reported in the literature. Therefore, the ternary Ni-Si-Mg system is of great interest since some new derivatives of the intermetallic compounds in the above binary systems may exist in the ternary system with attractive but yet unknown properties.

The present author reported a preliminary part of the Ni-Si-Mg phase diagram covering the Ni-rich area [95Son, 98Son[1]]. However, considering the recent interest in the binary $MgNi_2$ and Mg_2Ni phases for their capabilities as structural and functional materials it is important to extend the ternary Ni-Si-Mg ternary phase diagram in [96Son, 98Son[1]] to the Mg-rich area and also to the Si-rich area. This phase diagram, then, can be used as a guideline for the development of any novel structural or functional alloys in this alloy system.

In this part of the thesis, the phase equilibria at room temperature (established after homogenization and slow cooling to room temperature) and the stability of the phase equilibria at elevated temperature will be studied. Crystallographic (lattice structure and lattice parameters) and metallographic (melting and reaction temperatures) characteristics of the newly discovered phases in the present system will be investigated. In addition, the microstructural evolution of the investigated alloy and basic information such as the hardness of the intermetallic phases observed in this system will be presented.

2.2 Fracture behaviour and toughness of in-situ composites in the Ni-Si-Mg system

Fracture behaviour and fracture toughness of the in-situ intermetallic composites and selected single intermetallic alloys for the development of novel structural materials will be evaluated by chevron-notched beam (CNB) specimens. The effect of microstructure and the role of interface between phases on fracture toughness will be investigated through the fracture surface of tested specimens. In addition, the composite rule-of-mixture-like relationship between fracture toughness and volume fraction of phases will be tested.

Since many intermetallic alloys including Ni_3Si in the present work are reported to be susceptible to environmental embrittlement, selected intermetallic composites in the present work will be tested in dry oxygen or vacuum environment to investigate the environmental effect on fracture toughness.

The selection of the compositions to fabricate in–situ intermetallic alloys for fracture toughness test was carried out based on the microstructural evolution in each equilibrium phase region in the Ni-rich area in the Ni-Si-Mg ternary phase diagram established by the present author and the observation of the indentation fracture behaviour of each phase using microhardness test [96Son, 98Son[1]], considering the combination of brittle and ductile phases and the effective configuration of microconstituent phases having fine eutectic-like structures.

2.3 Indentation fracture toughness of intermetallic phases investigated in the present work

The microcracking behaviour, determination of indentation crack system and indentation fracture toughness of the newly discovered ternary intermetallic phases as well as binary phases observed in the present work will be investigated. Finally, a comparison between two different methods, i.e., indentation fracture toughness and chevron-notched toughness bend test will be attempted.

3. Intermetallics in binary Mg-Ni, Mg-Si, and Ni-Si systems

Some of the intermetallic phases in the binary Ni-Si, Mg-Ni and Mg-Si systems previously investigated for the development of structural or functional alloys are reviewed in this section. There is an ambiguity in the stoichiometric designation of the β_1 phase in the Ni-Si binary phase diagram in Fig. A.1 in Appendix A. The β_1 phase has been customarily designated as Ni_3Si, but it is designated as Ni_4Si in the second edition of 'Binary Alloy Phase Diagram' [90Mas]. See Ni-Si crystal structural data from [90Mas] and [91Nas] in Fig. A.1.1(a) and (b) in Appendix A, respectively. At this moment, it is difficult to determine whether the designation of the β_1 phase as N_4Si in the above reference book was made on purpose to distinguish it from the high temperature β_2-Ni_3Si and β_3-Ni_3Si phases or the designation of the β_1 phase as N_4Si is simply a typographical error. Based on the Ni-Si phase diagram in [90Mas], the β_1 phase was designated as Ni_4Si in the previous work by the present authors [96Son, 98Son[1], 98Son[2]]. In this work it will be designated Ni_3Si since it is predominantly designated as Ni_3Si even in the most recent journal papers [00Jan, 00Pik]. The γ phase in the Ni-Si phase system has been designated as $Ni_{31}Si_{12}$ [90Mas, 91Nas] since Frank et al. [71Fra]. However, this phase is also customarily designated as Ni_5Si_2 since it was originally referred to as Ni_5Si_2 in [64Sai]. Therefore, both designations $Ni_{31}Si_{12}$ and Ni_5Si_2 can be used for the γ phase. The γ phase was predominantly designated as Ni_5Si_2 in the previous work by the present authors [98Son[1]].

3.1 Characteristics of $L1_2$ Ni_3Si

$L1_2$ intermetallic alloys such as Ni_3Al are the leading intermetallic compounds which can be applicable practically in industry. Nickel silicide based on $L1_2$-type Ni_3Si is very attractive for high temperature structural applications because of its cubic crystal structure, low density, superior corrosion resistance, specifically in sulfurous and oxidizing environments, and because it displays a positive temperature dependence of the flow strength [50Low, 90Tak[1],

90Tak[2], 98Tak]. However, Ni_3Si suffers from low ductility at ambient temperature. The low ductility has been attributed to both an environmental effect and a poor grain-boundary cohesion [96Liu] as will be discussed in section 3.1.3.

3.1.1 Positive temperature dependence of yield strength

The mechanical strength of metallic crystals generally decreases with increasing temperature due to the thermally assisted motion of dislocations [84Hul]. However, as already mentioned, some of the $L1_2$ type intermetallics such as Ni_3Al [70Tho, 84Liu[2], 84Pop, 89Suz], Ni_3Ga [73Tak, 87Ezz], Ni_3Ge [78Aok, 79Aok[2]] and Fe_3Ga [84Sch] as well as Ni_3Si [90Tak[1], 98Tak] show an increase in strength with increasing temperature.

The positive temperature dependence of the strength was explained by the thermally activated transition via the cross slip mechanism of screw dislocations from {111} planes to {100} planes in this type of crystal structure [73Tak]. The driving force of this cross slip is the difference in the anti-phase boundary energies on {111} and {100} planes. The energy of the anti-phase boundary on {100} plane is decreasing with increasing temperature as compared to that on {111} plane, and thus the unit dislocation constituting a superdislocation on the {111} plane tends to cross slip onto the {100} plane reducing the total energy of superdislocation. However, since the mobility of the dislocation on the {111} plane is much larger than on the {100} plane, the cross slipped parts act as dragging points for the motion of screw dislocations on the {111} plane, thus raising the flow stress with increasing temperature [73Tak, 89Tak, 90Tak[1]]. At sufficiently high temperature where the dislocations on the {100} plane can move easily, the macroscopic slip on the {100} plane controls the deformation [73Tak].

The maximum yield strength of Ni_3Si was reported to occur in between 350°C~450°C [91Tak[1], 97Van], but the peak temperature could be increased up to about 600°C by addition of Ti to Ni_3Si, forming a ternary intermediate phase $Ni_3(Si,Ti)$ [91Tak[1]] which will be discussed in section 3.1.5.

3.1.2 Corrosion resistance

Besides the positive temperature dependence of the strength of Ni_3Si, the corrosion and oxidation resistance of this material is excellent due to the development of a protective silica

film on the surface [97Van]. For example, Hastelloy alloy D® (Hastelloy is a registered trademark of Haynes International, Inc. containing Ni-9 wt. % Si-3 wt. % Cu) is a corrosion-resistant alloy based on Ni_3Si intermetallic compound with unique ability to resist attack by sulfuric acid solutions [89Oli]. In 1993, Sumitomo Metals also developed a corrosion resistant and highly ductile Ni_3Si-3Cr-1Cu-0.005B (wt.%) alloy as a structural material for various environments in which corrosion and particularly sulfuric acid corrosion is severe. The Ni_3Si-3Cr-1Cu-0.005B alloy could be produced by hot working maintaining the corrosion resistance equivalent to Hastelloy D while Hastelloy D is cast alloy and could not be hot worked because of its poor hot ductility [93Tak].

3.1.3 Environmental effects and grain-boundary cohesion

In spite of the above advantages, the use of Ni_3Si has been restricted by the low ductility attributed to a propensity for intergranular fracture. The brittle grain boundary fracture in Ni_3Si is caused by two major factors: (1) moisture-induced hydrogen embrittlement, and (2) poor grain-boundary cohesion [96Liu].

The embrittlement involves the reaction of silicon with water vapour in air according to the following reaction:

$$Si+2H_2O \rightarrow SiO_2+4H$$

and the generation of atomic hydrogen that penetrates into grain boundaries at crack tips causing brittle intergranular fracture [91Liu, 96Liu, 00Pik]. Environmental embrittlement, an extrinsic factor, has also been reported to be a major cause for brittle fracture in many B2, $D0_3$ and $L1_2$ intermetallics such as Ni_3Al [93Liu, 95Geo], Co_3Ti [86Tak], FeAl [89Liu, 90Liu[2], 90Liu[3]], Fe_3Al [90Liu[3]].

Intrinsically weak grain boundaries in strongly ordered alloys such as $L1_2$ type A_3B intermetallic compounds are due to relatively poor grain boundary cohesion as compared with bulk material. Character of intermetallics in the ordered A_3B $L1_2$ structure depends strongly on the bond nature of A-B pair. The stronger covalent A-B bond nature is characterised by the directionality and heteropolarity of electronic charge distribution. As to the heteropolarity, B atoms tend to withdraw electrons from A-A bonds and form covalent A-B bonds. Therefore, the A-B covalent bonds perpendicular to the boundary plane are supposed to sustain grain boundary cohesion. However, according to the computer simulation of the

geometrical configuration in grain boundary region, the A-B bonds drastically decrease while A-A bonds remarkably increase in the grain boundary region. Thus, as a result, the defect structures of bond are introduced into grain boundaries [83Tak, 89Izu], rendering them weaker.

3.1.4 Effect of microalloying elements

Similarly to Ni_3Al and Ni_3Ga, doping of Ni_3Si with boron and carbon has the effects of dramatically improving the ambient tensile ductility by preventing intergranular fracture by hydrogen, improved grain boundary cohesion and strengthening the matrix [89Oli, 89Tau, 98Tak, 00Pik].

A single phase Ni_3Si alloy ($Ni_{77}Si_{23}$) doped with 0.1 at. % boron showed full bend ductility and complete transgranular fracture compared with brittle intergranular fracture for the undoped Ni_3Si [89Tau]. Carbon doping of Ni_3Si also improves bend ductility but is less effective than boron doping [89Tau]. Alloying with 0.1 at. % carbon produced full bend ductility but a mixed mode failure (~30 % transgranular). A $Ni_{81.1}Si_{18.9}$ alloy containing Ni_3Si and Ni(Si) phases doped with 50 ppm boron showed 18.9 % tensile elongation and transgranular fracture mode in air [00Pik] compared with ~0 % tensile elongation for the undoped $Ni_{77.5}Si_{22.5}$ alloy containing Ni_3Si and Ni(Si) [91Liu]. On the other hand, in case of a $Ni_{77.5}Si_{22.5}$ alloy containing Ni_3Si and Ni(Si) doped with 150 ppm boron it has been reported that boron appears to only suppress environmental embrittlement but not to enhance grain boundary cohesion [96Liu]. In this case, the alloy showed an increased tensile elongation (~7.0 %) in air compared with the undoped one, but failed in intergranular fracture mode. Auger analyses indicate that boron and carbon tend to segregate strongly to grain boundaries in Ni_3Si [89Tau] and their beneficial effect may come from reducing hydrogen diffusion, as indicated in B-doped Ni_3Al [94Wan], by blocking the hydrogen diffusion path along the boundary (e.g. by plugging defect sites at the boundary). However, at higher boron concentrations in Ni_3Si, borides are formed at the grain boundaries and the fracture mode becomes increasingly intergranular [89Tau]. Similar degradation in ductility has been observed in boron-doped $Ni_{76}Al_{24}$ and $Ni_{76}Ga_{24}$ alloys when the boron solubility limit is exceeded [84Tau, 85Liu, 89Tau].

As in the case of Ni_3Al and Ni_3Ga doped with boron that show improved ductility and a fully transgranular fracture morphology only for nickel-rich deviations from stoichiometry, that is, Ni concentration greater than 75 at. %, the ability of both boron and carbon to suppress intergranular fracture in Ni_3Si is greater for high nickel concentration [89Tau].

3.1.5 Effect of macroalloying elements

As summarized in Fig. 3.1 [84Och], the solid solubility of ternary elements is generally small in Ni_3Si in contrast to Ni_3Al except for Al, Ga, and Ge which substitute for Si and form continuous solid solutions up to their respective terminal $L1_2$ phases of Ni_3Al, Ni_3Ga, and Ni_3Ge [84Och, 98Tak]. Apart from these elements showing complete solid solubility in Ni_3Si, Ti can be accommodated up to about 11 at. % at 1173K. The solubility lobe deviates toward excess Ni composition at higher Ti contents [90Tak[2], 98Tak]. Mn and Nb are also soluble to some extent, while Cr, Cu, Fe and V are insoluble [84Och, 98Tak].

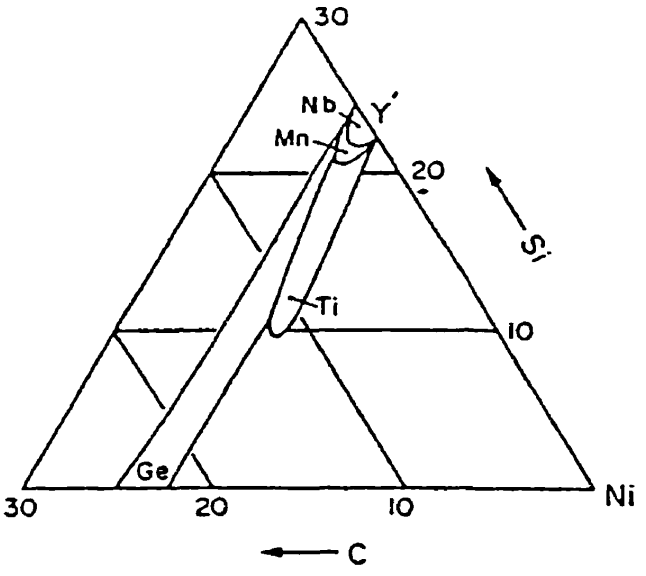

Fig. 3.1 Schematic diagram of the solubility lobes of ternary $L1_2$-type Ni_3Si phase at 1273 K for various elements [84Och]. 'C' stands for the alloying elements (Ge, Ti, Mn, and Nb).

The addition of Ti to Ni_3Si has been reported as a breakthrough to overcome the brittle intergranular fracture of Ni_3Si [86Oli, 90Tak[1]]. The yield strength and the peak temperature of the yield strength increase with increasing Ti concentration. The addition of 4.4 at. % to

11.3 at. % Ti to the as-cast Ni_3Si material resulted in the bend ductility in air at room temperature. This bend ductility was shown to become more obvious for Ni-rich composition [90Tak[1]]. The ductilization of the $L1_2$ ordered alloys can be obtained by controlling the chemical composition and thereby the electrochemical bonding nature at the grain boundary region of this structure [85Tak, 88Izu, 90Tak[2]].

Furthermore, the addition of more than 4 at. % Ti to Ni_3Si was shown to lead to a direct solidification of $L1_2$ phase from melt, and thereby to eliminate the isomorphic structure of Ni_3Si (Fig. A.1 in Appendix A). Thus, the $L1_2$-type Ni_3Si phase is stabilized up to its melting point by the addition of Ti [71Wil, 90Tak[2]].

Little is known about the effect of other substitutional solutes on the ductility and fracture of Ni_3Si because of low solubilities of those elements as mentioned earlier. However, the effect of some transition elements on the strength and fracture behaviour of the ternary $Ni_3(Ti,Si)$ alloys was examined [91Tak[1], 98Tak]. The addition of Hf and Nb to $Ni_3(Ti,Si)$ slightly reduced the tensile elongation at low temperatures but improved at high temperatures, whereas the addition of Cr, Mn, and Fe to $Ni_3(Ti,Si)$ improved the tensile elongation over the whole range of test temperatures [91Tak[1], 98Tak].

Recently, the influence of second-phase dispersion on environmental embrittlement of $Ni_3(Si,Ti)$ alloys with transition elements V, Nb, Zr, and Hf has been reported [99Tak]. In case of Zr- and Hf- added $Ni_3(Si,Ti)$ alloys showed lower tensile elongation than the unalloyed $Ni_3(Si,Ti)$ when deformed in vacuum as well as in air. Consequently, Zr- and Hf-containing second phase dispersions, Ni_3Zr ($D0_{19}$) and Ni_3Hf, respectively, have little effect of improving the moisture-induced embrittlement. However, in the V-added $Ni_3(Si,Ti)$ alloy with Ni solid solution, tensile elongation (around 32-33%) of the alloy deformed in air was almost identical to that of the V-added $Ni_3(Si,Ti)$ alloy deformed in vacuum and also to the unalloyed $Ni_3(Si,Ti)$ deformed in vacuum. In the $Ni_3(Si,Ti)$ alloy with Nb-containing second phase Ni_3Nb ($D0_a$), even if the alloy deformed in vacuum showed a lower tensile elongation than the unalloyed $Ni_3(Si,Ti)$ alloy in vacuum, the alloy deformed in air showed a higher tensile elongation than the unalloyed Ni(Si,Ti) deformed in air. By demonstrating the difference in the ductile-to-brittle transition (DBT) strain rate of unalloyed $Ni_3(Si,Ti)$, Nb-added $Ni_3(Si,Ti)$ alloy with Nb-containing second phase, and Nb-added $Ni_3(Si,Ti)$ $L1_2$ mono-phase alloy, they observed that Nb-added $Ni_3(Si,Ti)$ $L1_2$ mono-phase alloys have the highest

DBT strain rate, indicating that the Nb-added $Ni_3(Si,Ti)$ $L1_2$ mono-phase alloys are environmentally sensitive. Therefore, they excluded the effect of alloy composition of the $L1_2$ matrix and exclaimed that the second phases may be directly attributed to the improvement in environmental embrittlement. The possible mechanisms responsible for the beneficial effect are: hydrogen may be preferentially (1) absorbed into the second-phase dispersion, or (2) trapped at interface between the $L1_2$ matrix and the second-phase dispersion. Consequently, hydrogen would be depleted at the grain boundaries of $L1_2$ matrix. Other explanation is that heavily deformed plastic zone (consisting of high dislocation density) formed around the second-phase dispersion gives preferential trap site to hydrogen during deformation.

3.2 Characteristics of $MgNi_2$ Laves phase

3.2.1 General characteristics of Laves phases

$MgNi_2$ (see Mg-Ni binary system in Fig. A.2 in Appendix A) belongs to a group of intermetallic phases called 'Laves phases'. So, their general characteristics will be discussed first.

One important principle of compound formation that is based on the relative sizes of the component atoms was first set forth by Laves. Laves concept was that certain metallic structures might be understandable in terms of the creation of dense packings of atoms of different sizes, and this might then require both a limited range of radius ratio for the two species as well as a specific proportion of the components. Compounds of this type with the formula AB_2 have since been extensively studied and are known as Laves structures. When the component atoms differ in size by a factor of about 1.1-1.6 (ideally 1.225 [36Lav, 95Wes[2]]) it is possible for the atoms to fill space most efficiently if the atoms order themselves into one of the so-called Laves phases [81Por].

There are several factors governing lattice structure of metallic materials such as atomic number, size ratio, electrochemical difference, or electron/atom ratio [95Wes[1]]. Usually, the observed structure is a result of the combined action of two or more factors [95Wes[1]]. However, it was realized that only in the limiting cases will the action of a single one of the structure-determining factors be sufficient to determine structure and bonding type. Laves

phases are in such a limiting case. Only the size ratio for the two species as well as a specific proportion of the components is an important factor as a structure-determining factor. In Laves phases, the stability is mostly due to the increase in the coordination number in formation of these phases from the elemental components [95Wes^2]. In the structure of the cubic $MgCu_2$ Laves phases each Mg atom is surrounded by twelve Cu and four Mg atoms, whereas each Cu atom has six Mg and six Cu atoms as nearest neighbours [95Wes^2]. There are three types of Laves phases as follows:

- $MgCu_2$(C15), cubic cF24
- $MgZn_2$(C14), hexagonal hP12
- $MgNi_2$(C36), hexagonal hP24

Multilayer Laves phases based on the $MgZn_2$ type binary Laves phase were also observed in the Mg-Li-Zn ternary system and derivatives of the $MgZn_2$ and $MgCu_2$ type ternary Laves phases were also observed. For example, Mg_2Cu_3Si and $MnInCu_4$ are $MgZn_2$ type, and Mg_2Cu_3Al and $MgSnCu_4$ are $MgCu_2$ type.

3.2.2 Application of Laves phases as a structural material

One way to select candidate alloys of possible interest for high temperature applications is to require a combination of high melting temperature and low density. However, in general, the leading intermetallic alloys with $L1_2$ structure (FCC) (e.g., Ni_3Al) have relatively low melting points, T_m, and relatively high density [87Fle, 98Kim]. On the other hand, materials with complex structures (and hence little chance for ductility) have much better (T_m/density) combinations [98Kim]. Based on these type of considerations it appears that Laves phases or other complex structures may be good candidates as strengthening components for future high-temperature structural alloys and have received increasing attention in recent years [92Liv, 95Liu, 98Kim]. Generally speaking, Laves phases have high melting points and fairly low specific gravities [93Chu, 98Kim]. Even if these alloys are brittle at low temperature plastic deformation by dislocation motion is observed in these alloys at high temperatures, above 0.65 Tm [65Mor, 89Liv, 89Ohb, 98Kim]. If an alternate deformation mode, e.g., mechanical twinning, can be induced at low temperature, then the low temperature brittleness problem may be alleviated.

3.2.3 Deformation behaviour in Laves phases

Deformation behaviour and deformation induced defects in Laves phases has been studied [91Liv, 93Chu, 93Haz, 95Liu, 98Kim]. Twinning was reported in C15 intermetallic, $MgCu_2$ by Moran [65Mor] and in (Hf, Nb, Ti)V_2 alloys by Livingston et al. [90Liv]. Liu et al. [92Liu] observed both twining and stress-induced phase transformations (from C15 to C36) in $ZrFe_2$. Chu et al. [93Chu] observed twining, raising compressive ductility to about 3-4% below 300°C, and dislocation plasticity after deformation above 800°C in Hf-V-Nb C15 Laves phase. Study of single-phase C36 alloys of $MgNi_2$ and $MgCu_{0.4}Zn_{1.6}$ [91Liv] showed that after compression at high temperature, the dominant microstructural features were dislocations and high density of extended faults on the basal plane. Liu et al. [95Liu] also observed nonbasal faults on the pyramidal planes {1011} and {1012} and the prismatic plane {1010} in $MgNi_2$ after room-temperature compression.

3.3 Characteristics of Mg_2Ni

Mg_2Ni is a low density (the calculated density from its lattice parameters is 3.46g/cm^3) Mg rich intermetallic compound having 18 atoms in a hexagonal symmetry with the lattice parameters, a=0.519nm and c=1.321nm [85Vil]. The Mg_2Ni compound has recently gained an interest as a functional alloy for the development of nanostructured hydrogen storage alloys for fuel cells [98Abd, 98Cra].

3.3.1 Mg_2Ni-Mg based hydrogen storage alloys

The use of a hydrogen-storage medium, combined with a fuel cell to convert the hydrogen into electrical energy, is an attractive proposition for a clean transportation system. Ball-milled nanocrystalline magnesium and magnesium-based hydrogen storage alloys by forming metallic hydrides are promising energy conversion and storage medium because of their capability of absorbing hydrogen in large quantities, lower specific gravity, richer mineral resources, low material cost and so on [98Noh]. In terms of hydrogen absorption capacity magnesium (7.7 wt.%) seems to be a good candidate to be used in hydrogen combustion engine, but the hydrogen absorption-desorption process needs high temperature (>600K) with very low kinetics [98Abd, 99Sch]. Therefore, Mg rich intermetallic alloys are being

developed to solve this problem. Mg_2Ni (3.7 wt.% of hydrogen absorption capacity) or Mg_2Ni-based alloys is the most intensively studied [98Abd, 98Cra, 98Lia, 98Noh, 98Tes, 99Sch] since the hydrogen absorption and desorption kinetics in Mg_2Ni are better than in Mg. For example, in a Mg+Mg_2Ni eutectic alloy (6.3 wt.% of hydrogen absorption capacity), magnesium provides most of the hydrogen-storage capacity and the Mg_2Ni is to provide kinetic "gate" to accelerate the hydriding/dehydriding reaction. However, after all of the magnesium has been transformed to a hydride (MgH_2), and with additional hydrogen pressure, the Mg_2Ni phase also absorbs hydrogen to form Mg_2NiH_4 [99Sch]. Nevertheless, relatively high temperature (170-250°C) in the case of Mg_2Ni, is still required for reversible absorption and desorption of hydrogen at around atmospheric pressure [98Noh]. Therefore, the advent of such a system will require further research into magnesium based intermetallic alloys that provide a high hydrogen capacity, as high as Mg, good absorption and desorption kinetics, and a low operation temperature.

3.4 Characteristics of Mg_2Si

Mg_2Si is the only stable intermetallic phase in the Mg-Si binary system [90Mas] (see Fig. A.3 in Appendix A). The crystal structure of this compound is face centered cubic (C1-CaF_2 type) with 12 atoms in a unit cell [90Mas]. It has a density of about 2g/cm^3 [71Sim, 90Sch, 93Li[1], 93Var] and an elastic modulus of about 110-120GPa [71Sim, 90Sch, 93Li[1], 93Var], making it the intermetallic with the highest specific modulus as compared to other structural intermetallics [93Li[1], 93Var]. As will be mentioned in section 2.4, Li et al. [93Li[1]] and Varin et al. [93Var] studied Mg_2Si intermetallic alloys alloyed with 1 at. % of several different third elements such as Ni, Co, Cu, Ag, Zn, Mn, Cr, and Fe to improve its ductility and /or fracture toughness by a macroalloying effect for the development of a lightweight material, for medium- to high-temperature applications, especially in the automobile and transportation industries. [93Var, 93Li[1]]. Vickers indentation fracture toughness of Mg_2Si reported in [93Li[1], 93Var] was less than about 1.0 MPa.m$^{1/2}$ and chevron-notch beam (CNB) fracture toughness of Mg_2Si with 1 at. % addition of various third elements mentioned above less than 1.5 MPa.m$^{1/2}$ at room temperature. VHN of Mg_2Si at 100g load was reported to be in the range of 406-472. The highest Vickers hardness of the second phase in the Mg_2Si alloy was measured in the Ni-modified Mg_2Si to be 472 kg/mm^2 [93Li[1]]. The results of fracture

toughness test by four point bending of chevron-notched specimens indicated that Ni seemed to be the most efficient alloying element in improving fracture toughness by modifying the microstructure [93Li[I]]. This led to more investigation about the effect of a systematic increase in the Ni content on the microstructure, microhardness, strength, fracture toughness and microcracking of Mg_2Si-Ni alloys.

4. Ni-Si-Mg ternary alloy system

4.1 Intermetallic phases in the Ni-Si-Mg ternary system

Some earlier work reported the existence of Ni-Si-Mg ternary intermetallic phases $MgNi_6Si_6$ [81Buc] and Mg_2SiNi_3 [85Nor].

The Mg_2SiNi_3 was observed by Noreus et al. [85Nor] by alloying Mg_2Ni with Si for the development of alloys for hydrogen storage purpose. Both $MgNi_6Si_6$ and Mg_2SiNi_3 were reported as having a hexagonal structure with lattice parameters, a=0.4948nm and c=0.3738nm, and a=0.50044nm and c=1.10894nm, respectively. No physical or mechanical properties of the phases were reported. Recently, Pearson's Handbook Desk Edition (crystallographic data for intermetallic phases) [97Vil] reported structure types of $MgNi_6Si_6$ and Mg_2SiNi_3 as hexagonal Cu_7Tb and Fe_2Tb-type, respectively.

4.2 Ni-Si-Mg ternary phase diagram

4.2.1 Ni-Si-Mg ternary phase diagram by Varin and Li [93Li[1], 93Var, 94Li, 95Var]

Varin and Li carried out preliminary studies of intermetallics in the Mg-Si and Ni-Si-Mg alloy systems [93Li[1], 93Var, 94Li, 95Var]. As discussed in section 3.4, an attempt was made to add different third elements such as Ni, Co, Cu, Ag, Zn, Mn, Cr, and Fe to the brittle Mg_2Si intermetallic phase to improve its ductility and /or fracture toughness by a macroalloying effect [93Var, 93Li[1]]. Fig. 4.1 shows the originally proposed room temperature isothermal section of the ternary Ni-Si-Mg phase diagram in the Ni-rich area where the δ-Ni_2Si compound was proposed to accommodate up to about 22 at. % Mg [95Var]. Therefore, this new ternary single phase was designated as δ'-$Ni_2(Si,Mg)$ assuming that it was derived from

δ-Ni_2Si being a solid solution of Mg in δ-Ni_2Si. However, the nature of the phase was not well understood and its phase field was only tentatively outlined in Fig. 4.1.

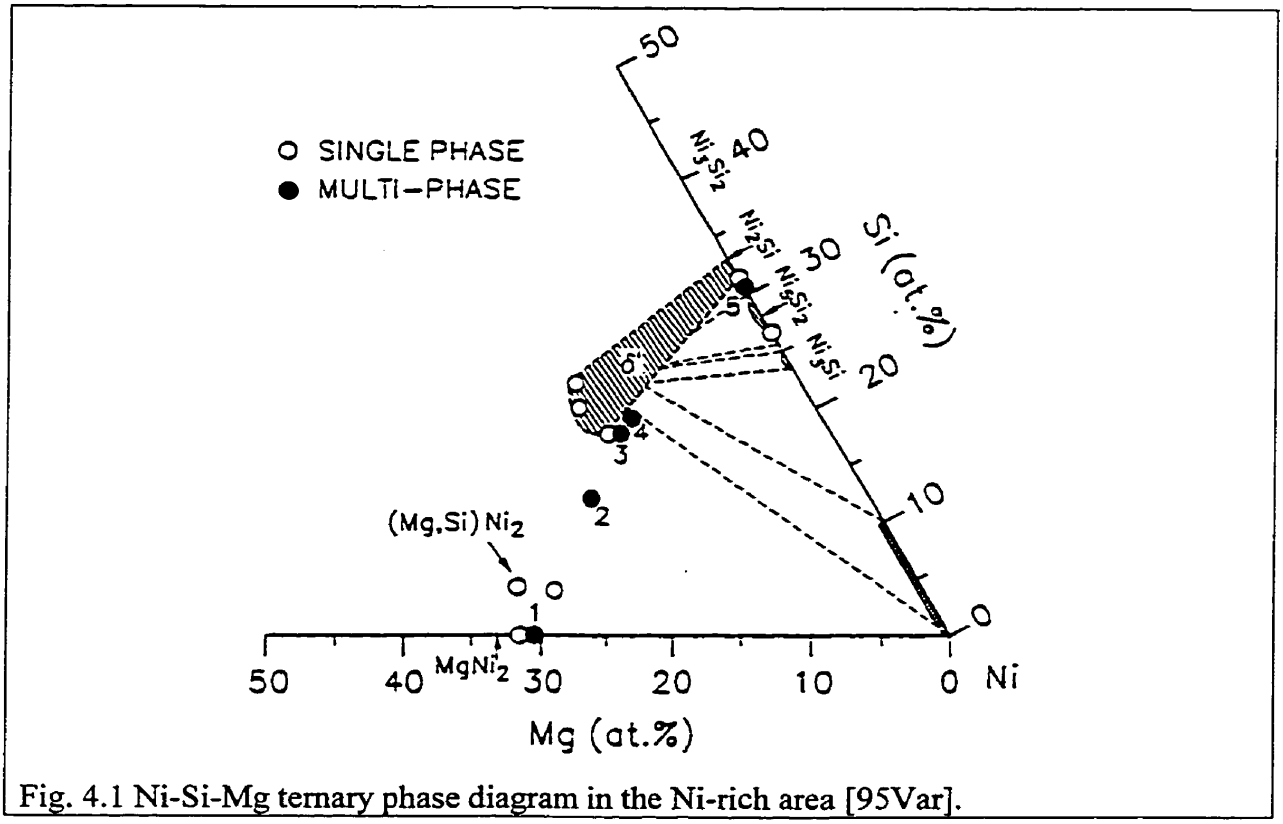

Fig. 4.1 Ni-Si-Mg ternary phase diagram in the Ni-rich area [95Var].

4.2.2 Ni-Si-Mg ternary phase diagram by Song and Varin [95Son, 98Son[1]]

The present author reported a preliminary part of the Ni-Si-Mg phase system covering the Ni- and Si-rich corner in the Master's thesis [96Son] and the following article [98Son[1]]. The Ni-Si-Mg ternary phase diagram after slow cooling of the investigated alloys from the homogenization temperature to room temperature was established by means of EDS analysis using high purity elemental standards and identification of all the phases by x-ray diffraction. As shown in Fig. 4.2 the locations of overall compositions and phase compositions of the alloys investigated by the present author after homogenization are shown in the phase diagram including data points obtained from previous study by Varin and Li [95Var] shown in Fig. 4.1. Ni_4Si in Fig. 4.2 is designated as Ni_3Si in the present work.

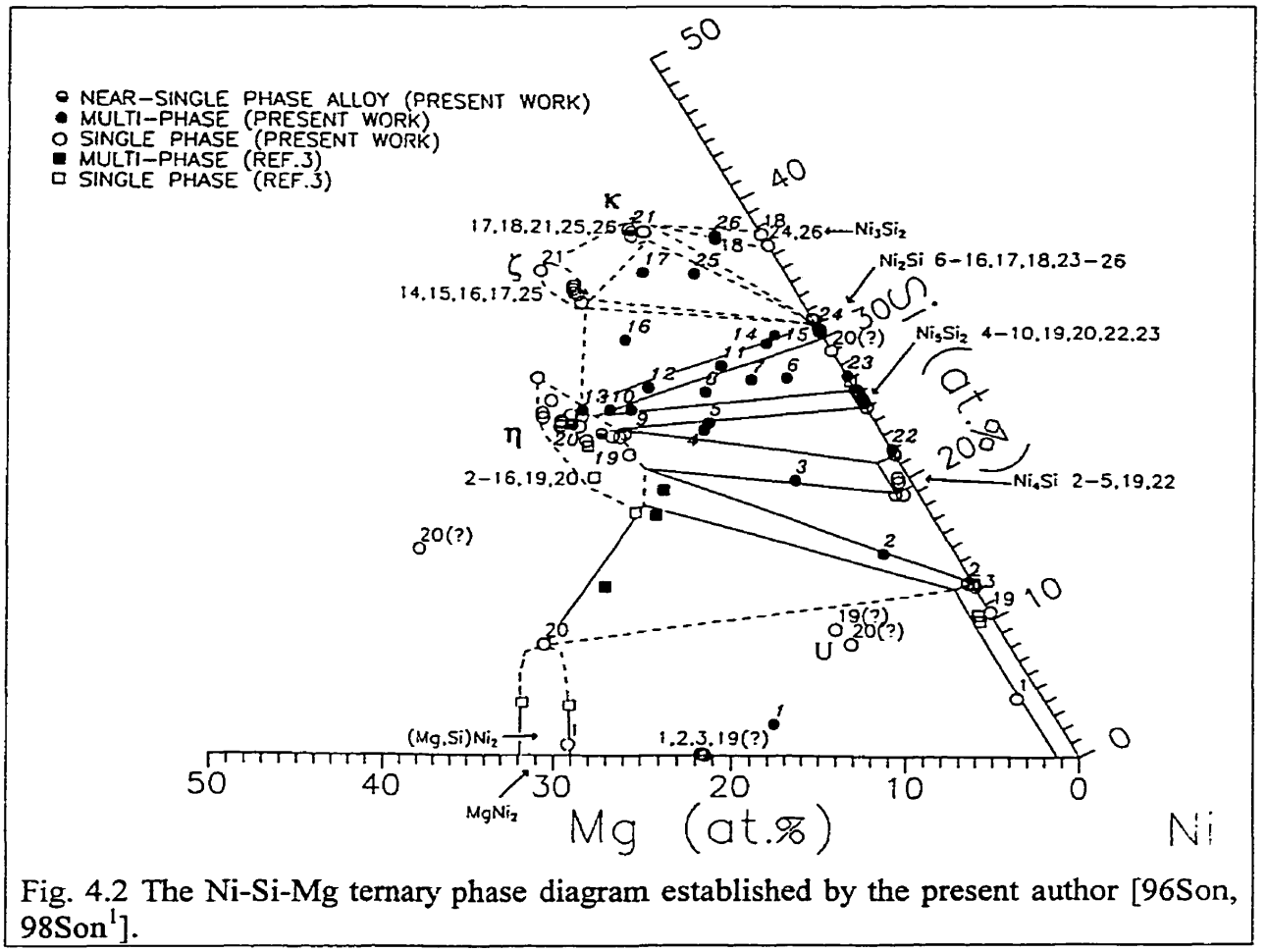

Fig. 4.2 The Ni-Si-Mg ternary phase diagram established by the present author [96Son, 98Son[1]].

As shown in the ternary phase diagram in Fig. 4.2, three ternary intermetallic phases, η, κ, ζ were discovered. The designations of the newly found ternary phases were arbitrarily chosen. The solid solubility of Mg in δ-Ni_2Si was found to be zero. None of δ-Ni_2Si in the phase diagram contained Mg. Therefore, the δ'-$Ni_2(Si,Mg)$ phase proposed by Varin and Li in [95Var] was not a solid solution of Mg in δ-Ni_2Si. The δ'-$Ni_2(Si,Mg)$ phase in [95Var] was redesignated as the η phase in Fig. 4.2. The stoichiometries of the Ni-Si binary phases, Ni_4Si (Ni_3Si), $Ni_{31}Si_{12}$ (or Ni_5Si_2), Ni_2Si, and Ni_3Si_2 in the ternary phase diagram are always about 2 at. % deficient in Si content as compared to those phases described in the Ni-Si binary phase diagram [90Mas]. The stoichiometry of the Mg-Ni phase, $MgNi_2$, even if it is not clearly determined in Fig. 4.2, is also deficient in Mg content.

Crystal structure identification was carried out for the η and the κ phases [96Son, 98Son[1]] by a pattern indexing computer program, TREOR [85Wer]. The lattice structure of the η phase was determined to be a cubic system with a=b=c=1.1281nm and a=b=c=1.1308nm from the two near single phase alloys, 19 and 20 in the η compositional ranges in Fig. 4.2, respectively. X-ray diffraction pattern of η was found to be the same as that of the phases having $Mn_{23}Th_6$ structure type (also cited as $Mg_6Cu_{16}Ni_7$, or $Mn_6Ni_{16}P_7$-type), which has a complicated face-centered cubic structure (F.C.C) with 116 atoms in a unit cell [85Vil]. In case of the κ phase, two possible lattice structures were obtained. One is an orthorhombic structure with the lattice parameters, a=1.1651nm, b=1.0060nm, and c=0.5812nm and the other is a hexagonal structure with the lattice parameters, a=b=1.1623nm, c=1.1650nm. However, hexagonal system seems to be more likely because hexagonal structure is more symmetrical than orthorhombic one and as such, it is more difficult to satisfy diffraction conditions for hexagonal structures. The determination of the crystallographic structure of the ζ phase was not attempted since there was difficulty with fabricating a single ζ phase alloy.

5. In-situ composite toughening

5.1 Toughening mechanisms and toughness calculations in composites

The concept of toughening intrinsically brittle intermetallic and ceramic materials by the introduction of soft and ductile reinforcements has been used in the design of advanced composites [89Eva, 92Rav, 93Her, 94ven]. Significant toughening can be achieved by incorporating ductile particles or fibers in low toughness materials. The presence of a ductile phase in a brittle matrix can enhance the overall fracture toughness of a two-phase material usually by accommodating plastic incompatibility at grain or phase boundaries, blunting of pre-existing flaws or bridging of the crack surfaces in the crack wake [93Cha[1]]. The enhancement in fracture toughness is simply due to the decrease in crack tip stress intensity by several toughening mechanisms when a sharp crack encounters the ductile phase.

The toughening mechanisms in composite materials can be considered either as intrinsic or extrinsic [87Rit, 92Cha, 94Cha[1], 94Cha[2], 95Cha[1]]. Intrinsic mechanisms affect the initiation toughness values. The term initiation toughness refers to the critical stress intensity at which crack extension commences and is customarily referred to as the K_{IC} value when plane strain condition prevails. In contrast, extrinsic mechanisms are expected to affect mostly the crack growth toughness by inducing a rising resistance curve behaviour through the formation of a bridged zone in the crack wake. The various toughening mechanisms, which result from the use of a ductile phase are summarized in Fig. 5.1. Toughening processes such as crack- tip blunting [68Hut, 68Ric, 85Rit, 89Ode, 90Cha[1], 92Cha, 93Cha[1], 94Noe], crack trapping [81Krs, 91Bow, 93Her], microcrack renucleation [93He, 93Her, 93Sha], and crack-tip interface debonding [89Eva, 90Dev, 90Eva, 91Cao, 93Cha[2], 93He], which originate from properties of the constituents can be considered as intrinsic mechanisms. Toughening processes such as crack bridging [88Bud, 88Ell, 89Ash, 89Cao, 89Fli, 89Mat, 92Mur, 95And, 96Ben, 96Sun], ligament toughening [91Cha, 92Cha 93Cha[1], 94Cha[2], 95Cha[2]], crack

deflection [85Sur, 90Eva, 90Cha[2], 92Cha, 92Sob, 93Sob[1]], which improve fracture resistance by lowering the near-tip stress intensity levels can be considered as extrinsic mechanisms.

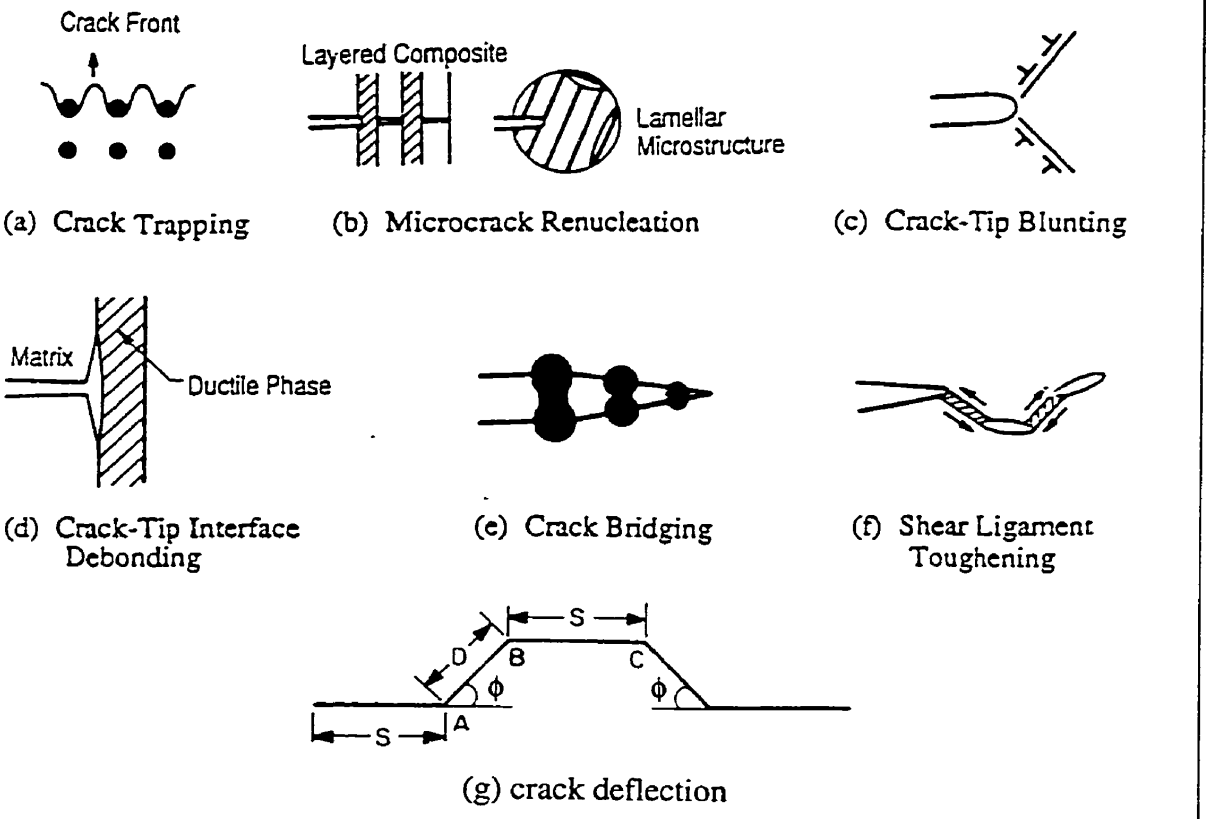

Fig. 5.1 Toughening mechanisms in composite materials [95Cha[1]].

Fig. 5.2 shows the relationships between toughening mechanisms and fracture resistance. The stress intensity curve for the brittle single-phase matrix shown as the lower dashed line, K_m in Fig. 5.2 is a straight line with zero slope. The initiation toughness, K_i of composites is higher than brittle single-phase materials. Once crack extension occurs, a higher K level may be required to extend the crack tip further, resulting in a rising fracture resistance curve, as shown by the solid line in Fig. 5.2. The initiation toughness, K_i, denotes the stress intensity level at the onset of stable crack growth, while the K_g value of the fracture resistance curve represents the crack growth toughness at the onset of unstable fracture. Both the initiation and crack growth toughness can be enhanced by the presence of a ductile phase in the microstructure.

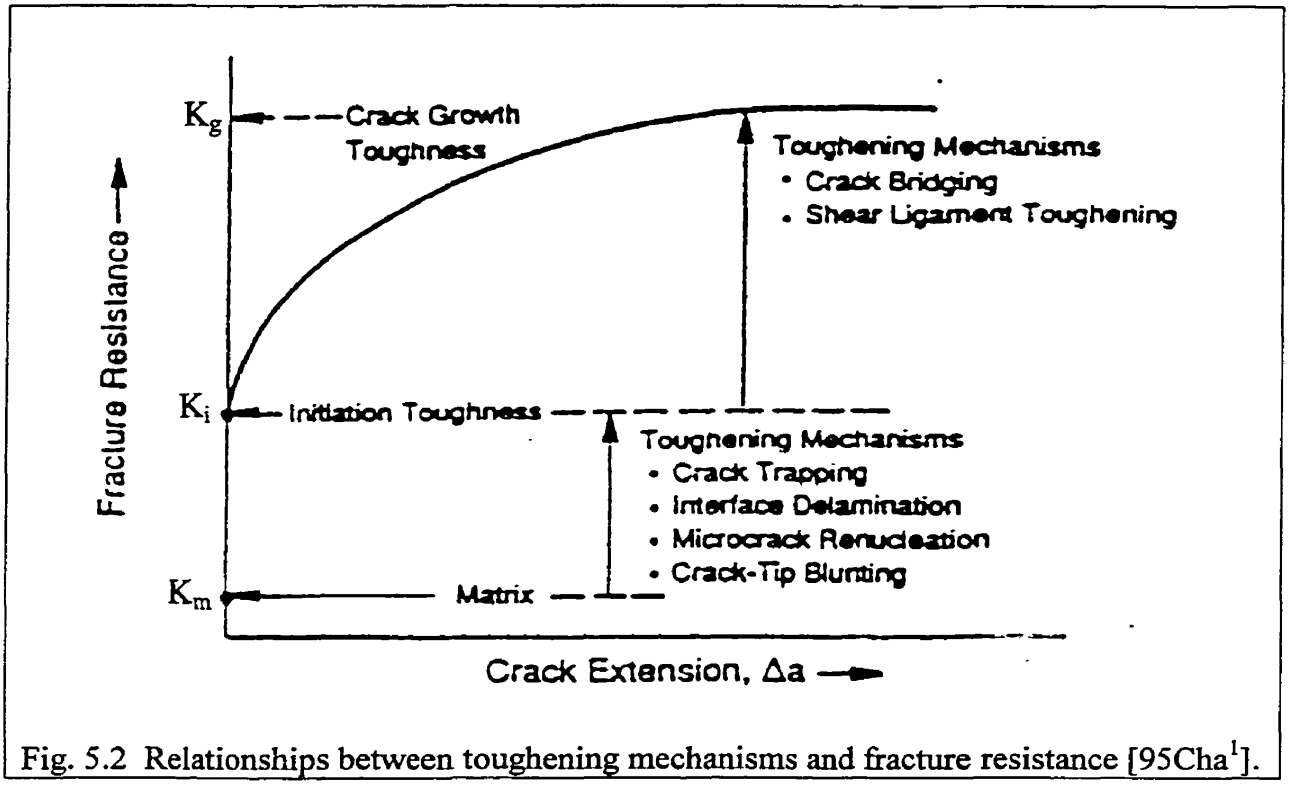

Fig. 5.2 Relationships between toughening mechanisms and fracture resistance [95Cha[1]].

As shown in Fig. 5.2, intrinsic toughening mechanisms increase the initiation fracture toughness, K_i, while extrinsic toughening mechanisms increase the crack growth toughness, K_g.

There have been many toughening mechanisms and analytical models proposed to evaluate the amount of enhancement of the stress intensity factor by the presence of a ductile phase. Several models for fracture behaviour and fracture toughness calculations in composite materials, and the factors affecting fracture toughness in each model will be discussed.

5.2 Intrinsic mechanisms

5.2.1 Crack-tip blunting by a ductile phase

One important aspect of a ductile phase in the fracture process of a two-phase microstructure containing a brittle intermetallic matrix is shown in Fig. 5.3. The ability of strain accommodation in a brittle intermetallic matrix is relatively low because of the propensity for grain-boundary or cleavage cracking which results from an insufficient number of

independent slip systems in the intermetallic matrix [90Kim, 92Cha]. The presence of a continuous ductile phase in the microstructure as shown in Fig. 5.3 provides an area for plastic accommodation at the grain or phase boundaries. One possible consequence of ductile-phase accommodation is that the matrix phase can be deformed to a greater extent without leading to the formation of microcracks at the adjoining grain or phase boundaries [90Cha[2]]. This would lead to a higher attainable strain accommodation near the crack tip and a higher K_{IC} value, as shown in Fig. 5.3.

Initiation of crack growth in ductile alloys can generally be considered in terms of a critical strain criterion, which assumes that fracture occurs when the strain at a characteristic distance from the crack tip exceeds a critical value [85Rit, 90Cha[1]].

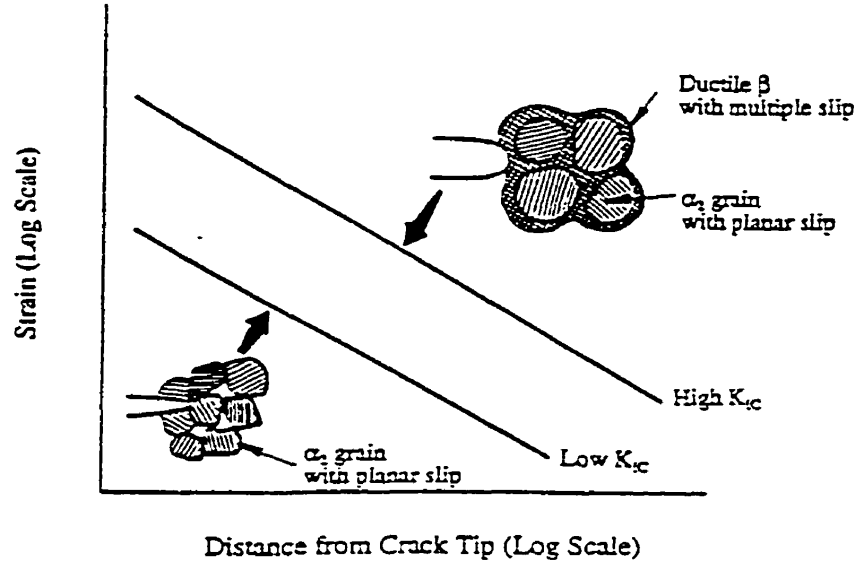

Fig. 5.3 Schematics showing the near-tip strain distribution and the K_{IC} values of a brittle intermetallic matrix (α_2) may be increased by the presence of a continuous ductile phase that blunts the crack tip and accommodates strain incompatibility at the α_2 grain boundaries [92Cha, 93Cha[1]].

Toughness enhancement resulting from crack-tip blunting by a ductile phase has been modelled by Chan [92Cha] using the Hutchinson, Rice, and Rosengren (HRR) crack-tip field [68Hut, 68Ric] and a critical strain fracture criterion whose value is increased by the presence of a ductile phase in the manner described in Fig. 5.3.

In particular, it is assumed that the yield stress, σ_y and effective fracture strain, $\bar{\varepsilon}_f$, of the two-phase microstructure are related to the corresponding properties of the constituent phases according to the rule of mixtures, leading to

$$\sigma_y^c = V_m \sigma_y^m + V_d \sigma_y^d \qquad (5.1)$$

$$\bar{\varepsilon}_f = V_m \bar{\varepsilon}_f^m + V_d \bar{\varepsilon}_f^d \qquad (5.2)$$

where V_m and V_d are the volume fraction of the matrix (β in Fig. 5.3) and ductile phase (α in Fig. 5.3). The $\bar{\varepsilon}_f^m$ and $\bar{\varepsilon}_f^d$ represent the effective fracture strain values for the matrix and ductile second phases, respectively.

From the HRR theory [68Hut, 68Ric] the near-tip effective strain distribution can be described by

$$\bar{\varepsilon}_m = \alpha' \varepsilon_y^m \left[\frac{J_m}{\alpha' \varepsilon_y^m \sigma_y^m I_n r} \right]^{n/(n+1)} \bar{\varepsilon}(\theta, n) \qquad (5.3)$$

for the matrix and

$$\bar{\varepsilon}_c = \alpha' \varepsilon_y^c \left[\frac{J_c}{\alpha' \varepsilon_y^c \sigma_y^c I_n r} \right]^{n/(n+1)} \bar{\varepsilon}(\theta, n) \qquad (5.4)$$

for a composite containing a brittle matrix, reinforced with a ductile second phase, when the hardening exponents, n, for the matrix and composite are identical. I_n is an integration constant that depends on n, α' a dimensionless constant, $\bar{\varepsilon}_m$ effective strain of matrix, $\bar{\varepsilon}_c$ effective strain of composite, ε_y^m yield strain of matrix, ε_y^c yield strain of composite, σ_y^m yield stress of matrix, and σ_y^c yield stress of composite.

Dividing Eq. (5.4) by Eq. (5.3) leads to

$$\frac{\bar{\varepsilon}_c}{\bar{\varepsilon}_m} = \frac{\varepsilon_y^c}{\varepsilon_y^m} \left[\frac{J_c}{J_m} \right]^{n/(n+1)} \left[\frac{\varepsilon_y^m \sigma_y^m}{\varepsilon_y^c \sigma_y^c} \right]^{n/(n+1)} \qquad (5.5)$$

leading to

$$\frac{\bar{\varepsilon}_c}{\bar{\varepsilon}_m} = \left[\frac{J_c}{J_m} \right]^{n/(n+1)} \left[\frac{\sigma_y^m}{\sigma_y^c} \right]^{(n-1)/(n+1)} \left[\frac{E_m}{E_c} \right]^{1/(n+1)} \qquad (5.6)$$

when $\varepsilon_y^c = \sigma_y^c / E_c$ and $\varepsilon_y^m = \sigma_y^m / E_m$. Equation (5.6) can be combined with

$$J = \frac{(1-\nu^2)K^2}{E} \qquad (5.7)$$

in plane strain condition to give

$$\frac{K_c}{K_m} = \left[\frac{\sigma_y^c}{\sigma_y^m}\right]^{(n-1)/2n}\left[\frac{\bar{\varepsilon}_c}{\bar{\varepsilon}_m}\right]^{(n+1)/2n}\left[\frac{E_c}{E_m}\right]^{(n+1)/2n} \qquad (5.8)$$

leading to

$$\frac{K_c}{K_m} = \left[1+(\Sigma-1)V_d\right]^{(n-1)/2n}\left[1+(\Lambda-1)V_d\right]^{(n+1)/2n}\left[\frac{E_c}{E_m}\right]^{(n+1)/2n} \qquad (5.9)$$

where $\Sigma = \dfrac{\sigma_y^d}{\sigma_y^m}$ and $\Lambda = \dfrac{\bar{\varepsilon}_f^d}{\bar{\varepsilon}_f^m}$

by substituting Eqs. (5.1) and (5.2) into Eq. (5.8) and assuming the Poisson's ratios for the matrix and composite are equal.

Fig. 5.4 shows the calculated values of the toughening ratio as a function of the volume fraction of the ductile phase for various values of Σ and Λ in Eq. (5.9), for the case where E_c=E_m. As expected, the toughening ratio increases with increasing values of Σ and Λ. In addition, the toughening ratio increases with the volume fraction of the ductile phase in a non-linear manner.

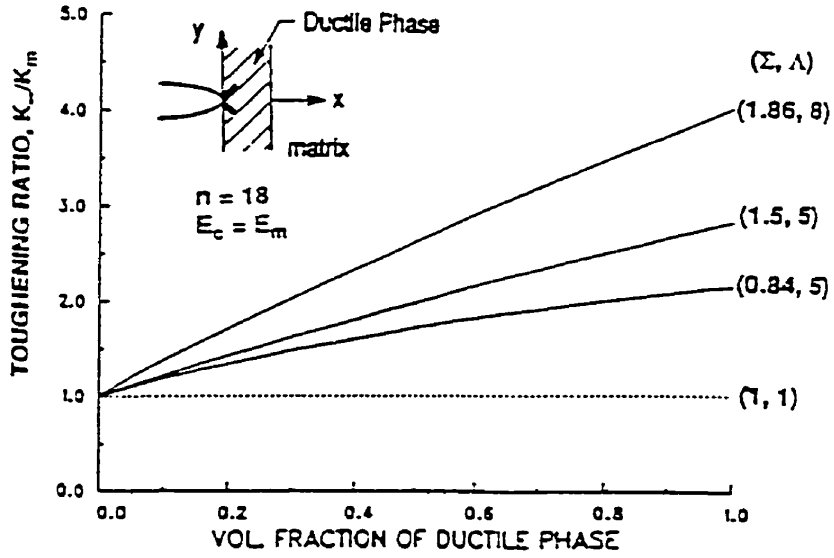

Fig. 5.4 Calculated values of the toughening ratio due to ductile-phase blunting of the crack tip as a function of volume fraction of the ductile phase for various assumed values of Σ and Λ [92Cha].

5.2.2 Microcrack renucleation

When the crack front cannot loop around the ductile phase, as is the case in a layered composite, the initiation toughness may be determined by the renucleation of a microcrack in the matrix ahead of the main crack [95Cha[1]].

In materials having a layered microstructure, with alternating brittle and ductile layers, crack extension is impeded at the interface [91Cao, 93Her]. The impediment occurs by plastic blunting when the interface has good integrity, or by splitting (debonding) when the interface decoheres. In both cases, the intervening ductile layer modifies the stress ahead of the crack front [93Her]. Because of the existence of this ductile layer, the next brittle layer experiences diminished stress. Consequently, a crack renucleation phenomenon must occur at this reduced stress level before crack growth can proceed.

Microcrack renucleation has been modelled by Shaw *et al.* [93Sha] by using metal/ceramic layered composites. In layered metal/ceramic composites, the important concept is how cracks that first form in brittle layer deliver further damage to the neighbouring layers. For a crack located in a brittle layer with its tip incident upon a ductile layer (as illustrated in Fig. 5.5) two limiting responses can be identified: i) a small-scale yielding (SSY) limit, wherein the plastic zone extends completely through the ductile layer but only a small distance compared to the crack length along the layer and ii) a large-scale yielding (LSY) limit, characterized by the plastic zone extending a relatively large distance normal to the crack. The SSY limit exhibits relatively large stress concentrations and is expected to result in local load sharing. Local load sharing results in a stress concentration around an initial crack, which causes damage to progress laterally, often as a dominant mode I crack. In contrast, the LSY (large scale yielding) limit is characterised by much smaller stress concentrations and may allow global load sharing. When global load sharing applies, the stress redistribution, caused by a crack results in a uniformly increased stress in all of the remaining uncracked layers.

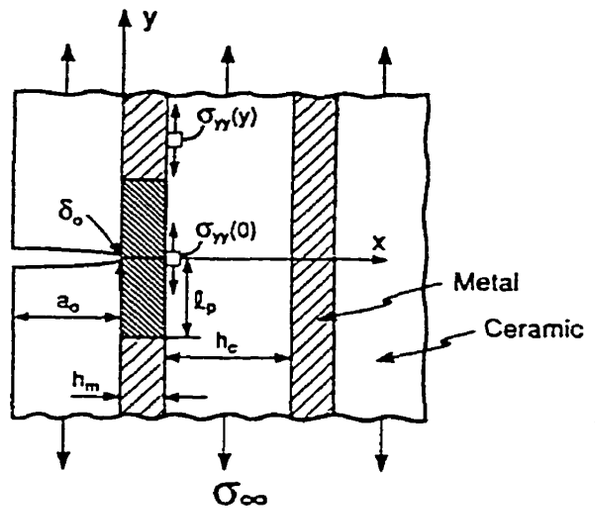

Fig. 5.5 Schematic illustrating the crack geometry and the parameters measured in the experiments [93Sha].

Fig. 5.5 illustrates the crack geometry and the parameters measured in the experiments. In Fig. 5.5, δ_0 is the opening displacement of the cracked ceramic layer adjacent to the metal and ℓ_p is the plastic zone size. The σ_{yy} (y) stress in Fig. 5.5 can then be estimated using the plane stress relation [34Tim]

$$(1-\nu_m^2)\sigma_{yy}(y) = E_m[\varepsilon_{yy}(y)+\nu_m\varepsilon_{xx}(y)] \qquad (5.10)$$

where ν_m is Poisson's ratio of the ceramic matrix (Al_2O_3), E_m is Young's modulus of the ceramic matrix and ε_{yy} is the strain in the neighbouring ceramic.

Shaw et al. [93Sha] observed that the cracks renucleated sequentially in adjoining layers on nearly the same plane as the notch. The damage is therefore viewed as a dominant mode I crack, with the crack tip taken to be the edge of the furthest cracked ceramic layer. Two values of the stress intensity factor characterize crack growth; i) that needed for initial crack renucleation across intact metal layers, K_N, and ii) that needed for subsequent crack growth, K_g. Initial crack growth is controlled by crack renucleation in the ceramic layer ahead of the crack tip, whereas K_g increases during subsequent crack growth because of the bridging effect of intact metal layers in the crack wake.

The stress distributions, $\sigma_{yy}(y)$, along the edge of the Al_2O_3 layer ahead of the crack-tip indicate that local stress concentrations exist ahead of the crack tip similarly to the theoretical

predictions based on small-scale yielding limit. Therefore, the SSY predictions are in reasonable agreement with the experimental results.

The renucleation stress intensity factor, K_N, therefore, can be estimated based on the stress distribution by SSY predictions. In the small-scale yielding limit, the stresses along the crack plane closely approximate the elastic solution [91Cao, 93Sha]

$\sigma_{yy}(x,0) \approx K_I / \sqrt{2\pi x}$ $(x \geq h_m)$

where K_I is for an elastically homogeneous medium. This result holds even when the plastic zone extends both through the metal layer and laterally up to a distance several times the metal layer thickness. The corresponding stresses in the intact ceramic layer alongside the metal/ceramic interface ($x=h_m$, see Fig. 5.5) are given by [75Law[1]]

$$\sigma_{ij} = \frac{K_I}{\sqrt{2\pi r}} f_{ij}(\theta) \qquad (5.11)$$

with

$$\sigma_{yy}(r,\theta) = \frac{K_I}{\sqrt{2\pi r}} \left(\cos\left(\frac{\theta}{2}\right)\left[1 + \sin\left(\frac{\theta}{2}\right)\sin\left(\frac{3\theta}{2}\right)\right]\right) \qquad (5.12)$$

where r and θ are the radial and angular coordinates from the crack tip (in Fig. 5.5)

$$r = \sqrt{h_m^2 + y^2} \text{ and } \theta = \arctan\left(\frac{y}{h_m}\right)$$

The stress distributions at $x=h_m$ in the ceramic layer ahead of the crack tip can be used in conjunction with the measured strength of the ceramic to predict failure of the ceramic layer and thus, the renucleation stress intensity factor, K_N. A simple estimate is obtained by equating the stress (at $x=h_m$, y=0) from Eq. (5.12) to the fracture strength of the brittle ceramic matrix, σ_f^m. This gives

$$K_N = \sigma_f^m \sqrt{2\pi h_m} \qquad (5.13)$$

5.2.3 Crack trapping

When a straight crack intersects a row of tough particles, part of the crack front can bow out and loop around the particles (Fig. 5.1(a)). The increased crack curvature increases the local stress intensity factor and can lead to fracture of the ductile particles without the formation of bridging particles in the crack wake, or would allow the particles left in the crack wake to

remain intact, which can lead to an additional toughening by crack bridging depending on the toughness of the particles [91Bow].

The fracture toughness increase by the crack trapping mechanism has been modelled by Bower et al. [91Bow] assuming that the particles are perfectly bonded to the matrix material, and will fracture in the wake of the crack. Fig. 5.6 shows a semi-infinite crack pinned by parallel rows of obstacles.

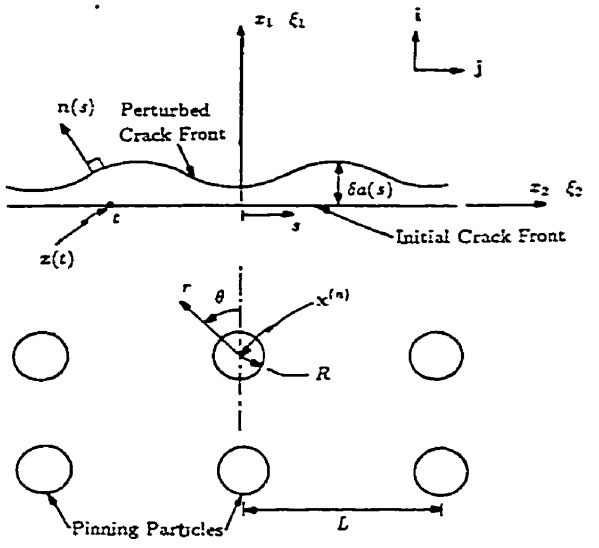

Fig. 5.6 Semi-infinite crack pinned by parallel rows of obstacles, showing notation and sign convention [91Bow].

When a crack meets a row of tough particles the crack may surmount the row of obstacles in one of two ways. If the toughness of the particles exceeds that of the matrix by only a small amount, they are penetrated by the crack, which propagates through them. Alternatively, if the toughness ratio of the particle and the matrix (K_p/K_m) exceeds a critical value (to be determined), the segments of crack front bowing out between the particles coalesce, and the particles are left intact in the wake of the crack. Fig. 5.7 shows the shape of one wavelength of the crack front, as it propagates around the first row of tough particles.

When the remotely applied stress intensity factor, K_∞, reaches a magnitude, K_m (K_c^{mat} in Fig. 5.7 is designated as K_m in this study as a critical stress intensity factor for the matrix), the

crack starts to propagate through the matrix. Parts of the crack front contacting the particles arrest, while the remainder of the front bows out between the particles. The variation of remote stress in the ratio of K_∞ to K_m as the crack propagates around the row of particles reaches a maximum of 1.68 without breaking the particles and subsequently decreases as areas of the crack front ahead of the particles start to attract one another. Its shape is determined by the condition that K(s) (crack tip stress intensity factor) is equal to K_m over propagating regions, while $\delta a(s)=0$ (Fig. 5.6) over the regions in contact with the tougher material. Due to the change in crack geometry, the stress intensity factor increases over

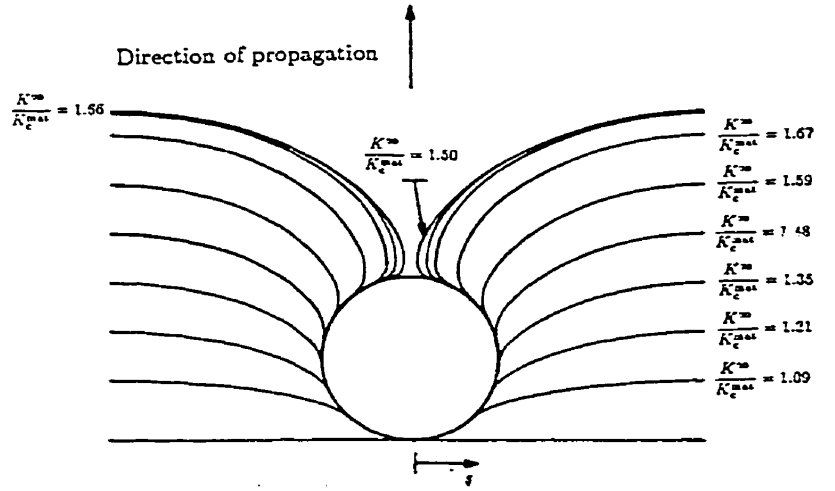

Fig. 5.7 The shape of a semi-infinite crack as it bypasses a single row of obstacles [91Bow]. $L/2a_0=6.667$

regions of the crack which contact the particles. When the crack is bowing out further, the local stress intensity around the particle increases with the highest local stress intensity at the point of first contact of the crack front with the obstacle. The resulting distribution of the crack-tip stress intensity factor, K(s), on the region of the crack in contact with the particle reaches a maximum value, $K(s)/K_m = 2.84$ at $s=0$, when $K_\infty/K_m=1.68$.

Consequently, if $K_p/K_m > 2.84$, the crack bypass the first row of obstacles, leaving a row of pinning particles where K_p is the critical stress intensity factor of particles. On the other hand, if $K_p/K_m < 2.84$, the crack front penetrates the particles and no bridging particles are formed. When the particles are fully penetrated by the crack, that is, in case of $K_p/K_m<2.84$, the

maximum load occurs when the line fraction of the crack front inside the obstacles is a maximum. In this case, the toughening due to trapping can be calculated by means of the following equation proposed by Rose [75Ros].

$$K^{\infty} = \sqrt{\left(\frac{1}{L}\int_0^L K^2(x_2)dx_2\right)} \qquad (5.14)$$

where L is one wavelength of the crack front (Fig. 5.6).

By substituting $K(x_2)=K_p$ for $|x_2| \le R$ (that is, the region where crack is in contact with particles) and $K(x_2)=K_m$ otherwise,

$$K^{\infty} = \sqrt{\left[\frac{1}{L}\left(2\int_0^R (K_p)^2 dx + \int_R^{L-R} (K_m)^2 dx\right)\right]} \qquad (5.15)$$

Therefore,

$$K^{\infty} = \left\{(K_m)^2 + \frac{2R}{L}\left[(K_p)^2 - (K_m)^2\right]\right\}^{1/2} \qquad (5.16)$$

By the relationship between volume fraction of ductile particles, V_d, and R/L [91Bow],

$$\frac{R}{L} = \sqrt{\left(\frac{V_d}{\pi}\right)}$$

Eq. (5.16) can be rewritten as

$$K^{\infty} = \left\{(K_m)^2 + 1.128(V_d)^{1/2}\left[(K_p)^2 - (K_m)^2\right]\right\}^{1/2} \qquad (5.17)$$

By equating K_{∞} with K_c, Eq. (5.17) can be rewritten as

$$K_c = \left\{(K_m)^2 + 1.128(V_d)^{1/2}\left[(K_p)^2 - (K_m)^2\right]\right\}^{1/2} \qquad (5.18)$$

5.2.4 Crack-tip interface debonding

As a crack encounters a planar interface, slip and debonding along the interface can cause a stress redistribution across the interface, that is favourable for toughness enhancement. Crack-tip stress analyses [89Ash, 93Cha2, 93He] have shown that crack-tip interface debonding significantly reduces the normal stresses near the crack tip and shifts the peak stress away from the crack tip, but increases the work-of-fracture of ductile reinforcements [89Ash]. In addition, interface debonding is a necessary precursor for subsequent crack bridging, leading to a further increase in fracture resistance. However, there is not any

quantitative model available in the literature describing the relationship between the fracture toughness and interface debonding.

5.3 Extrinsic mechanisms

5.3.1 Ductile phase bridging

The presence of intact ductile particles in the crack wake can increase the fracture resistance of the composite by crack bridging. The basic concept of toughening by ductile phase bridging is that the crack surfaces of the dominant crack in the brittle matrix would be bridged by the ductile phase particles [86Eva, 87Rose, 88Bud, 89Ash, 93Cha1]. The bridging forces exerted by the particles would reduce the crack surface opening and lower the near-tip stress intensity factor of the dominant crack. As a result, the remotely applied stress intensity factor must be increased when the crack and the bridged zone increase in length, thereby leading to a higher crack growth toughness. The mechanics of crack bridging by ductile particles are well understood [86Eva, 87Ros, 88Bud, 89Ash]. In this study, convenient expressions modelled by Ashby at al. [89Ash] for the fracture resistance associated with ductile phase bridging in a lead/glass composite and by Budiansky [88Bud] on the basis of the theoretical hypothesis will be introduced.

5.3.1.1 Crack bridging by Ashby et al. [89Ash]

Fig. 5.8 shows an illustration explaining the bridging mechanism and showing the brittle matrix bridged by a ductile phase. If the particle is so weakly bonded to the matrix that it easily pulls free as the crack approaches, then it is not stretched and there is almost no contribution to the toughness. But if it is strongly bonded, it is constrained and then its force-displacement curve is very different from that of the unconstrained material as measured (for instance) in an ordinary tensile test. This is an important difference because the energy absorbed in stretching the particle, crucial in calculating the contribution to the toughness, depends strongly on the degree of constraint. A number of early models [67Coo, 70Coo, 71Ger, 72Hin] assumed that the flow strength and fracture strain of the plastic material was the same as that measured in a simple tensile test on the unconstrained material but this assumption is false.

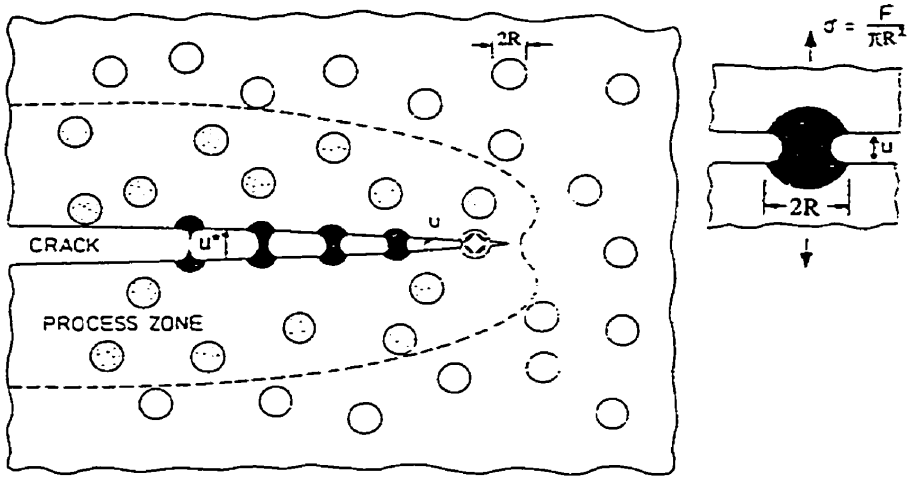

Fig. 5.8 A crack in a brittle matrix, intersected by ductile particles. The particles stretch and fail as the crack opens. The work of stretching contributes to the toughness of the composite [89Ash].

The nominal stress carried by the stretching particle for a given crack opening, u, is

$$\sigma(u) = \frac{F(u)}{\pi R^2} \qquad (5.19)$$

where F is the force and R is the radius of a particle, as shown in Fig. 5.8. The increase in toughness of the composite is related to the function σ(u) as

$$\Delta G_c = V_d \int_0^{u^*} \sigma(u)du \qquad (5.20)$$

where V_d is the area-fraction of ductile material intercepted by the crack and u* is the crack opening at the point when the ductile material fails, as shown in Fig. 5.8.

The integration term in Eq. (5.20) is the work-of-fracture defined simply as the total energy consumed to stretch particles and designated as

$$W = \int_0^{u^*} \sigma(u)du \qquad (5.21)$$

Therefore, $\Delta G_c = V_d W$

Now, it is necessary to calculate W for a ductile phase to stretch as it is in the brittle matrix. The fracture behaviour of ductile phase (lead in this model) in ceramic materials (glass) were observed. The fracture surface of the unconstrained lead wire is shown in Fig. 5.9. It failed

by drawing down to a point as shown in Fig. 5.9. However, when the ductile phase, lead, is constrained in glass, the response of the lead is quite different as shown in Fig. 5.10.

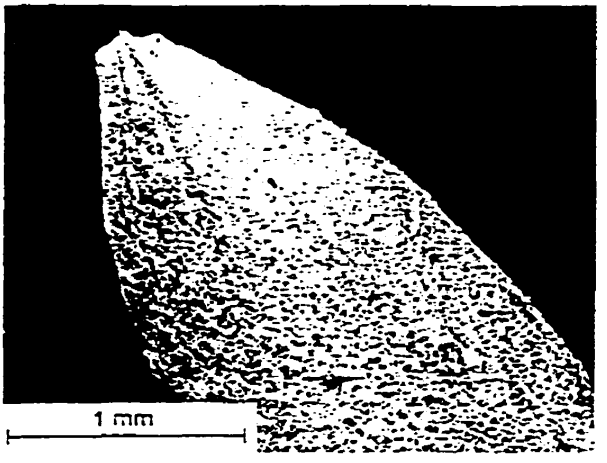

Fig. 5.9 A fracture surface of a lead wire [89Ash].

None of the fractured surfaces of the ductile lead in composites in Fig. 5.10 fractured as that in Fig. 5.9 for unconstrained lead. Most of the samples failed by the nucleation of a single internal cavity, which grew until it occupied most of the section. Fig. 5.10(a) shows no sign of decohesion and Fig. 5.10(b) shows a little decohesion. Occasionally, several voids grow simultaneously, as in Fig. 5.10(c), which also shows limited decohesion. When the lead remained bonded to the glass, the glass itself often fractured by the formation of cracks concentric with the core, as shown in Fig. 5.10(d).

Samples fractured with minimal damage as shown in Fig. 5.10(a) and (b) absorbed the smallest amount of energy and displacement in stretching the lead to fracture compared to other samples as shown in Fig. 5.10(c) and (d), but have a maximum of the strain constraint (σ/σ_y) of about 6. For the samples as shown in Fig 5.10(c), and (d), even if the maximum strain constraint is smaller than those as shown in Fig. 5.10(a) and (b), more energy is consumed when decohesion between the brittle matrix and ductile phase occurred or when the matrix fractured.

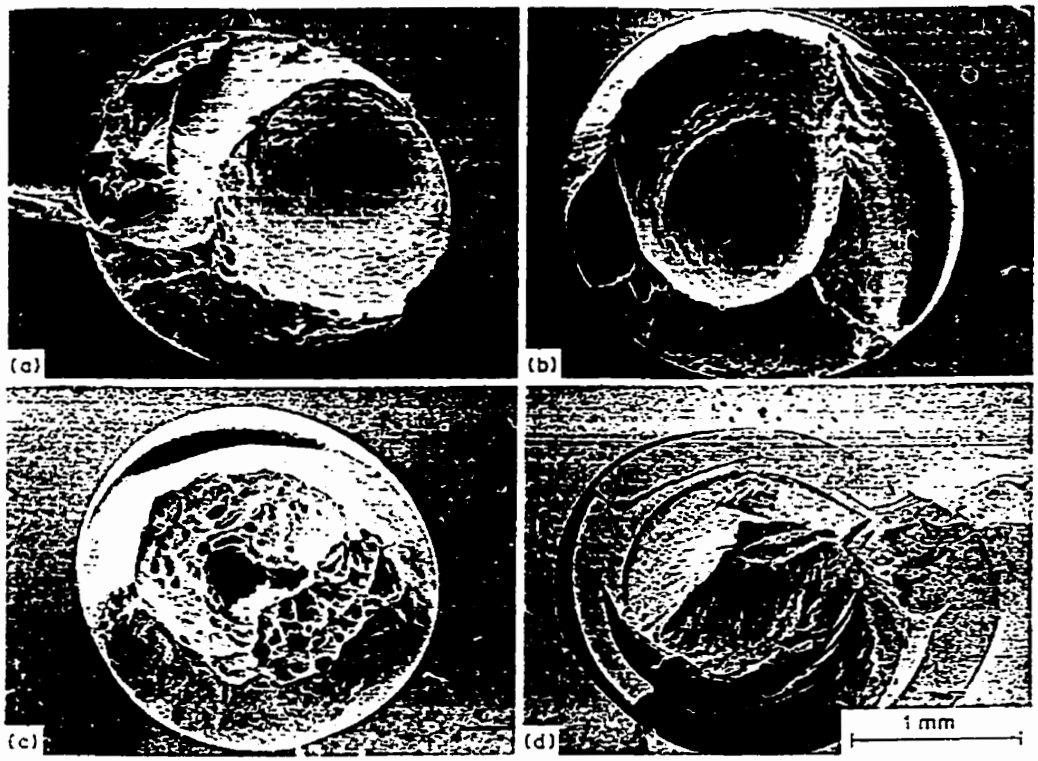

Fig. 5.10 (a) Failure by the growth of a single internal void. The lead/glass junction remained intact and glass is not fragmented. (b) Failure involving decohesion plus the growth of an internal void. (c) Failure involving decohesion with multiple voiding. (d) Failure involving matrix cracking [89Ash].

When the lead-glass bond was weak the interface was separated, leaving the lead core less constrained, so it was drawn down at a lower stress. The peak stress was lower, but the energy absorption was greater than for minimal decohesion forming a central void. If energy absorption is the goal, full constraint is not ideal; some (limited) decohesion or matrix fracture is desirable.

By analysing the experimental data, the following equation was obtained

$$\frac{W}{\sigma_y R} = 2.5\frac{u_{max}}{R} \qquad (5.22)$$

$$W = 2.5\frac{u_{max}}{R}\sigma_y R \qquad (5.23)$$

Therefore,

$$W=C\sigma_y R \qquad (5.24)$$

where $C=2.5u_{max}/R$.

Therefore, the energy absorbed is

$$\Delta G_c = V_d \int \sigma(u) du$$

$$= C V_d \sigma_y R \qquad (5.25)$$

The constant C is equal to 1.6 for complete bonding with no matrix fracture, but rises to as much as 6 with limited debonding or matrix fracture.

The result can be rewritten in terms of stress intensity factor ΔK for plane stress, $\Delta K_c = (E \Delta G_c)^{1/2}$.

Therefore,

$$\Delta K_c = \left[C V_d E_c \sigma_y R \right]^{1/2} \qquad (5.26)$$

Here, ΔK represents the increment of fracture toughness which arises only from the bridging effect by the reinforced ductile phase.

According to Eq. (5.26), the greatest toughening is obtained from inclusions with a high modulus, E, a high strength, σ_y, and a large diameter, 2R. If limited decohesion is allowed, the contributions more than double.

5.3.1.2 Crack bridging by Budiansky et al.[88Bud]

The fracture toughness of a composite consisting of a brittle matrix containing ductile phase particles was studied theoretically on the basis of the hypothesis that the ductile particles toughen the brittle matrix by the mechanism of crack bridging as shown in Fig. 5.11.

Budiansky et al. [88Bud] first described the crack bridging mechanism by ductile phase particle as shown in Fig. 5.11 using the bridging-spring model for the partially pinned crack as sown in Fig. 5.12 and they derived the equations with respect to the problem of particulate reinforcement from the associated bridging-springing equations. In this model they limit the situation to the case of small-scale bridging, in which bridge length is small relative to crack length, specimen dimensions, and distances from the crack to the specimen boundaries.

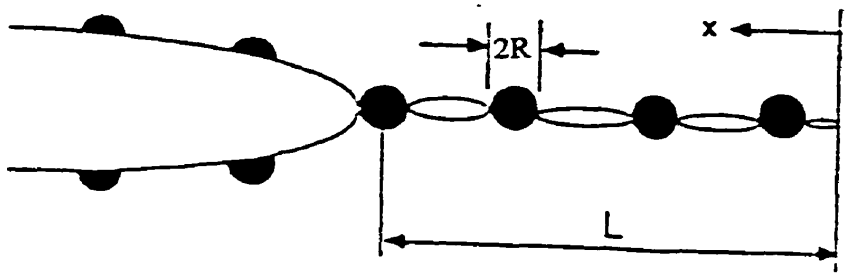

Fig. 5.11 Crack bridging by ductile phase particle [88Bud].

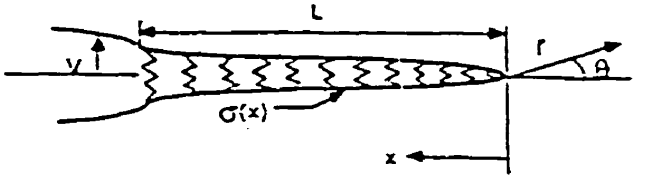

Fig. 5.12 Bridging-spring model [88Bud].

Budiansky et al. [[88Bud] analysed ductile-phase toughening by treating the bridging particles as elastic, elastic/perfectly plastic, and rigid/perfectly plastic springs using J-integral. The solutions for the elastic particle, elastic/perfectly plastic, rigid/perfectly plastic cases are in Eq. (5.27), Eq. (5.28), and Eq. (5.29), respectively.

$$K_c = K_m \left\{ \varpi(1-V_d) + \frac{\pi}{2} \frac{\sigma_f^{d^2} R V_d \varpi (1-\sqrt{V_d})(1-V_d)}{K_m^2} \right\}^{\frac{1}{2}} \tag{5.27}$$

$$K_c = K_m \left\{ \varpi(1-V_d) + \frac{\pi}{2} \frac{\sigma_f^{d^2} R V_p \varpi (1-\sqrt{V_d})(1-V_d)}{K_m^2} \left(1 + 2\frac{u^*}{u_y} \right) \right\}^{\frac{1}{2}} \tag{5.28}$$

$$K_c = K_m \left\{ \varpi(1-V_p) + \frac{2V_p E_c \sigma_f^d u^*}{K_m^2(1-\nu_c^2)} \right\}^{\frac{1}{2}} \qquad (5.29)$$

where $\varpi = \dfrac{E_c(1-\nu_m^2)}{E_m(1-\nu_c^2)}$

and σ_f^d is the particle stress at failure, V_p, concentration of the particles, u^*, displacement at failure, u_y, displacement at yielding, E_m, Young's modulus of matrix, ν_m, Poisson's ratio of the matrix. For Al_2O_3/Al composite, the rigid-plastic model was found to be appropriate.

Based on the J-integral approach, the first term on the right within the bracket in Eq. (5.27), (5.28), and (5.29) is the contribution of the matrix phase to the overall strain energy release rate of the particle reinforced composite, while the second term is the contribution due to the plastic work consumed in fracture of the ductile particles in the bridging zone.

5.3.2 Shear ligament toughening

This toughening mechanism results from the formation of noncoplanar microcracks ahead of a crack that deflects from the Mode I path. As the main crack zigzags between grains, the angle of deflection and plane of microcracking are likely to be different among individual grains. Therefore, the crack planes in the various grains are unconnected at either grain or phase boundaries and are separated by ligaments, as shown in Fig. 5.13. The formation of these ligaments by noncoplanar crack planes leads to an enhancement of the fracture toughness because they must be fractured in order for total separation of the crack surfaces to occur. The deformation and fracture of these ligaments, usually by shear is commonly termed shear ligament toughening [91Cha, 93Cha[1], 95Cha[1]]. Shear ligament toughening has been modelled by Chan [91Cha] by treating the shear ligaments as a ductile phase that bridges the crack surfaces.

Evidence for the formation of shear ligaments by mismatched crack planes is shown in Fig. 5.13 (a) for a Ti-24Al-11Nb alloy with an equiaxed α_2 + β microstructure. Because of mismatched planes of cracking, the microcracks are separated from each other by ligaments that are subjected to shear deformation. The location of the shear ligaments are further illustrated by the sketch shown in Fig. 5.13(b).

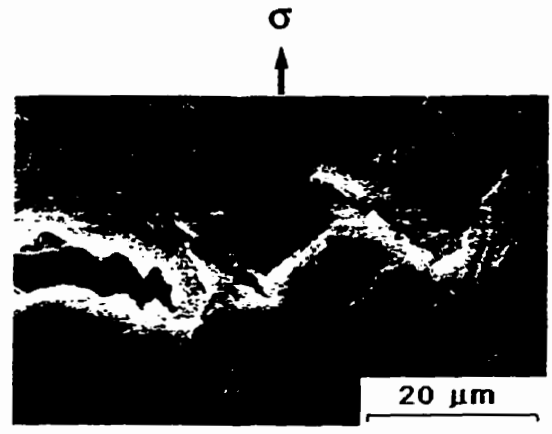

(a)

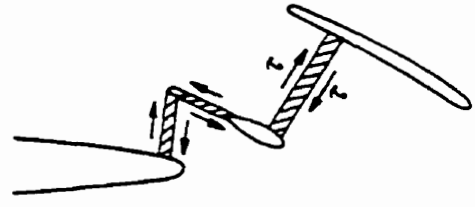

(b)

Fig. 5.13 Shear ligaments in Ti-24Al-11Nb : (a) SEM micrograph and (b) a sketch of the ligaments [91Cha].

The basis of the analysis is an energy balance given by

$$J_c = J_m + J_\ell \qquad (5.30)$$

where J_c, J_m, and J_ℓ are the values of the J-integral supplied by the remote load existing in the matrix, and dissipated by the shear ligaments, respectively.

By considering shearing to occur in rigid, perfectly plastic ligaments under a shear stress τ_ℓ, and an incremental plastic shear strain $d\gamma_\ell$, the dissipated plastic work per unit area of crack extension, J_ℓ, by N shear ligaments fractured at γ_ℓ^* in the process zone of length L_S and the thickness w, in a specimen of thickness t is given by [91Cha]:

$$J_\ell = \frac{N}{tL}\int_0^{\gamma_\ell^*} \tau_\ell d\gamma_\ell (\ell w L_S) \qquad (5.31)$$

which can be rewritten as

$$J_\ell = V_\ell \tau_\ell \gamma_\ell^* \bar{\ell} \qquad (5.32)$$

Where

$$_\ell = Nw / t \qquad (5.33)$$

is the area fraction of the shear ligaments and the average ligament length $\bar{\ell}$ is

$$\bar{\ell} = \ell\left[1+\left(\frac{L_S}{\ell}\tan\theta\right)\right] \qquad (5.34)$$

Substituting Eq. (5.32) into Eq. (5.30) leads to

$$\frac{(1-\nu_c^2)K_c^2}{E_c} = \frac{(1-V_\ell)(1-\nu_m^2)K_m^2}{E_m} + V_\ell \tau_\ell \gamma_\ell^* \bar{\ell} \qquad (5.35)$$

since $J = \dfrac{(1-\nu^2)K^2}{E}$ in plane strain condition.

By rearranging Eq. (5.35)

$$K_c = K_m\left\{(1-V_\ell)\omega + V_\ell \Gamma_\ell (\ell / D)\left[1+\left(\frac{L}{\ell}\right)\tan\theta\right]\right\}^{1/2} \qquad (5.36)$$

with

$$\omega = \frac{E_c\,(1-\nu_m^2)}{E_m\,(1-\nu_c^2)}$$

and

$$\Gamma_\ell = \frac{E_c \tau_\ell \gamma_\ell^* D}{(1-\nu_c^2)K_m^2}$$

where D is the average grain size.

On this basis, strong effects of shear ligament toughening prevail at large values of $_\ell$, ℓ, and Γ_ℓ, that is, the toughening ratio depends on the area fraction, length, and toughness of the ligaments (a critical shear strain, γ_ℓ^* and a fracture stress in shear, τ_f of the ligaments) as well as the process zone size and the angle of crack deflection.

5.3.3 Crack deflection

Toughening by crack deflection is the result of a reduction in the local stress intensity factor when a crack deviates from its original path as shown in Fig. 5.1(g). The toughening due to

crack deflection through an angle, ϕ, was estimated by Suresh [85Sur]. The local tensile opening (Mode I) stress intensity, k_1 and sliding (Mode II) stress intensity factors, k_2, deviated from a straight path by a deflection angle, ϕ, are given by [80Cot, 85Sur]:

$$k_1 = \cos^3(\phi/2)K_\infty \qquad (5.37)$$

and

$$k_2 = \sin(\phi/2)\cos^2(\phi/2)K_\infty .$$

The effective crack-tip stress intensity, K_m, for coplanar growth was assumed from the maximum strain energy release rate criterion to be

$$K_m = \left(k_1^2 + k_2^2\right)^{1/2} \qquad (5.38).$$

Therefore,

$$K_\infty = K_m\left(\frac{1}{\cos^2(\phi/2)}\right) \qquad (5.39).$$

5.4 Factors affecting fracture toughness

From the literature review for the present work, a summary of the important factors for improving fracture toughness in composites can be drawn for various toughening mechanisms, as in Table 5.1. The fracture toughness of composites designated as K_c refers to the initiation fracture toughness, K_i for the intrinsic mechanisms such as ductile phase blunting, microcrack renucleation, and crack trapping. Also, K_c refers to the crack growth toughness, K_g for the extrinsic mechanisms such as ductile phase blunting, shear ligament toughening, and crack deflection as in Fig. 5.2. In Table 5.1, V_d stands for volume fraction of ductile phase, σ_y^d yield stress of ductile phase (toughening phase), $\bar{\varepsilon}_f^d$ effective fracture strain of ductile phase, σ_f^m fracture stress of matrix, h_m ductile phase layer thickness, R particle radius, W work of fracture, u^* crack opening displacement at the point when the ductile material fails, V_ℓ volume fraction of shear ligament, γ_ℓ^* critical shear strain of ligaments τ_f fracture stress in shear of ligaments, and ϕ crack deflection angle.

Many of the factors in Table 5.1 such as K_m, σ_f^m, K_p, E_c, and σ_y etc. are material properties (constants), so those factors cannot be improved artificially. However, microstructural factors

such as volume fraction, size, and work-of-fracture (which is related to the plastic constraint in ductile phase bridging) of the ductile phase are considered as variable factors.

Table 5.1 Summary of important factors affecting fracture toughness in composites.

Mechanisms	Factors
Ductile phase blunting [92Cha]	$K_c \propto K_m, V_d, \sigma_y^d, \bar{\varepsilon}_f^d$
Microcrack renucleation [93Sha]	$K_c \propto \sigma_f^m, h_m$
Crack trapping [91Bow]	$K_c \propto K_m, K_p, R, V_d$
Ductile phase bridging by Ashby et al. [89Ash]	$\Delta K_c \propto K_m, E_c, V_d, W(\propto R, \sigma_y)$
Ductile phase bridging by Budiansky et al. [88Bud]	$K_c \propto \sigma_f^d, V_d, u^*, R$
Shear ligament toughening [91Cha]	$K_c \propto K_m, V_\ell, \Gamma_\ell (\propto E_c, \gamma_\ell^*, \tau_\ell)$
Crack deflection [85Sur]	$K_c \propto K_m, \phi$

5.4.1 Volume fraction of toughening phase

The volume fraction of the ductile phase affects both initiation and crack growth toughness as shown in Fig. 5.14(a) and (b). Fig. 5.14 (a) shows a comparison of the experimental K_{IC} (initiation toughness) data and crack-tip blunting model, Eq. (5.9). As already mentioned, the ductile phase accommodates any plastic incompatibility that might develop at the interface, resulting in an enhanced initiation toughness. Fig. 5.14(b) shows a comparison of the experimental K_g (crack growth toughness) and shear ligament model, Eq. (5.36). In the case of shear ligament toughening, the ligaments act like the ductile phase bridging the crack surfaces, leading to an enhancement of the crack growth toughness. The effect of volume fraction on the fracture toughness of composite materials will be discussed in the following section.

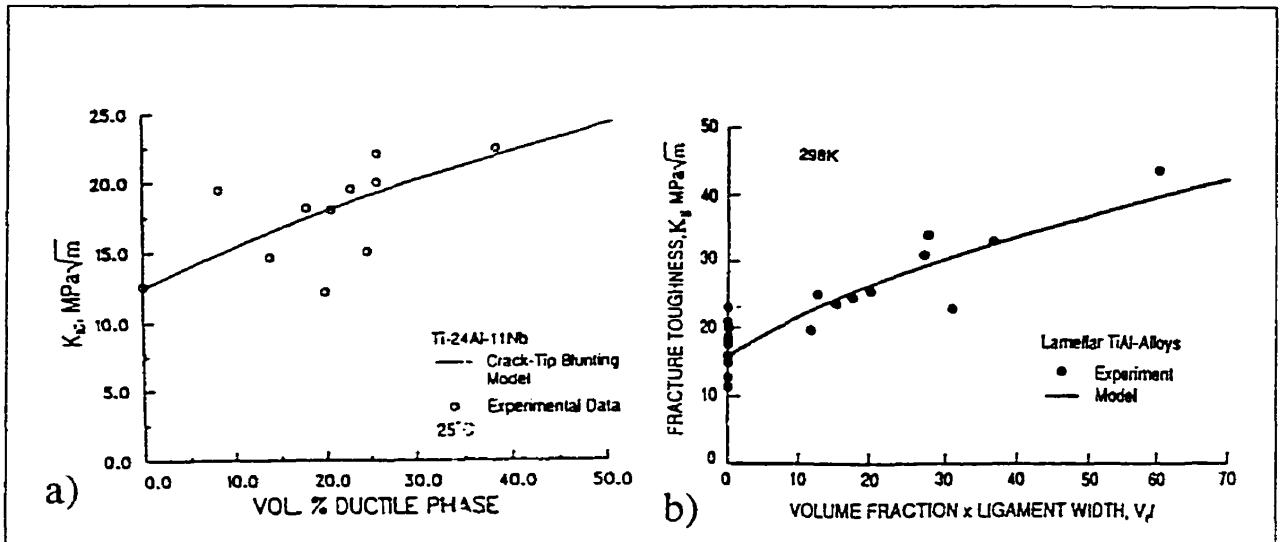

Fig. 5.14 (a) Dependence of initiation toughness on volume fraction of the ductile β phase (Nb) in Ti_3Al alloys [92Cha, 95Cha[1]]. (b) Crack growth toughness, K_g, increases with the volume fraction of the shear ligaments in TiAl alloys [95Cha[1]].

5.4.2 Effects of layer thickness and particle radius

In case of microcrack renucleation, crack trapping, and ductile phase bridging, the fracture toughness increases with increasing either the ductile layer thickness, h_m in Eq. (5.13) for microcrack renucleation or the particle radius, R in Eq. (5.16) for crack trapping and in Eq. (5.26) for ductile phase bridging by Ashby et al.. Fig. 5.15 shows the dependence of initiation toughness for microcrack renucleation, K_N, on the metal thickness based on the microcrack renucleation process, Eq. (5.13). A thick ductile layer ahead of a crack tip reduces the normal stress that acts on the neighbouring brittle layer by positioning the brittle phase away from the crack tip. As a result, the K level required for crack renucleation in the brittle phase is increased, thereby raising the initiation toughness. Conversely, in lamellar TiAl-alloys, both the initiation and crack growth toughness increase with decreasing interlamellar spacing, similar to the Hall-Petch relation [95Cha[3]].

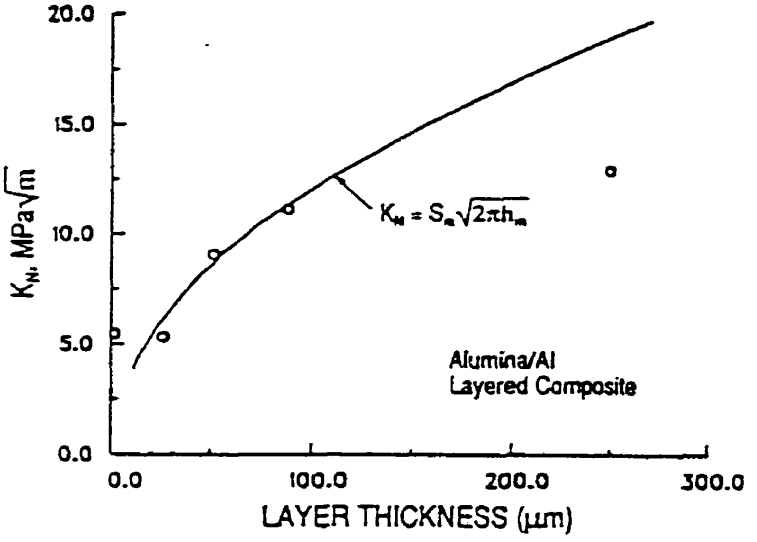

Fig. 5.15 Increase of initiation toughness with ductile phase thickness in Al_2O_3/Al layered composites [93Sha].

5.4.3 Work-of-fracture

The work-of-fracture of the ductile phase is an important factor for improving fracture toughness based on ductile phase bridging, and is strongly dependent upon the degree of constraint of the ductile phase in the brittle matrix. When the constraint of the ductile phase is high, the brittle mode of fracture is favoured, and the strain to fracture is reduced.

The work-of-fracture can be significantly increased in composites when the constraint is relaxed by partial debonding between the ductile phase and the brittle matrix as shown in lead/glass composites (in Ashby et al. model in section 5.3.1.1), which illustrates the beneficial effect of a weak interface.

5.5 Composite rule-of-mixtures-like relationship in fracture

There have been attempts to understand and predict the increase in fracture toughness values with increasing the volume fraction of the toughening phases [93Ash, 93Str, 96Cha, 96Dav] analogous to the composite rule of mixture (ROM) for prediction of elastic modulus [93Ash].

The modulus of a composite, E_c, can be estimated using simple composite rule-of-mixtures. The upper bound is obtained by postulating that, on loading, the two components suffer the same strain (isostrain situation); the stress is then the volume-average of the local stresses and the composite modulus follows a rule of mixtures [93Ash]

$$E_{c(u)} = V_d E_d + V_m E_m . \quad (V_m=1-V_d) \qquad (5.40)$$

Here $E_c(u)$ is the upper bound of Young's modulus of the composite, and E_d is the Young's modulus of the reinforcement and E_m that of the matrix. The lower bound is found by postulating instead that the two components carry the same stress (isostress situation); the strain is the volume-average of the local strains and the composite modulus is [93Ash]

$$E_{c(l)} = \frac{E_m E_d}{V_d E_m + (1-V_d) E_d} . \qquad (5.41)$$

Both of the elastic moduli of composite in Eq. (5.40) and (5.41) depend on the volume fraction of reinforcement as illustrated in Fig. 5.16.

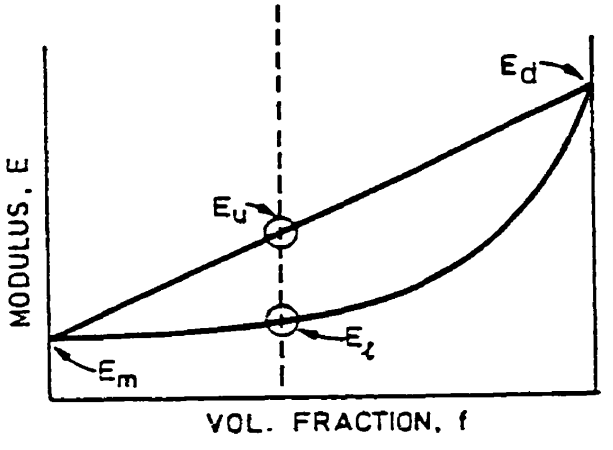

Fig. 5.16 Two values of modulus: an upper bound, derived from Eq. (5.40), and a lower bound, from Eq. (5.41) [93Ash].

E-modified ROM line has also been used by Davidson et al. [96Dav]. The improvement in toughness due to ductile phase reinforcement assessed in terms of G, the fracture energy, can be estimated [83Krs, 93Sob[2]] as given below analogous to the upper bound of ROM line in Eq. (5.40), based on the assumption that the ductile phase in a composite fractures in the same

manner as in the bulk form, i.e., the plastic constraint exerted on the ductile phase by the rigid matrix was not considered [83Krs].

$$G_c = V_m G_m + V_d G_d \qquad (5.42)$$

From the relationship between G and K, $G = (1-\nu^2)K^2/E$ in plane strain condition ($G=K^2/E$ in plane stress condition), Eq. (5.42) was derived as given in Eq. (5.43) in terms of the fracture toughness, K in the present work.

$$K_c = \left\{ \frac{E_c}{(1-\nu_c^2)} \left[\frac{(1-\nu_m^2)(1-V_d)K_m^2}{E_m} + \frac{(1-\nu_d^2)V_d K_d^2}{E_d} \right] \right\}^{\frac{1}{2}} \qquad (5.43)$$

Davidson et al. [96Dav] also expressed the ROM line as a straight line for the prediction of fracture toughness of composites versus volume fraction of ductile phase analogous to the upper bound of the ROM line for elastic modulus in Fig. 5.16 and Eq. (5.40). This yields

$$K_c = V_m K_m + V_d K_d . \qquad (5.44)$$

However, no justification of the above approach to express the ROM line for fracture toughness was given in [96Dav].

An attempt was made by Ashby [93Ash] to establish the ROM-like relationship between fracture toughness and volume fraction of phases in a composite by estimating upper and lower limits for toughness in terms of J_{IC}. The lower limit of the model by Ashby [93Ash] assumes that the crack is growing only in the continuous brittle matrix and the upper limit was derived by considering crack bridging. The lower limit and the upper limit for composite toughness are Eq. (5.45) and Eq. (5.46), respectively [93Ash].

$$(J_{IC})_c^{low} = (J_{IC})_m \left(\frac{(1+2V_d)^{\frac{1}{2}}}{1-V_d^{\frac{1}{2}}} \right), (J_{IC})_c < (J_{IC})_d \qquad (5.45)$$

and

$$(J_{IC})_c^{upp} = V_d (J_{IC})_m + V_m (J_{IC})_m + \left(\frac{V_d V_m E_d}{40} \right) \frac{\pi a^*}{E_c} \qquad (5.46)$$

where 2a* is the length of the maximum acceptable crack in the component.

The first two terms on the right in Eq. (5.46) describe a rule of mixtures, the last term is the additional energy absorbed by the work done against the bridging forces. Recalling that $J_{IC} = (1-\nu^2)K_{IC}^2 / E$ in plane strain condition, Eq. (5.45) and (5.46) can be expressed in terms of K_{IC} as Eq. (5.47) and Eq (5.48), respectively [93Ash].

$$(K_{IC})_c^{low} = K_m \left[\frac{(1-\nu_m^2)(1+2V_d)^{\frac{1}{2}} E_c}{(1-\nu_c^2)(1-V_d^{\frac{1}{2}})E_m} \right]^{\frac{1}{2}} \qquad (5.47)$$

and

$$(K_{IC})_c^{upp} = \left\{ \frac{E_c(1-V_d)K_m^2}{E_m} + \frac{V_d K_d^2}{E_d} + \left[\frac{V_d(1-V_d)E_d}{40} \right]^{\frac{1}{2}} \pi a^* \right\}^{\frac{1}{2}} \qquad (5.48)$$

Fig. 5.17 shows the improvements in fracture toughness with increasing volume fraction of ductile phase as estimated by the models described previously. The properties of the ductile phase used in the calculations were selected from the corresponding properties of Ni, i.e., Young's modulus E_d=200GPa [96Her], fracture strength σ_f^d=317Mpa [90Met], yield strength σ_y^d=60MPa [90Met]. Some of the material properties were arbitrarily assumed for the calculation since they did not change the trend showing the improvements in fracture toughness with increasing volume fraction of ductile phase. The fracture toughness of the brittle matrix was assumed to be 2 MPa.m$^{1/2}$ and that of the toughening phase 50 MPa.m$^{1/2}$. Poisson's ratio of composite (ν_c) was assumed to be 0.3. Young's modulus of composite (E_c) varying with increasing volume fraction of ductile phase in the brittle matrix was calculated from the upper bound of composite rule-of-mixture for elastic modulus given in Eq. (5.40) assuming Young's modulus of brittle matrix (E_m) is 300GPa. Shear strength of the toughening phase (τ_f) was assumed to be 150MPa. The constant, C and radius of reinforced fibers, R used for ductile phase bridging model in Eq. (5.26) by Ashby were 1.6 and 2μm, respectively. Displacement at failure, u* in Eq. (5.29) was assumed to be 4μm. Shear strain to failure, γ_ℓ^*, process zone length, ℓ, and diameter of grain, D in Eq. (5.36) for shear ligament toughening were assumed to be 0.1, 10μm, and 50μm, respectively. For shear ligament toughening [91Cha], the x-axis in Fig. 5.17 indicates the area fraction of shear

ligaments rather than the volume fraction of ductile phase. For ductile phase bridging by Ashby [89Ash], the y-axis indicates only the increment of fracture toughness (ΔK) by bridging effect. The number, 1.128 in the crack trapping model in Eq. (5.18) changed to 1.0 to yield the fracture toughness of composite equal to that of ductile phase when the volume fraction of ductile (V_d) phase is 1.0. Even if the magnitude of the increase in fracture toughness with increasing volume fraction of ductile phase in Fig. 5.17 will change depending on the values used for the calculations, the trend of the change in the fracture toughness values versus volume fraction, i.e., whether or not the prediction lines follow the lower bound, straight ROM line, or above the straight ROM line will not change. All the predictions made by the models show something similar to synergism effect, showing the prediction lines

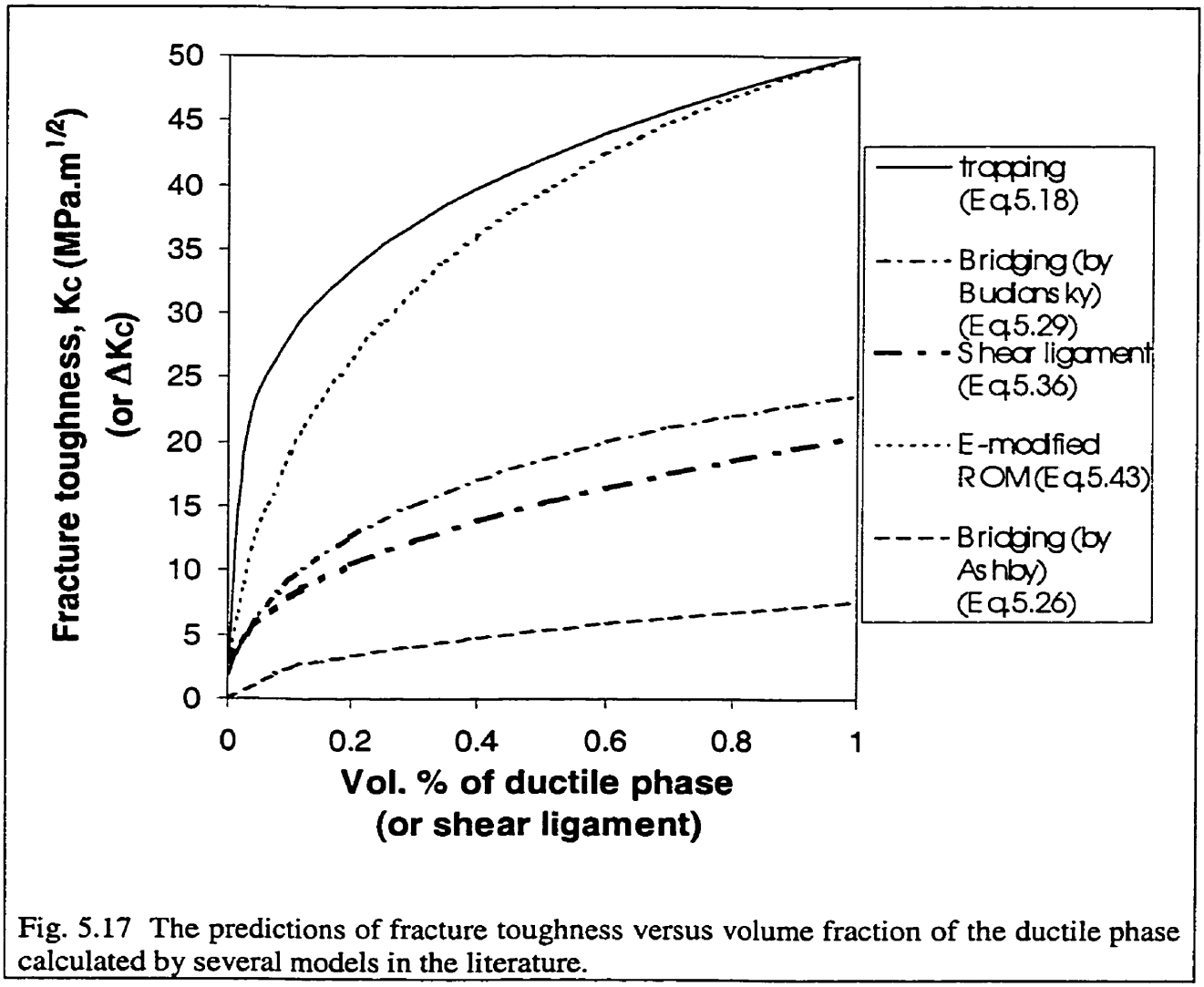

Fig. 5.17 The predictions of fracture toughness versus volume fraction of the ductile phase calculated by several models in the literature.

convex upward. The two models, the lower and upper limits of fracture toughness by Ashby [93Ash] are omitted since those lines are far below and above the other lines.

However, the fracture toughness values obtained experimentally as a function of the volume fraction of ductile phase have shown that the experimental results are very different from predictions by the models proposed in the literature. Fig. 5.18 shows the graphs exhibiting the composite rule-of-mixture-like relationship between fracture toughness and volume fraction of ductile phase, particularly, in the whole range of volume fraction of ductile phase.

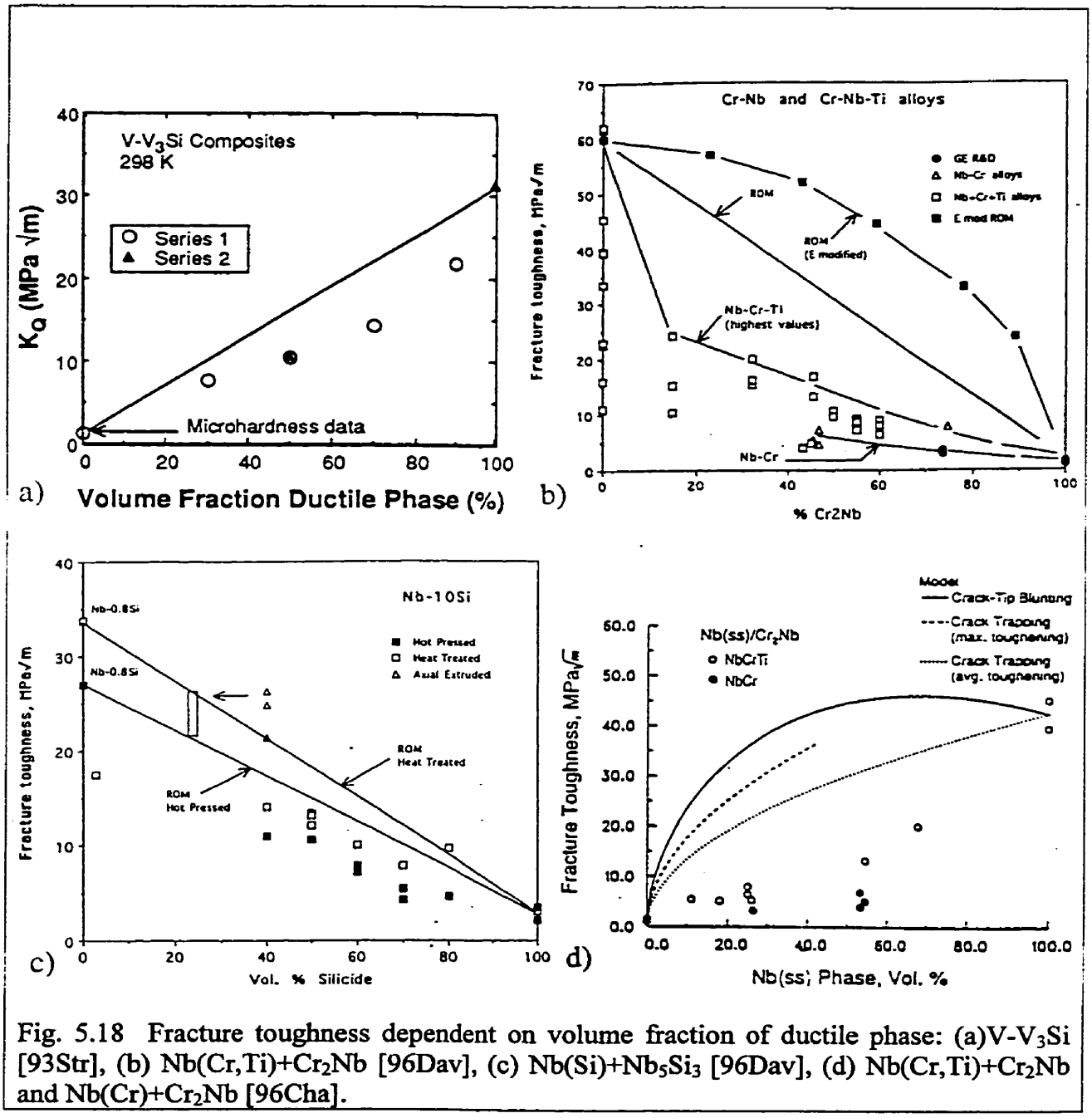

Fig. 5.18 Fracture toughness dependent on volume fraction of ductile phase: (a)V-V_3Si [93Str], (b) Nb(Cr,Ti)+Cr_2Nb [96Dav], (c) Nb(Si)+Nb_5Si_3 [96Dav], (d) Nb(Cr,Ti)+Cr_2Nb and Nb(Cr)+Cr_2Nb [96Cha].

There are more graphs found in the literature, showing the effect of volume fraction of ductile phase on fracture toughness, but others show the fracture toughness values for the limited volume fraction of ductile phase as that shown in Fig. 5.14, which can be fitted flexibly.

In all the graphs in Fig. 5.18, the fracture toughness values of composites obtained experimentally as a function of the toughening phase are generally located below the upper bound of the ROM line, opposed to the predictions by the proposed models. Regarding the amount of toughness increase in Nb(Cr,Ti)+Cr_2Nb system, which is less than even that calculated by the proposed models and the straight ROM line, Chan [96Cha] suspected that it might arise from the development of a high plastic constraint in the solid-solution phase by the nondeformable hard Cr_2Nb phase. Theoretical analysis of crack bridging by ductile particles has revealed a reduction in plastic dissipation in the bridging particles when the matrix/particle interface is strong and the constraint in the ligament is high [92Tve, 96Cha]. Based on this consideration, it has been justified that the hard Cr_2Nb particles induced high triaxial stress in the Nb(Cr, Ti) or Nb(Cr) matrix and therefore a lower initiation toughness value [89Ash, 93Xia, 95Men, 96Cha].

6. Fracture toughness by CNB specimens

Application of the chevron-notched bend (CNB) specimen has been suggested as an excellent technique for measuring plane strain fracture toughness, K_{IC} of brittle materials, such as glass, ceramic, and concrete because it does not require complicated precracking procedure which is costly and extremely difficult to introduce successfully in the brittle materials [80Mun[1]]. Another advantage of the CNB specimens is the feasibility of testing at high temperatures in compressive loading systems. The intended high temperature application of structural ceramics and intermetallics, where some of them are intended to replace Ni-base superalloys, requires that test methods be extended to an extremely high temperature regime, about 1400° C or greater [81Shi].

For chevron-notched bend bars, the apex of the CNB specimen gives rise to a high stress concentration such that crack initiation and propagation occurs at relatively low loads, introducing a sharp natural crack during the test [89Gho]. The linear elastic plane strain stress intensity factor, K_{IC} of a CNB specimen is given by an equation of the form [72Poo, 80Mun[2]]

$$K_{IC} = \frac{P_{max}}{B\sqrt{W}} Y^{*} \qquad (6.1)$$

where B is the specimen thickness, W is the specimen width, and Y^{*} is the stress intensity factor coefficient (compliance function) of a CNB specimen. Fig. 6.1 illustrates the geometry of a four point bend CNB specimen and the relative lengths of chevron notch and crack, $\alpha=a/W$, $\alpha_0=a_0/W$, and $\alpha_1=a_1/W$ [92Sal]. The plane strain fracture toughness values for CNB may be different from actual K_{IC} calculated from the test procedure in ASTM E399-90 [90AST]. However, the plane strain fracture toughness for a CNB is similar to actual K_{IC} under the following two assumptions [84Wu[1]].

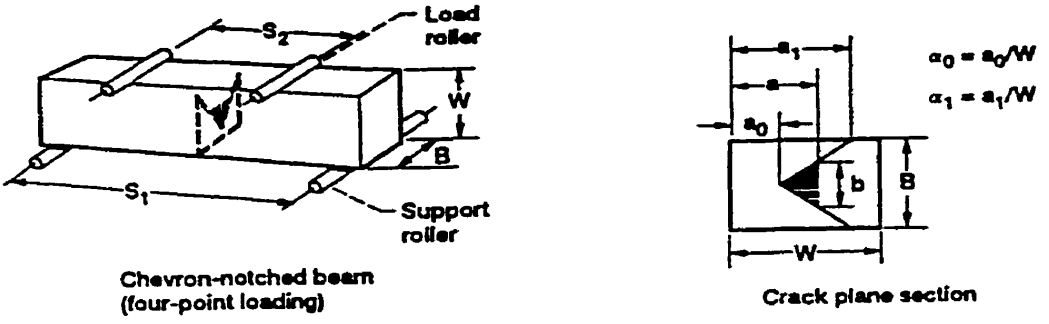

Fig. 6.1 Four point loading arrangement and specimen geometry for a chevron-notched bend specimen [92Sal].

Assumption 1: During crack growth, the plane strain state remains along the crack front.

Assumption 2: The plane strain crack growth resistance curve of tested material is flat.

The above basic assumptions are likely to be satisfied for brittle materials.

A schematic of a typical load-load line displacement (P-LLD) curve for CNB undergoes a linear P-LLD curve until the crack propagation commences and then becomes non-linear just before it reaches P_{max}. Several possible load-load line displacement (P-LLD) curves are shown in Fig. 6.2 in which no valid values can be obtained from curves III and IV [87Him].

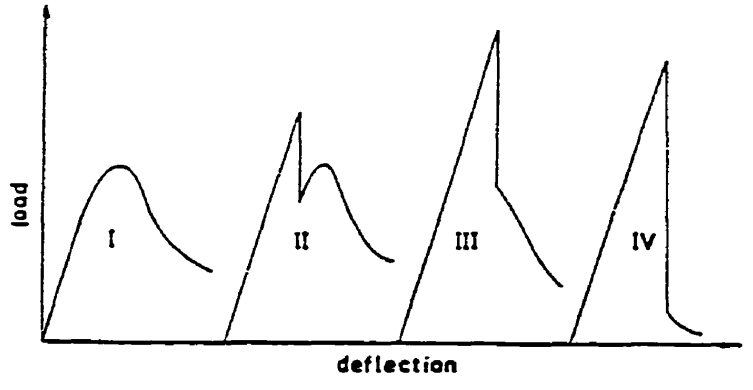

Fig. 6.2 Typical load-load line displacement (P-LLD) curves for a CNB specimen [87Him].

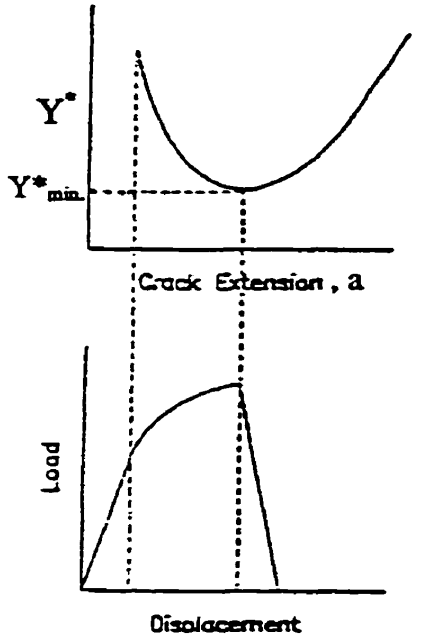

Fig. 6.3 Stress intensity factor coefficient, Y* vs. crack extension, a, and load vs. load line displacement curves for a CNB specimen [89Sun].

The non-linearity just before P_{max} is caused by the geometry of the chevron-notched bend bar. The curve of the stress intensity factor coefficient, Y* in Eq. (6.1) passes through a minimum at a certain geometry dependent crack length as shown in Fig. 6.3 [89Sun].

From Eq. (6.1) at a constant K_{IC}, when Y* is decreasing, the applied load to propagate the crack has to be increased (Fig. 6.3). At P_{max}, a balance is achieved between the increasing crack area and the resistance to crack propagation by the material and the crack driving force for the external loading. At this point the stress intensity function Y* is at its minimum, i.e., Y^*_{min}, (Fig. 6.3) and therefore, in combination with P_{max} gives a value of the critical stress intensity factor [89Goh] (Eq. (6.1)). A comparison of experimental results from fracture toughness tests on SiC using the conventional CNB specimen (as in Fig. 6.1) and a specimen sharply ground to the stability position prior to loading (as shown in Fig. 6.4) revealed that the conventional CNB specimen in Fig. 6.1 promotes failure at lower applied load (and hence stress intensity) than the specimen sharply ground to the stability position as shown in Fig. 6.4, even though there is less load bearing area initially in the latter specimen geometry [91Wit]. This observation provides strong support for the methodology of chevron notch testing.

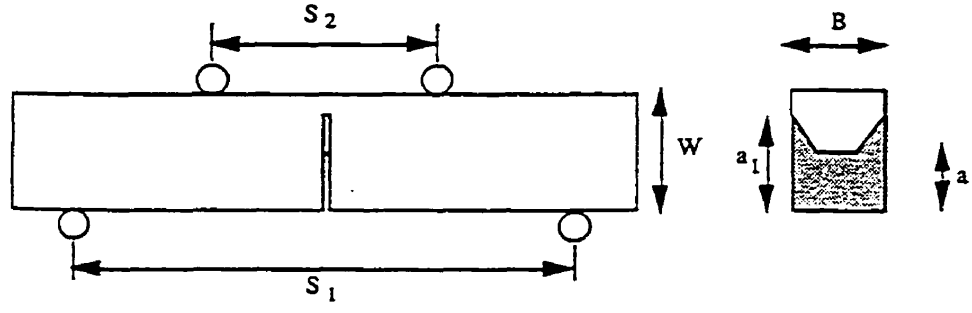

Fig. 6.4 Specimen sharply ground to the stability position prior to loading [91Wit].

Therefore, for CNB specimens, it is assumed that stable crack growth must precede the final unstable crack growth. If a P-LLD curve shows an extensively elastic region prior to fracture as in the case of III and IV in Fig. 6.2, this result may be unacceptable for valid K_{IC} determination [87Him, 89Sun]. This linear elastic deformation before fracture without stable crack growth region is supposed to be caused by an overload greater than P_{max} which results in an overestimation of fracture toughness. However, it has been observed that on many occasions, a sharp drop in the load occurs immediately at the end of a linear portion of the P-LLD curve [81Shi, 84Chu, 84Wu[1], 91Wit, 95Hor], and nevertheless, some of the results still give valid K_{IC} values [81Shi, 84Chu, 91Wit, 95Hor]. Sometimes, a sharp drop in the load without stable crack growth might be caused by an improper specimen preparation with a wide chevron notch width as discussed in [84Wu[1]], and [84Chu]. Regarding notch width, N, Barker [83Bar] recommended that for short-rod and short-bar chevron specimens in tension, the notch width gap should be less than 0.03B. The smaller notch width tends to give stable crack growth more readily and valid fracture toughness values, but the critical notch width does not seem to be a universal one and therefore must be determined for each material. Withey et al. [91Wit] mentioned that in extremely brittle material ($K_{IC} \leq 4.0 MPam^{1/2}$) it appears that valid toughness values may be obtained even without any indication of non-linear compliance changes prior to failure. Besides notch width, also cross head speed for a chevron-notched bend bar may change the type of the P-LLD curve [89Sun]. Lower the crosshead speed, the more probable it is, that it will exhibit the stable crack growth region.

6.1 CNB test in ASTM

There is no standard test method in ASTM for CNB specimens in bending for metallic materials. The only standard in ASTM available for the determination of fracture toughness of metallic materials using chevron-notched specimens is on the chevron-notched bar and rod in tension, E1304-89 [89AST[1]]. An ASTM provisional test method for the determination of fracture toughness using CNB specimens in bending is available. However, it is designed only for advanced ceramics, PS 70-97 (provisional test method) [97AST]. It is worth reviewing the requirements of the specimen geometry and test conditions for the test to be considered valid.

6.1.1 ASTM E1304-89

In ASTM E1304-89, the plane strain fracture toughness determined by using chevron-notched bar and rod specimens in tension for metallic material is designated as K_{Iv} or K_{IvM}. Particularly, when plane strain fracture toughness is determined based on the maximum load, the designation, K_{IvM}, is used. In order for a test result to be considered valid, it is required that the thickness of the specimen, B equals or exceeds 1.25 $(K_{IvM}/\sigma_{YS})^2$, i.e, $B \geq 1.25 (K_{IvM}/\sigma_{YS})^2$, where σ_{YS} is the 0.2 % offset yield strength. The required notch width, N, is $N \leq 0.02B$ with a round bottom or $N \leq 0.03B$ with an angular bottom having a notch root radius, $R \leq 0.01B$ and angle, $\theta \leq 60°$. If the actual crack surface deviates from the intended crack plane, as defined by the chevron slots, by more than 0.04B when the width of the crack front is one third B, then the test is considered invalid.

6.1.2 ASTM PS 70-97

In ASTM provisional test method, PS 70-97 [97AST], the fracture toughness of advanced ceramics at room temperature determined by the chevron-notched beam specimen in bending is designated as K_{Ivb}. Specimens can be loaded in four point or three point bending mode. In order for the test to be considered valid the P-LLD curve should exhibit stable crack propagation before the maximum load and the material should have a flat R-curve. The notch width, N, should be less than 0.25mm and less than 0.15mm at the root radius of the chevron. However, larger notch widths are acceptable provided that stable crack extension occurs.

Loading rate is recommended to be 0.0005 to 0.005mm/s. As already mentioned for the chevron-notched rod or short bar specimen, the actual crack surface should not deviate severely from the intended crack plane, otherwise the test may be invalid. There are four recommended specimen geometries, which specify the exact length, width, thickness, α_0, and α_1 in PS 70-97. However, this standard focuses on simply established geometries which reflect a base of experience (that is, those geometries that have been used, studied, and applied under a range of conditions to a variety of materials) because no generalized, parametric error and sensitivity analysis studies have been conducted on chevron-notched ceramic specimen geometries. The size requirement, such as $B \geq 1.25 (K_{IvM}/\sigma_{YS})^2$ in ASTM E1304-89 is not specified either.

6.2 Determination of specimen's geometry and loading mode

6.2.1. Geometry of the specimen

Since there is no standard test method in ASTM for the determination of plane strain fracture toughness using CNB specimens of metallic materials, the specimen geometry was decided mainly by consulting the literature. However, the specimen geometries in ASTM E1304-89 and PS70-97 were also considered to a certain extent and compared with the specimen geometry used in the present work. Considering the size requirement for a valid K_{IC} for a CNB specimen, in the following form: $B \geq 1.25 (K_{IC}/\sigma_{YS})^2$ in [89AST[1]], it would be safer to start with B=4mm, expecting relatively high σ_{YS} and low K_{IC} for intermetallic compounds. W/B ratios reported in the literature are 1.0 [92Jen], 1.25 [80Mun[3], 83Mun, 90Wit], 1.33 [89Sun], 1.43 [92Sal], 1.5 [84Wu[1], 84Wu[2]], 1.82 [81Shi], and 2 [84Wu[2], 99Loc] by analogy to the requirement in the ASTM standard for a single edge-notched and fatigue precracked bending specimen, $1 \leq W/B \leq 4$ [90AST]. In ASTM PS 70-97, the recommended specimens have the ratio of W/B in the range of 1 to 2. In this work, W/B=1.25 will be used, and, therefore, W is 5mm.

Notch preparation is critical in the determination of the plane strain fracture toughness in the chevron notched bending test. As mentioned before, this might be the major factor to obtain

stable crack propagation before load reaches the maximum, yielding valid fracture toughness values [84Wu[1], 84Chu].

Barker [83Bar] recommended that notch slot width, N be less than 0.03B as already mentioned and smaller notch width, 0.02B is recommended in the ASTM standard E1304-89 [89AST[1]] for the chevron-notched bar and rod specimen with a round bottom. Even if it is recognized that smaller notch width is best, the notch width is determined by the machining technique. In this work, the notch was machined by EDM with 0.1mm thickness wire, yielding a notch width of about 200μm. Therefore, the notch slot width, N=0.05B. However, the notch width of the specimen used in the present work is smaller than N<0.25mm, recommended in PS 70-97.

For four point bend CNB specimens in which the interaction of the stress field between the load roller and the crack does not need to be considered, α_1 =1 or close to 1 (Fig. 6.1) was predominantly used [92Sal, 84Chu, 80Mun[3], 83Mun]. Particularly, Munz et al. [80Mun[3]] observed that for four point bend specimens with α_1=1, K_{IC} values were independent of initial crack length ratio α_0 at $0.073 \leq \alpha_0 \leq 0.372$. The effect of α_0 on K_{IC} with CNB three point bend loading was systematically studied by Wu [84Wu[1], 84Wu[2]]. Wu [84Wu[1]] found that when the initial crack length ratio, $\alpha_0 \geq 0.3$ the difference in K_{IC} values calculated from the straight through crack assumption [80Mun[2], 80Mun[3]] and the Blumh's [80Mun[3], 75Blu, 77Blu] slice model is small [84Wu[1]] and K_{IC} values obtained from the ASTM standard method [90AST] and by CNB specimens are in good agreement with one another for $\alpha_0 \geq 0.3$ [84Wu[1], 84Wu[2]].

Chuck et al. [84Chu] also observed the effect of α_1 and the notch angle, θ, on K_{IC}. When α_1 was increased from 0.41, 0.60, to 0.893 (correspondingly the notch angle, θ is 120°, 90°, and 60°, respectively at constant α_0=0.2), they obtained valid K_{IC} values only at α_1= 0.893 and θ =60°. From the analysis of the results in the literature, the optimal specimen could have the crack length parameters, α_1=1 and α_0 = 0.3. Therefore, the notch angle, θ, which depends on α_1 and α_0 will be independently chosen as about 60°. α_1 of the specimens recommended in ASTM standard PS 70-97 is 0.95-1.0 for three of the four recommended specimens and 0.7 for the other, and α_0 is in the range of 0.2 to 0.4. The specimen geometry used for the present work does not deviate from the specimen geometries recommended in ASTM PS 70-97, except the length of the specimen. The length of the specimen used in the present work was

38.7mm which allowed an outer support roller span (S_1) of 35mm. The recommended length and the outer support roller span (S_1) of the specimen in PS 70-97 are 45mm and 40mm, respectively.

6.2.2 Loading mode

A CNB specimen can be loaded in three-point or four-point bending. There is no clear criterion in the literature to determine the best loading mode for CNB specimens. However, in four-point bending the specimen alignment is not very critical because of the constant moment between the inner loading points [83Mun]. Additionally, interaction between the load roller stress field and the crack stress field, which can happen in three point loading, is avoided [83Mun]. Therefore, four-point bend loading will be used in this work. In ASTM PS 70-97, three of the four recommended specimen geometries are for four point bend fixture.
The four point bending test needs an additional span between the load rollers, therefore, the length of the specimen, of course, will be much longer than that for the three point bending mode, in which a nominal support span, S equals 4W. For four point bending (Fig. 6.1), ratio of the support roller span to the specimen width, S_1/W=7.5-8 was normally used [80Mun[3], 84Chu, 90Wit, 92Sal] except Salem et al. [92Sal] who tested two of their specimens with S_1/W=3.07 and obtained the K_{IC} values similar to those obtained from the specimens S_1/W=8. Sung et al. [89Sun] used S_1/W=5, but for the in-test subcritical precracked specimens. The effect of S_1/W ratio on K_{IC} has not been systematically studied and therefore, it is not clear. In this work, it would be interesting to investigate the effect of S_1/W on K_{IC} with some selected alloys and will be worth for the foregoing research in terms of ingot preparation and effective use of intermetallic alloys which are normally fabricated in limited size in the laboratory system. In this work, S_1=35mm and 16mm with the constant S_2=4.7mm will be used, yielding S_1/W=7 and 3.2, respectively at the same S_2/W. As mentioned previously, to give more possibility of stable crack growth during the test, a very low loading rate, 0.05mm/min. will be used for the Instron machine. The specimen dimensions selected in the present work are summarized in Table 8.2 in Chapter 8.

6.3 Calculation of fracture toughness

6.3.1 Calculation of fracture toughness from the maximum load

As mentioned previously fracture toughness of CNB specimens can be calculated from the maximum load, P_{max}, as in Eq. (6.1), in which Y* is the stress intensity factor coefficient dependent only on specimen geometry. Y* is defined by [80Mun^2, 80Mun^3, 90Wit]

$$Y^* = \left[\frac{1}{2}\frac{dC_V(\alpha)}{d\alpha}\left(\frac{\alpha_1 - \alpha_0}{\alpha - \alpha_0}\right)\right]^{\frac{1}{2}} \qquad (6.2)$$

where $C_V(\alpha)$ is the dimensionless compliance of the specimen. To calculate K_{IC} from the maximum load, P_{max}, the compliance function $C_V(\alpha)$ of chevron-notched specimen must be known. There are two approximate methods for calculation of $C_V(\alpha)$. The simplest method is the straight-through crack assumption (STCA) proposed by Munz et al. [80Mun^2, 80Mun^3]. It assumes that for a chevron-notch specimen, the derivative of the compliance with respect to α, $dC_V(\alpha)/d\alpha$, is the same as for a straight-through crack specimen, $dCs(\alpha)/d\alpha$ [80Mun^2, 80Mun^3, 84Wu^1], i.e.,

$$\frac{dC_V(\alpha)}{d\alpha} = \frac{dC_S(\alpha)}{d\alpha} \qquad (6.3)$$

where $C_S(\alpha)$ is the dimensionless compliance of straight-through-crack specimen. For a specimen with a straight-through crack subjected to pure bending, the stress intensity factor can be rewritten from the ASTM standard E399-90 [90AST],

$$K_{IC} = \frac{P}{B\sqrt{W}}Y \qquad (6.4)$$

and then

$$Y = \left(\frac{S}{W}\right).f\left(\frac{a}{W}\right) \qquad (6.5)$$

Using the relation for a straight-through crack [80Mun^3, 90Wit]

$$\frac{dC_s(\alpha)}{d\alpha} = 2Y^2 \qquad (6.6)$$

$dC_S(\alpha)/d\alpha$ (or Y) can be directly obtained from the K-calibration of specimen [84Wu[1], 89AST[1], 76Sra[1]].

For four point bending, Y is given as below [76Sra[2], 80Mun[3], 90Wit,]

$$Y=\frac{S_1-S_2}{W}\frac{3}{2}\frac{\alpha^{\frac{1}{2}}}{(1-\alpha)^{\frac{3}{2}}}\left\langle 1.9887-1.326\alpha-\frac{(3.49-0.68\alpha+1.35\alpha^2)\alpha(1-\alpha)}{(1+\alpha)^2}\right\rangle \qquad (6.7)$$

Also, by using the relation, $\frac{dC_S(\alpha)}{d\alpha}=2Y^2$ the K_{IC} for chevron-notched specimen using STCA can be rewritten as

$$K_{IC}=\frac{P_{max}}{B\sqrt{W}}Y\left(\frac{\alpha_1-\alpha_0}{\alpha-\alpha_0}\right)^{\frac{1}{2}} \qquad (6.8)$$

and the relation between Y* and Y, comparing Eq. (6.2) with Eq. (6.8)

$$Y^*=\left[\frac{1}{2}\frac{dC_S(\alpha)}{d\alpha}\left(\frac{\alpha_1-\alpha_0}{\alpha-\alpha_0}\right)\right]^{\frac{1}{2}}=Y\left(\frac{\alpha_1-\alpha_0}{\alpha-\alpha_0}\right)^{\frac{1}{2}} \qquad (6.9)$$

The compliance of the specimen, $C_V(\alpha)$ can also be calculated in a more refined way using an approach offered by Bluhm [75Blu, 77Blu], which is as follows:

$$\frac{1}{C_V(\alpha)}=\frac{\alpha-\alpha_0}{\alpha_1-\alpha_0}\frac{1}{C_S(\alpha)}+\frac{\kappa}{\alpha_1-\alpha_0}\int_{\alpha}^{\alpha_1}\frac{1}{C_S(\zeta)}d\zeta \qquad (6.10)$$

where κ is the shear transfer coefficient between the slice and $C_S(\zeta)$ is the dimensionless compliance of a thin slice with a through thickness crack of normalized depth ζ. Eq. (6.10) was then reduced to an analytical expression as follows [84Wu[1], 90Wit]:

$$\frac{1}{C_V(\alpha)}=\left[\frac{\alpha-\alpha_0}{\alpha_1-\alpha_0}\right]\left[\frac{1}{\gamma+\beta\tan^2\left(\frac{\pi\alpha}{2}\right)}\right]+\frac{\kappa}{(\alpha_1-\alpha_0)(\gamma-\beta)}\times$$

$$\left\{(\alpha_1-\alpha)-\frac{2}{\pi}\left(\frac{\beta}{\gamma}\right)^{\frac{1}{2}}\left[\arctan\left\langle\left(\frac{\beta}{\gamma}\right)^{\frac{1}{2}}\tan\left(\frac{\pi\alpha_1}{2}\right)\right\rangle-\arctan\left\langle\left(\frac{\beta}{\gamma}\right)^{\frac{1}{2}}\tan\left(\frac{\pi\alpha}{2}\right)\right\rangle\right]\right\} \qquad (6.11)$$

where the value of γ given in [75Blu, 80Mun[3], 90Wit] is

$$\gamma = \left(\frac{S_1 - S_2}{W}\right)^2 \left\langle \frac{S_1 + 2S_2}{4W} + \frac{(1+\nu)W}{2(S_1 + S_2)} \right\rangle \text{ (ν: Poisson's ratio),} \qquad (6.12)$$

the value of β is

$$\beta = 2.7\left(\frac{S_1 - S_2}{W}\right)^2 \qquad (6.13)$$

and the value of κ is

$$\kappa = 1 + 0.444(\alpha_1)^{3.12} \text{ for } \phi \geq 1 \qquad (6.14)$$

$$\text{or } \kappa = 1 + (\alpha_1)^{3.12}\left(2.236\phi - 4.744\phi^2 + 4.699\phi^3 - 1.77\phi^4\right) \text{ for } \phi \leq 1 \qquad (6.15)$$

where ϕ=0.5(π-θ) and θ is the chevron notch angle.

6.3.2 Calculations of fracture toughness by work of fracture

The stable P-LLD curves which is one important advantage of bending tests of chevron-notched specimens can be used to determine the work-of-fracture [89Gho, 92Jen, 66Tat]. The work-of-fracture (γ_{wof}) is defined simply as the total energy consumed to produce a unit area of fracture surface during the entire fracture process [89Gho, 92Jen, 66Tat], i.e.,

$$\gamma_{wof} = \frac{\int pdu}{2A_T} \qquad (6.16)$$

where A_T is the projected fracture area of the specimen and Ipdu is the total energy as shown in Fig. 6.5.

In brittle, linear elastic materials, the work of fracture can be used as an estimate of the fracture surface energy of a material and to calculate the apparent fracture toughness using linear elastic fracture mechanics (LEFM) energy balance criterion [92Jen].

The relationship between the work-of-fracture and the apparent fracture toughness is given by the equation [89Gho]

$$K_{wof}^2 = \frac{2E\gamma_{wof}}{(1-\nu^2)} \qquad (6.17)$$

where ν is the Poisson's ratio.

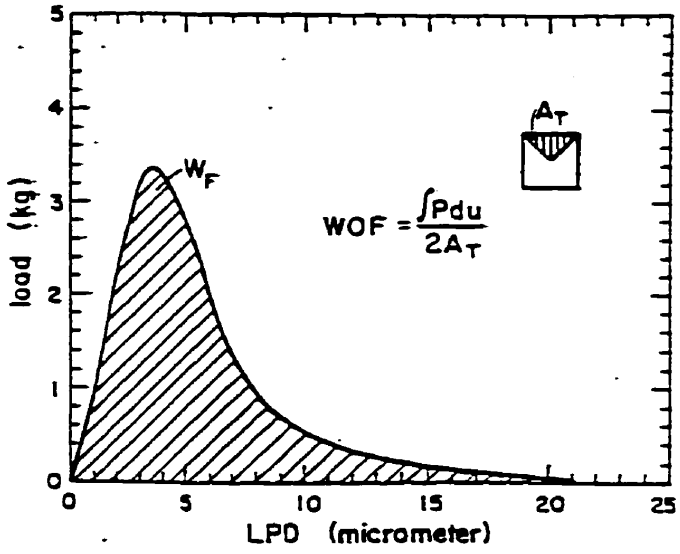

Fig. 6.5 Schematic of calculating work of fracture [89Gho].

For linear elastic materials with flat R-curve behaviour, Jenkins et al. [92Jen] observed that the work-of-fracture values were approximately equal to the fracture surface energy of the tested materials such as α-SiC and the fracture toughness values calculated from the work of fracture were in good agreement with the fracture toughness values calculated from the maximum load in a CNB test.

7. Indentation fracture toughness

The application of indentation fracture toughness has become wide spread for evaluating mechanical properties of brittle materials because the indentation fracture toughness method is very simple and requires only a very small amount of materials [83Nii, 89Pon[2]]. In many cases, the indentation fracture toughness method has shown its applicability for fracture toughness calculation, producing reasonable fracture toughness values similar to actual K_{IC} [89Pon[1], 92Mer, 93Cho]. But as a number of different formulas exist and fracture toughness depends on the indenter load and on the different means of measuring crack length, a comparison with other methods is necessary [92Mer].

7.1 Determination of the crack system

Indentation cracks can be classified into two groups depending on the geometrical shape of the cracks beneath the indentation [82Lan, 89Pon[2], 91Gla]. One is the half-penny shaped crack system (also called median or radial-median crack system) and the other is the Palmqvist crack system. A simple way to differentiate between them is to polish away the surface layers. The median cracks will remain connected to the corner of the diagonal while the Palmqvist crack will become detached as shown in Fig. 7.1. The parameters such as a, l, and c for both the crack systems are also designated in Fig. 7.1.

There is also another way to judge the crack system by the relation between the crack length and indentation load. Exner [69Exn] defined a crack resistance (also called Palmqvist crack resistance parameter), W, based on the observed linear relationship between indentation load (P) and the average crack length (l) at the corner of the Vickers indent:

$$W=P/4l \qquad (7.1)$$

On the other hand, Lawn and Fuller [75Law[2]] discussed the fracture mechanics analysis of the half-penny cracks (radial-median cracks) in soda-lime glass and observed experimentally the following relation between the crack length, c, (Fig. 7.1) and the indentation load, P,

$$c=KP^{2/3} \qquad (7.2)$$

where the constant K is a function of the Young's modulus, hardness, and fracture toughness of the ceramic and the geometry of the indenter.

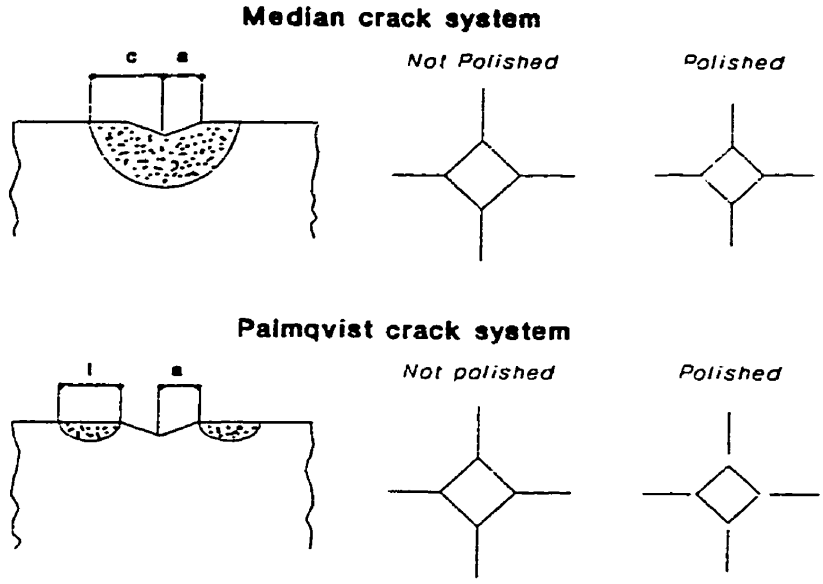

Fig. 7.1 Crack systems induced by Vickers indentation [91Gla]. 'a' is indentation half diagonal, '*l*' is the crack length emanated from the indentation corners, and 'c' is the crack length from the center of the indentation.

As shown by Eq. (7.1), the Palmqvist cracks (*l*) follow a linear dependence on indentation load, while according to Eq. (7.2) the median cracks (c) follow a 2/3 power dependence on indentation load.

Shetty et al. [85She[1], 85She[2]] tried to clearly identify the crack system by using the load dependence of crack lengths, c versus load, P with Eq. (7.1) for the Palmqvist system and Eq. (7.2) for the median crack system (by converting the relationship between *l* vs. P to that between c vs. P for the Palmqvist crack system). Eq. (7.1) was rewritten in the following way with respect to c, where H is the mean contact or indentation pressure exerted by the Vickers indenter given by $P/2a^2$ [89Pon[2]]

$$c = l + a$$

$$= P/4W + (P/2H)^{1/2} \qquad (7.3)$$

As Shetty et al. [85She[1]] mentioned, in deriving the best fit model of Eq. (7.3), *l* and a were obtained from the least square fits for the *l*-P data and the hardness fit from the relationship between indentation half diagonal, a and load, P, respectively.

Kaliszewski et al. [94Kal] and Pajares et al.[95Paj] determined the crack profiles by serial sectioning of Vickers indents in Y_2O_3-stabilized ZrO_2 ceramics for various loads. They found

that the shape of cracks changes from the radial cracks (Palmqvist cracks) at low loads to the "kidney-shaped" cracks at intermediate loads and further, to a half-penny shaped crack at sufficiently high indentation loads, with the exception of the core zone directly underneath the indent, which is not cracked after indentation [95Paj]. The radius of the core zone is approximately equal to the indentation half diagonal. They suggested that no cracks in the core zone indicated the existence of compressive residual stresses acting in the core zone making it highly resistant to crack propagation. This was also provided by the secondary indentation made in the core zone [95Paj] and a stable crack propagation experiment [94Dra] by four point bending test after generating indentation cracks. These recent results indicate that serial sectioning method is required to determine the crack system through the crack profiles beneath the indentations.

7.2 Indentation fracture toughness calculations

There are many models reported for indentation fracture toughness calculations in the literature and most of them require the value of Young's modulus (E) [89Pon^2]. Since indentation fracture toughness calculations will be applied for the new phases observed in the present work, and the Young's modulus of the phases are not known, the selection of the equations from the literature is limited to those not requiring the knowledge of elastic modulus.

Even if there have been attempts to differentiate between the two crack systems, there still remains an ambiguity whether there is actual difference between the half-penny shaped and Palmqvist crack systems, particularly, associated with the relationship between indentation load (P) and crack length (c or *l*). Therefore, the indentation fracture toughness calculations will be carried out for both the half-penny shaped and Palmqvist crack systems.

7.2.1 Palmqvist crack system

7.2.1.1 Shetty et al. model

Niihara [83Nii] and Warren and Matzke [83War] have independently suggested a relationship of the form

$$K_{IC}=\beta(HW)^{1/2} \qquad (7.4)$$

where W, Palmqvist crack resistance, is P/4l as in Eq. (7.1) and β is a nondimensional constant dependent , in Niihara's model, on the ratio of Young's modulus (E) to hardness, and H is $P/2a^2$ as already defined for Eq. (7.3). The value of the constant, β, in Warren and Matzke's analysis is unspecified. On the other hand, Shetty et al. [85She[1]] derived the following equation

$$K_{IC}=[1/[3(1-\nu^2)(2^{1/2}\pi^{5/2}\tan\theta)^{1/3}]][HP/(4l)]^{1/2} \qquad (7.5)$$

and rewrote Eq. (7.5) in the following form:

$$K_{IC}=[1/[3(1-\nu^2)(2^{1/2}\pi^{5/2}\tan\theta)^{1/3}]](HW)^{1/2} \qquad (7.6)$$

Therefore, by comparing Eq. (7.4) with Eq. (7.6)

$\beta= 1/[3(1-\nu^2)(2^{1/2}\pi^{5/2}\tan\theta)^{1/3}]$ where ν is Poisson's ratio of the material and 2θ is the angle of the opposite faces of Vickers indenter.

To calculate the K_{IC} values it was necessary to simplify Eq. (7.5) by substituting 0.25 and 68° for ν and θ, respectively. Poisson's ratio, ν was chosen based on the approximate values for brittle intermetallic and ceramic materials [92Ric, 95Nak]. The angle of the indenter used in the present work is $2\theta=136°$. Then, β is calculated as 0.0902. H is the mean contact or indentation pressure exerted by the Vickers indenter given by $P/2a^2$ [89Pon[2]]. From the relation between H and H_v ($H_v=0.4636P/a^2$ rewritten from Vickers hardness equation, $H_V=1.8544P/d^2$ by substituting 2a for d where d is a diagonal length), H can be substituted by 1.078 H_V. Finally, Eq. (7.6) can be written as

$$K_{IC}= 0.0937(H_VW)^{1/2} \qquad (7.7)$$

where Hv must be substituted in N/m^2 and W in N/m, then K_{IC} is in $MPa\cdot m^{1/2}$.

7.2.2 Half-penny shaped crack system

7.2.2.1 Lawn and Swain model

Lawn and Swain [75Law[3], 89Pon[2]] derived an equation for the stress-intensity factor, K in terms of the indenter load, P (MN) and the median crack depth, D (m) for a well-behaved median crack. The equation for Vickers pyramid indentations

$$K_{IC}=[(1-2\nu)/2\pi^{5/2}](HP/D)^{1/2} \quad \text{(where } H=P/2a^2 \text{ (MN/m}^2\text{))}$$

$$= 0.0143(HP/D)^{1/2} \qquad (7.8)$$

assuming the Poisson's ratio, ν is equal to 0.25 as already mentioned, and K_{IC} is in MPa·m$^{1/2}$. Ponton and Rawlings [89Pon^2] changed this equation based on the fact that the results for soda-lime glass have shown that D≈c [75Law^2, 79Mar] and the substitution of c for D in Eq. (7.8) is also acceptable for opaque materials [79Mar]. Therefore,

$$K_{IC}=0.0143(HP/c)^{1/2} \qquad (7.9)$$

7.2.2.2 Lawn and Fuller model

Lawn and Fuller [75Law^2] derived an equation as below

$$K=2P_{\perp}/(\pi D)^{3/2} \qquad (7.10)$$

where $P_{\perp}$ is the indentation force normal to the median plane and

$$P_{\perp} = P/2\ (\tan\psi') \quad \text{where } \psi' = \psi \pm \arctan\mu$$

Therefore,

$$K =P\tan(\psi \pm \arctan\mu)/(\pi D)^{3/2} \qquad (7.11)$$

where ψ is the indenter cone half-angle and μ is the coefficient of sliding friction between the indenter and the material. By taking ψ as 68° even if the Vickers indenter is not a conical indenter and assuming μ=0, the above equation can be rewritten as

$$K_{IC}=0.0726P/D^{3/2} \qquad (7.12)$$

where P is in MN, D is in m, and K_C is in MPa·m$^{1/2}$.

The depth of the indentation crack, D can also be substituted by the surface crack length, c [75Law^2, 79Mar] as mentioned above. Then the above equation yields

$$K_{IC}=0.0726P/c^{3/2} \qquad (7.13)$$

7.2.2.3 Evans and Charles model

Evans and Charles [76Eva] derived an equation for a half-penny shaped crack system as below. The derivation of the equation is very well explained in [89Pon^2].

$$K_C\phi/Ha^{1/2}=0.15\kappa(c/a)^{-3/2} \qquad (7.14)$$

If this is rewritten for the indenter with 68° half-angle from the equation in [89Pon^2], that is, P*=P/(2tan68) [75Law^2, 89Pon^2]

$$K_C\phi/(Hva^{1/2})=0.2113\kappa(c/a)^{-3/2} \qquad (7.15)$$

By taking the correction factor, κ=3.2 as in [76Eva] and assuming ϕ=2.7

$$K_{IC}=0.1161P/c^{3/2} \qquad (7.16)$$

where P is in MN, c is in m and K_{IC} is in MPa·m$^{1/2}$.

7.2.2.4 Lawn and Evans, and Hagan model

Lawn and Evans [77Law], and Hagan [79Hag] derived equations for indentation fracture toughness calculations in which only the minimum load for crack nucleation is required.

Lawn and Evans [77Law] derived an equation as below

$$P_C = (54.47\alpha/\eta^2\theta^4)\,(K_{IC}/H)^3 K_{IC} \qquad (7.17)$$

where P_C is the critical load to propagate a fortuitous critical flaw, α is a dimensionless factor determined by indenter geometry, η is a dimensionless factor dependent on the ratio of the spatial extent over which the tensile component of the elastic/plastic indentation field acts to the characteristic contact dimension (indentation half diagonal, a), θ is a dimensionless factor dependent on the ratio of the maximum tension at the elastic/plastic interface to the hardness, H. By substituting $\alpha=2/\pi$, $\eta\approx1$, $\theta=0.2$, and $H=P/2a^2$, the above equation can be rewritten as below:

$$P_C = 2.2 \times 10^4 (K_{IC}/H)^3 K_{IC} \qquad (7.18)$$

Hagan [79Hag] also derived a similar type of equation as Lawn and Evans [77Law] given below

$$P_C = 885[K_{IC}/H]^3 K_{IC} \qquad (7.19)$$

where P_C is the critical load to nucleate flaws in MN, H in MN/m^2 and K_{IC} in $MPa\cdot m^{1/2}$. In this case the presence of any fortuitous flaws of critical dimensions in the materials is not required since the flaws are nucleated by the deformation (dislocation process) in the deformation zone.

8. Experimental procedure

8.1 Preparation of intermetallic alloys

8.1.1 Alloys for the determination of phase equilibria

All the alloys were prepared from pure elements, nickel (99.9 pct.) and magnesium (99.8 pct.), except silicon that was supplied as a technical purity metal (98.4 pct). The as-received Ni pellets (3-25mm diameter) were pickled in $3HCl:HNO_3$ solution for several hours to remove the oxide on the surface of the pellets before melting. A graphite crucible with a lid was used and the inner walls of the crucible and the lid were coated with boron nitride spray (Boron Nitride Aerosol Lubricoat®, ZYP Coatings, Inc., Oak Ridge, USA) to eliminate a reaction between the molten metal and the crucible. Ingots were fabricated by induction melting under a high purity argon atmosphere and subsequently solidified in the crucible inside the induction furnace. The size of the solidified cylindrical ingots (50-70g) was about 40mm in diameter and 5-8 mm in height. Light elements such as Mg and Si were placed at the bottom of the crucible and heavy element, Ni was placed on top of Mg and Si. The temperature of the melt was measured within an accuracy of ±5°C by a W-5%Re and W-25%Re thermocouple inserted into the graphite crucible just above the melt level. One of the difficulties in fabricating the Mg-Ni-Si ternary alloys is the ability to control the Mg content in the alloys, particularly with intermediate Mg and Si content. Since the melting temperatures of Ni (1455°C) and Si (1414°C) are much higher than that of magnesium (650°C), the melting temperature to fabricate the ternary alloys also had to be kept much higher than the boiling point (1090°C). This caused substantial loss in Mg because of the severe evaporation and splashing of Mg during melting, as evidenced by the difference between the initial and fabricated alloy compositions in Table B.1 in Appendix B. Even if alloys 1 to 24 were already reported in [96Son], those alloys are also included in Table B.1 since new EDS analysis method was applied in the present work and resulted in more accurate EDS readings.

Severe loss in Mg content occurred during melting, particularly in some alloys with intermediate Mg and Si content (e.g. alloys 4, 5, 9, 10, 12, 19, 20, 30-35). Parallel to the decrease in the Mg content, the alloys were substantially enriched in Ni. The loss in Mg during melting was very little for the alloys with relatively low Mg (<10 at. %) such as 3, 6, 7, 8, 14, 15, 17, 18, 21, 25, 26, 27, and 28. Interestingly, high Mg but low (<10 at. %) or Si-free alloys such as 1, 36, 37, 38, 39, 40, and 41 also showed a minimal loss in Mg during melting. In general, the Si content of the alloys either changes in positive (Si enriched) manner or is left unchanged depending on the amount of the loss in the Mg content. The alloy is enriched in Si when the loss in Mg is substantial, but the Si content in the alloy is unchanged when the loss in Mg is negligible.

To reach the target composition after melting, we started with higher Mg content in the initial mixture of elements than the Mg content necessary for the target composition to compensate for the loss in Mg.

The amount of loss in Mg for the alloys containing intermediate Mg and Si which were melted at ~1350°C could be estimated from the regression fit showing the decrease in the Mg content versus the initial Mg content established in the previous work [96Son, 98Son[1]].

The melting temperatures of alloys were chosen differently depending on the Mg content in the target composition. Most of the Ni-rich alloys were melted at 1350°C, and the ternary and binary alloys containing high Mg content were melted in the range of 1080°C to 1300°C. The binary Ni-Si alloys fabricated for the previous work [96Son, 98Son] were melted at 1400°C or 1420°C. Arabic numerals were used for the designation of the alloys fabricated for microstructural observation and determination of phase equilibria. The details of the melting procedure are shown in Table 8.1. The melting temperature applied for each alloy is given in Table B.1 in Appendix B.

As-solidified ingots, wrapped in stainless pouches (Sen/Pak® heat treatment containers) to minimize oxidation, were homogenized in a high purity argon atmosphere in a tubular furnace and subsequently furnace cooled at the cooling rate ~1.3°C/min.. The homogenization temperature was selected in the range from 480°C to 900°C, depending on the melting temperature and transformation temperature of individual microconstituent phases existing in the alloys. The ingots were typically homogenized for 100 h, but additional homogenizing heat treatments were carried out up to 500 h for alloys 3, 16, 22, 25 and 52, which were

determined by a metallographic observation to be still in a non-equilibrium state after a 100h homogenization. Even after a 500h homogenization, alloy 52 contained four phases, indicating that it was still in a non-equilibrium state.

Table 8.1 Induction melting procedure

Alloy Type	DESCRIPTION
Mg-Ni Binary or Mg-Ni-Si Ternary Alloys	1. Evacuation of induction melting chamber to 5kPa or below. 2. Heating up to 400°C in vacuum. 3. Evacuation of induction melting chamber to 5kPa or below. 4. Pressurization of the chamber with high purity argon gas (130kPa). 5. Slow heating to 700°C and holding for 5 min. at 700°C. 6. Moderate heating to intended melting temperatures (1080°C - 1350°C). 7. Holding for 10 or 15min. at the intended melting temperature. 8. Turning off the furnace and cooling down to room temperature in the induction furnace (about 3h).

8.1.2 In-situ composites for fracture toughness testing of chevron-notched specimens

Four or five small ingots of the size appropriate for the observation of microstructural evolution (50-70g) were fabricated to make one big ingot. A detailed procedure of melting to make small ingots is the same as for the alloys fabricated for the microstructural observation and the determination of phase equilibria as described in the previous section (Table 8.1). After grinding off the surface of the small ingots to remove the surface product, they were co-melted at 1350°C for 10min. by induction melting in the graphite crucible coated with the boron nitride spray. The melt of the small ingots were then cast into a graphite mould with the size of 38.7x38.7x36.3 (mm^3) (almost a cube), which was placed in the vacuum induction furnace chamber and preheated in a cylindrical Kanthal wire resistance heating furnace (8cm in diameter) to about 400°C. Subsequently, the ingots were homogenized in the tubular

furnace in a high purity argon atmosphere. The designation of in-situ composites fabricated for CNB fracture toughness testing will be distinguished from that for the determination of phase equilibria by placing the letter 'F' in front of the Arabic numerals (e.g., F1, F2, and so on). Homogenization time and temperature were selected based on the result of the microstructural evolution and phase equilibria in the specific phase region [98Son[1]]. Homogenization for alloy F21 was carried out at a relatively low temperature of 600°C, because of the appearance of small wrinkle-like defects resembling fine microcracks; these were observed after homogenization at 900°C during the first attempt. Alloys F6 and F22 intended for the fabrication of single phase η and $MgNi_2$ were just solidified in the melting crucible because of the difficulty in controlling the Mg contents during casting of such high Mg alloys.

8.2 Microstructural characterization

Microstructural characterization of as-solidified and homogenized alloys for the determination of phase equilibria and fracture toughness test was carried out by optical microscopy with Nomarski interference contrast and scanning electron microscopy (SEM). Specimens for microstructural observations were cut from the ingots using an electro-discharge machine (EDM) or a microcutter with a silicon carbide wheel. The surface of each mounted specimen was ground with #280, #400, #800, and #1200 silicon carbide papers followed by polishing with 1.0, 0.3, and 0.06μm alumina powder lapping. For microstructural observations, the polished surface was etched with 15 or 20% nital depending on the nature of microconstituent phases in the alloys. However, near-Ni_3Si single phase alloys F9 and near- Ni_2Si single phase alloys F16 were etched with 60 ml HCl, 15 ml CH_3COOH, 15 ml HNO_3, and 15 ml H_2O solution [90Tak[2]] to reveal the grain boundaries for grain size measurement in alloy F9 and to reveal twin boundaries in alloy F16. Some alloys with high Si content such as alloys 28, 29, and 52 were also etched with 60 ml HCl, 15 ml CH_3COOH, 15 ml HNO_3, and 15 ml H_2O solution [90Tak[2]] for better contrast.

The chemical composition of alloys and phases was determined using fully quantitative energy dispersive x-ray spectroscopy (EDS) (QX2000 LINK system, accelerating voltage 20kV) with standard spectra created from the Mg_2Ni compound for Mg and Ni, and from the

Ni_2Si compound for Si. Five EDS readings were taken to determine the overall compositions and three EDS readings for the phase identification.

The volume fraction of various microconstituents in all the homogenized alloys for fracture toughness test was measured using an image analyzing software, Image Pro. Porosity in all the homogenized alloys for fracture toughness test was also measured on unetched specimens using Image Pro.

The melting points of the phases were measured using differential thermal analysis (DTA) carried out in a Simultaneous Differential Techniques module (SDT 2960 by TA Instrument) capable of performing both thermogravimetric analysis (TGA) and differential thermal analysis (DTA) at the same time. Scan rate used in the DTA experiments was 20°C/min.

Density of the selected alloys for microstructure observation and all the in-situ composites for the fracture toughness test was measured by a densitometer by the Archimedian method using Diethyl Phthalate of specific gravity 1.20.

8.3 Lattice parameter determination from X-ray diffraction (XRD)

In general, the microconstituent phases were identified by measuring compositions using EDS. However, microconstituent phases in some alloys were also identified using X-ray diffraction (XRD) patterns obtained from a Siemens D500 diffractometer equipped with a nickel filter and graphite monochromator using Cu-Kα radiation. A step size of either 0.05° or 0.02° per second from 10° to 85° in 2θ was used. To identify the lattice structure and determine the lattice parameters of the newly discovered ω phase, a pattern indexing computer program, TREOR [85Wer] was used. For the lattice parameter determination of the binary $MgNi_2$ and the ternary $Mg(Ni,Si)_2$ phases, both a pattern indexing computer program, TREOR [85Wer], and an extrapolation of measured lattice parameters against Nelson-Riley function [78Cul] were used for comparison. The average wavelength of Cu-Kα radiation ($CuK\alpha_{ave.}$ $\lambda = 0.15418$ nm) was used for lattice parameter determination. From the following relationship [78Cul]:

$$\frac{a'-a}{a} = K\left(\frac{\cos^2\theta}{\sin\theta} + \frac{\cos^2\theta}{\theta}\right) \qquad (8.1)$$

where 'a'' is the computed value for each peak (2θ) on XRD pattern, 'a' the true value of lattice parameter, and K is a constant, the Nelson-Riley function of the bracketed terms converges to 0 as the θ in the bracketed terms increases to 90°. Therefore, 'a'' must be equal to 'a' in Eq. (8.1) at θ=90°. If the value of 'a'', computed for each peak on the pattern is plotted against the Nelson-Riley function, $\left(\frac{\cos^2\theta}{\sin\theta}+\frac{\cos^2\theta}{\theta}\right)$, a straight line should result, and 'a', the true value of lattice parameter, can be found by extrapolating this line to $\left(\frac{\cos^2\theta}{\sin\theta}+\frac{\cos^2\theta}{\theta}\right)$=0. For a hexagonal symmetry such as $MgNi_2$ or $(Mg,Si)Ni_2$, lattice parameter 'c' also can be obtained in the same way as described for 'a'.

However, in hexagonal crystals, the position of a peak which has indices *hkl* is determined by two parameters, a and c, (i.e., $\frac{1}{d^2}=\frac{4}{3}\left(\frac{h^2+hk+k^2}{a^2}\right)+\frac{l^2}{c^2}$) it is impossible to calculate both of them from the observed 2θ value of each peak alone. Therefore, the peaks indexed with *hkl* were ignored and the remainder was divided into two groups, those with indices *hk*0 (e.g. (100), (110), (300), and (220)) and those with indices 00*l* (e.g. (004), (008), and (00$\underline{12}$)). A value of 'a'' is calculated for each *hk*0 peak and a value of 'c'' from each 00*l* peak. Two separate extrapolations are then made to find 'a' and 'c'. The results of extrapolations of measured lattice parameters against the Nelson-Riley function for the determination of the lattice parameters, a and c for both the $MgNi_2$ and the $(Mg,Si)Ni_2$ are given in Appendix C.1 The estimation of the accuracy of lattice parameter calculations is also given in Appendix C.2

8.4 Mechanical testing

8.4.1 Indentation techniques

All the indentation techniques, i.e., indentation fracture toughness, determination of crack profiles underneath the indentations, and hardness measurements were performed with a Shimadzu Micro Hardness Tester HMV-2000. A Vickers diamond indenter with the angle between the opposite faces at the vertex of 136° was used. Specimens were mounted and polished as for the specimens for microstructural observation in section 8.2. All the

measuring procedure such as the measurement of the length of the indentation diagonal for hardness measurement or indentation crack length for indentation fracture toughness calculation was done as soon as the indentations were made.

A systematic study of indentation crack profiles developed underneath the indentations and indentation fracture toughness measurement was performed on the η and the κ phases. For indentations fracture toughness calculations for the η and the κ phases, indentations were made at various loads, 300g, 500g, 1000g, and 2000g with 15s dwell time. A minimum number of 15 indentations were made at each load and at least seven acceptable indentations which show clear indentation corners as well as corner cracks without severe lateral cracks were chosen for indentation fracture toughness calculations. Some indentations which developed severe lateral cracks and cracks emanating from the sides of indentations on the η and the κ phases were not used for the calculations.

Crack profiles along the depth of the indentations for the η and the κ phases at different loads, 200g, 500g, and 2000g were obtained by a serial sectioning method [94Kal]. After each step of material removal by mechanical polishing using 0.06μm alumina powder, the crack lengths and polished-off depths were measured. To measure the crack length at each step the sample was slightly etched with 15% nital for about 20 seconds to clearly reveal the cracks. The depth of material removal at each step was measured with Mitutoyo BHN305 co-ordinate measuring machine.

For the indentation fracture toughness calculations of single phase alloys other than η and κ, indentations were made at 100g and 500g loads. The diagonal of the indentations and the corresponding crack lengths were measured using Image Pro.

Microhardness test was performed on various microconstituent phases at 100g and 500g loads with 15s dwell time.

8.4.2 Fracture toughness by chevron-notched bend specimen (CNB)

The chevron-notched specimens were tested in four point bending. The bend specimens were cut out by an electro-discharge machine (EDM) as shown in Fig. 8.1 and polished with #280, #400, #800, and #1200 silicon carbide papers followed by 1.0, and 0.3μm alumina powder

lapping. The chevron notch was electro-discharge machined in the polished test bar by a 0.1mm (100μm) copper wire. The notch slot width, N, measured on an optical microscope using Image Pro was about 200 μm. The initial crack lengths, a_0 and a_1 as shown in Fig. 6.1 were measured from the fractured specimens also using Image Pro.

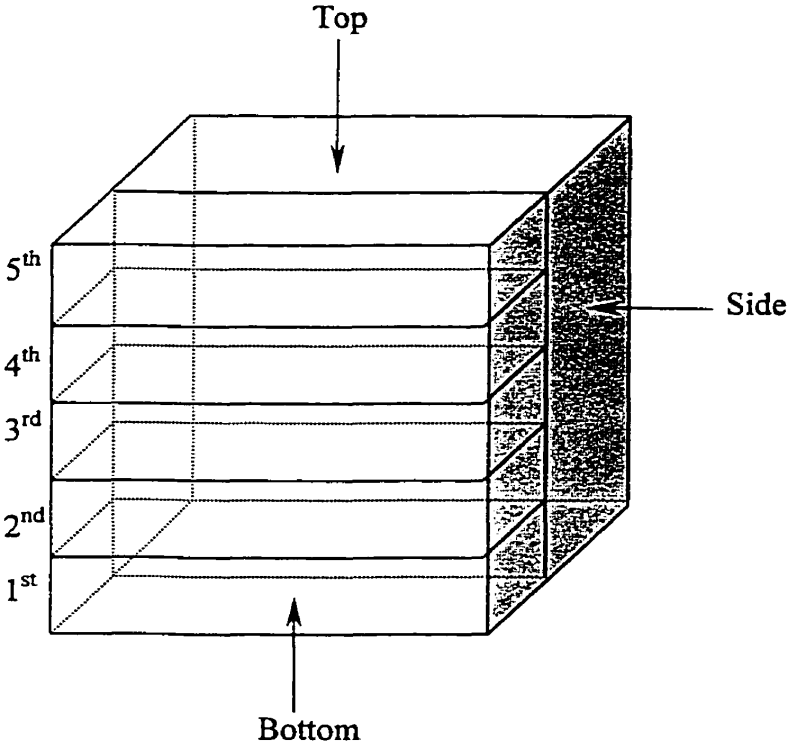

Fig. 8.1 A schematic illustrating the location of cut-out CNB specimens in the ingot. The side and the bottom of the ingot were in contact with the mould.

The cross head speed during test was 0.05mm/min, which was the lowest one available on the Instron machine (Model 4206). Load versus load-line displacement (P-LLD) was recorded digitally by a computer.

Fracture toughness values were calculated from the maximum load (K_{QIvM}) using Eq. (6.1) in which the stress intensity factor coefficient, Y* was calculated by approximation of the compliance function, $C_v(\alpha)$ using Eqs. (6.11) to (6.15). The 'ϕ' in Eqs. (6.14) and (6.15) is in the range of 0.9-1.1 depending on the chevron notch angle, θ. 'Maple' software was used for the calculation. Fracture toughness of some of the composites was also calculated using Eq.

(6.17) by determining the work-of-fracture given in Eq. (6.16) (fracture toughness is denoted K_{wof}, i.e., for work-of-fracture).

8.4.2.1 CNB test in air

The chevron notched specimens were tested in four point bending with S_1=35mm and S_2=4.7mm, fixed by the geometry of loading roller (Fig. 8.2(a)). For selected alloys, broken half of the S_1=35mm specimens was also tested in four point bending in a jig (Fig. 8.2) that allows adjustable S_1, applying S_1=16mm and S_2=4.7mm to investigate the effect of span S_1 on the fracture toughness.

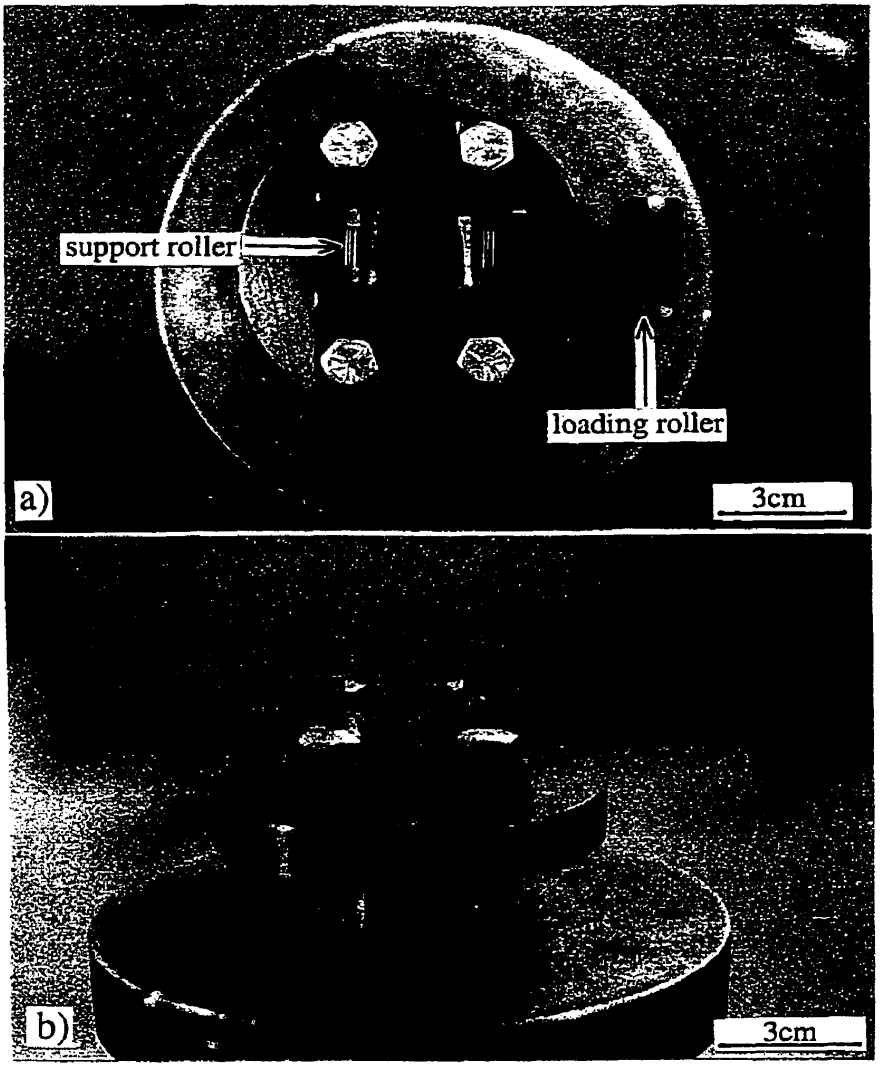

Fig. 8.2 Photographs showing (a) the top and (b) front view of a span-adjustable jig used for the CNB test in air. The loading block with loading rollers used with the jig is also shown in (a).

The specimen dimensions selected in the present work are summarized in Table 8.2. The specimen dimensions B, W, α_0, and α_1 in Table 8.2 are targeted in machining of the actual specimens, but are slightly different from the actual specimen dimensions due to machining inaccuracy as given in Table I.1 in Appendix I.

Table 8.2 The specimen dimensions selected in the present work.

B	W	α_0	α_1	S_1/W (S_1=35mm)	S_1/W (S_1=16mm)	Notch width (N)
4mm	5mm	0.3	~1	7	3.2	200μm (N=0.05B)

8.4.2.2 CNB test in vacuum and oxygen atmosphere

Fracture toughness tests of selected alloys were performed in vacuum or dry oxygen atmosphere to investigate environmental effects in single phase intermetallics and in intermetallic composites. The purity of the dry oxygen used in the present work was 99.993% and the oxygen contained 3ppm water, 40ppm argon, 10ppm nitrogen, and 1ppm hydrocarbons. Most of the selected alloys were tested in dry oxygen atmosphere with a pressure of 10.8×10^4 Pa (gauge pressure=12psi), back filled after the evacuation of the testing chamber to about 1.3×10^{-4} Pa (10^{-6} torr) using a diffusion pump assisted with liquid nitrogen for condensation of moisture. Only two specimens of composite F9 were tested in a vacuum of about 1.3×10^{-4} Pa (10^{-6} torr). The CNB specimens for the investigation of environmental effects were tested in four point bending with S_1=25.9mm and S_2=9.28mm which are different from the S_1 and S_2 for the specimens used in air testing since the jig used for the environmental test was not adjustable (Fig. 8.3). The set-up used for the investigation of environmental effect on fracture toughness was the same set-up used by Zbroniec [99Zbr] and is shown in Fig. 8.4. In Fig. 8.4, some portion of the set-up was changed. Flanges 7 and 11 in Fig. 8.4 were fixed by 6 small bolts which are directly screwed into the flanges without using the flange clamps (part 8 in Fig. 8.4) and the bolt (part 10 in Fig. 8.4). The loading rod (part 17) with rotational loading fixture (parts 28-33) in Fig. 8.4 was replaced by a loading rod with a flat bottom. More pictures showing the whole set-up including the vacuum system and Instron machine, etc., are given in [99Zbr].

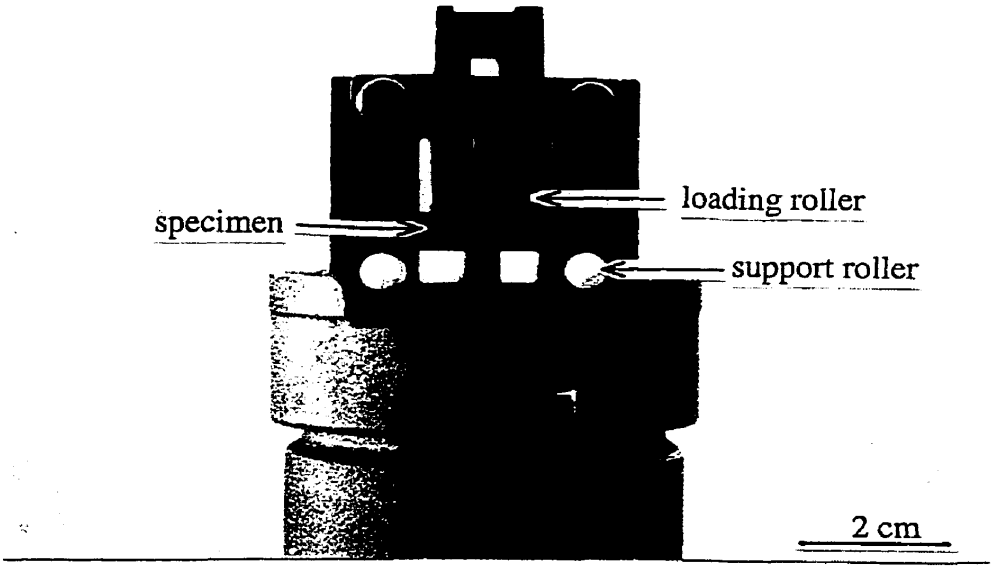

Fig. 8.3 A photograph of a jig used for the environmental test. Span S_1 is not adjustable.

The parts in the set-up in Fig. 8.4 are as follows [99Zbr]:

Part list:

1 - adapter
2 - clamp collar
3 - clamp collar bolt
4, 15 - bellow fixing plates
5 - bellow fixing bolts
6 - distance sleeve
7,11- flanged sleeves
8 - clamp
9 - "o"-ring closing environmental chamber from the top
10 - bolts squeezing the last "o"-ring
12, 23, 27, 51 - Water-cooling coils
13 - "o"-ring sealing upper flange of the bellow
14 - upper flange of the bellow
16 - "o"-ring squeezing and bellow's upper flange fixing bolts
17 - loading rod
18 - thin walled, copper bellow
19 - lower flange of the bellow
20 - "o"-ring sealing lower flange of the bellow
21 - bolts squeezing the lower flange "o"-ring

22 - flanged sleeve
24 - bolts squeezing the "o"-ring sealing vacuum chamber
25 - "o"-rings
26 - nut
28 - fixing collar
29 - bolt
30 - nut holding intermediate insert
31 - intermediate insert
32 - nut holding Ni_3Al intermetallic insert
33 - Ni_3Al intermetallic insert
34 - Al_2O_3 ceramic main loading rod
35 - Ni_3Al intermetallic loading block
36 - strip positioning loading rod
37 - bolt
38 - nut
39 - Al_2O_3, ceramic loading rollers
40 - fracture toughness specimen
41 - Al_2O_3, ceramic support rollers
42 - Ni_3Al intermetallic support insert
43 - thermocouple
44 - water container
45 - balls allowing the load to be transferred uniformly to the load cell
46 - ball's positioning block
47 - vacuum seal
48 - environmental chamber
49 - "o"-ring, sealing connection between environmental chamber and diffusion pump
51 - vacuum valve
52 - pressure gage
53 - tubular furnace

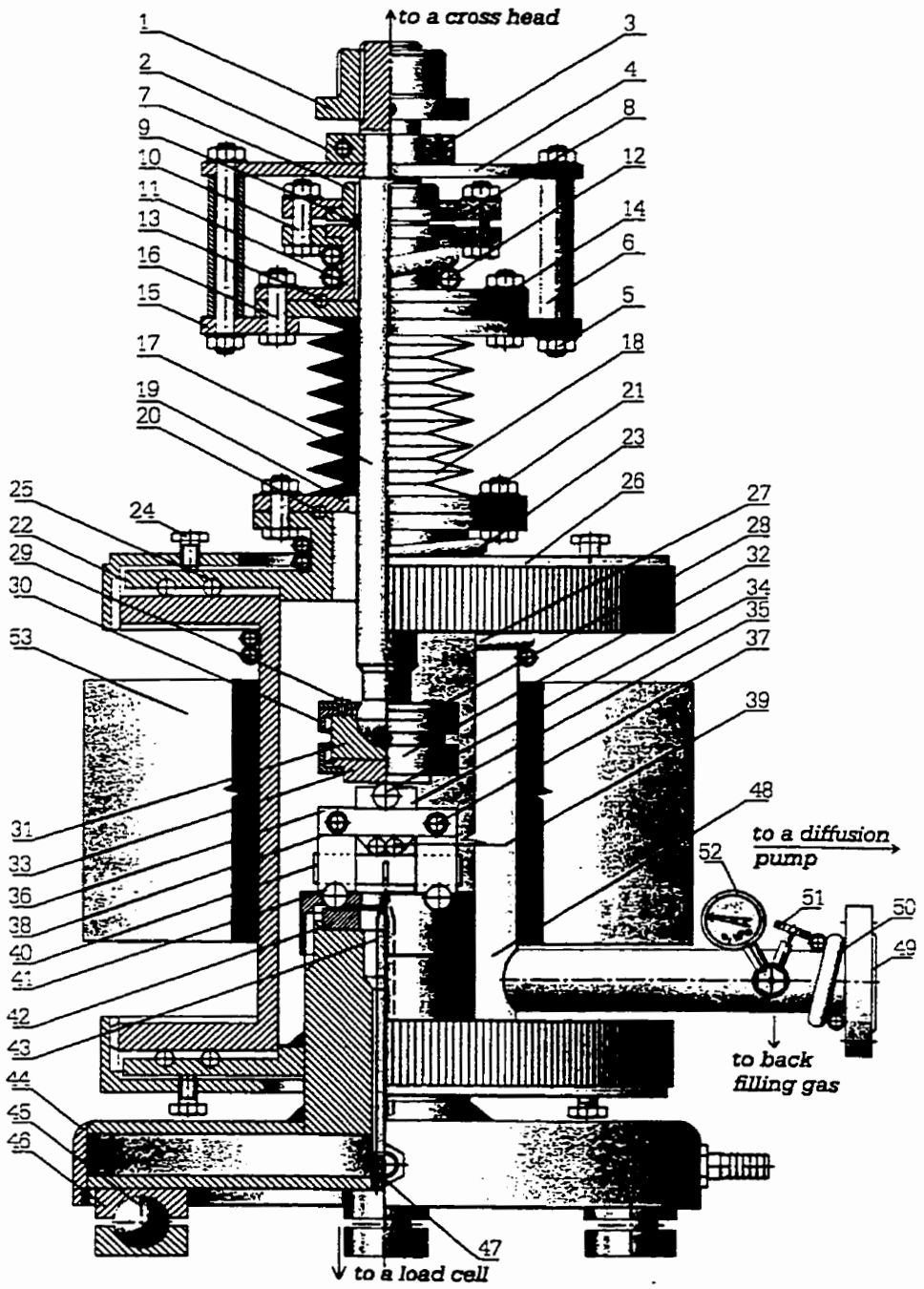

Fig. 8.4 Fracture toughness testing set-up used in the present work [99Zbr].

8.4.3 Compression test

The yield strength σ_{ys} or fracture strength of composites was obtained by conducting compression tests according to ASTM standard E9-89a [89AST^2]. The rectangular specimen with about 3.5x3.5x7mm^3 (specimen with a length to diameter ratio, L/D, of 1.5 or 2.0 are the best adapted for determining the compressive strength of high-strength materials [89AST^2]) was subjected to an increasing axial compressive load at a cross-head speed at 0.05mm/min, resulting in an initial strain rate in the range of $5.5x10^{-3}$ to $8.7x10^{-3}$ min^{-1} depending on the length of the specimens. Even if the initial strain rate of $5x10^{-3}$ min^{-1} is recommended in ASTM E9-89a, it could not be achieved in this work because the limit of the lowest cross-head speed of the Instron machine, 0.05mm/min. resulted in a slightly higher initial strain rate for the specimens prepared for the compression test. Load versus displacement was recorded digitally by a computer. To reduce the friction between the bearing blocks inserted at the end of the pushing rods and the specimen, which can cause barrelling, molybdenum disulphide was applied to the ends of the specimens.

Since the machine is also elastically deformed when the specimen is being tested, the rate at which the actual strain is applied to the specimen is lower than the velocity of the cross-head motion when no sample is being applied. However, if one knows the specimen stiffness, K_{spec}, calculable from the geometry and Young's modulus of the specimen using Eq. (8.2), it is possible to correct the whole load-displacement curve obtained during test as shown in Fig. 8.5. The specimen stiffness, K_{spec} is [84Mey]

$$K_{spec} = \frac{EA}{L} \qquad (8.2)$$

where A, L, and E are the cross-sectional area, height of sample, and Young's modulus, respectively.

In Fig. 8.5, K_1 is the specimen stiffness, K_{spec} and K_2 is the slope of the direct load-displacement. The arrows in Fig. 8.5 show how this correction is made. The curve is shifted to the left by an amount given by the distance between the two elastic lines K_1 and K_2 at that specified value of load. In Fig. 8.5, AB=CD. The difference in the direct and corrected curves arises from the effect of the machine stiffness and the relationship between K_{spec} (K_1), K_2, and K_{mach} designated in Fig. 8.5 is

$$\frac{1}{K_2} = \frac{1}{K_{mach}} + \frac{1}{K_{spec}} \qquad (8.3)$$

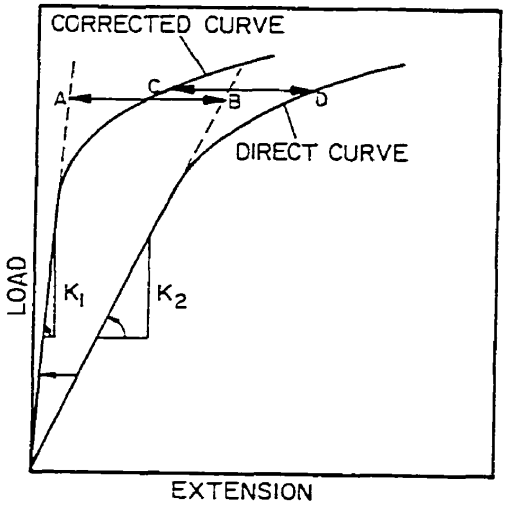

Fig. 8.5 Load-displacement curves showing both the direct curve and corrected curve [84Mey].

In the present work, some of the composites fractured before yielding and some of the composites showed yielding behaviour before fracture during compression test. For the samples which fractured before yielding, fracture strength was calculated from the direct load-displacement curve since there is no difference in fracture load in the direct and corrected load-displacement curves when it is in the linear portion of the load-displacement curve. While 0.2% offset yield strength was calculated from both the corrected and direct load-displacement curves for the samples which showed yielding behaviour.

To correct the direct curve, it is necessary to know the Young's modulus of the in-situ composites to calculate the K_{spec}. Most of the alloys which showed yielding before fracture contain Ni, Ni_3Si, and η phases as microconstituents (alloys F1, F2, F7-F12). Young's moduli of in-situ composites containing Ni, Ni_3Si, or η were calculated from the composite rule of mixtures equation (Eq. 5.41) using the Young's modulus and volume fraction of Ni, Ni_3Si, and η phases in the composites. Young's moduli of Ni(Si) and Ni_3Si phases used for calculations are 200GPa [96Her] and 210GPa [93Ulv], respectively, based on the fact that

Young's moduli of pure Ni and slightly alloyed Ni_3Si (with 0.05-0.1 at. % B and 2-4 at. % Ti and Cr) are reported to be about 200GPa [96Her] and 200-220GPa [93Ulv], respectively. Since Young's modulus of the η phase was not known, it was estimated from the indentation fracture toughness equations, assuming that the fracture toughness 1.7 $MPa.m^{1/2}$ (Table 9.11), of the η phase measured by CNB specimens represents the plane strain fracture toughness of the η phase. The indentation fracture toughness equations used to calculate the Young's modulus of the η phase are selected from the review paper by Ponton and Rawlings [89Pon^2]. The selected equations are designated as 'ED' and 'JL' in [89Pon^2] and originated from [79Eva] and [82Lan], respectively. Both the equations designated as 'ED' and 'JL' were recommended for indentation fracture toughness calculations in [89Pon^1] since the indentation fracture toughness values calculated using the equations provided the fracture toughness values close to the K_{IC} values obtained by the conventional method according to the experimental results in [89Pon^1].

The equation designated as 'ED' [79Eva] is

$$K_C = 0.4636(P/a^{\frac{3}{2}})(E/H_V)^{\frac{2}{5}}(10^F) \qquad (8.4)$$

where P is the indentation load, 'a' the length of indentation diagonal (Fig. 6.6), and $F= -1.59-0.34B-2.02B^2+11.23B^3-24.97B^4+16.32B^5$ and B=log(c/a).

The equation designated as 'JL' [82Lan] is

$$K_C = 0.0363(E/H_V)^{\frac{2}{5}}(P/a^{1.5})(a/c)^{1.56} \qquad (8.5)$$

By taking K_C=1.7 $MPa.m^{1/2}$, a (in m) and c (in m) for the η phases at respective load as given in Table 8.3, Young's modulus, E, and standard deviations of the η phase was calculated. The equations, ED and JL resulted in quite similar values to each other. Therefore, the average value of 320 GPa calculated from both equations was considered as the Young's modulus of the η phase in this work. Young's moduli of the selected in-situ composites calculated from Eq. (5.41) based on the volume fraction of phases for each composite (Table 9.10 in section 9.3.1) are listed in Table 8.4.

Table 8.3 Young's modulus of the η phase estimated from the indentation fracture toughness equations.

Indentation load, g	Young's modulus (GPa)	
	ED [79Eva, 89Pon[2]]	JL [82Lan, 89Pon[2]]
300	304	268
500	368	328
1000	282	253
2000	400	357
Average of each equation	339±55	302±49
Average from both equations	320±52	

Table 8.4 Young's moduli (E) of selected composites calculated using a rule of mixture and Young's moduli of individual phases.

In-situ composite	F1	F2	F6	F7	F8	F9	F10	F11	F12
E (GPa)	235	249	318	219	237	210	209	213	245

9. Results

9.1 EDS quantitative analysis

There is a discrepancy between the chemical compositions determined using EDS with standard spectra created from pure elements and from compounds. When standard spectrum files created from pure elements were used, the EDS analysis did not provide very accurate results, having the stoichiometries of the intermetallic compounds in the binary Ni-Si and Ni-Mg systems slightly deviated from those in the equilibrium phase diagrams as can be noticed in Fig. 4.2. The comparison between the EDS results obtained by using standard spectra created from pure elements and from compounds is given in Table 9.1 for the selected phases such as $Ni_{31}Si_{12}$ (or Ni_5Si_2) and Ni_2Si in the Ni-Si system, and $MgNi_2$ in the Mg-Ni system. The composition of the selected phases must not vary since $Ni_{31}Si_{12}$ (Ni_5Si_2) and Ni_2Si are line compounds, and $MgNi_2$ has a very narrow homogeneity range [90Mas] (Appendix A). The compositions of the $Ni_{31}Si_{12}$, Ni_2Si and $MgNi_2$ phases in the equilibrium binary phase diagram are 27.9 at.% Si and 72.1 at. % Ni, 33.3 at. % Si and 66.6 at. % Ni, and 33.3 at. % Mg and 66.6 at. % Ni, respectively as given in Table 9.1. When the chemical compositions were determined using EDS with pure elemental standards, the heavy element, Ni was overestimated and the light elements Mg and Si were underestimated. The Si contents of $Ni_{31}Si_{12}$ and Ni_2Si in the Ni-Si binary system were underestimated by about 2.2 at. % and 2.5 at. %, respectively and the Mg content of the $Mg(Ni,Si)_2$ phase was also underestimated by about 4.5 at. % on the average, compared to the compositions of the phases in the existing equilibrium phase diagrams. However, when the chemical compositions were determined using EDS with compound standards the measured phase compositions of the selected phases were almost identical to the compositions in the binary equilibrium phase diagrams as given in Table 9.1. One may also compare the position of the binary Ni-Si and Ni-Mg phases in Fig. 4.2 established using EDS with pure elemental standard spectra and in Fig. 9.1 re-established with compound standard spectra in section 9.2.1.

Table 9.1 Comparison of the compositions of selected phases measured with EDS by using two different standard spectra, i.e., pure elemental spectra and compound spectra.

Phase	Alloy No	Pure elemental standard		Compound standard	
		Si or Mg*	Ni (or Ni+Si)**	Si or Mg*	Ni (or Ni+Si)**
$Ni_{31}Si_{12}$ (or Ni_5Si_2) (Ni:Si= 72.1:27.9)	4	25.5±0.4***	74.5±0.4	28.8±0.3	71.2±0.4
	5	25.5±0.3	74.5±0.3	28.3±0.4	71.7±0.4
	6	25.5±0.5	74.5±0.5	28.4±0.2	71.6±0.3
	7	25.8±0.1	74.2±0.1	28.4±0.2	71.6±0.4
	8	25.8±0.3	74.2±0.3	28.3±0.2	71.7±0.3
	9	25.9±0.1	74.1±0.2	28.6±0.2	71.4±0.1
	10	25.8±0.4	74.2±0.5	28.4±0.4	71.6±0.4
	22	25.3±0.5	74.7±0.5	28.2±0.2	71.8±0.3
	23	26.0±0.3	74.0±0.4	28.0±0.1	72.0±0.5
	Average	25.7±0.2****	74.3±0.2	28.4±0.2	71.6±0.2
Ni_2Si (Ni:Si = 66.6:33.3)	6	30.7±0.5	69.3±0.5	33.3±0.3	66.7±0.5
	7	30.7±0.4	69.3±0.5	33.0±0.1	67.0±0.3
	8	30.5±0.2	69.5±0.3	33.3±0.3	66.7±0.2
	9	30.4±0.2	69.6±0.2	33.4±0.2	66.6±0.1
	10	30.7±0.3	69.3±0.3	33.5±0.2	66.5±0.3
	11	30.8±0.3	69.2±0.2	33.6±0.2	66.4±0.2
	12	31.0±0.1	69.0±0.1	33.6±0.3	66.4±0.1
	13	30.6±0.4	69.4±0.4	33.9±0.1	66.1±0.1
	14	30.8±0.2	69.2±0.2	33.8±0.1	66.2±0.1
	15	31.1±0.3	68.9±0.3	33.3±0.6	66.7±0.5
	16	30.9±0.4	69.1±0.6	34.2±0.2	65.8±0.2
	17	31.3±0.3	68.7±0.2	34.0±0.1	66.0±0.1
	18	31.2±0.5	68.8±0.5	34.2±0.3	65.8±0.3
	23	30.8±0.3	69.2±0.3	33.2±0.2	66.8±0.2
	24	30.7±0.4	69.3±0.3	33.8±0.2	66.2±0.3
	Average	30.8±0.3	69.2±0.3	33.6±0.4	66.4±0.4
$Mg(Ni,Si)_2$ ((Ni+Si):Mg = 66.6:33.3)	1	28.8±0.4	(70.5±0.3 + 0.8±0.2) = 71.3	32.7±0.1	(66.6±0.1 + 0.7±0.1) = 67.3

*: the compositions in this column stand for Si content in case of $Ni_{31}Si_{12}$ and Ni_2Si, and for Mg for $Mg(Ni,Si)_2$ which is a ternary intermediate phase of $MgNi_2$.
**: the composition in this column stands for Ni content in case of $Ni_{31}Si_{12}$ and Ni_2Si, and for (Ni+Si) for $Mg(Ni,Si)_2$.
***: the standard deviation of the phase composition in each alloy was calculated from three EDS readings.
****: the standard deviation of the average phase composition was calculated from the average composition of each alloy.

The discrepancy between the EDS results obtained using different standards, i.e., pure element standards and alloy (compound) standards, was also observed by Chen et al. [94Che] in a Ti-42.7Al-7.9Nb alloy. They related this discrepancy to the fact that their alloy system contained both heavy and light elements, i.e. Nb, and Al, respectively. By analogy, the

compositional discrepancy caused by using different standards in the present Ni-Si-Mg system can also be related to the coexistence of both heavy element Ni and light elements Si and Mg. The content of impurities such as oxygen was lower than the detectability limit of the windowless EDS technique.

9.2 Phase equilibria and intermetallic phases in the Ni-Si-Mg system

9.2.1 The phase diagram and microstructure of selected alloys

The isothermal Mg- and Si-rich section of the ternary Ni-Si-Mg phase diagram has been established based on the results of the microstructural examinations, EDS, and x-ray measurements as shown in Fig. 9.1. The Ni-rich section of the ternary Ni-Si-Mg phase diagram established by the alloys designated by numbers from 1 to 26 in Fig. 4.2 and published by the present author [98Son[1]] has also been modified as shown in Fig. 9.1 based on the EDS analysis using intermetallic compound standards. The overall composition of 28 alloys from alloy 27 to 54 investigated in the present work, their homogenization treatment and phases identified in each alloy, are given in Table D.1 in Appendix D. Designations of the newly found ternary phases by Greek letters were arbitrarily chosen and the $MgNi_2$ phase with Si, forming a ternary intermediate phase was designated as $Mg(Ni,Si)_2$.

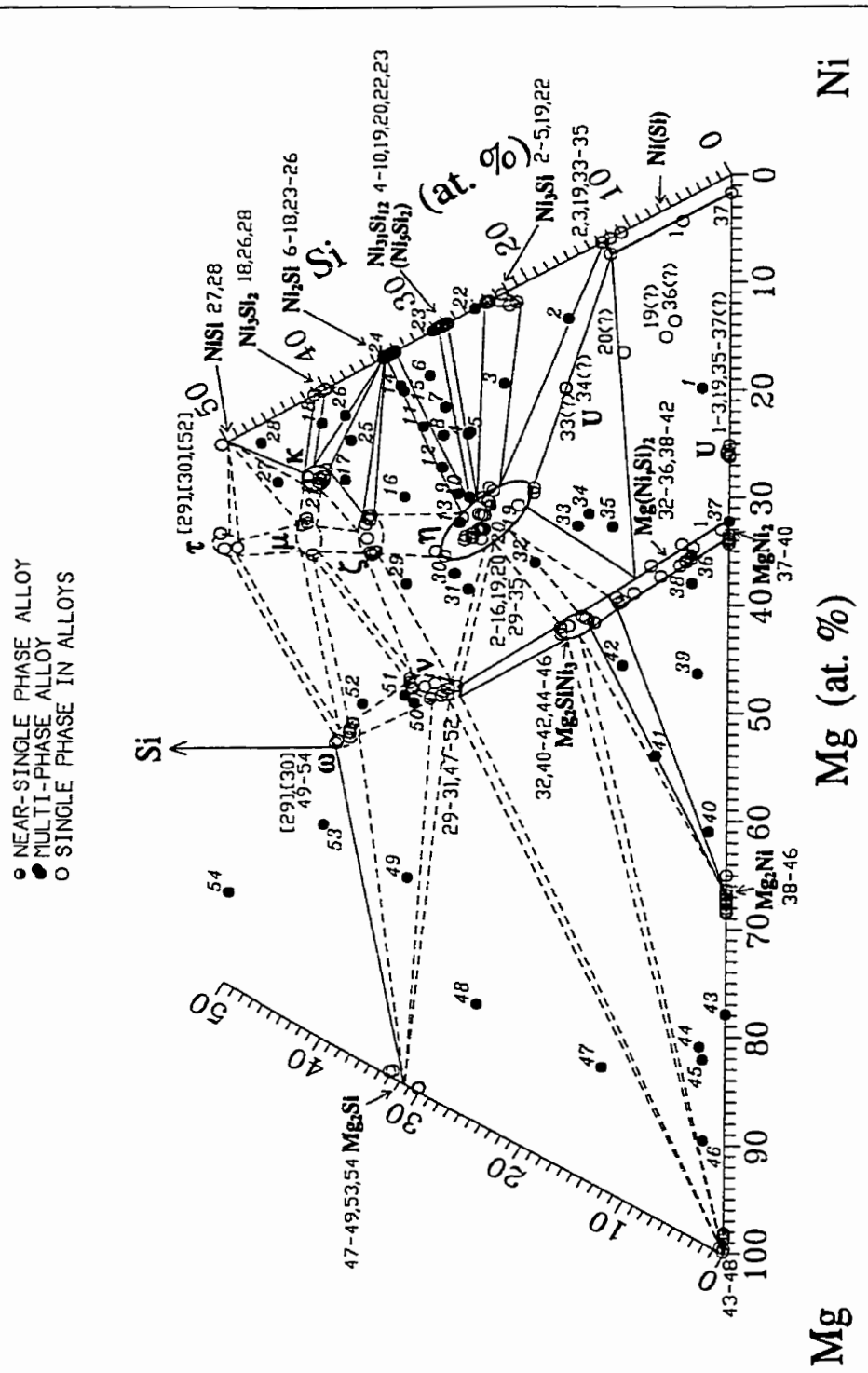

Fig. 9.1 The proposed Ni-Si-Mg ternary phase diagram established after slow cooling to room temperature. The numbers in the brackets correspond to the non-equilibrium alloys containing the given phases. The solid circles designated with italic numbers indicate overall compositions. The alloy numbers, which are not included in the phase diagram for clarity, are 14-17, 25, 29-30 for ζ, 17, 18, 21, 25-28 for κ, and 27, [29], [30], 52 for μ.

9.2.1.1 Microstructural observations

Microstructural observations for the alloys numbered from 1 to 26 have already been reported in the Master's thesis [96Son] and the following article [98Son[1]] by the present author. The alloys 27 to 54 investigated in the present work were also investigated in the as-solidified condition and after homogenization. Microstructure of the selected alloys in various phase regions on the phase diagram in Fig. 9.1 shows the microstructural evolution dependence on composition and also illustrates how the phase diagram in Fig. 9.1 was established.

As an example, the characteristic microstructure of only one of the alloys in the pertinent equilibrium phase region is presented in this section since the alloys in the same equilibrium phase region consist of exactly the same microconstituent phases with only different volume fraction. Microstructure of some other alloys, which are not introduced in this section, is shown in Fig. F.1 in Appendix F.

9.2.1.1.1 Microstructure of alloys 27 (NiSi, κ, and μ), 28 (NiSi, Ni_3Si_2, and κ), and 29 (ζ, η, and ν)

The rounded NiSi phase in the microstructure was solidified first in alloys 27 and 28 (Fig. 9.2(a) and (b)). Numerous cracks are seen in the (κ+μ) mixture (Fig. 9.2(a)). In alloy 28, the NiSi phase is also observed in the fine eutectic-like mixture of (κ+NiSi) as well as attached to the rounded Ni_3Si_2 phase. The latter (rounded Ni_3Si_2) seems to be formed at 845°C by a peritectoid reaction from (θ-Ni_2Si+NiSi) eutectic structure according to the Ni-Si binary phase diagram [90Mas]. NiSi attached to Ni_3Si_2 seems to be a remaining phase from the peritectoid reaction. A fine, three-phase mixture of (κ+NiSi+Ni_3Si_2) was also occasionally observed as shown in Fig. 9.2(c) but without the rounded Ni_3Si_2 phase.

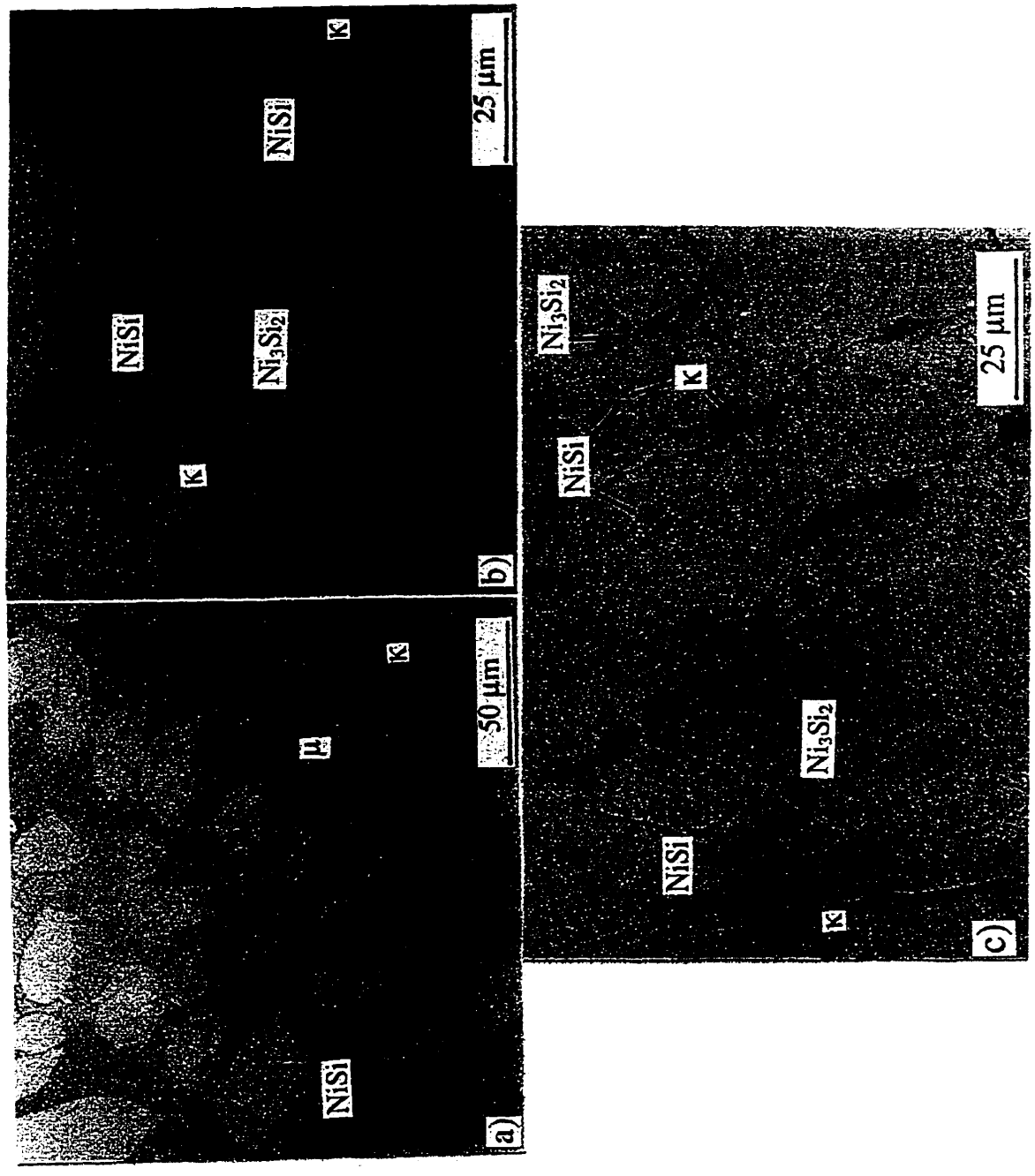

Fig. 9.2 Optical micrographs of alloys (a) 27 and (b-c) 28 after homogenization.

The as-solidified microstructure of alloy 29 in Fig. 9.3(a) contains four phases. A non-equilibrium phase mixture designated as 'N' is embedded in the phase designated as ζ. Fig. 9.3(b) is a magnified SEM micrograph of 'N' in alloy 29. Most probably, the "N" is a decomposition product which is a three-phase mixture of the ω phase with about 30.8±0.5 at.

% Mg, 36.8±0.4 at. %. Si and 32.4±0.2 at. % Ni, μ with 11.6+0.6 at. % Mg, 41.7±0.6 at. %. Si and 46.7±0.7 at. %. Ni, and τ with 9.9±0.5 at. % Mg, 50.2±0.7 at. % Si and 39.9±0.4 at. % Ni. In some other area, a two-phase mixture of (μ+ω) was also observed. Two or three phase mixtures were also observed in the as-solidified alloy 30 which is in the same equilibrium phase region with alloy 29. Fig. 9.3(c) shows the highly magnified 'N' mixture observed in the as-solidified alloy 30. In this alloy, the two-phase mixture consists of the ω phase with 32.5±0.8 at. % Mg, 36.9±0.7 at. %. Si and 30.5±0.1 at. % Ni and τ phase with 10.4±0.9 at. % Mg, 48.9±0.7 at. %. Si and 40.7±0.3 at. %. Ni. In the three phase mixture in alloy 30, the μ phase with 14.8±1.1 at. % Mg, 41.1±0.1 at. % Si and 43.9±1.0 at. % Ni coexists with ω and τ. Fig. 9.3(d) shows that the 'N' mixture in alloy 29 disappeared after homogenization. It is noted that the ν phase in Fig. 9.3(d) is revealed in two distinguishable contrasts. Some portion of the ν phase appears grey, but some other portion of the ν phase is bright. The EDS compositional difference between the two distinguishable regions in the ν phase is negligible. Therefore, different contrast might be induced by the differences in crystallographic orientation. However, an Electron Backscattered Diffraction (EBSD) technique would be needed for obtaining crystallographic orientation.

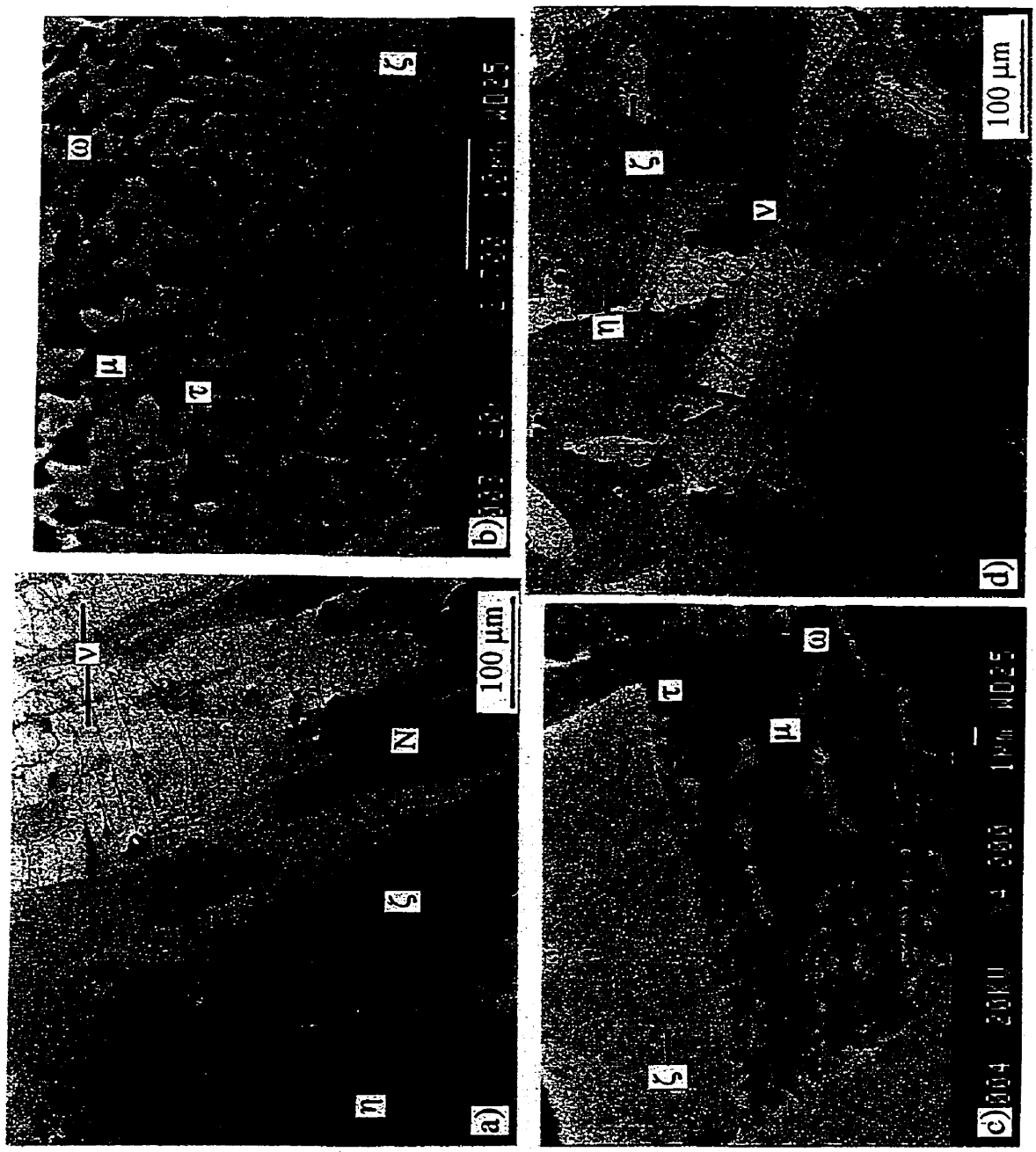

Fig. 9.3 Optical micrographs of (a) as-solidified alloy 29 and the highly magnified non-equilibrium phase mixture in as-solidified alloy 29 (b) and 30 (c), and (d) as-homogenized alloy 29.

9.2.1.1.2 Microstructure of alloy 33 (η, $Mg(Ni,Si)_2$, and Ni(Si))

In the as-solidified alloy 33 (Fig. 9.4(a)), the $Mg(Ni,Si)_2$ matrix is divided into two distinctive regions. The 'High Si-$Mg(Ni,Si)_2$' region, enveloped by small η particles, has a high Si content (~10 at % Si) and the other region, referred to as the 'Low Si-$Mg(Ni,Si)_2$', which is sharing a boundary with η or (η+Ni(Si)) phase region, has a low Si content (~5 at. % Si). Fine η particles enveloping 'High Si-$Mg(Ni,Si)_2$' in as-solidified structure (Fig. 9.4(a)), seem to indicate the occurrence of a eutectic reaction (L→η particles+$Mg(Ni,Si)_2$) during solidification.

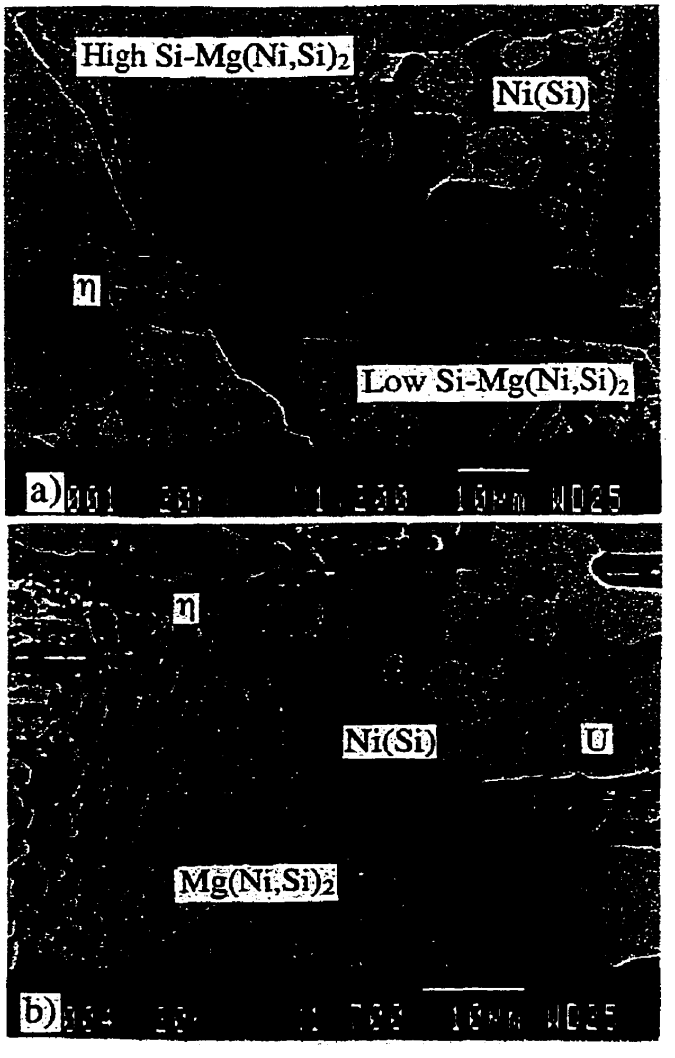

Fig. 9.4 SEM micrographs showing the as-solidified (a) and homogenized (b) microstructures in alloy 33.

After homogenization (Fig. 9.4(b); different field of view than Fig. 9.4(a)) the η particles also appeared within both the former 'High Si-$Mg(Ni,Si)_2$' and 'Low Si-$Mg(Ni,Si)_2$' regions. They seem to result from a decrease in the size of the $Mg(Ni,Si)_2$ homogeneity range with decreasing temperature, similarly as proposed in the binary Mg-Ni phase diagram [90Mas]. The size and fraction of the η particles within the former 'High-Si $Mg(Ni,Si)_2$' are much larger than those within the former 'Low-Si $Mg(Ni,Si)_2$'. This is not clearly understood. It is to be noted that the overall composition of the 'High-Si $Mg(Ni,Si)_2$' region in the as-solidified state (32.2±0.5 at. % Mg, 10.6±0.4 at. % Si and 57.2±0.7 at. % Ni) and after homogenization (29.5±0.9 at. % Mg, 11.7±0.4 at. % Si and 58.8±0.8 at. % Ni), are slightly different. The unidentified phase designated "U" with the composition of ~12 at. % Mg, 16 at. % Si, and 72 at. % Ni is also observed after homogenization (Fig. 9.4(b)).

9.2.1.1.3 Microstructure of alloys 37 ($MgNi_2$ and Ni) and 38 (Mg_2Ni and $Mg(Ni,Si)_2$)

Microstructure of the top portion of the ingot 37 is different from the bottom portion. In the top portion of the ingot in as-solidified state, the $MgNi_2$ matrix was solidified first, leaving the elongated phase designated as 'U' (unidentified) (Fig. 9.5(a)). According to the binary Mg-Ni phase diagram [90Mas] a eutectic mixture of Ni and $MgNi_2$ exists in equilibrium with the $MgNi_2$ matrix. However, the 'U' phase morphology is rod or lath-like rather than eutectic one, with the composition ~25 at.% Mg and 75 at.% Ni, close to the $MgNi_3$ stoichiometry. Needle–like, linear precipitates, presumably elongated along the solidification direction are also observed in the matrix. According to the Mg-Ni phase diagram [90Mas] they might be the Ni phase precipitated during cooling due to the decrease in the solubility of Ni in the $MgNi_2$ phase with decreasing temperature. Precipitate denuded regions are also seen surrounding the large rods (laths) of the 'U' phase in Fig. 9.5(a). After homogenization, the "U' phase associated with the precipitate denuded regions still exists and the former linear precipitates are now agglomerated as small particles (Fig. 9.5(b)). Surprisingly, contrary to the expectation that the precipitates were the Ni phase, EDS analysis of the agglomerated particles showed that their composition was the same as that of the U phase. The second phase region, formed after solidification of the $MgNi_2$ matrix, in the bottom portion of the ingot contains the (Ni+$MgNi_2$) eutectic mixture and Ni, in addition to the U phase (Fig. 9.5(c)). However, the (Ni+$MgNi_2$) eutectic mixture disappeared after homogenization (Fig. 9.5(d)) leaving behind only interconnected Ni and U phases in the second phase region.

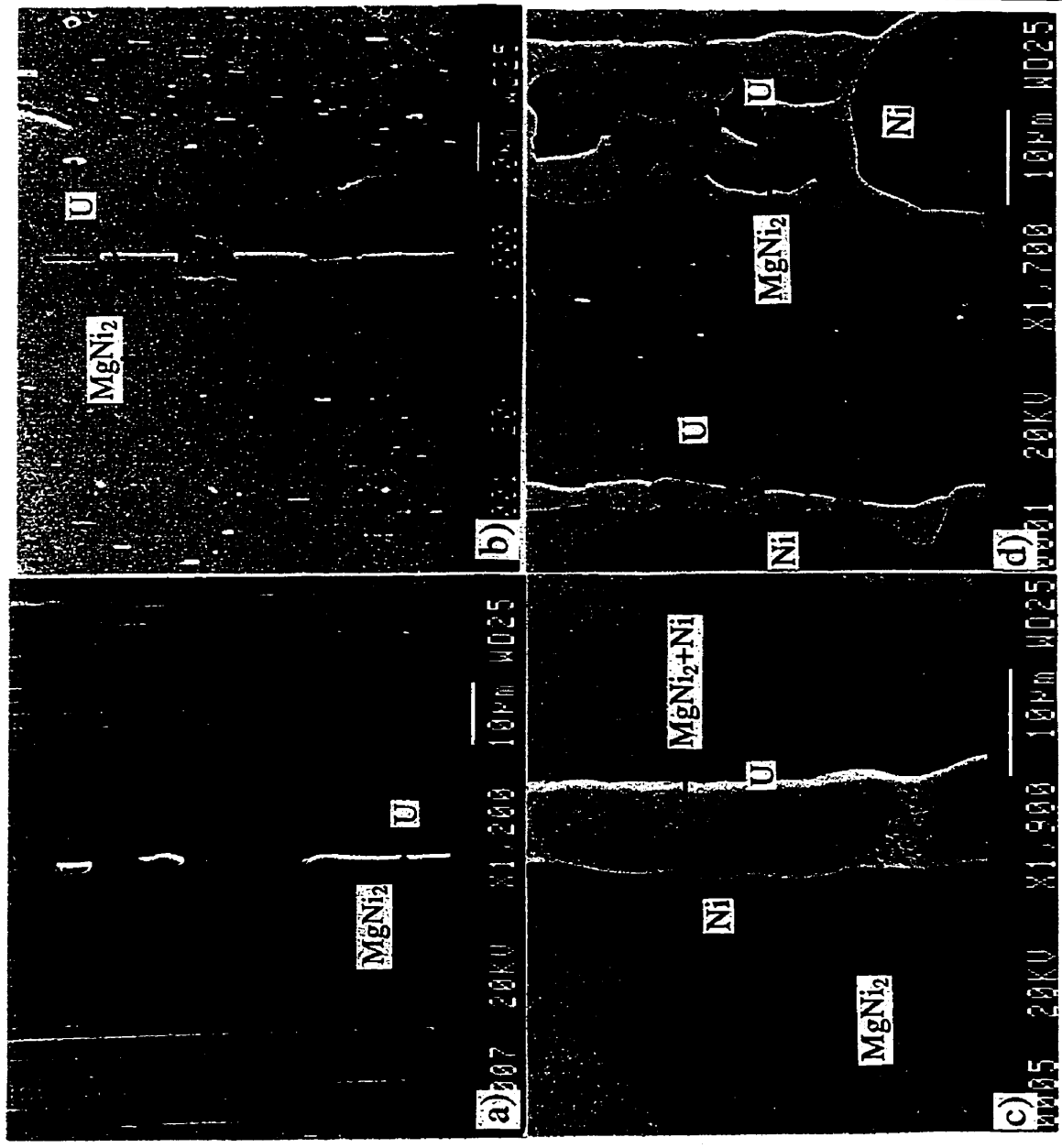

Fig. 9.5 SEM micrographs showing the top portion of ingot 37 in (a) as-solidified and (b) homogenized state, and the bottom portion of the same ingot in (c) as-solidified and (d) homogenized state. An unidentified phase is designated "U".

Fig. 9.6(a) shows the as-solidified microstructure of the ternary alloy 38. The faceted, plate-like $Mg(Ni,Si)_2$, i.e. a Si–bearing ternary intermediate phase based on the binary $MgNi_2$, solidified first. The Mg_2Ni phase in between the plate-like $Mg(Ni,Si)_2$ phase was most probably formed by a peritectic reaction: $L+MgNi_2 \rightarrow Mg_2Ni$ at 760°C, as indicated in the

binary Ni-Mg phase diagram [90Mas]. In fact, the pure binary $MgNi_2$ phase (no Si) embedded in the binary Mg_2Ni matrix was also observed (the pure $MgNi_2$ phase is not recognizable under low magnification in Fig. 9.6(a)). Fig. 9.6(b) shows that even after homogenization, both the Si-bearing ($Mg(Ni,Si)_2$) and Si-free $MgNi_2$, which are virtually the same phases having the same crystallographic structure, still coexist by sharing the interface instead of forming a uniform composition. The homogenized morphology of $MgNi_2$ still retains its faceted shape.

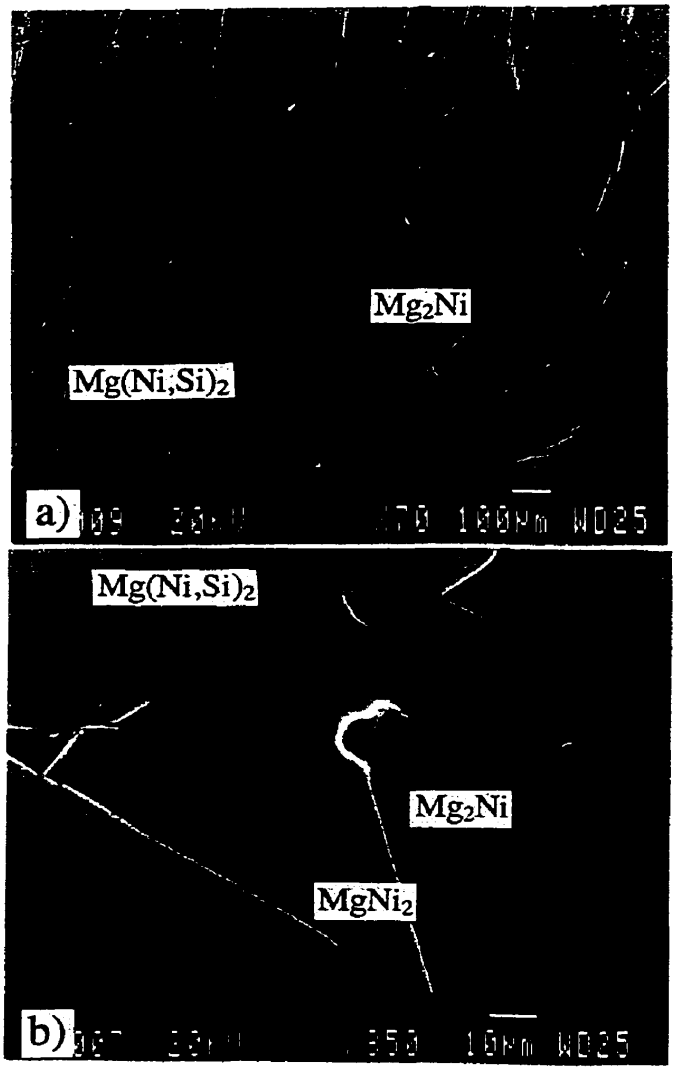

Fig. 9.6 SEM micrographs of (a) as-solidified and (b) homogenized alloy 38.

9.2.1.1.4 Microstructure of alloy 32 (η, Mg_2SiNi_3, and $Mg(Ni,Si)_2$)

The as-solidified microstructure of alloy 32 is not shown here since the microstructures of the top and bottom of the ingot are quite identical with those of the corresponding portions of the homogenized alloy (Fig. 9.7), except that the Mg_2SiNi_3 particles in the (Mg_2SiNi_3+$Mg(Ni,Si)_2$) mixture were finer in as-solidified alloy.

The appearance of homogenized microstructure of alloy 32 in the top (Fig. 9.7(a) and (b)) is different from that in the bottom portion (Fig. 9.7(c) and (d)) of the ingot. The EDS results show that the overall composition of the top (26.1±0.1 at. % Mg, 20.0±0.7 at. % Si, and 53.9±0.3 at. % Ni) and the bottom (27.0±0.9 at. % Mg, 19.0±1.0 at. % Si, and 53.9±0.9 at. % Ni) is very close to one other, and the phases and their compositions in both the top and bottom are the same. Homogenized microstructure of the top portion (Fig. 9.7(a) and (b)) shows large, blocky η accompanied by smaller and elongated η, the Mg_2SiNi_3 layer enveloping η, and finally, the (needle-like Mg_2SiNi_3+$Mg(Ni,Si)_2$) mixture. The morphology of the phases is different in the bottom portion (Fig. 9.7(c)) but the rounded primary solidified η phase, the Mg_2SiNi_3 phase enveloping the η phase and the (Mg_2SiNi_3+$Mg(Ni,Si)_2$) mixture are still observed. Approximate composition of small bright particles in Fig. 9.7(b) and (d), existing within the Mg_2SiNi_3 phase surrounding the η phase, is close to $Mg(Ni,Si)_2$. The Si content of ~13.3 at. % in the $Mg(Ni,Si)_2$ matrix, a part of the (Mg_2SiNi_3+$Mg(Ni,Si)_2$) mixture in the as-solidified state, is much higher than that of ~10.5 at. % after homogenization. This indicates that the solid solubility limit of Si in $MgNi_2$, decreases with decreasing temperature.

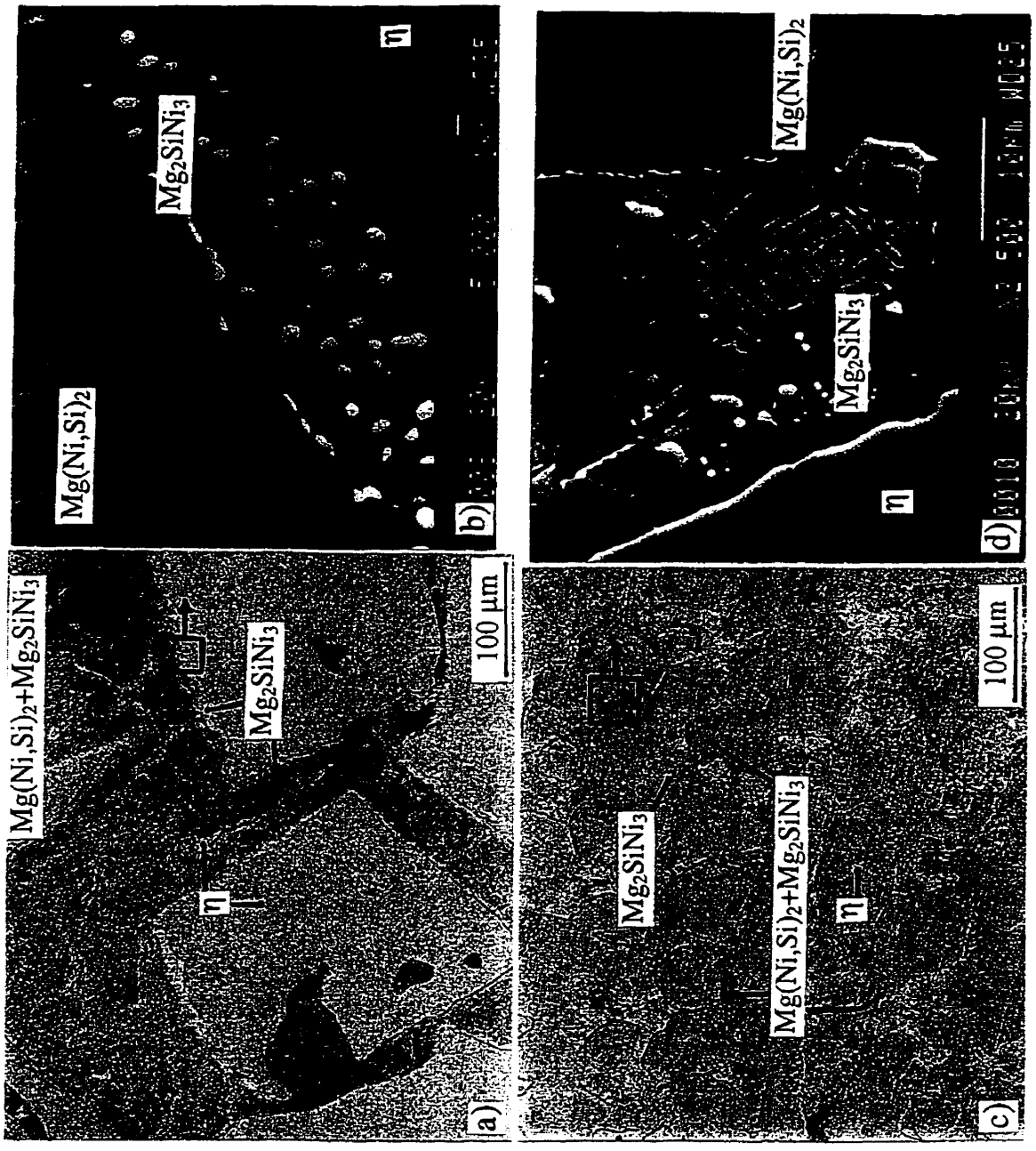

Fig. 9.7 Optical micrographs of (a) the top portion and (c) the bottom portion of the ingot of alloy 32 after homogenization. Figures (b) and (d) show the magnified SEM microstructures corresponding to the designated area (square) in (a) and (c), respectively.

9.2.1.1.5 Microstructure of alloys 42 ($Mg(Ni,Si)_2$, Mg_2Ni, and Mg_2SiNi_3), 44 (Mg, Mg_2Ni, and Mg_2SiNi_3), 48 (Mg, Mg_2Si, and ν), 49 (Mg_2Si, ν, and ω), 51 (ν and ω), 52 (ν, ω, μ, and [τ]), and 54 (Mg_2Si, Si, and ω)

The microstructure of the homogenized alloy 42 (Fig. 9.8(a)) consists of the blocky, rounded Mg_2SiNi_3 phase, the plate-like, faceted $Mg(Ni,Si)_2$ phase and the interdispersed Mg_2Ni. In general, the $Mg(Ni,Si)_2$ and $MgNi_2$ phases are observed to solidify in a faceted morphology (Fig. 9.8(a), and Fig. 9.6(a) and (b)). Fig. 9.8(b) shows the microstructure of the homogenized alloy 42 after heavy etching. The Mg_2Ni phase is almost completely etched out,

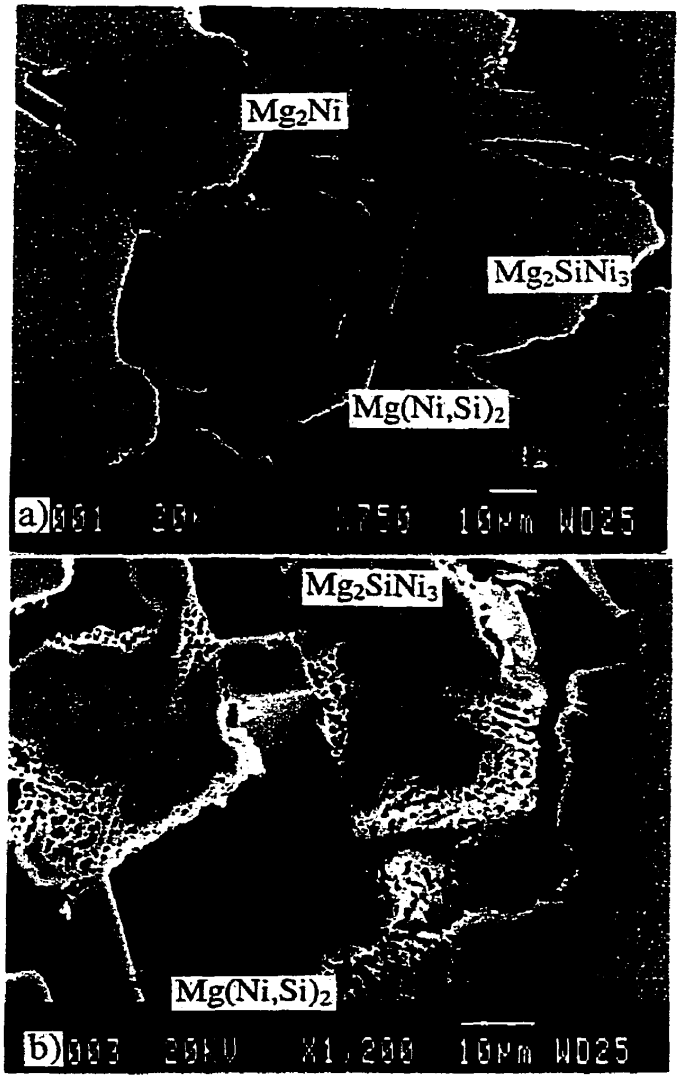

Fig. 9.8 SEM micrographs of alloy 42 (a) before etching and (b) after etching showing the morphology of Mg_2SiNi_3 and $Mg(Ni,Si)_2$ underneath the surface.

leaving only the blocky Mg_2SiNi_3 and plate-like $Mg(Ni,Si)_2$ phases. It is very likely that the blocky, rounded Mg_2SiNi_3 phase solidified first.

Fig. 9.9(a) shows the microstructure of alloy 44 after homogenization. The nearly dendritic Mg_2SiNi_3 connected with a blocky Mg_2Ni are embedded in the (Mg_2Ni+Mg) eutectic matrix. Fig. 9.9(b) shows the microstructure of alloy 48 after homogenization. It shows a three phase morphology with the (Mg_2Si+v) mixture resembling a eutectic microstructure coexisting with the small islands of the Mg phase.

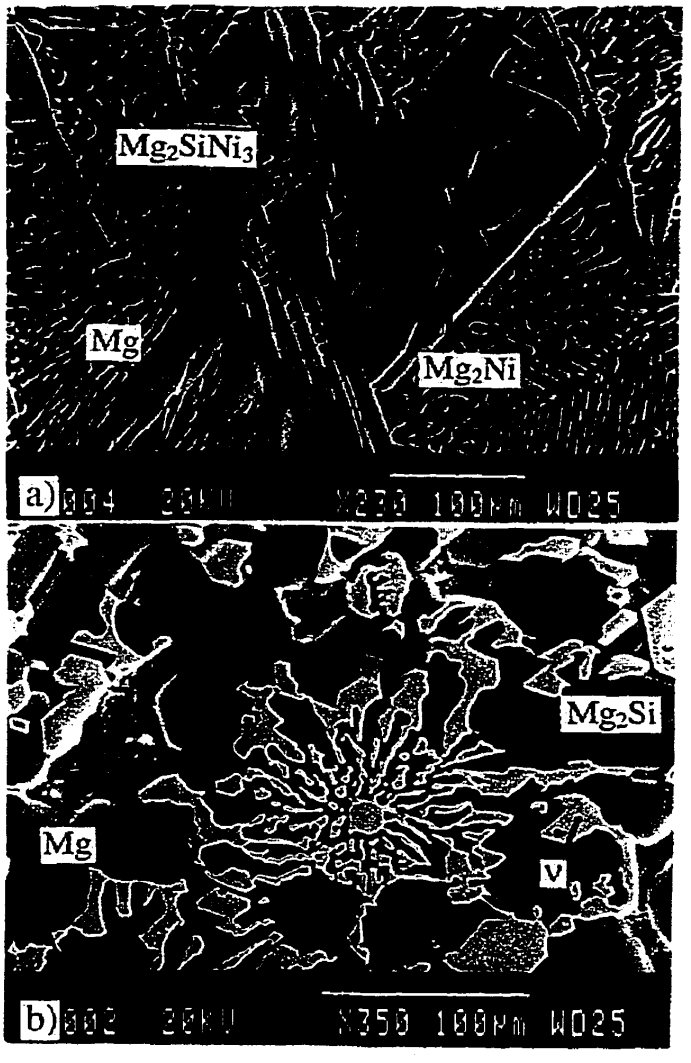

Fig. 9.9 SEM micrographs of homogenized alloys (a) 44 and (b) 48 without etching.

Fig. 9.10 shows the homogenized microstructure of alloys 49, 51, 52 and 54. Alloy 49 in Fig. 9.10(a) shows three-phase morphology. The dark Mg_2Si phase region looks blurry because of severe etching used to reveal the phase boundary between the ν and ω phases. Alloy 51 in Fig. 9.10(b) also shows three-phase morphology. However, the compositional difference between the core ν phase and the phase surrounding it (like a rim) is too small to deduce whether or not they are two different phases as discussed in section 9.2.2. Fig. 9.10(c) shows a four-phase morphology of alloy 52 indicating that it is still in a non-equilibrium state even after 500 h homogenization. According to the overall composition of alloy 52 (see Fig. 9.1 and Table D.1 in Appendix D), the τ phase seems to be the non-equilibrium phase, but the τ phase in contact with the ω and μ phases (Fig. 9.10(c)) is very stable and still remains even after long time homogenization. In alloy 54 (Fig. 9.10(d)) Mg_2Si appears to be the phase solidified first which coexists with the (Si+Mg_2Si) or (Si+Mg_2Si+ω) phase mixtures.

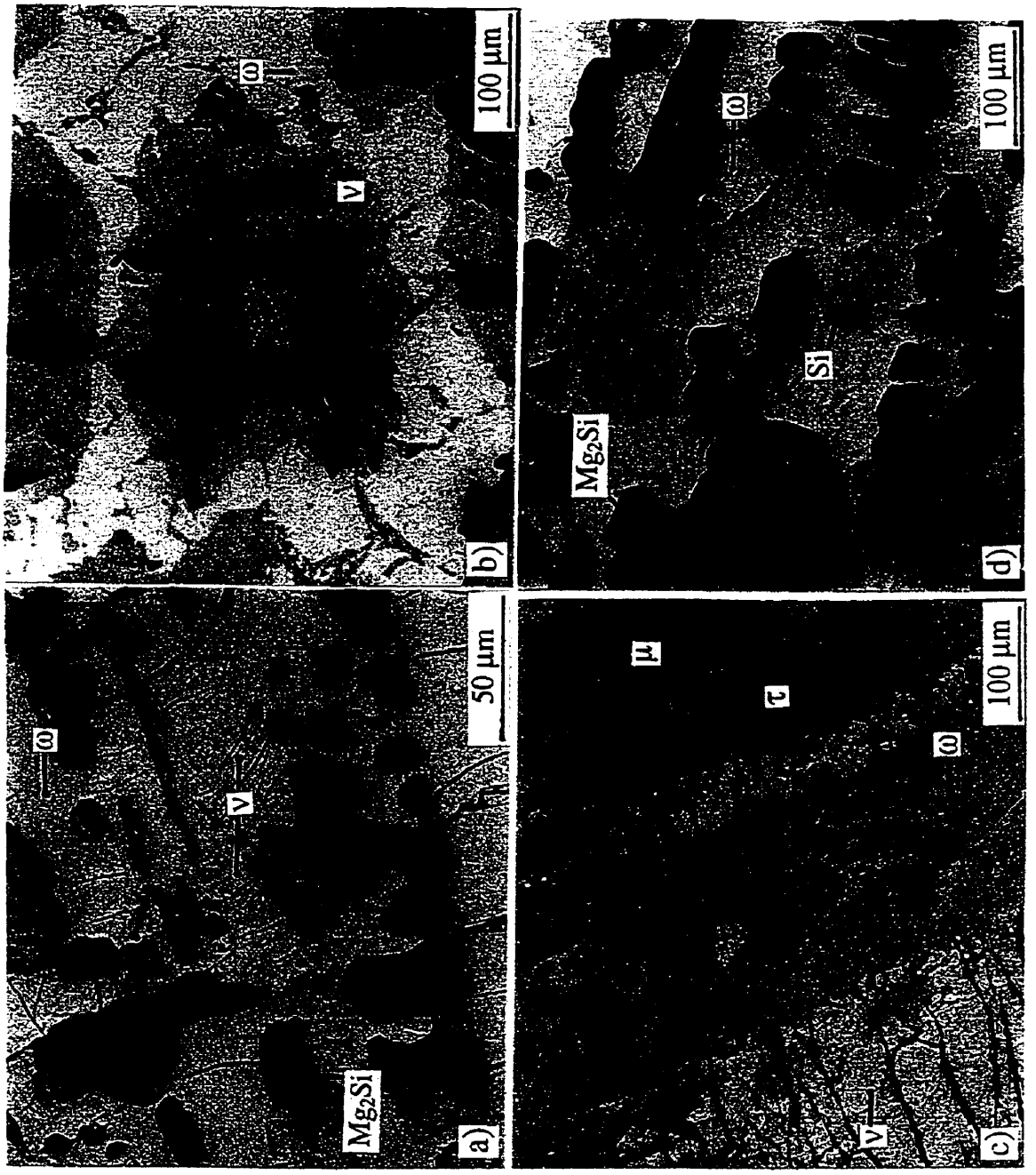

Fig. 9.10 Optical micrographs of alloys (a) 49, (b) 51, (c) 52, and (d) 54 after homogenization.

9.2.2 Discussion of the phase diagram and intermetallic phases after homogenization and subsequent slow cooling to room temperature

The compositions of the binary compounds in the Ni-Si and Mg-Ni systems in Fig. 9.1 are almost identical to those reported in the equilibrium Ni-Si and Mg-Ni binary phase diagrams [90Mas]. The locations and boundaries of the binary intermetallic phases in the Ni-Si and Mg-Ni systems in Fig.9.1 are still quite comparable with that in Fig. 4.2 established by EDS analysis using pure element standards.

The composition range of some ternary phases such as ζ, ν, τ, ω and μ, and the exact position of the equilibrium phase lines are still uncertain since the number of investigated alloys is still insufficient. Therefore, some portions of the phase diagram are drawn with broken lines. The identity of the two ternary phases, η and κ were already reported in the previous paper [96Son, 98Son[1]] by the present author and the identity of ζ still remains unknown.

The single-phase fields for the ω, μ, and τ phases in the ternary phase diagram in Fig. 9.1 also include the compositions of these phases existing as the non-equilibrium phases in the as-solidified alloys 29 and 30. The tentative τ phase field was delineated based on the compositions obtained from the as- solidified alloys 29 and 30 (Fig. 9.3) and homogenized alloy 52 (Fig. 9.10) where τ seems to be a non-equilibrium phase. Such an approach is justified because non-equilibrium phases are also observed to exist as real equilibrium phases in other equilibrated alloys. For example, the ω and μ non-equilibrium phases in as-solidified alloys 29 and 30 were also observed and classified as equilibrium ones in alloys 27, and 49 to 54 after homogenization.

According to the phase diagram established in the present work, the stoichiometry of the $MgNi_6Si_6$ phase reported by Buchholz and Schuster [81Buc] does not match with any of the phases discovered in the present work. The position of this stoichiometry on the phase diagram (Fig. 9.1) is on the right hand side, slightly above the μ phase. However, even considering an inherent experimental error of the EDS analysis, the locations of the μ phase ($Mg_{13}Ni_{45.5}Si_{41.5}$) and the stoichiometric $MgNi_6Si_6$ composition ($Mg_{7.7}Ni_{46.15}Si_{46.15}$) are still quite apart from one another to be considered as the same phase. $MgNi_6Si_6$ has the prototypic

Cu_7Tb structure [97Vil] and the composition of the μ phase ($Mg_{13}Ni_{45.5}Si_{41.5}$) can also be rearranged in such a way as to fit this structure, i.e. $(Ni_{45.5}Si_{41.5})Mg_{13} \approx (Ni_{0.52}Si_{0.48})_7Mg$. The size of the μ phase region is relatively small in Fig. 9.1 ruling out any extended solubility for Ni and Si. That means that the μ phase has almost exactly fixed stoichiometry as given above. The possibility of the μ phase having the same crystallographic structure as $MgNi_6Si_6$ (Cu_7Tb type) will also be discussed in section 9.2.2.1.

The homogeneity range of the ν phase is not well established yet, because there is a discrepancy between the phase determinations by microstructural observation and by compositional measurement. As discussed in section 9.2.1.1.5, a clear boundary between the core region and the rim surrounding the core region in the ν phase is observed in alloy 51 (Fig. 9.10(b)). These regions appear like two different phases. However, the difference in composition between the core region: 34.1±0.7 at. % Mg, 27.9±0.2 at. % Si, and 38.0±0.6 at %. Ni and the rim region: 31.2±0.4 at. % Mg, 31.2±0.3 at. % Si, and 37.6±0.6 at. % Ni, is relatively small. The same phenomenon for the ν phase was also observed in alloy 50. Differences in crystallographic orientation might be responsible but EBSD technique would be needed to confirm this. It was also considered that the ν phase might possibly extend to the ω phase, forming a single phase with a narrow and long homogeneity range. However, according to the x-ray diffraction spectra from alloys 53 and 54, the peaks identified as arising from the ω phase (Table 9.4 in section 9.2.2.1) do not match well with those, which are determined to arise solely from the ν phase (Table E.1 in Appendix E) in alloys 47 and 48 (microconstituent phases; Mg, Mg_2Si, and ν). Similarly, the μ phase, which was also originally considered as possibly being the same phase as the ζ phase, was determined to be a different phase. XRD peaks determined to arise from the μ phase (Table 9.3 in section 9.2.2.1) in alloy 27 do not match those corresponding to the ζ phase in alloy 17 studied in [96Son].

Unidentified phases are marked with a question mark beside the alloy number in the phase diagram in Fig. 9.1. A single-phase appearance of these phases in some of the alloys is not clearly understood. Particularly, the unidentified binary phase with about 25 at. % Mg and 75 at. % Ni was observed in the binary alloy 37 ("U" in Fig. 9.5(a)-(d)), but there is no binary phase in the published Ni-Mg phase diagram [90Mas] in such a composition range. Its

composition ($MgNi_3$) is the same as AB_3 type intermetallic compounds existing in many binary alloy systems, such as Ni-Al, Cu-Au, Ti-Al, and Fe-Al, etc. [90Mas].

Density measurements for several alloys in Fig. 9.1 were also performed since the density of the materials for structural applications in the aerospace and transportation industries is an important property. They are listed in Table 9.2.

Table 9.2 Density of selected alloy

Alloy no.	Constituent phases	Density (g/cm^3)
32	η, Mg_2SiNi_3, $Mg(Ni,Si)_2$	5.63
44*	Mg, Mg_2Ni, Mg_2SiNi_3	2.97
48	Mg, Mg_2Si, ν	2.81
51	ν, ω	4.58
54	Mg_2Si, Si, ω	2.93

*: Since the ingot of alloy 44 does not have a completely homogeneous microstructure through the whole ingot exhibiting slightly different microstructure at the top and the bottom as already mentioned in section 8.1.1, the density of alloy 44 was measured only from the bottom portion sliced out from the ingot. The microstructure for alloy 44 in Fig. 9.9(a) also corresponds to the bottom portion of the ingot.

9.2.2.1 Lattice structures of the μ and the ω phases

An attempt was made to determine whether or not the crystallographic structure of $MgNi_6Si_6$ phase reported by Buchholz and Schuster [81Buc] corresponds to the μ phase in the present work. The diffraction peaks, which were determined to arise only from the μ phase in the XRD spectrum of alloy 27 (microconstituent phases; κ, NiSi and μ), were indexed assuming that the μ phase had a hexagonal $MgNi_6Si_6$ structure with the lattice parameters, a = 0.4948nm and c = 0.3738nm [81Buc]. It was found that each value for the observed interplanar spacing ($d_{obs.}$) was reasonably close to the calculated interplanar spacing ($d_{cal.}$) for the $MgNi_6Si_6$ as shown in Table 9.3. This indicates that the $MgNi_6Si_6$ phase reported in [81Buc] most probably corresponds to the μ phase in the present work. Since $MgNi_6Si_6$ is classified as having the structure type of Cu_7Tb [97Vil], the stoichiometric formula for the μ phase suggested in section 9.2.2, i.e., $Mg(Si_{0.48}Ni_{0.52})_7$ based on its composition ($Mg_{13}Si_{41.5}Ni_{45.5}$), seems to be more reasonable than $MgNi_6Si_6$.

Table 9.3 The x-ray diffraction peaks for the μ phase indexed based on the assumption that the μ phase has the same crystallographic structure as the $MgNi_6Si_6$ phase in [81Buc].

Diffraction angle (obs.-2θ°)	d, interplanar spacing (nm)		Intensity ($I/I_{0\ obs.}$)	Reflection (hkl)
	$d_{obs.}$	$d_{cal.}$*		
20.773	0.4276	0.4285	42.6	1 0 0
23.875	0.3727	0.3738	29.9	0 0 1
42.312	0.2136	0.2143	47.0	2 0 0
43.953	0.2060	0.2063	56.8	1 1 1
48.775	0.1867	0.1869	19.0	0 0 2
49.112	0.1855	0.1859	100.0	2 0 1
53.559	0.1711	0.1713	17.0	1 0 2
56.946	0.1617	0.1619	3.0	2 1 0
66.500	0.1406	0.1408	17.0	2 0 2
70.787	0.1331	0.1334	8.2	3 0 1
77.323	0.1234	0.1237	17.9	2 2 0

*: $d_{cal.}$ was calculated based on the lattice parameters reported in [81Buc] and the reflection plane in Table 9.3.

The lattice parameter determination of the ω phase was based on the XRD spectra from alloys 53 and 54 containing the Si, Mg_2Si, and ω phases. The diffraction peaks common to both alloys, except for those arising from the Si and Mg_2Si, were selected and used as standard diffraction peaks considered to occur solely from the ω phase. The values of interplanar spacing ($d_{obs.}$) calculated from the XRD spectrum of alloy 53 were used for computation using TREOR since alloy 53 contains higher volume fraction of the ω phase than alloy 54. Two possible lattice structures were obtained: an orthorhombic structure with the lattice parameters, a = 1.1709nm, b = 0.8268nm and c = 0.6746nm, and a hexagonal structure with the lattice parameters, a = 1.3511nm and c = 0.8267nm. The indexed diffraction data based on the hexagonal symmetry for the ω phase are given in Table 9.4 because hexagonal system seems to be more likely than orthorhombic one. First, hexagonal structure is more symmetrical than orthorhombic one and as such, it is more difficult to satisfy diffraction conditions for hexagonal structures. Second, when the ω phase is considered to have a hexagonal lattice the determined lattice parameters given above are very close to those of Ag_7Te_4 [66Ima, 85Vil] (a = 1.348nm, c = 0.849nm) intermetallic phase having 55 atoms in a unit cell. The composition of the ω phase, $Mg_{33}Ni_{30}Si_{37}$, can be rewritten as the stoichiometric formula of the Ag_7Te_4-type being ~$(Mg_{0.52}Ni_{0.48})_7Si_4$. It should be noted that

the Mg and the Ni atoms in the lattice do not form a solid solution, but are arranged in an ordered manner in case of the ω phase.

Table 9.4 The x-ray diffraction peaks for the ω phase indexed by TREOR.

Diffraction angle (obs.-2θ°)	d, interplanar spacing (nm)		Intensity ($I/I_{0\ obs.}$)	Reflection (hkl)
	$d_{obs.}$	$d_{cal.}$*		
13.210	0.6702	0.6752	22.6	1 0 1
15.192	0.5832	0.5850	11.7	2 0 0
17.002	0.5215	0.5231	9.5	1 1 1
18.613	0.4767	0.4776	3.8	2 0 1
20.084	0.4421	0.4422	21.7	2 1 0
21.489	0.4135	0.4134	5.2	0 0 2
22.860	0.3890	0.3898	34.5	1 0 2
25.272	0.3524	0.3526	17.6	1 1 2
26.408	0.3375	0.3376	29.1	2 0 2
29.589	0.3019	0.3020	8.0	2 1 2
35.165	0.2552	0.2552	4.4	1 1 3
36.040	0.2492	0.2493	11.5	2 0 3
37.717	0.2385	0.2388	15.0	4 0 2
38.487	0.2339	0.2339	32.4	2 1 3
40.811	0.2211	0.2211	9.2	4 2 0
41.558	0.2173	0.2173	7.7	3 3 1
42.312	0.2136	0.2136	7.5	4 2 1
43.796	0.2067	0.2067	21.1	0 0 4
44.498	0.2036	0.2036	8.5	5 0 2
45.200	0.2.006	0.2006	17.5	4 0 3
45.901	0.1977	0.1977	20.2	3 3 2
46.548	0.1951	0.1950	44.2	6 0 0
48.609	0.1873	0.1873	100.0	4 1 3
49.945	0.1826	0.1826	57.6	3 0 4
51.204	0.1784	0.1784	6.0	5 0 3
51.859	0.1763	0.1763	4.3	2 2 4
52.467	0.1744	0.1744	38.7	4 3 2
57.372	0.1606	0.1606	10.1	1 1 5
69.586	0.1351	0.1351	30.4	7 2 2
71.655	0.1317	0.1316	12.7	7 3 0
72.225	0.1308	0.1308	30.0	4 4 4
74.336	0.1276	0.1276	11.2	2 2 6

*: $d_{cal.}$ was calculated based on the lattice parameters and reflection plane determined as results from TREOR.

9.2.3 The phase equilibria at 500°C and 900°C

9.2.3.1 Microstructural observations

The isothermal sections of the Ni-Si-Mg ternary phase diagram at 500°C and 900°C in the Ni-rich region containing alloys from 1 to 26 were determined by water quenching of some selected alloys (3, 4, 15, 16, 18, 25, and 26). This has been done to investigate the change in phase equilibria at elevated temperatures under the assumption that the microstructures of the specimens quenched from the respective temperatures represent the phase equilibria at these temperatures. The microconstituent phases in all of the selected alloys quenched from 500°C are exactly the same as for the equilibrium alloys investigated after slow cooling to room temperature as shown in Fig. 9.1, implying that the phase equilibria at 500°C and room temperature are the same. However, the microconstituent phases of some of the selected alloys (15, 16, 18, 25, 26) quenched from 900°C are different from those in the alloys found in equilibrium at room temperature and 500°C. The homogenized microstructures of alloys 16, 25, and 26 are shown in Fig. F.2 in Appendix F.

The morphology of the blocky η phase in alloy 16 in Fig. 9.11(a) is quite similar to that observed after slow cooling to room temperature in the same alloy (Fig. F.2(a) in Appendix F). In between the blocky η phase, the white elongated δ-Ni_2Si phase and the mixture of (needle-like δ-Ni_2Si precipitates+θ-Ni_2Si) are formed. The fine two phase mixture seems to form during quenching by the precipitation of δ-Ni_2Si from θ-Ni_2Si. Fig. 9.11(b) shows the three phase morphology of alloy 25 quenched from 900°C. The blocky ζ phase is normally surrounded by the κ phase and the matrix is θ-Ni_2Si. Fig. 9.11(c) shows the two phase morphology of alloy 26 with big round θ-Ni_2Si phase in the κ matrix phase. The blocky δ-Ni_2Si phase and the fine mixture of δ-Ni_2Si+ε-Ni_3Si_2 observed after slow cooling to room temperature in Fig. F.2(c) in Appendix F transformed into the θ-Ni_2Si phase. The presence of the θ-Ni_2Si phases in alloy 26 (Fig. 9.11 (c)) was proven by x-ray diffraction pattern (Table E.2 in Appendix E).

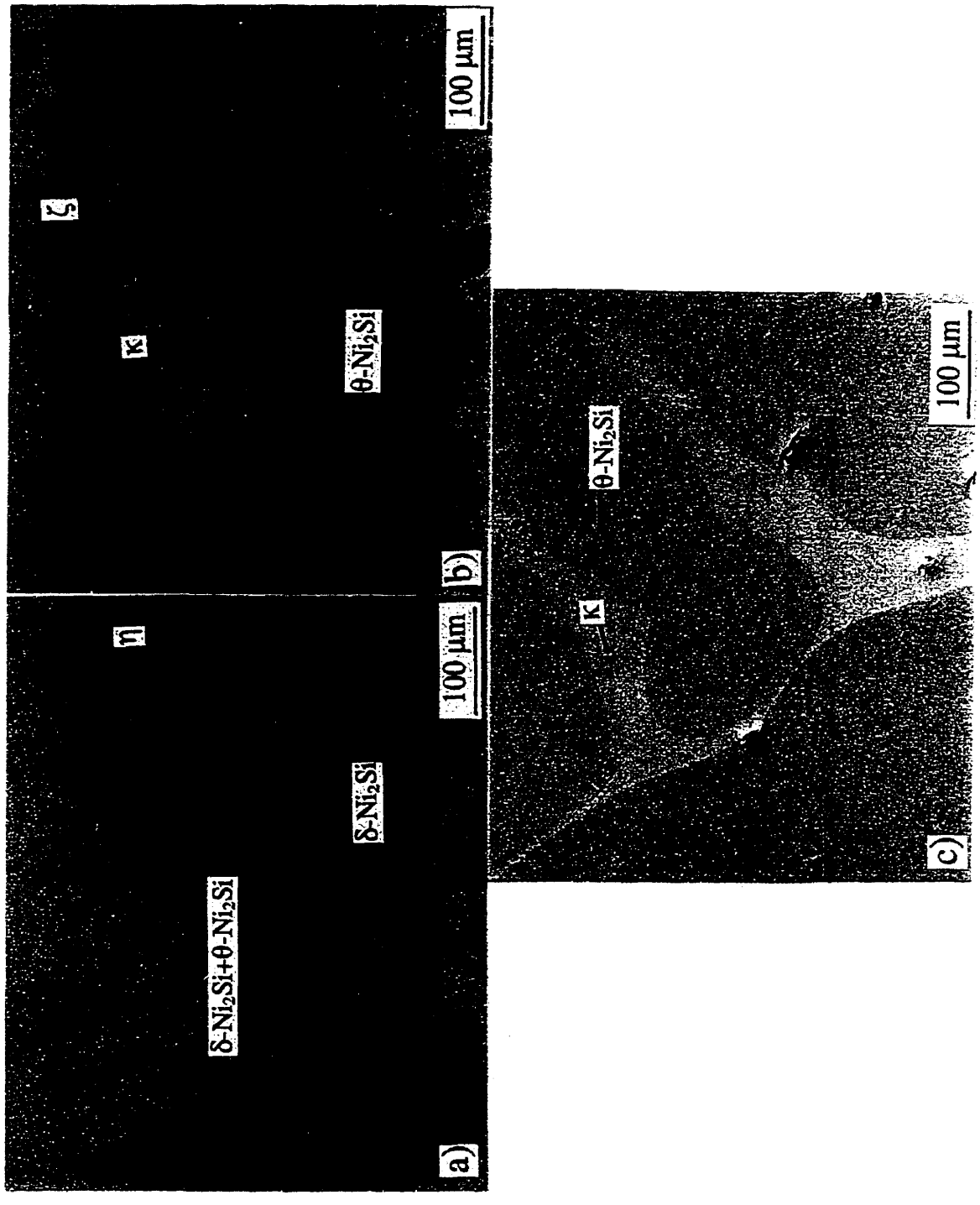

Fig. 9.11 Microstructures of alloys (a) 16, (b) 25, and (c) 26 quenched from 900°C.

9.2.3.2 The phase diagram at 900°C

The isothermal section of the Ni-Si-Mg ternary phase diagram at 900°C has been established by means of the microstructural observations and EDS analysis of the selected alloys quenched from 900°C.

The results of EDS analysis of the selected alloys quenched from 900°C are summarized in Table 9.5. Since the microconstituent phases in all of the selected alloys quenched from 500°C are exactly the same as for the equilibrium alloys investigated after slow cooling to room temperature, the isothermal section of the phase diagram of the area containing alloys from 1 to 26 at 500°C is considered the same as that in Fig. 9.1.

Alloys 3 and 4 did not change their microconstituent phases, and thus, conform to the equilibrium phase diagram at room temperature (Fig. 9.1). The volume fraction of Ni in alloy 3 becomes negligible after quenching from 900°C. However, this seems to be caused either by the slight shift of the phase equilibrium line, distinguishing the η, Ni_3Si, Ni three phase region from the η and Ni_3Si two phase region at 900°C or by the possibility of the microstructure of alloy 3 observed after slow cooling to room temperature in slightly non-equilibrium state. Note that the overall composition of alloy 3 in Fig. 9.1 is almost on the phase equilibrium line described above.

Table 9.5 The overall compositions and phases in the selected alloys water quenched from 900°C.

Alloy No.	Overall compositions (at.%)			Microconstituent Phases
	Mg	Si	Ni	
3	6.39±0.6	20.35±0.2	73.26±0.8	η, Ni_3Si, Ni(almost disappeared)
4	9.07±0.6	24.25±0.4	66.69±0.4	η, Ni_3Si, $Ni_{31}Si_{12}$ (or Ni_5Si_2)
15	2.11±0.5	31.70±0.3	66.19±0.5	η, δ-Ni_2Si, θ-Ni_2Si
16	12.05±1.3	27.74±0.2	60.21±0.5	η, δ-Ni_2Si, θ-Ni_2Si
18	1.96±0.6	38.06±0.1	59.97±0.6	κ, θ-Ni_2Si
25	3.85±0.3	36.17±0.3	59.99±0.5	κ, ζ, θ-Ni_2Si
26	2.18±0.5	37.34±0.3	60.48±0.9	κ, θ-Ni_2Si

Fig. 9.12 shows the phase equilibria of the ternary Mg-Si-Ni phase diagram at 900°C modified from the room temperature phase diagram in Fig. 9.1 based on the results of EDS analysis in Table 9.5 for the alloys quenched from 900°C. The changes in the equilibrium phases in the alloys 15, 16, 18, 25, and 26 above the δ-Ni_2Si and the η equilibrium phase region (Fig. 9.12) will be discussed in the following section.

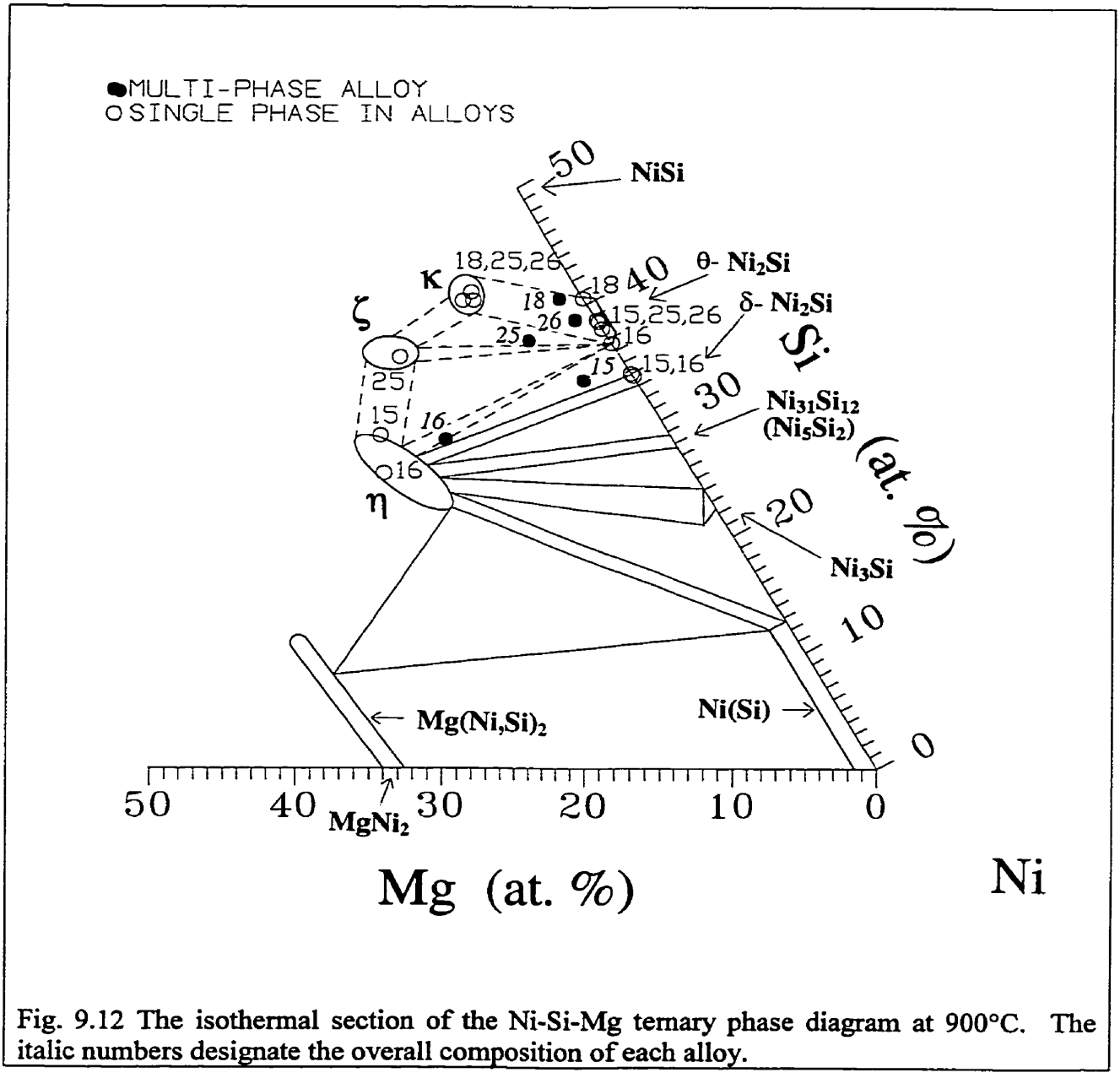

Fig. 9.12 The isothermal section of the Ni-Si-Mg ternary phase diagram at 900°C. The italic numbers designate the overall composition of each alloy.

9.2.4 The phase equilibria and temperature stability of phases at high temperatures

In this section, the temperature stability of phases or phase equilibria in the Ni-Si-Mg ternary phase diagram in Fig. 9.1 will be discussed based on the DTA results (Appendix G) and the phase equilibria established from the quenched specimens described in the previous section.

The only change in the high temperature phase equilibria obtained from specimens quenched from 900°C, relative to the phase equilibria at room temperature, was observed in the region dominated by alloys 14-18 and 24-26 (Fig. 9.1). No change in the phase equilibria was observed after quenching from 500°C. According to the DTA result from alloy 16 [Appendix G, Fig. G.1], the first phase transformation occurred at 818°C, which is close to the high temperature θ-Ni_2Si phase formation in the binary Ni-Si phase diagram [90Mas]. The θ-Ni_2Si phase was also observed to be an equilibrium phase in alloy 16 (Fig. 9.11) at 900°C confirming that the phase transformation at 818°C is due to the formation of the high temperature θ-Ni_2Si phase.

Therefore, the proposed equilibrium Ni-Si-Mg ternary phase diagram established after slow cooling to room temperature is expected to remain unchanged at least up to 900°C (as determined by quenched specimens) in the area dominated by alloys 1 to 13, and up to about 820°C in the area dominated by alloys 14-18 and 24-26 (Fig. 9.1). Since the phase region dominated by alloy 1 contains only the Ni and the $Mg(Ni,Si)_2$ phases, it will follow the phase transformation sequence in the binary Mg-Ni phase diagram, according to which the first phase transformation occurs at the ($Ni+MgNi_2$) eutectic temperature, i.e. 1097°C [90Mas]. Therefore, the phase region dominated by alloy 1 in Fig. 9.1 is expected to remain unchanged even up to ~ 1097°C.

In the area dominated by alloys 29-31, there was no substantial microstructural changes observed after homogenization at 850°C (Table D.1 in Appendix D). In alloy 32, according to a DTA result, first phase transformation occurred at 1138°C which is very close to the melting temperature of $MgNi_2$ (1147°C). In the area dominated by alloys 36-42, the lowest temperature phase transformation is supposed to involve the peritectic phase transformation $Mg_2Ni \leftrightarrow L+MgNi_2$ at 760°C in the Mg-Ni system [90Mas]. According to DTA results, the

transformation of the Mg_2Ni into the $L+MgNi_2$ (i.e., $Mg_2Ni \rightarrow L+MgNi_2$) on heating occurred at 762°C for alloy 38 and at 758°C for alloy 40, i.e. close to the reported temperature of 760°C. In the phase region dominated by alloys 43-46 which includes the ($Mg+Mg_2Ni$) eutectic structure, as shown in Fig. 9.9(a) for alloy 44, the first phase transformation, $Mg+Mg_2Ni \rightarrow L$, on heating will occur at about 506°C [90Mas]. Therefore, in the Mg-rich area dominated by alloys 43-46 the proposed equilibrium Ni-Si-Mg phase diagram (Fig. 9.1) shows the phase equilibria at least up to the limit of about 506°C. In the area dominated by alloys 47 and 48, the first phase transformation on heating will involve the melting of Mg at 650°C or $Mg+Mg_2Si$ eutectic at 637°C. Hence, one can safely assume that this region of the ternary phase diagram remains unchanged up to ~637°C. The solidification sequences and phase transformation temperatures involved in the area dominated by alloys 27, 28, and 49-54 are not predictable at the moment. However, the phase transformation temperatures and melting temperatures characteristic for the alloys in the Si-rich area (alloys 49-54) are expected to be quite high compared to the Mg-rich area.

Fig. 9.13 schematically shows the summary of the temperature limits of the stability of phase equilibria on the Ni-Si-Mg ternary phase diagram divided into several regions, indicating that the phase equilibria in each region are retained up to their designated temperature.

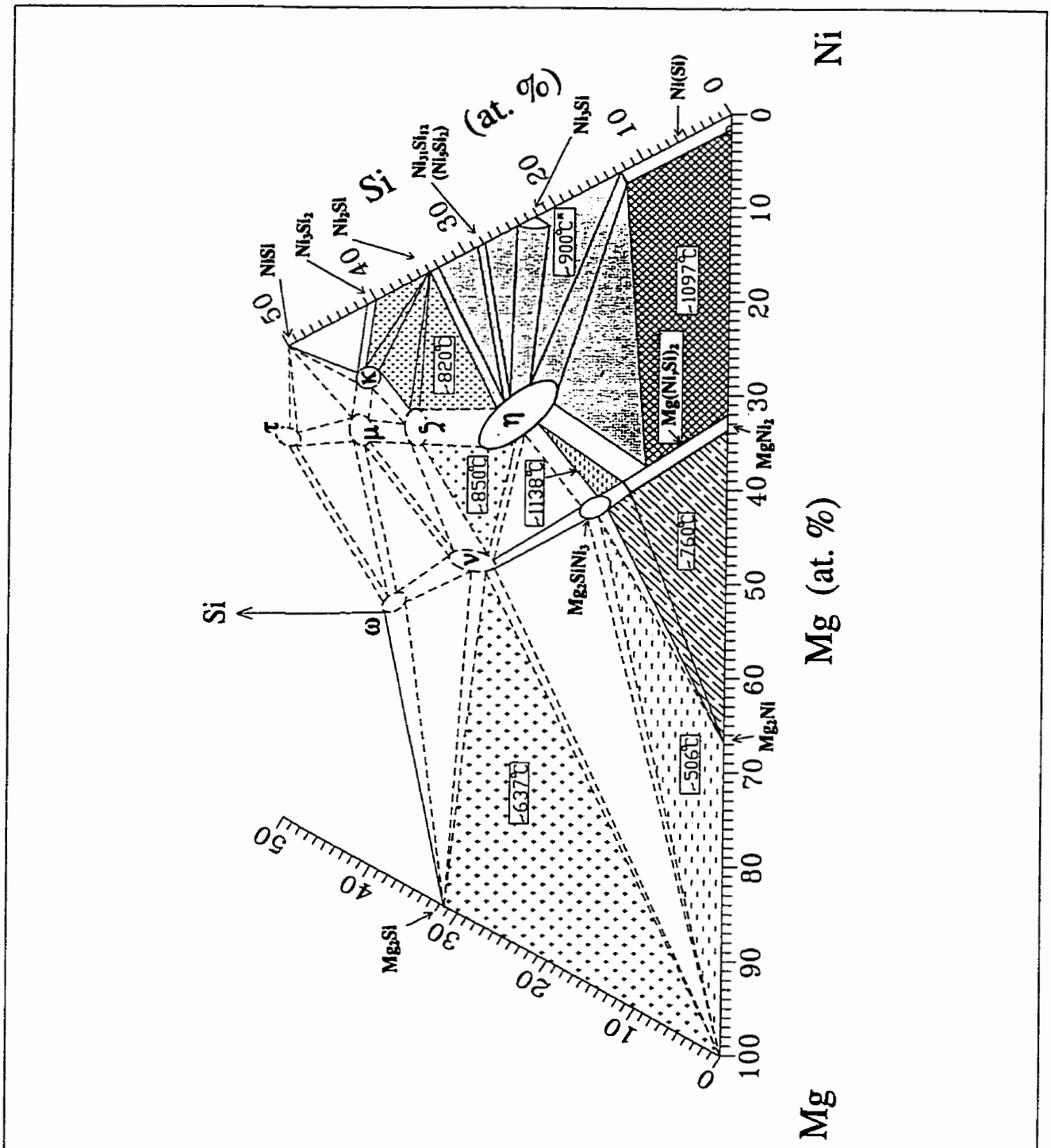

Fig. 9.13 The proposed Ni-Si-Mg ternary phase diagram divided into several regions. The designated temperature in each region indicates that the phase equilibria in this region are retained up to approximately the indicated temperature. The phase equilibria in the region marked with ~900°C* are retained up to at least 900°C since the phase equilibria in the region were determined by specimens quenched from 900°C.

9.2.5 Summary of crystallographic and metallurgical characteristics of the intermetallics investigated in the present work

The crystallographic structure and the melting (reaction) temperature of the intermetallic and metallic phases investigated in the present study are summarized in Table 9.6 and 9.7. The phases which are already reported in the literature (i.e., their crystallographic and metallurgical characteristics are already known) are included in Table 9.6 and the phases discovered by the present author in this system are included in Table 9.7. Some of the known phases such as $MgNi_2$ and Ni_2Si are included in Table 9.7 as well as Table 9.6 since determination of crystallographic structure or melting temperatures of the phases were also carried out in the present work.

The melting temperatures of the η and κ phases were determined to be 1271°C, and 920°C, respectively, by DTA. The melting temperature of unalloyed $MgNi_2$ measured from alloy 37 is 1154C°, which is only slightly higher than that proposed in the binary Mg-Ni equilibrium phase diagram i.e., 1147±3°C [90Mas]. The melting temperature of the $Mg(Ni,Si)_2$ phase with 4.2 at. % Si in alloy 38 was 1139°C. Therefore, the melting temperature of the $MgNi_2$ phase seems to decrease by the formation of a ternary $Mg(Ni,Si)_2$ intermediate phase.

Table 9.6 Characteristics of known intermetallic and metallic phases investigated in the present work.

Phase	Pearson Symbol	Lattice parameters, (nm) a	b	c	Proto-type	Reaction or melting temperature (°C)	References
Ni	cF4	0.35232	-	-	Cu	Melting, 1455°C	[85Vil],[90Mas]
Ni_3Si	cP4	0.3504	-	-	$AuCu_3$	Peritectoid , 1035°C	[85Vil],[90Mas]
$Ni_{31}Si_{12}$ (Ni_5Si_2)	hP43	0.6671	-	1.2288	$Ni_{31}Si_{12}$	Congruent, 1242°C	[85Vil],[90Mas]
Ni_2Si	oP12	0.704	0.500	0.373	Co_2Si	Peritectic, 1255°C	[85Vil],[90Mas]
Ni_3Si_2	oC80	1.2229	1.0805	0.6924	Ni_3Si_2	Polymorphic, 830°C	[85Vil],[90Mas]
Mg	hP2	0.32089	-	0.52101	Mg	Melting, 650°C	[85Vil],[90Mas]
$MgNi_2$	hP24	0.4824	-	1.5826	$MgNi_2$	Congruent, 1147±3°C	[85Vil],[90Mas]
Mg_2Ni	hP18	0.5198	-	1.321	Mg_2Ni	Peritectic, 760°C	[85Vil],[90Mas]
Mg_2SiNi_3	hR6	0.50044	-	1.10894	Fe_2Tb	?	[85Nor],[97Vil]
Mg_2Si	cF12	0.6338	-	-	CaF_2	Congruent, 1085°C	[85Vil],[90Mas]
Si	cF8	0.54286	-	-	C	Congruent, 1414°C	[85Vil],[90Mas]

Table 9.7 Characteristics of known or newly discovered intermetallics in the present work or in [98Son[1]]. The information in italic letters is determined by the present author.

Phase	Pearson Symbol	Lattice parameters, (nm) a	b	c	Proto-type	Reaction or melting temperature (°C)	References
Ni_2Si	oP12	*0.7064*	*0.5004*	*0.3730*	Co_2Si	Peritectic, 1255°C	[90Mas],[98Son[1]]
$MgNi_2$	hP24	*0.4827*	-	*1.5753*	$MgNi_2$	*Congruent, 1153°C*	[90Mas], Pres.*
$Mg(Ni,Si)_2$	hP24	*0.4824***	-	*1.5780*	$MgNi_2$	*Congruent, 1139°C****	Pres.
η**** ($Mg_6Si_7Ni_{16}$)	cF116	*1.1308*	-	-	$Mn_{23}Th_6$	*Congruent, 1271°C*	[98Son[1]], Pres.
κ ($Mg_2Si_{10}Ni_{13}$)	hP ?	*1.1622*	-	*1.1650*	?	*Congruent, 920°C*	[98Son[1]], Pres.
ζ ($Mg_3Si_7Ni_{10}$)	?		?		?	?	[98Son[1]], Pres.
ω ($Mg_{0.52}Ni_{0.48})_7Si_4$	hP55	*1.3511*	-	*0.8267*	Ag_7Te_4	?	Pres.
μ ($Mg(Si_{0.48}Ni_{0.52})_7$)	hP8	0.4948	-	0.3738	Cu_7Tb	?	[97Vil], Pres.
ν ($Mg_{11}Si_{10}Ni_{12}$)	?		?		?	?	Pres.
τ ($MgSi_5Ni_4$)	?		?		?	?	Pres.

Note: the lattice parameters of alloys calculated in the present work in this table were calculated from TREOR.

*: "Pres." stands for present work.

**: the lattice parameters were calculated from $Mg(Ni,Si)_2$ with 3.72 at.% Si in alloy 36.

***: the melting temperature was measured with alloy 38 containing $Mg(Ni,Si)_2$ with 4.21 at. % Si.

****: stoichiometries of ternary phases discovered in the present work are in Table 10.1 in section 10.1.1.

Since the lattice parameter of $MgNi_2$ is supposed to depend on the Si content, it was attempted to see its variation with the change in the Si content. Table 9.8 shows the lattice parameter of a hexagonal $MgNi_2$ with varying Si content (the $Mg(Ni,Si)_2$ ternary intermediate phase) calculated by both TREOR and extrapolation of measured lattice parameters against the Nelson-Riley function [78Cul]. Lattice parameter, 'c' calculated by both methods increases with increasing Si content in $MgNi_2$ while 'a' is almost constant, which leads to the increase in the unit cell volume. In general, the unit cell volume depends on the atomic size of the substituting atoms. The atomic size of Si substituting for Ni in the $MgNi_2$ phase, is reported in many references as being smaller than that of the Ni atoms [91Cal, 96Ask]. (0.1176 nm and 0.118 nm for Si radius [91Cal, 96Ask], and 0.1243 nm and 0.125 nm for Ni radius [91Cal, 96Ask]). This implies that the unit cell volume should decrease. However, if one considers the larger atomic radius for Si, 0.1173 nm than for Ni, 0.1154 nm reported in Table 11-1 in [60Pau] where they were calculated based on the observed interatomic distances in crystals of metallic elements and the nature of the bonds, the observed increase in the unit cell of $Mg(Ni,Si)_2$ might be justified.

Microhardness values of the intermetallic phases measured at 100g and 500g loads are listed in Table 9.9. Mg_2Ni and Mg_2Si phases showed the lowest hardness values, 459 kg/mm^3 and 458 kg/mm^3, respectively, among all the intermetallics investigated in the present work. The hardness of the $MgNi_2$ phase increases with increasing Si content. In general, hardness of ternary intermetallics discovered in the present work, increases with the Si content in the phases (Table 9.11).

Table 9.8 The comparison of lattice parameters of $Mg(Ni,Si)_2$ with various Si content calculated by the extrapolation method using Nelson-Riley extrapolation function [78Cul] and TREOR [85Wer].

Alloy No.	Si content in $Mg(Ni,Si)_2$ (at. %)	Lattice parameters (nm) calculated by extrapolation function and unit cell volume (nm^3)			Lattice parameters (nm) calculated by TREOR and unit cell volume (nm^3)		
		a	c	volume	a (nm)	c (nm)	volume
37	0.0	0.4827	1.5753	0.3178	0.4817	1.5800	0.3175
36	3.7	0.4824	1.5780	0.3181	0.4813	1.5854	0.3181
40	11.1	0.4829	1.5785	0.3188	-*	-	-

*: there was an insufficient number of peaks deflected from $Mg(Ni,Si)_2$ in alloy 40 to run TREOR.

Table 9.9 Vickers hardness values measured at 100 and 500g of the ternary intermetallics phases in the order of Si at. % in the present work.

Alloy No.	Phases	Si content in the phases (at. %)	VHN of Phases (kg/mm^2)	
			100g	500g
40	Mg_2Ni	0	459±10	392±14
37	$MgNi_2$	0	646±17	562±5
38	$Mg(Ni,Si)_2$	4.2	673±13	592±15
40	$Mg(Ni,Si)_2$	11.1	727±12	N.A.*
42	Mg_2SiNi_3	14.0	860±12	N.A.*
20	η	24.4	852±7	784±12
47	ν	26.7	815±27	743±23
48	Mg_2Si	30.0	458±12	N.A.*
29	ζ	35.0	936±7	820±6
53	ω	38.5	748±22	666±27
21	κ	40.5	916±20	876±13
28	NiSi	50.5	560±24	N.A.*

*: the phase area to make indentations at 500g load was not large enough.

9.3 CNB fracture toughness of in-situ intermetallic composites

9.3.1 Microstructural characteristics of in-situ intermetallic composites for CNB fracture toughness test

Selected in-situ intermetallic composite alloys containing the newly discovered phases and near single phase alloys were fabricated to investigate fracture behaviour and mechanical properties, particularly, fracture toughness and yield strength.

The locations of overall compositions of the alloys fabricated for CNB fracture toughness test are shown in the Ni-Si-Mg ternary phase diagram in the Ni-rich area in Fig. 9.14. The selection of the compositions of the in-situ intermetallic composite alloys was carried out based on the observed microstructural evolution of the alloys in the investigated area of the equilibrium Ni-Si-Mg phase diagram (Fig. 9.1), particularly, in the Ni-rich area, considering the combination of brittle and ductile phases and the effective configuration of microconstituent phases having fine eutectic-like structures. In particular, alloys F1, F2, F3, and F4 containing only Ni(Si) and η phases and alloys F10, F11, F12, and F13 containing mostly Ni_3Si and η in various volume fractions were fabricated to investigate the change (possibly increase) in fracture toughness with increasing volume fraction of toughening phases, Ni(Si) or Ni_3Si, relative to the fracture toughness of η single phase alloy (F6). Specifically, it was important to establish whether or not fracture toughness could be expressed by the composite rule-of-mixtures dependence on volume fraction of Ni(Si) or Ni_3Si.

More information such as the volume fraction of microconstituent phases, density, porosity, heat treatment histories as well as overall composition of the in-situ composites from Fig. 9.14 are tabulated in Table 9.10.

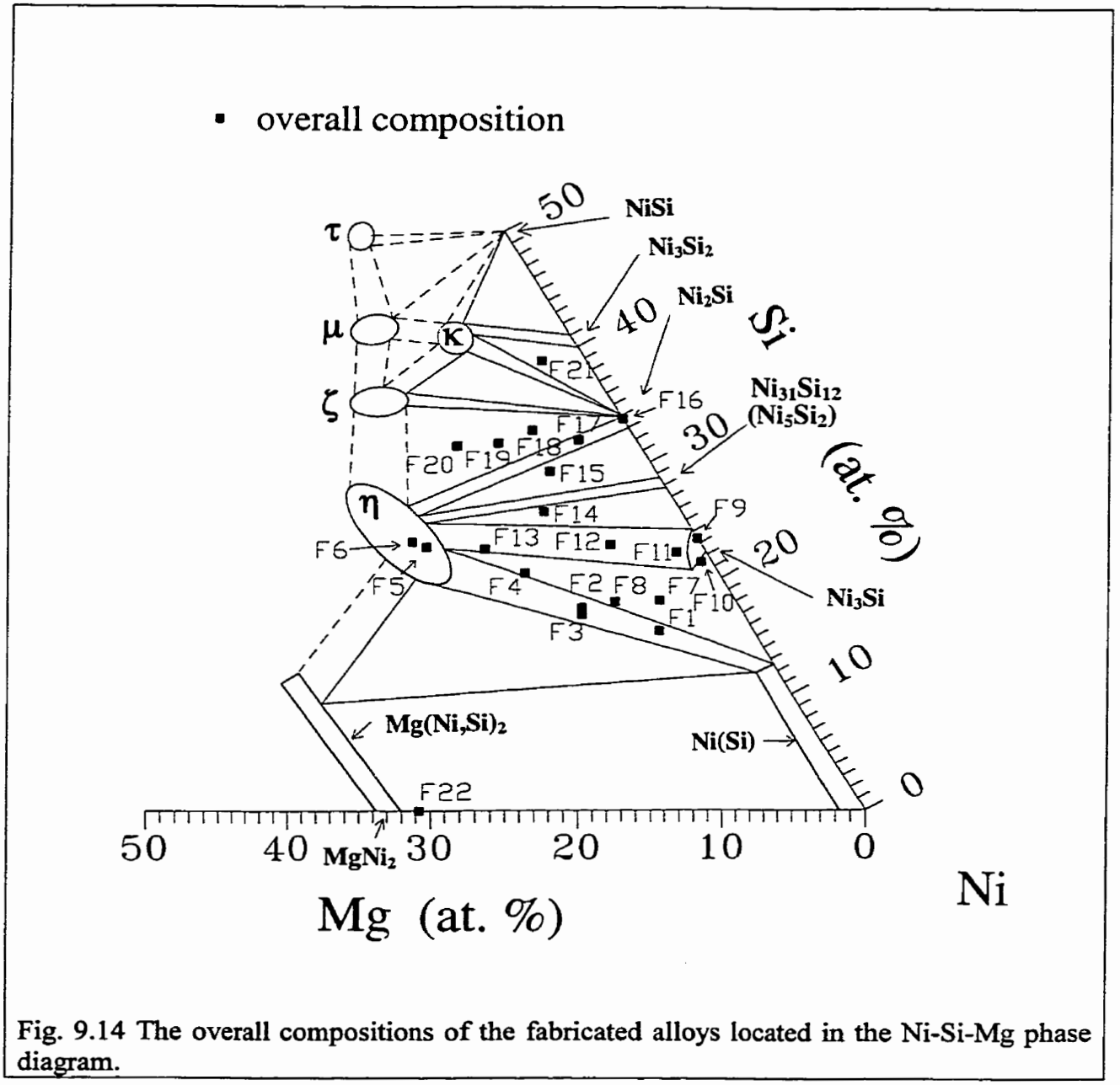

Fig. 9.14 The overall compositions of the fabricated alloys located in the Ni-Si-Mg phase diagram.

Table 9.10 Overall composition, volume fraction of phases, density, porosity, and heat treatment of intermetallic alloys used for CNB fracture toughness test (Fig. 9.14).

Alloy No.	Overall composition (at. %)		Volume fraction of Phases		Density (g/cm^3)	Porosity (%)	Heat treatment
F1	Mg	6.62±0.7	Ni(Si)	60.7	7.66	0.09	800°C/100h
	Si	15.47±0.3	η	39.3			
	Ni	77.91±1.0					
F2	Mg	10.97±0.4	η	52.6	7.26	0.06	800°C/100h and 1000°C/40h
	Si	17.46±0.3	Ni(Si)	47.4			
	Ni	71.57±0.4	Ni_3Si	Negl.*			
F3	Mg	11.25±1.0	η	52.6	7.22	0.07	800°C/100h and 1000°C/40h, Solidified**
	Si	16.87±0.5	Ni(Si)	47.4			
	Ni	71.89±0.7	Ni_3Si	Negl.			
F4	Mg	13.34±0.8	η	61.7	6.78	0.36	800°C/100h
	Si	20.48±0.4	Ni(Si)	38.3			
	Ni	66.18±1.1	Ni_3Si	Negl.			
F5	Mg	18.87±1.0	η	91.5	6.20	2.16	700°C/100h
	Si	22.75±0.4	Ni(Si)	7.6			
	Ni	58.38±0.7	U***	0.9			
F6	Mg	19.63±0.8	η	98.9	6.02	2.50	800°C/100h, Solidified**
	Si	23.18±0.2	Ni(Si)	1.1			
	Ni	57.00±0.9	U,(Mg,Si)Ni_2	Negl.			
F7	Mg	5.29±0.4	Ni_3Si	49.8	7.80	0.25	900°C/100h
	Si	18.1±0.4	Ni(Si)	34.6			
	Ni	76.6±0.7	η	15.6			
F8	Mg	8.44±0.8	Ni(Si)	62.4 (Ni(Si) + Ni_3Si)	7.49	0.15	800°C/100h and 1000°C/40h
	Si	17.97±0.2	Ni_3Si				
	Ni	73.59±0.7	η	37.6			
F9	Si	23.42±0.4	Ni_3Si	97.1	7.95	0.12	900°C/200h
	Ni	76.44±0.3	Ni(Si)	2.9			

Table 9.10 continued

F10	Mg	0.75±0.7	Ni_3Si	94.0	7.93	0.50	900°C/200h
	Si	21.4±0.3	Ni(Si)	5.2			
	Ni	77.68±0.4	η	0.8			
F11	Mg	2.07±0.5	Ni_3Si	86.9	7.69	1.36	900°C/200h,
	Si	22.20±0.3	Ni(Si)	7.2			
	Ni	75.73±0.7	η	5.1			
			$Ni_{31}Si_{12}$	0.8			
F12	Mg	6.27±0.9	Ni_3Si	58.7	7.39	0.52	900°C/100h
	Si	22.90±0.2	η	41.1			
	Ni	70.83±0.8	$Ni_{31}Si_{12}$	0.2			
F13	Mg	15.03±0.7	η	81.7	6.53	0.55	900°C/100h
	Si	22.56±0.3	Ni_3Si	18.3			
	Ni	62.41±0.7	Unidentified	Negl.			
F14	Mg	9.41±0.7	η	52.6	6.96	0.56	900°C/100h
	Si	25.77±0.4	$Ni_{31}Si_{12}$	30.6			
	Ni	64.82±0.6	Ni_3Si	16.8			
F15	Mg	7.26±0.5	η	50.12	6.86	0.41	900°C/100h, pre-existing cracks after casting****
	Si	29.24±0.4	$Ni_{31}Si_{12}$	48.88			
	Ni	63.50±0.4	Ni_2Si				
F16	Si	33.75±0.2	Ni_2Si	100	7.36	0.28	800°C/100h and 1000°C/40h
	Ni	65.98±0.3	-	-			
F17	Mg	3.94±0.6	Ni_2Si	77.9	7.07	0.30	900°C/100h and 780°C/100h
	Si	31.96±0.4	η	21.3			
	Ni	64.10±0.3	ζ	0.8			
F18	Mg	6.70±1.0	Ni_2Si	57.0	6.82	0.29	900°C/100h and 780°C/100h
	Si	32.78±0.5	η	22.5			
	Ni	60.52±0.6	ζ	20.5			
F19	Mg	9.56±0.5	Ni_2Si	46.0	6.56	0.62	900°C/100h and 780°C/100h
	Si	31.67±0.3	ζ	35.2			
	Ni	58.78±0.4	η	18.8			

Table 9.10 continued

F20	Mg	12.43±0.3	ζ	40.5	6.32	1.15	900°C/100h and 780°C/100h
	Si	31.46±0.6	Ni_2Si	32.9			
	Ni	56.12±0.6	η	26.6			
F21	Mg	3.04±0.8	Ni_3Si_2	44.5	6.62	0.30	600°C/100h
	Si	38.79±0.3	κ	35.1			
	Ni	58.17±0.6	Ni_2Si	20.4			
F22	Mg	30.78±1.6	$MgNi_2$	96.5	5.84	0.65	700°C/24h, Solidified** Pre-existing cracks****
	Ni	69.19±1.6	Ni(Si)	2.1			
			Unidentified	1.4			

*: 'Negl.' stands for 'negligible amount' and indicates the amount which is much less than 1.0 % (<<1.0%).
**: the alloys were solidified while the others were cast.
***: indicates the unidentified phase containing the composition of about 25 at. % Mg and 75 at. % of Ni.
****: pre-existing cracks were observed in as cast structure.

9.3.1.1 Microstructures of composites F1-F5 containing Ni(Si) and η

The microstructures of composites F1-F5 show the evolution of microstructures in the Ni(Si) and η two phase region (Fig. 9.14). The designation of the phase Ni(Si) indicates that Ni phase contains Si atoms as a solid solution. Composites F2-F5 contain some other non-equilibrium phases, but their amount is negligible (<1.0 vol. %).

The primary dendritic Ni(Si) phase and the (Ni(Si)+η) eutectic mixture are seen in homogenized alloy F1 (Fig. 9.15(a)). The microstructures of homogenized composites F2 and F3 in Fig. 9.15(b) and (c), respectively, are quite similar to each other, containing a fine eutectic mixture of (Ni(Si)+η). The overall compositions of the two alloys are also almost identical (Table 9.10). However, alloy F2 (Fig. 9.15(b)) was cast while alloy F3 (Fig. 9.15(c)) was solidified in the crucible. The distribution and shape of the Ni(Si) phase in the (Ni(Si)+η) mixture in alloy F3 (solidified) are more directional and uniform than those in alloy F2 (cast). The microstructures of homogenized alloys F4 (Fig. 9.15(d)) and F5 (Fig. 9.15(e)) show the large primary dendritic η phase and interdendritic Ni(Si) or (Ni(Si)+η) mixture phases.

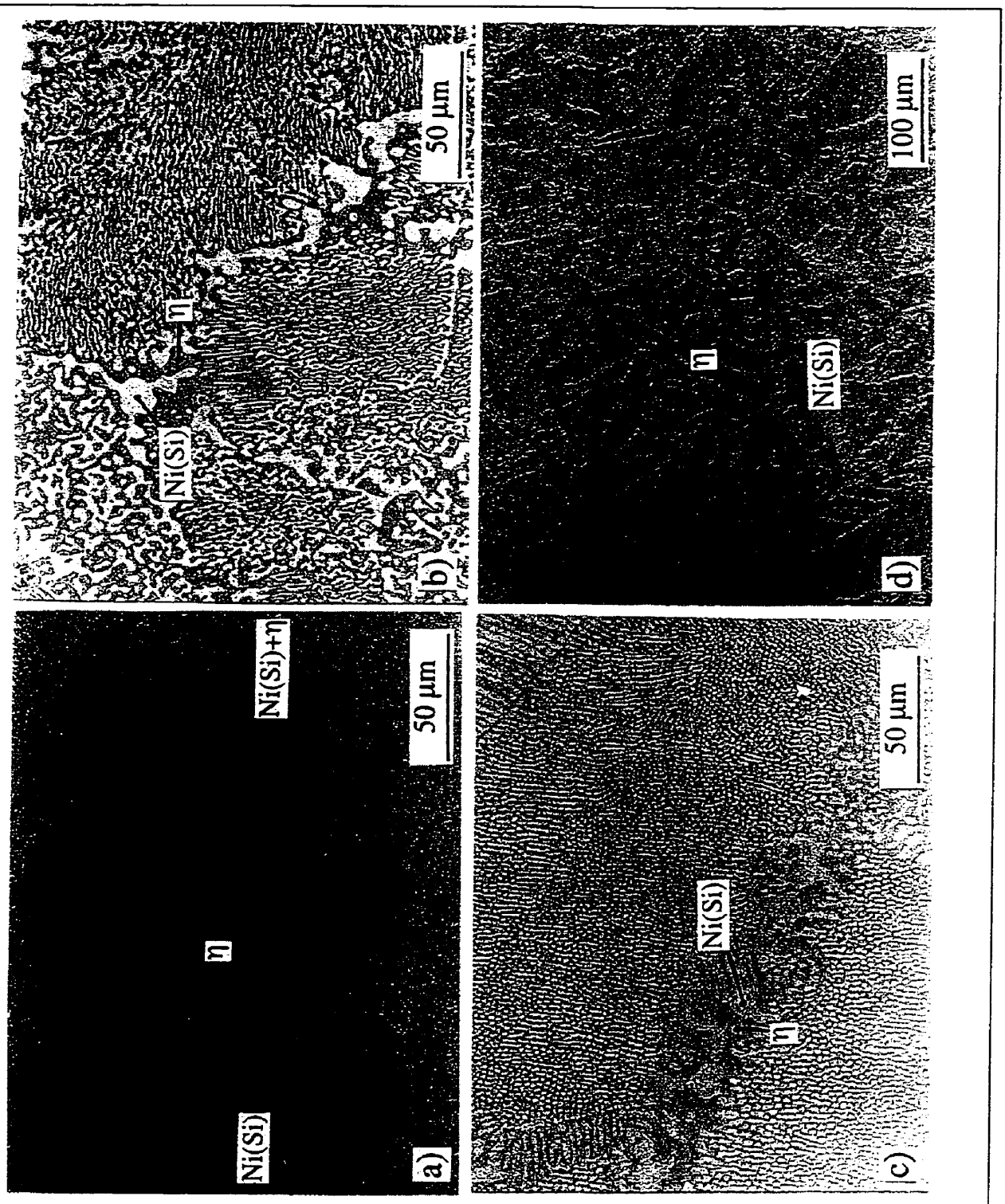

Fig. 9.15 Homogenized microstructures of alloys (a) F1, (b) F2, (c) F3, (d) F4, and (e) F5. Alloy F3 was solidified and the others were cast.

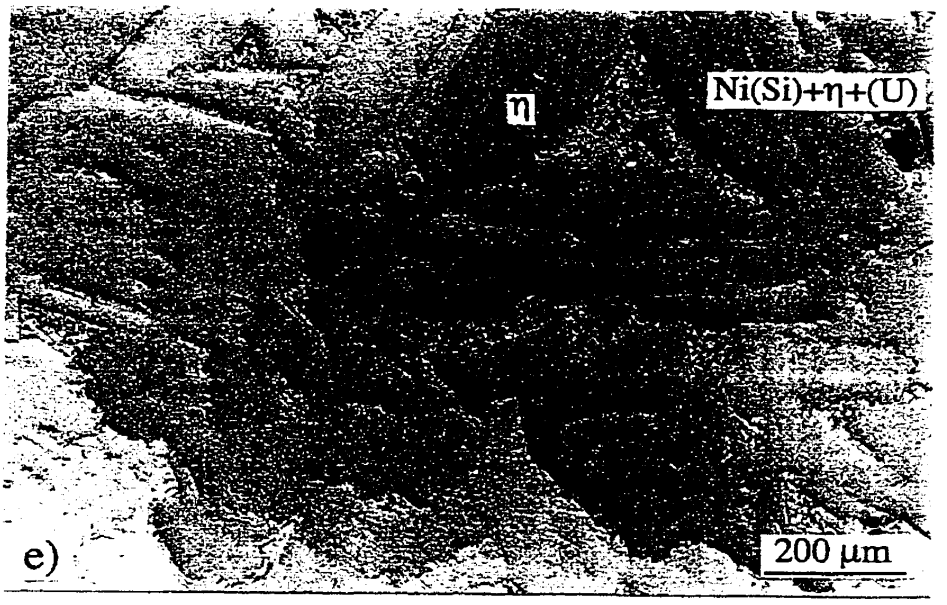

Fig. 9.15 Homogenized microstructures of alloys (a) F1, (b) F2, (c) F3, (d) F4, and (e) F5. Alloy F3 was solidified and the others were cast.

In the fine interdendritic region in F5 (Fig. 9.15(e)), three phases such as Ni(Si), η and 'U' (about 25 at. % Mg and 75 at. % Ni) were observed. The 'U' (unidentified) phase in a very small volume fraction (<<1.0 vol. %) is definitely a non-equilibrium phase as described in section 9.2.2. With increasing Mg content in composites from F1 to F5, the primary phases in the alloys in this region changes from Ni(Si) as shown in F1 to the η phase as shown in alloys F4 and F5 depending on whether the overall composition of the alloy is on the Ni-rich or Mg-rich side compared to the Ni(Si)+η eutectic composition as in composites F2 and F3.

9.3.1.2 Microstructure of near η single phase alloy F6

An attempt was made to fabricate alloy F6 as a single η phase. It contains small amount of other phases (Table 9.10). Homogenized microstructures of alloy F6 taken at low and high magnifications are shown in Fig. 9.16(a) and (b), respectively. Note that at a first glance the most of the area which appears to be the second phase region in Fig. 9.16(a), is also the η phase as shown in Fig. 9.16(b) taken at higher magnification. The Ni(Si), $MgNi_2$ and 'U' phases are apparently non-equilibrium phases, but longer homogenization time is required to remove them.

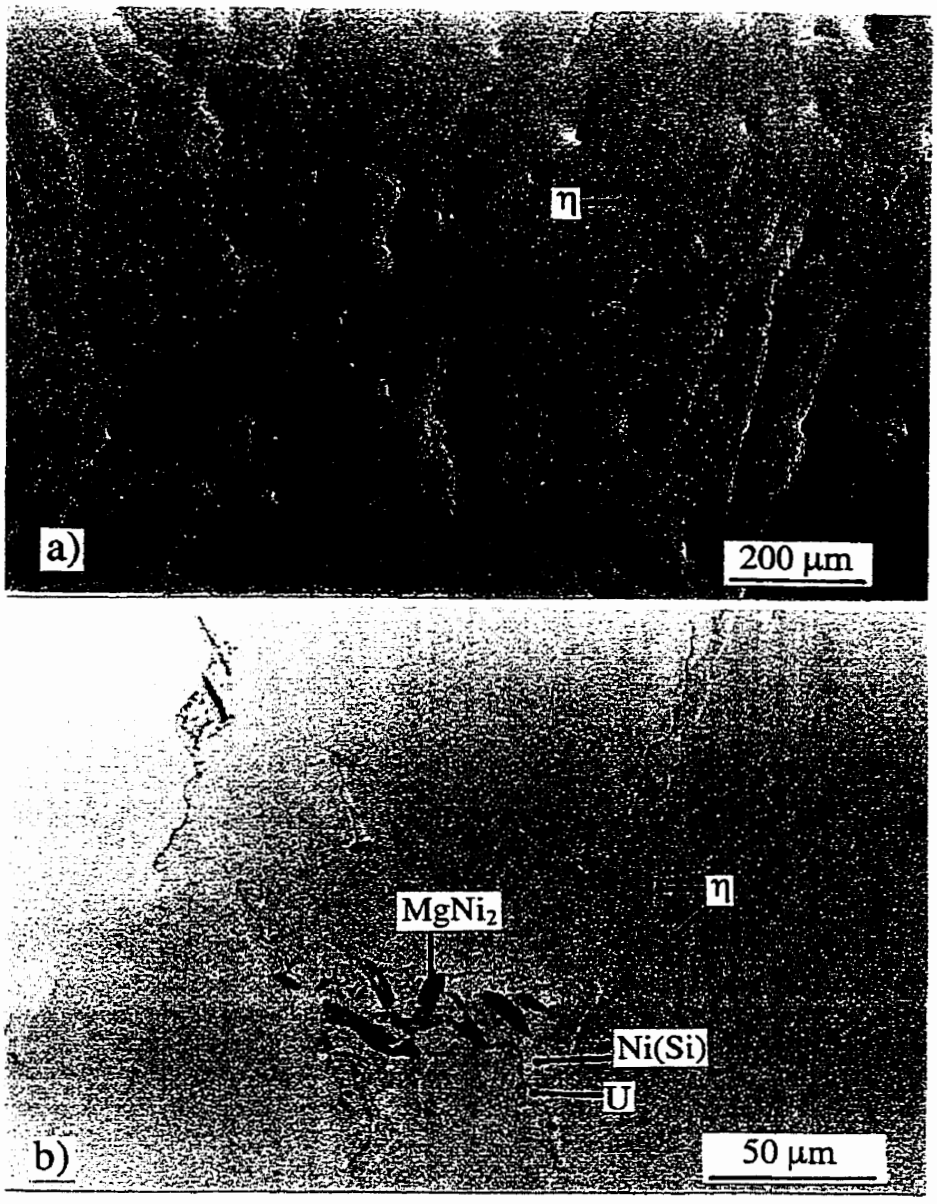

Fig. 9.16 Homogenized microstructures of solidified composite F6 taken at (a) low and (b) high magnifications.

9.3.1.3 Microstructures of F7 and F8 containing Ni(Si), η, and Ni_3Si

The microstructure of homogenized in-situ composite F7 is different from the top (Fig. 9.17(a)) to the bottom (Fig. 9.17(b)) of the ingot. The highly magnified SEM views of the top and the bottom of the ingot are presented in Fig. 9.17 (c) and (d), respectively. The microstructures of the bottom of the ingot (Fig. 9.17(b) and (d)) have a finer and more

continuous distribution of (Ni(Si)+Ni_3Si) than those of the top of the ingot (Fig. 9.17(a) and (c)).

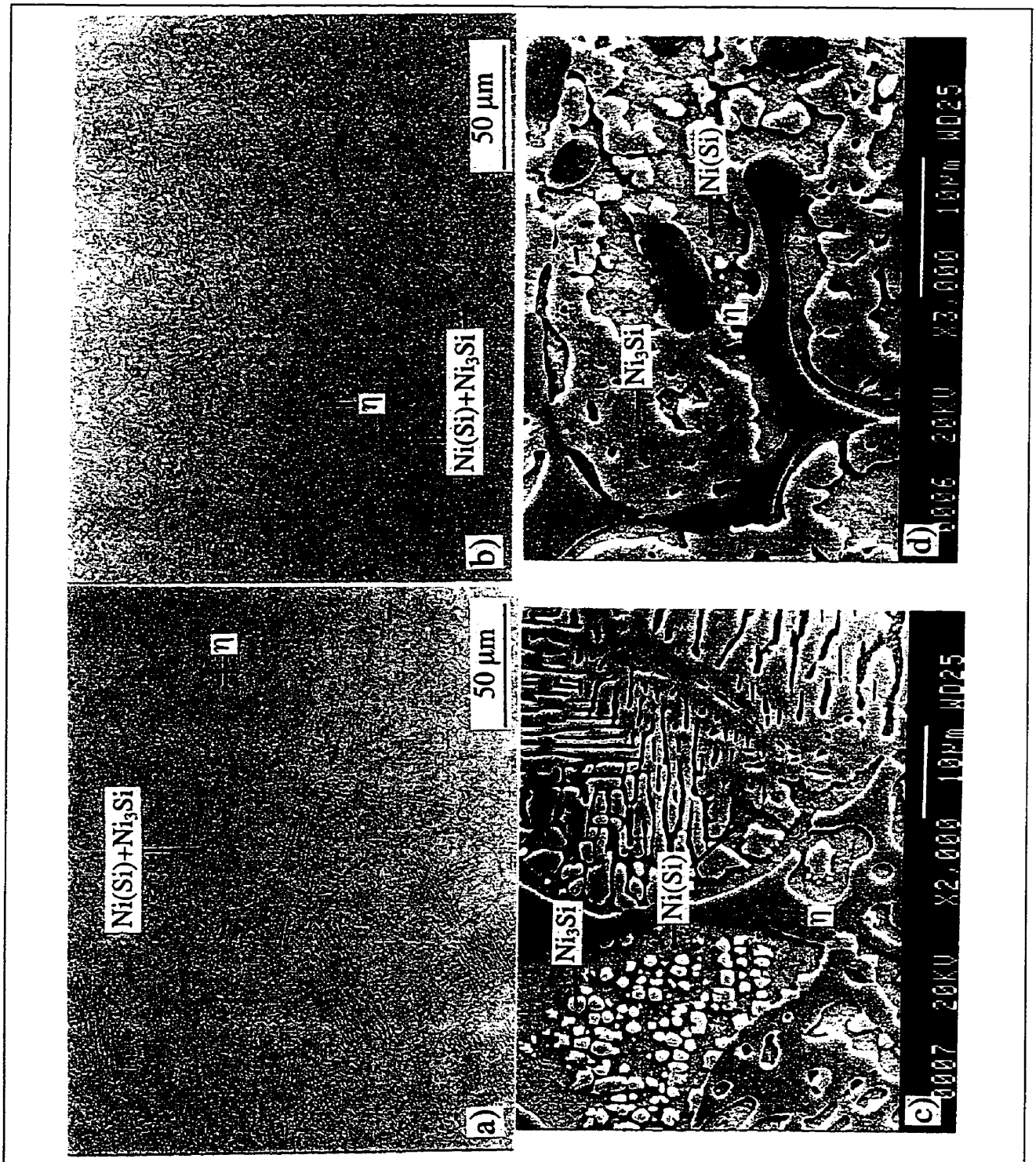

Fig. 9.17 Optical microstructures of homogenized composites F7 taken from (a) the top and (b) the bottom of the ingot and SEM microstructures of (c) the top and (d) the bottom.

The phases in F8 (Fig. 9.18) is the same as those in F7. The small rounded microconstituent in the mixture with the η matrix as well as the large, rounded microconstituent contains the Ni(Si) and Ni_3Si phases (Fig. 9.18(a) and (b)).

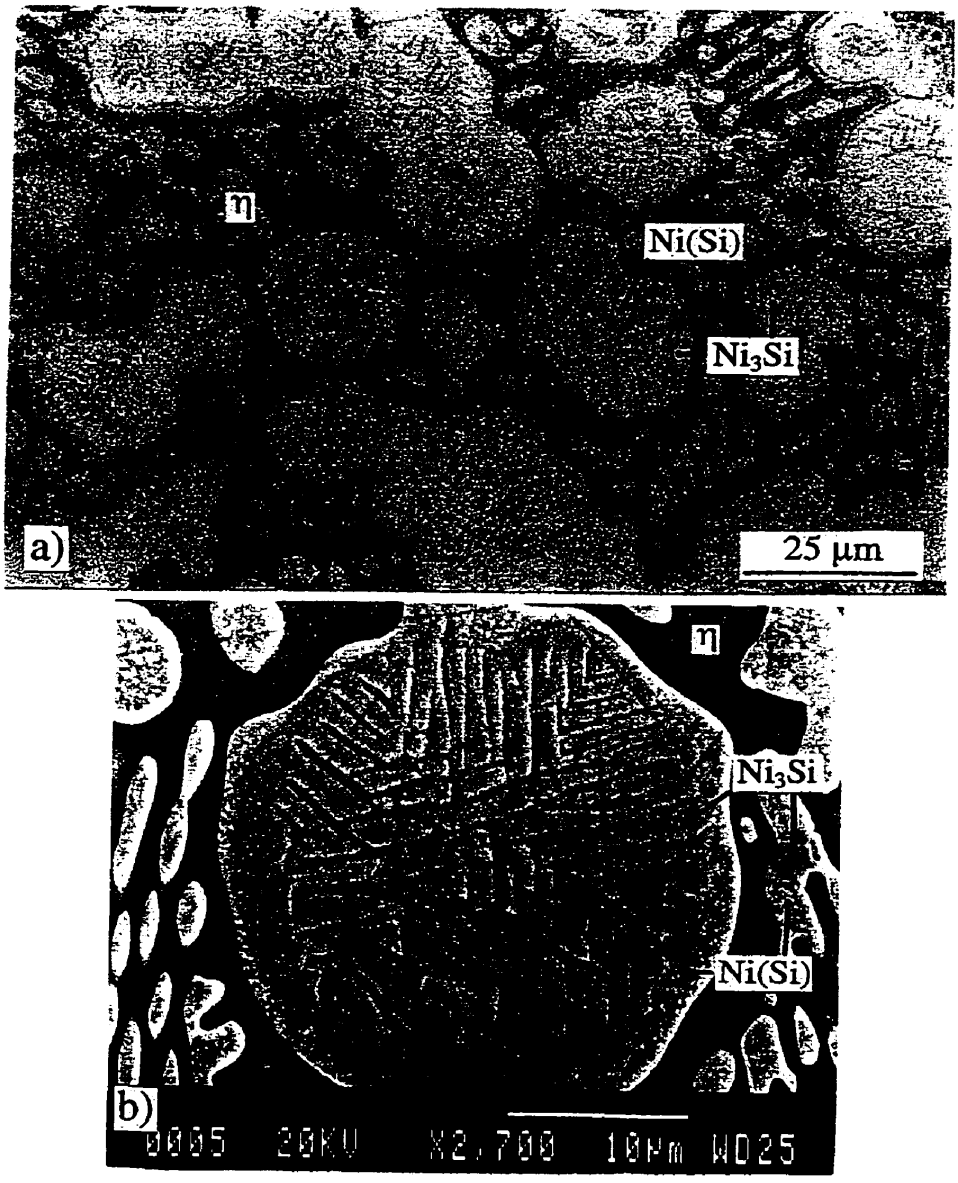

Fig. 9.18 Optical (a) and SEM (b) microstructures of homogenized composites F8.

9.3.1.4 Microstructure of binary Ni_3Si-based alloy F9

Alloy F9 was fabricated to be a single phase Ni_3Si alloy. However, it still contains Ni(Si) phase which is a non-equilibrium phase if one considers its composition with 23.42 at. % Si (Table 9.10) according to the Ni-Si binary phase diagram [90Mas] (Appendix Fig.A.1). The non-equilibrium Ni(Si) phase might be removed by homogenizing for about 500h at 900°C as it was achieved in the case of alloy 22 in Fig. 8 in [98Son[1]]. However, longer homogenization was not applied here for a couple of reasons. First, this might result in the formation of Kirkendall porosity as in the case of alloy 22 (Fig. 8 in [98Son]). Second, the grain size of Ni_3Si might grow larger than that to be considered as a limit for a valid fracture toughness test of a polycrystalline material.

Fig. 9.19 shows the as-cast microstructures of alloy F9. Large elongated columnar microconstituent and fine dendrites in between the large elongated columnar microconstituent are a mixture of Ni_3Si and $Ni_{31}Si_{12}$ which was formed by a non-equilibrium solidification (see Ni-Si binary phase diagram in Fig. A.1 in Appendix A). The (Ni_3Si+$Ni_{31}Si_{12}$) microconstituent was first solidified as $Ni_{31}Si_{12}$ and seems to be on the way of phase transformation from $Ni_{31}Si_{12}$ to Ni_3Si.

Fig. 9.20 shows the microstructures of Ni-Si binary alloy F9 after 200h homogenization at 900°C taken from the top (Fig. 9.20(a) and (b)) and bottom (Fig. 9.20(c)) of the ingot. The top of the ingot contains two distinguishable areas, i.e., the area with high vol. % of fine (Ni(Si)+Ni_3Si) mixture (Fig. 9.20(a)) and the other area with high vol. % of fine-grained Ni_3Si (Fig. 9.20(b)). However, dispersed Ni(Si) particles (black particles in Fig. 9.20(b)) are intermixed with fine-grained Ni_3Si. The volume fraction of Ni(Si), fine (Ni(Si)+Ni_3Si) mixture, or fine-grained Ni_3Si in the bottom of the ingot is much lower than that in the top. The morphology of fine (Ni(Si)+Ni_3Si) mixture in Fig. 9.20(a) taken at high magnification is shown in Fig. 9.20(d). In fact, the areas with fine-grained Ni_3Si originated from the (Ni_3Si+$Ni_{31}Si_{12}$+Ni(Si)) mixture present in the as-cast microstructure as shown in Fig. 9.19. The as-homogenized microstructures in Fig. 9.20 are quite comparable to the as-cast microstructures in Fig. 9.19. The (Ni_3Si+$Ni_{31}Si_{12}$) and (Ni_3Si+$Ni_{31}Si_{12}$+Ni(Si)) mixtures converted into Ni_3Si after homogenization by dissolving Ni(Si), resulting in substantial decrease in vol. % of Ni(Si). In some fine-grained Ni_3Si areas, Ni(Si) was still left as shown in Fig. 9.20(a), but in some other areas, Ni(Si) was almost totally dissolved (Fig. 9.20(b)).

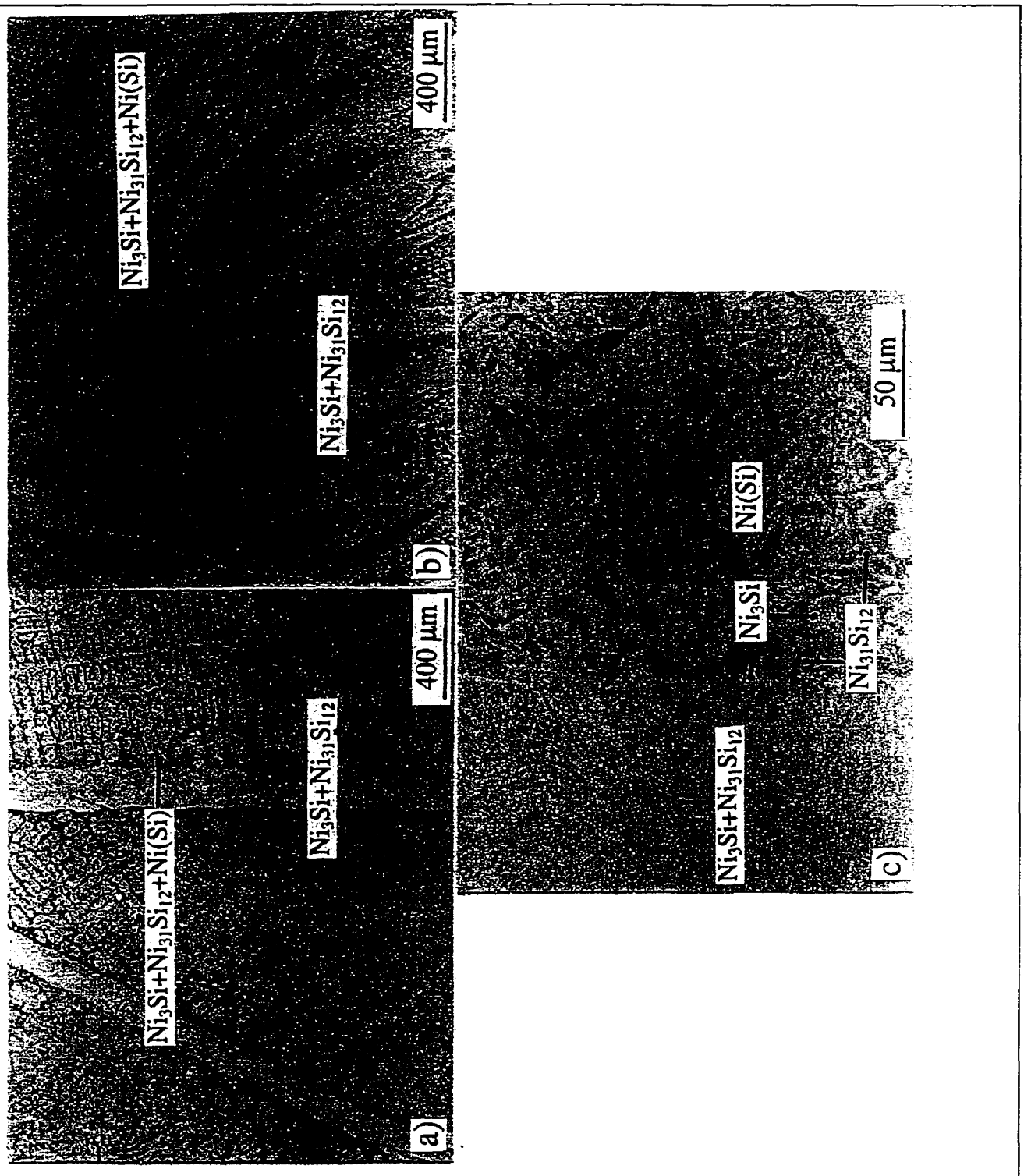

Fig. 9.19 The as-cast microstructure of alloy F9 from (a) the top and (b) bottom of the ingot. The highly magnified view of the (Ni_3Si+$Ni_{31}Si_{12}$) and (Ni_3Si+$Ni_{31}Si_{12}$+Ni(Si)) mixtures observed in the top of the ingot is shown in (c).

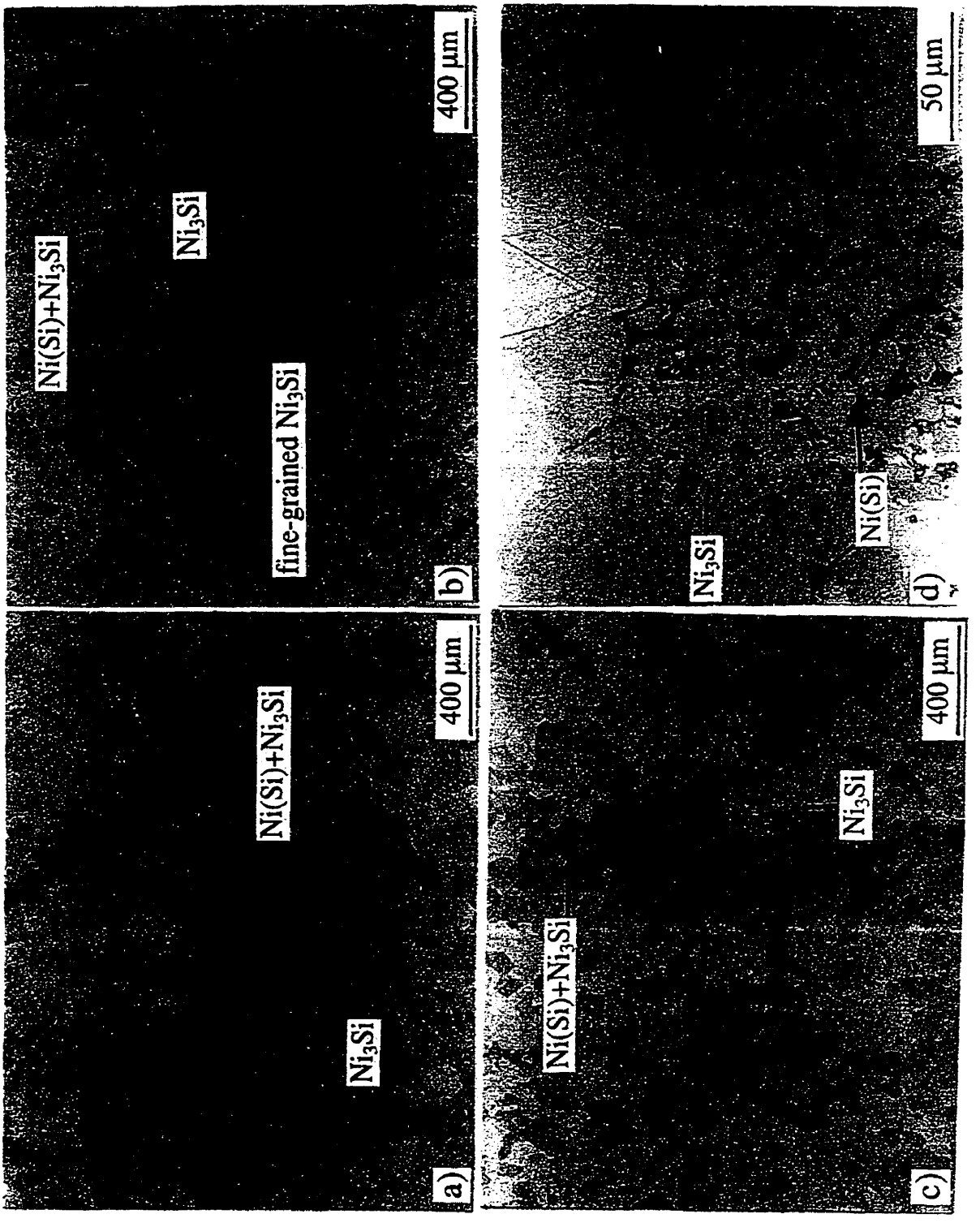

Fig. 9.20 The microstructure of alloy F9 from (a-b) the top and (c) the bottom of the ingot after homogenization for 200h at 900°C. The highly magnified view of the fine (Ni(Si)+Ni_3Si) mixture observed in the top of the ingot is shown in (d).

The volume fraction of Ni(Si) phase in F9 in Table 9.10 is the average value calculated from the volume fraction of the Ni(Si) in the individual specimen listed in Table 10.2 in section 10.2.2.1. The average grain size of the large Ni_3Si grains is about 58±7 μm and the Ni_3Si grains of fine-grained, nearly-single phase Ni_3Si is about 34±1μm.

9.3.1.5 Microstructures of alloys F10-F13 containing Ni_3Si and η

Composites F10-F13 contain mostly Ni_3Si and η in various volume fractions, but composites F10 and F11 also contain small amount of Ni(Si) whereas composites F11 and F12 additionally contain small amount of $Ni_{31}Si_{12}$ (Ni_5Si_2) (Table 9.10).

The microstructure of alloy F10 in Fig. 9.21(a) shows a similar microstructure to that of composite F9 in Fig. 9.20. However, F10 contains a very small amount of the η phase, and also contains more amount of fine (Ni(Si)+Ni_3Si) mixture compared to composite F9 (Fig. 9.20(a) and (b)).

The microstructure of F11 in Fig. 9.21(b) shows the four phase morphology, but overall volume fraction of $Ni_{31}Si_{12}$ phase embedded in Ni_3Si is negligible. The microstructure of the complex three phase region is quite similar to that of F7 (Fig. 9.17(a)). Microstructures of F12 and F13 are also shown in Fig. 9.21(c) and (d), respectively.

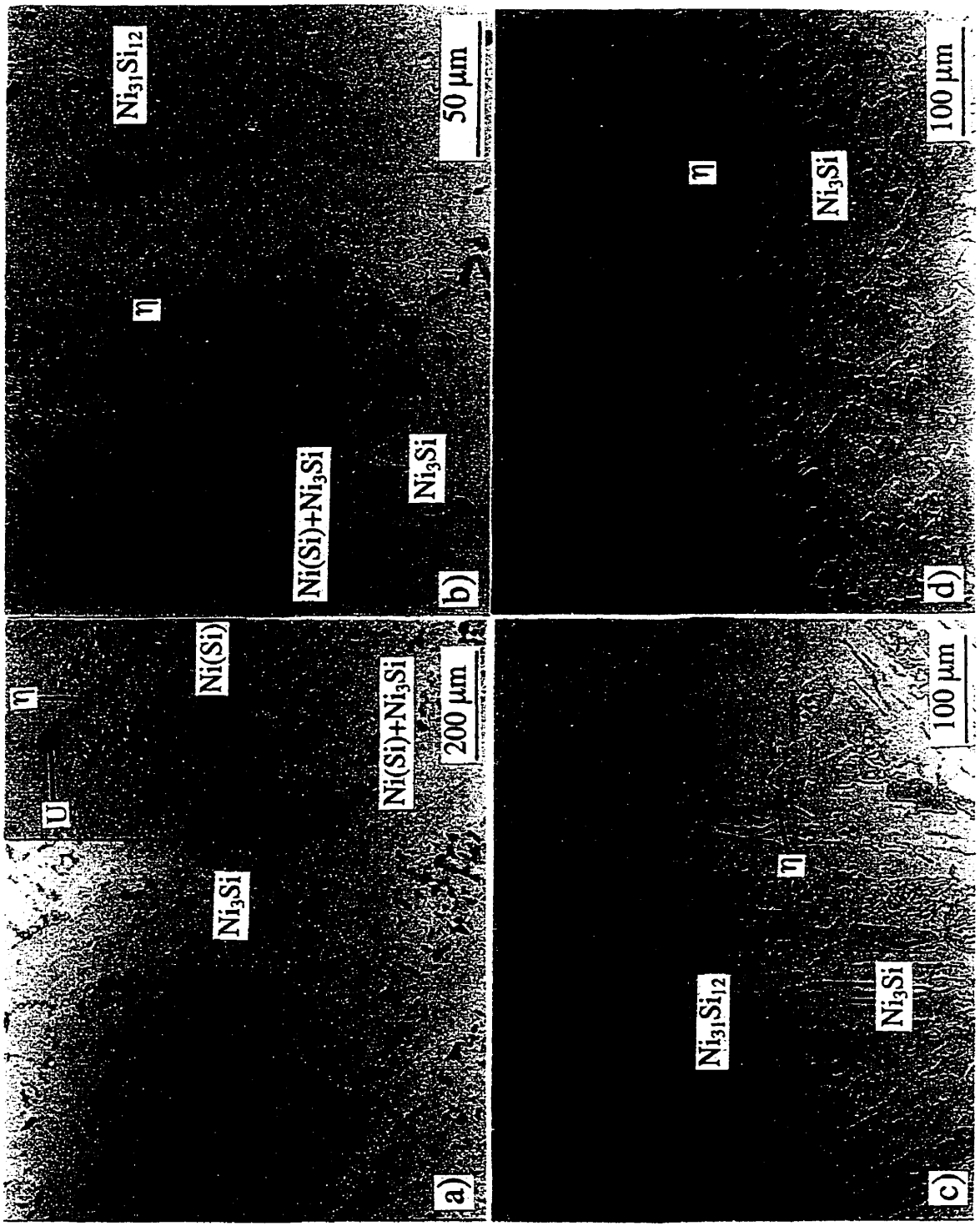

Fig. 9.21 Microstructures of alloys (a) F10, (b) F11, (c) F12, and (d) F13 after homogenization.

9.3.1.6 Microstructures of alloy F14 and F15

Fig. 9.22 shows the microstructures of F14 and F15 containing three phases η, Ni_3Si, and $Ni_{31}Si_{12}$, and η, $Ni_{31}Si_{12}$, and Ni_2Si, respectively. Both in-situ composites contain very fine eutectic mixtures. The fine eutectic mixture in F14 (Fig. 9.22(a)) is the $Ni_{31}Si_{12}$+η. The fine eutectic mixture in F15 (Fig. 9.22(b)) is mostly η+Ni_2Si, but η+Ni_2Si+ $Ni_{31}Si_{12}$ ternary eutectic mixture might also exist as already observed in alloy 7 in Fig. 5(b) in [98Son].

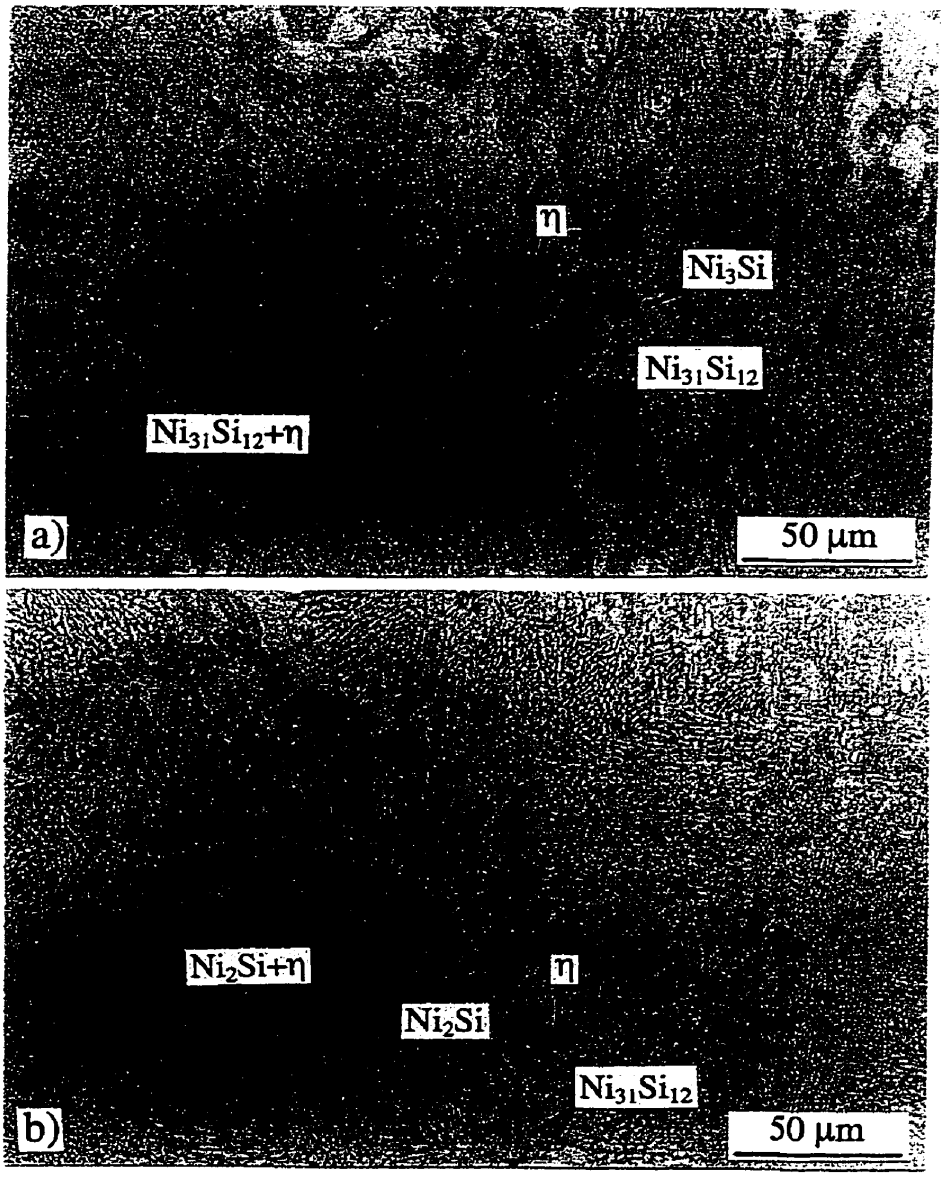

Fig. 9.22 Microstructures of (a) F14 and (b) F15 after homogenization.

9.3.1.7 Microstructure of Ni_2Si single phase alloy F16

Microstructure of Ni_2Si single phase alloy F16 is shown in Fig. 9.23. No other phases were observed. Different crystallographic orientations of grains reveal distinctive contrast. Numerous annealing twins are also noticeable.

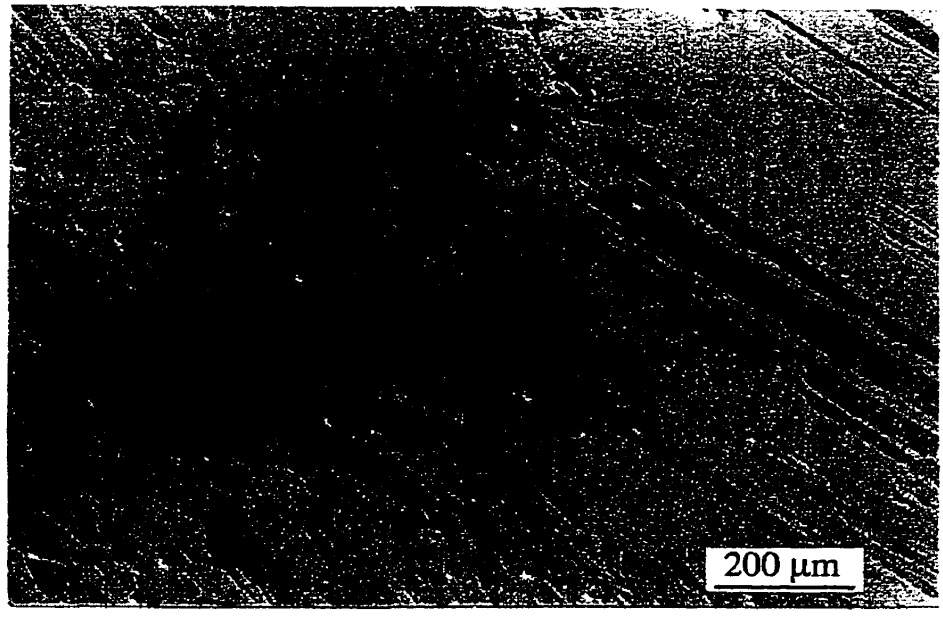

Fig. 9.23 Microstructure of Ni_2Si single phase alloy F16 after homogenization.

9.3.1.8 Microstructures of alloy F17-F20 containing η, ζ, and Ni_2Si

Fig. 9.24 shows the microstructures of alloy F17-F20 after homogenization. Volume fraction of Ni_2Si is decreasing with increasing alloy number, i.e. from F17 to F20. The solidification sequences and phase transformations occurred in the alloys in this region of the phase diagram are quite complex as already mentioned in [96Son, 98Son].

Fig. 9.24 Microstructures of composites (a) F17, (b) F18, (c) F19, and (d) F20 after homogenization.

9.3.1.9 Microstructure of alloy F21

The fine mixture of ((δ)-Ni_2Si+(ε)-Ni_3Si_2) and blocky Ni_2Si in the rounded microconstituent embedded in the κ matrix are shown in Fig. 9.25. As already mentioned for alloy 26 in Fig. 5 in [98Son], the fine mixture of Ni_2Si+Ni_3Si_2 and blocky Ni_2Si in the rounded microconstituent seems to be formed from the following reactions: θ-Ni_2Si phase→primary blocky δ-Ni_2Si, and (δ-Ni_2Si+ε′-Ni_3Si_2) by a eutectoid reaction from θ-Ni_2Si at 825°C→ primary blocky δ-Ni_2Si, and δ-Ni_2Si formed by a eutectoid at 825°C + (δ-Ni_2Si +ε-Ni_3Si_2) by a eutectoid reaction from ε′-Ni_3Si_2 at 820°C.

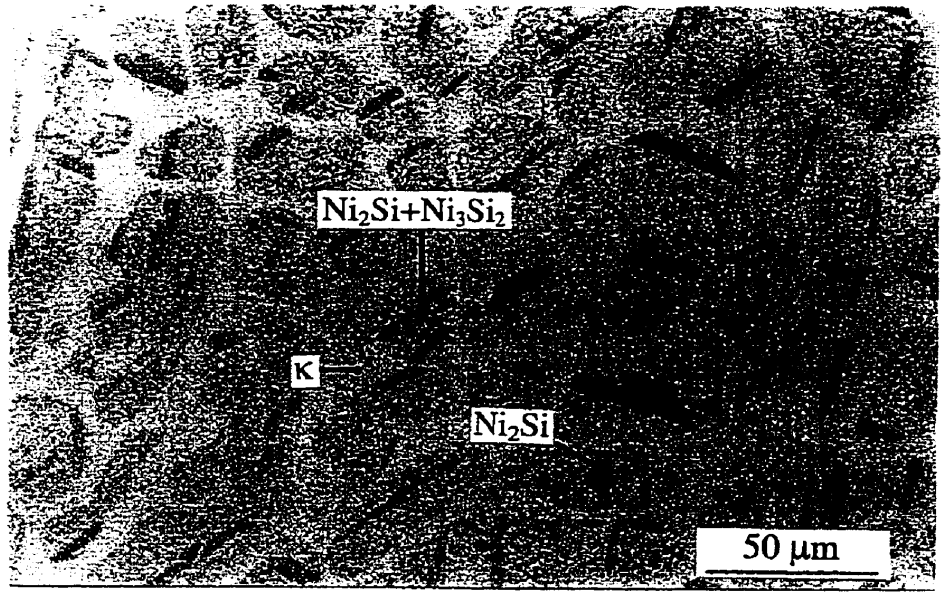

Fig. 9.25 Microstructure of alloy F21 after homogenization.

9.3.1.10 Microstructure of alloy F22

Alloy F22 was intended to be a $MgNi_2$ single phase alloy. However, it comprises a small fraction of other phases (Ni and 'U') after homogenization (Table 9.10). An optical micrograph showing the overall morphology and a SEM micrograph showing the magnified view of the interdendritic second phase region in F22 are seen in Fig. 9.26(a) and (b), respectively.

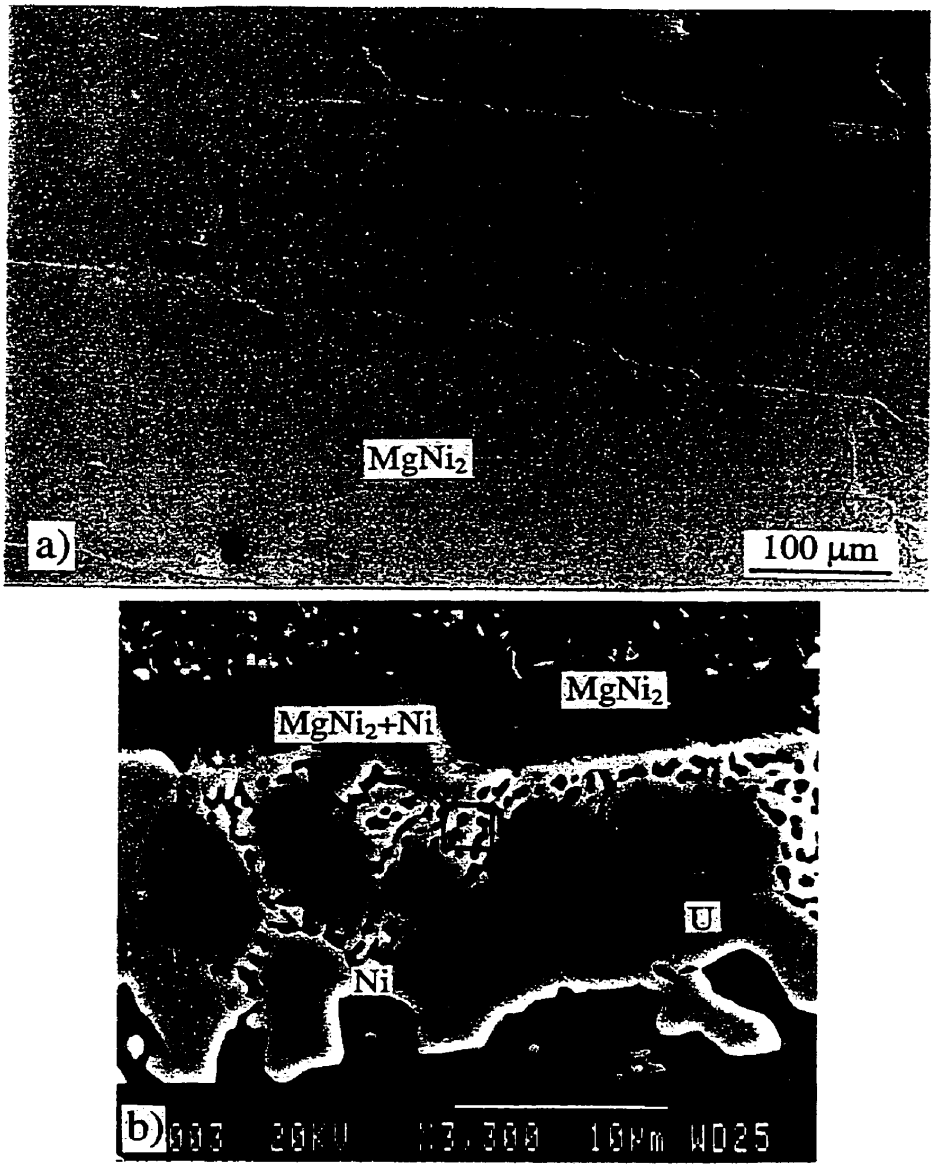

Fig. 9.26 An optical and a SEM micrographs are showing (a) the overall morphology and (b) the magnified view of the interdendritic second phase region in solidified alloy F22 after homogenization, respectively.

9.3.2 CNB fracture toughness test in air

9.3.2.1 Load-load line displacement curves (P-LLD) of CNB specimens tested in air

P-LLD curves for CNB specimens investigated in the present work showed quite diverse shapes (Fig. 9.27). The P-LLD curves were arbitrarily divided into eight typical types depending on whether the stable crack extension or tail existed or whether the crack propagated in a serrated or smooth manner. Fig. 9.27(a) shows a P-LLD curve with a stable crack extension prior to the maximum load and long tail (Type I) and Fig. 9.27(b) shows a stable crack extension and short tail (Type II). The term 'long tail' is used when the displacement to failure in the P-LLD curve is over 0.15mm. Fig. 9.27(c) shows a serrated P-LLD with a stable crack extension and short tail (Type III). Fig. 9.27(d) shows a linear P-LLD curve prior to the maximum load and long tail (Type IV). Fig. 9.27(e) shows a pop-in (overloading prior to crack initiation followed by stable crack extension) and short tail (Type V). Fig. 9.27(f) shows a stable crack extension without tail (Type VI). Fig. 9.27(g) shows a linear P-LLD curve without tail (Type VII). Fig. 9.27(h) shows a stable crack extension in a serrated manner without tail (Type VIII).

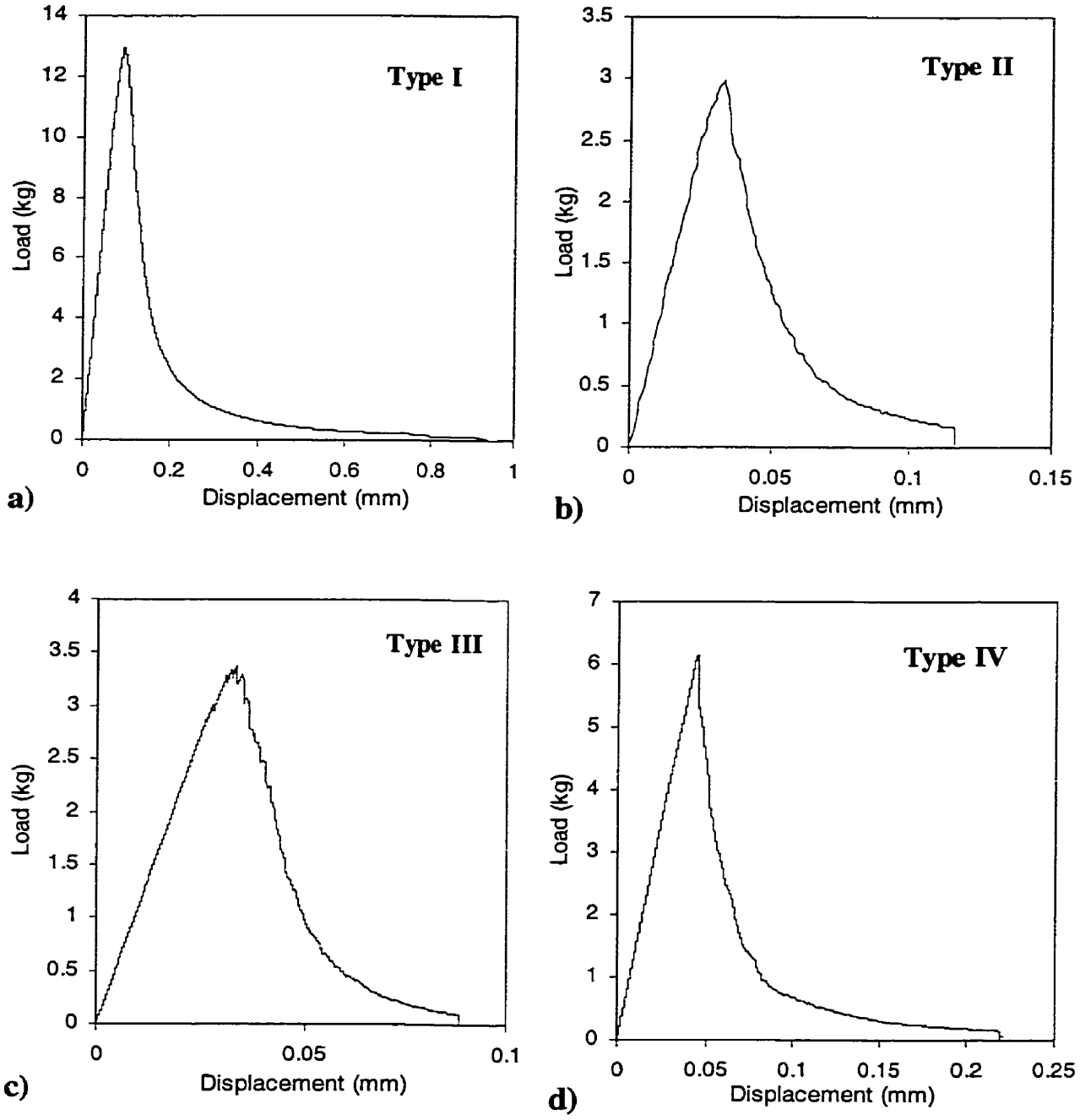

Fig. 9.27 Typical P-LLD curves observed in the present work. The curves are from (a) F1-3rd-35 (b) F13-3rd-35 (c) F14-2nd-35 (d) F16-5th-35 (e) F3-2nd-32 (f) F7-1st-16 (g) F18-2nd-16 (h) F18-3rd-16. The designation, F1-3rd-35 indicates the 3rd specimen from the bottom of the ingot (composite) F1 tested by applying S_l=35mm.

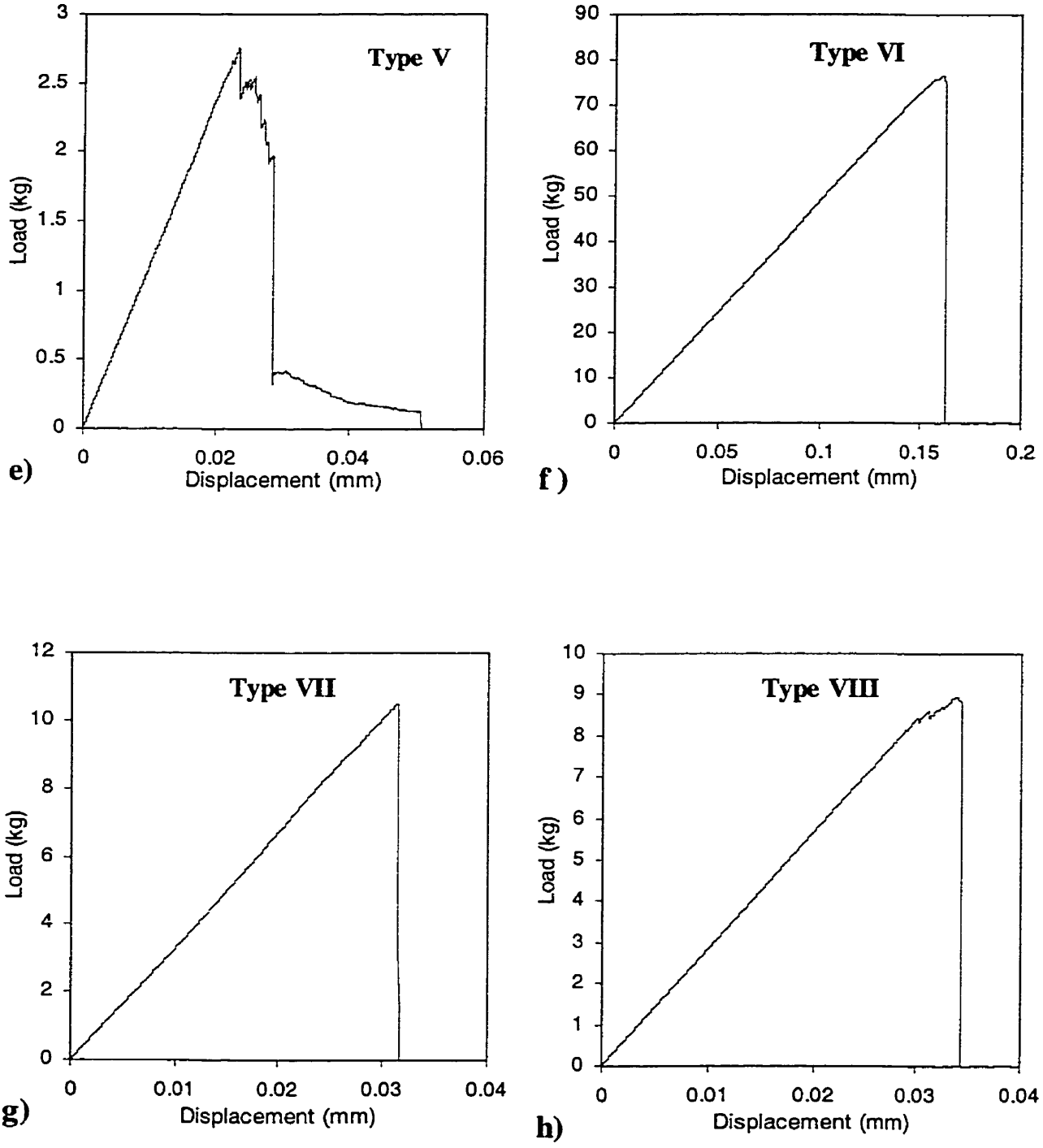

Fig. 9.27 Typical P-LLD curves observed in the present work. The curves are from (a) F1-3rd-35 (b) F13-3rd-35 (c) F14-2nd-35 (d) F16-5th-35 (e) F3-2nd-32 (f) F7-1st-16 (g) F18-2nd-16 (h) F18-3rd-16. The designation, F1-3rd-35 indicates the 3rd specimen from the bottom of the ingot (composite) F1 tested by applying S_1=35mm.

9.3.2.2 Fracture toughness values of in-situ composites tested in air and calculated from the maximum load

Table 9.11 shows the fracture toughness values calculated from the maximum load (Eq. (6.1)), the lower and upper span (S_1 and S_2, respectively), and the type of P-LLD curve defined in Fig. 9.27 for each specimen (in parentheses). Since the P-LLD curves defined as types IV and VII did not show any evidence of initial stable crack growth which is one of the criteria for the test to be considered as valid, types IV and VII are designated with bold letters in Table 9.11. The validity of the test results for the specimens which showed the linear P-LLD curves defined as type IV and VII will be discussed in section 10.2.1.1. Some of the in-situ composites were tested by applying two different lower support spans (S_1), that is, 35mm and 16mm. The specimens tested with S_1=16mm were prepared from broken half of the specimens tested with S_1=35mm of the same alloy.

When the P-LLD curves were Type V (Fig. 9.27(e)), the maximum load, P_{max} for fracture toughness calculation was taken from the second peak following the first overloaded maximum peak. In the present work, the designation, K_{IvM} for the plane strain fracture toughness determined by using chevron-notched bar and rod specimens and based on the maximum load for metallic materials in ASTM E 1304-89 [89AST[1]] will be adopted. However, the designation, K_{QIvM} will be used until the fracture toughness values are verified to be the valid plane strain fracture toughness values based on the specimen size requirement ($B \geq 1.25\ (K_{IvM}/\sigma_{YS})^2$, where B is the thickness of the specimen and σ_{YS} is the 0.2 % offset yield strength) in ASTM E 1304-89 [89AST[1]].

In Table 9.11 one may notice that the fracture toughness values of composites F7, F9, and F11 show a trend indicating that fracture toughness values of the specimens cut out from the bottom of the ingots are higher than those cut out from the top (see Fig. 8.1). Quite a high fracture toughness value of sample F9-5th tested with S_1=35mm seems to arise from the abnormal crack initiation as shown in Fig. H.1 in Appendix H. A large scatter in fracture toughness values of composite F9 is also noticeable.

Table 9.11 Fracture toughness values, type of P-LLD curve and the lower span (S_1) at a constant S_2=4.7mm for specimens tested in air.

Alloy No.	S_1 (mm) at S_2=4.7mm	Fracture toughness, K_{QIvM} (MPa.m$^{1/2}$) of the N_{th} specimen from the bottom of the ingot					
		1st	2nd	3rd	4th	5th	Average
F1	35	15.8 (I)	14.6 (I)	16.4 (I)	15.3 (I)	16.1 (I)	15.6±0.7
F2	35	12.4 (I)	12.0 (I)	12.0 (I)	11.8 (I)	-	12.1±0.3
	16	12.3 (VI)	12.2 (VI)	12.6 (VI)	12.7 (VI)	-	12.5±0.2
F3	32	9.9 (I)	9.2 (**IV***)	10.0 (I)	8.7 (V)	-	9.5±0.6
F4	35	7.1(II)	7.6 (II)	7.4 (II)	7.3 (II)	7.1 (II)	7.3±0.2
F5	25	3.2 (II)	2.6 (II)	3.1 (II)	2.9 (V)	-	3.0±0.3
F6	22	1.7 (**IV**)	1.7 (**IV**)	2.5 (II)	-	-	2.0±0.5
F7	35	28.0 (I)	23.4 (I)	19.0 (I)	-	17.8 (I)	22.1±4.6
	16	28.8 (VI)	26.5 (VI)	26.7 (**VII**)	31.2 (VI)	25.1 (VI)	27.7±2.4
F8	35	15.9 (I)	12.7 (I)	12.4 (I)	12.6 (I)	12.4 (I)	13.2±1.5
F9	35	38.7 (I)	30.1 (I)	27.7 (I)	21.4 (V)	(35.1 (I))**	29.5±7.2
	16	37.8 (I)	35.4 (**IV**)	-	28.9 (**IV**)	22.5 (I)	31.2±6.9
F10	35	29.7 (I)	27.2 (I)	21.5 (I)	31.2 (I)	26.2 (I)	27.2±3.7
F11	35	17.7 (I)	-	14.0 (I)	11.3 (I)	-	14.3±3.2
F12	35	10.5 (I)	9.0 (I)	7.2 (I)	7.7 (I)	7.4 (I)	8.4±1.4
F13	35	4.8 (II)	4.7 (II)	4.1 (II)	4.6 (II)	4.9 (II)	4.6±0.3
F14	35	4.8 (III)	4.4 (III)	5.0 (III)	4.7 (III)	4.4 (V)	4.7±0.3
	16	6.4 (**VII**)	4.9 (VI)	5.0 (**VII**)	5.1 (**VII**)	5.0 (VI)	5.3±0.6
F15	16	2.6 (**VII**)	4.6 (**VII**)	4.9 (**VII**)	-	2.9 (**VII**)	3.8±1.2
F16	35	4.7 (II)	5.1 (II)	6.1 (II)	6.3 (II)	6.5 (IV)	5.7±0.8
F17	35	5.5 (**IV**)	3.7 (III)	4.4 (III)	3.5 (III)	4.2 (III)	4.3±0.8
F18	35	5.4 (V)	3.3 (III)	3.4 (III)	4.6 (III)	4.1 (III)	4.2±0.9
	16	-	5.0 (**VII**)	4.0 (VIII)	3.5 (**VII**)	4.6 (**VII**)	4.3±0.7
F19	35	3.5 (V)	3.4 (V)	3.9 (III)	3.6 (III)	3.7 (III)	3.6±0.2
F20	35	3.1 (III)	3.1 (III)	3.8 (III)	3.8 (III)	3.7 (III)	3.5±0.4

Table 9.11 continued

F21***	32	3.0 (III)	2.8 (V)	3.6 (III)	3.4(V)	3.8 (III)	3.3±0.4
F22***	22	-	2.4 (IV)	2.9 (III)	-	-	2.7±0.4

( ): the Roman numbers in parentheses indicate the type of P-LLD curves defined in Fig. 9.27.

*: the P-LLD types IV and VII which exhibited the linear P-LLD curves prior to the maximum load are in bold letters.

**: fracture toughness value of the specimen is not included to calculate the average fracture toughness of F9 since the fracture surface of the specimen shows that the crack started in an abnormal manner from the chevron tip.

***: specimens were cut from a side of the ingots.

As already mentioned in section 8.4.2.1, selected composites such as F2, F7, F9, F14, and F18 were tested by applying both short (S_l=16mm) and long (S_l=35mm) lower span, to investigate the effect of the lower span, S_l on fracture toughness test. The fracture toughness values obtained by applying S_l=16mm are very close to those obtained by applying S_l=35mm for F2, F14, and F18 whose fracture toughness values are in the range of about 4-12 MPa.m$^{1/2}$. This indicates that there seems to be no effect of the lower span length when fracture toughness values are lower or equal to 12 MPa.m$^{1/2}$. However, it is not very clear whether or not the lower span, S_l, affected the fracture toughness values in the higher range of 18-39 MPa.m$^{1/2}$ for F7 and F9. On the one hand, comparing fracture toughness values for the first F7 and F9 specimens (i.e., F7-1st and F9-1st, i.e., bottom of the ingot) in Table 9.11, measured by applying S_l=16mm and S_l=35mm, there seems to be no effect of the lower span length, S_l on their fracture toughness. On the other hand, the fracture toughness values for the 2nd to 5th F7 and F9 specimens obtained from S_l=16mm are consistently higher than those obtained from S_l=35mm. However, if there was an effect of S_l on fracture toughness it should be visible also for the F7-1st and F9-1st specimens because fracture toughness values of these specimens are higher than those of the others. It can be hypothesized that the difference in fracture toughness values in the 2nd to 5th F7 and F9 specimens obtained from two different spans is probably induced by the difference in microstructure expected to occur from the center to the side of the ingot, similarly to the difference from the bottom to the top.

As a summary, the distribution of fracture toughness values depending on the overall compositions and microconstituents of in-situ composites is shown on the Ni-Si-Mg ternary phase diagram in Fig. 9.28 only for the specimens tested with S_l=35mm in Table 9.11.

Fracture toughness values of the composites are relatively low (<6.0 MPa.m$^{1/2}$) and similar to each other when the composition of the in-situ composites is away from the Ni_3Si and Ni(Si) phase fields (higher Si and Mg contents), implying that Ni_3Si and Ni(Si) are the major toughening phases in the present composites.

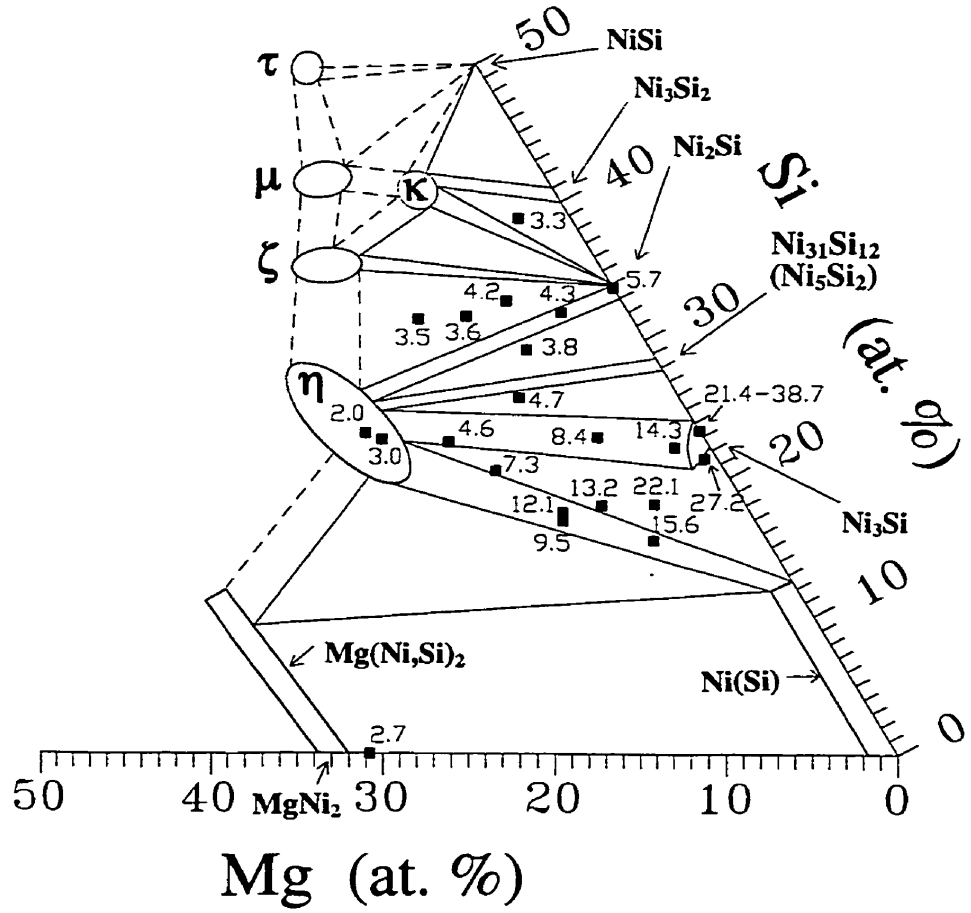

Fig. 9.28 Overall compositions of composites and their average fracture toughness values for the specimens tested with S_1=35mm in air are marked on the Ni-Si-Mg ternary phase diagram. A range of fracture toughness value is marked for F9 since a large scatter in fracture toughness was observed.

9.3.2.3 Fracture toughness in air calculated from work of fracture

Fracture toughness of selected in-situ composites such as F1, F2, F7-F12, and F20 containing only two or three Ni(Si), Ni_3Si, and η phases was also estimated by determining the work-of-fracture. Young's moduli of the selected composites used to calculate the work of fracture are already given in Table 8.4 in section 8.4.3.

The fracture toughness values (K_{wof}) of the selected in-situ composites calculated from Eq. (6.17) by determining the work-of-fracture given by Eq. (6.16) are listed in Table 9.12 and compared with the fracture toughness values (K_{QIvM}) from Table 9.11 which were calculated from the maximum load.

In general, K_{wof} values are much higher than K_{QIvM} values for the most of the selected in-situ composites. A possible explanation of this might be that the projected fracture area of CNB specimens calculated from their geometry and used to calculate the work-of-fracture (γ_{wof}) is smaller than the real fracture surface area, particularly for composites with high fracture toughness, giving rise to the overestimation of the work-of-fracture (γ_{wof}) as given in Eq. (6.11). Therefore, the overestimation of the work-of-fracture (γ_{wof}) results in the overestimation of K_{wof} as given in Eq. (6.16), resulting in higher K_{wof} compared to K_{QIvM}. Another reason could be related to the nature of the crack resistance curve (R-curve) which is unknown for the in-situ composites studied in the present work. As already mentioned in section 6.3.2, the work-of-fracture values are approximately equal to the fracture surface energy for the materials with flat R-curve [92Jen] but could be different for materials with rising R-curve.

Table 9.12 Comparison between the fracture toughness values in air calculated through the work-of-fracture (Eq. 6.17) and from the maximum load (Eq. 6.1).

Composites (S_1=35mm S_2=4.7mm)	K_{QIvM} Or K_{wof}	Fracture toughness (MPa.m$^{1/2}$) of the Nth specimen From the bottom of the ingot					Average
		1st	2nd	3rd	4th	5th	
F1	K_{QIvM}	15.8	14.6	16.4	15.3	16.1	15.6±0.7
	K_{wof}	21.5	22.0	24.6	22.5	25.1	23.1±1.6
F2	K_{QIvM}	12.4	12.0	12.0	11.8	-	12.1±0.3
	K_{wof}	14.4	14.5	15.5	14.8	-	14.8±0.5
F6	K_{QIvM}	1.7	1.7	2.5	-	-	2.0±0.5
	K_{wof}	3.2	3.6	3.3	-	-	3.4±0.2
F7	K_{QIvM}	28.0	23.4	19.0	-	17.8	22.1±4.6
	K_{wof}	32.4	33.7	24.5	-	28.6	29.8±4.2
F8	K_{QIvM}	15.9	12.7	12.4	12.6	12.4	13.2±1.5
	K_{wof}	19.5	16.4	16.2	16.6	16.4	17.0±1.4
F9	K_{QIvM}	38.7	30.1	27.7	21.4	35.1	30.6±6.7
	K_{wof}	45.0	42.0	53.4	49.3	53.4	48.6±5.1
F10	K_{QIvM}	29.7	27.2	21.5	31.2	26.2	27.2±3.7
	K_{wof}	42.0	31.6	32.9	37.9	45.2	37.9±5.8
F11	K_{QIvM}	17.7	-	14.0	11.3	-	14.3±3.2
	K_{wof}	34.6	-	23.6	25.6	-	27.9±5.8
F12	K_{QIvM}	10.5	9.0	7.2	7.7	7.4	8.4±1.4
	K_{wof}	19.2	13.9	12.3	15.3	12.8	14.7±2.8

Fig. 9.29 represents a graphical comparison of K_{wof} and K_{QIvM}. The solid line is the best fit line to the data points representing the values from individual specimens and the broken line represents the ideal line for which K_{wof} equals as K_{QIvM}. K_{wof} values are on average ~1.45 times higher than K_{QIvM}. However, for composites F2, F6, and F8, K_{wof} values are relatively close to K_{QIvM} values.

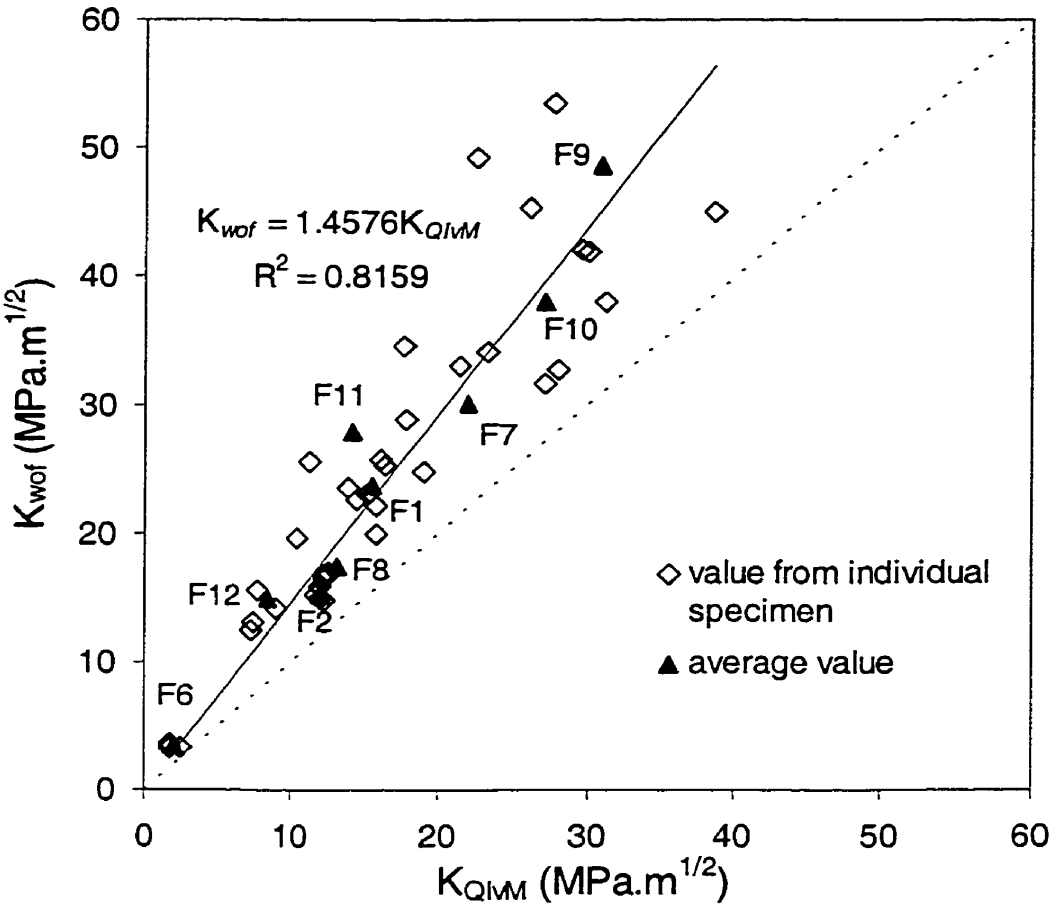

Fig. 9.29 Graphical representation of the difference in K_{QIvM} and K_{wof} values of selected composites. The solid line is the best fit line to the data points representing the values from individual specimen and the broken line represents the ideal line for which K_{wof} equals as K_{QIvM}.

9.3.3 Fracture toughness test in dry oxygen and vacuum

9.3.3.1 P-LLD curves and fracture toughness values of selected composites tested in dry oxygen and vacuum

Fracture toughness values as well as the type of P-LLD curve of selected composites tested in vacuum and dry oxygen atmospheres are tabulated in Table 9.13. Most of the specimens were tested by applying S_1=26mm and S_2=9.3mm, but three of the specimens were tested with S_1=16mm and S_2= 4.7mm (Table 9.13). The average fracture toughness values were calculated without differentiating between the values obtained from specimens tested with

different lower span (S_1) since the effect of span on fracture toughness seems to be negligible according to the results of fracture toughness measurement by CNB specimens tested in air (Table 9.11). On the one hand, no clear evidence of environmental effect on fracture toughness was observed for F6, F12, F14, F16 and F21, if one compares the fracture toughness values in Table 9.11 (air) with those in Table 9.13. On the other hand, the average fracture toughness value for F9 tested in dry oxygen is increased about 25% (Table 9.13) compared to the test in air (Table 9.11). However, comparing only the highest fracture toughness value obtained for the specimens tested in air and in dry oxygen, one finds that the difference is minor. This will be discussed further in section 10.2.2.1.

Table 9.13 Type of P-LLD and fracture toughness values of selected composites tested in vacuum or dry oxygen.

Alloy No. (phases)	Span (mm)		Test Environ-ment	Fracture toughness, K_{QlvM} (MPa.m$^{1/2}$) of the Nth specimen from the bottom of the ingot					
	S_1	S_2		1st	2nd	3rd	4th	5th	Ave.
F6	26	9.3	Oxygen	1.7(VIII)	-	-	-	-	2.4±0.9
(η, Ni(Si)*)	16	4.7	Oxygen	-	3.0(**VII****)	-	-	-	
F9	26	9.3	Oxygen	40.3 (I)	35.4***(I)	-	-	42.7***(I)	39.5±3.7
(Ni_3Si, Ni(Si)*)	26	9.3	Vacuum	-	-	29.4(I)	36.3(I)	-	32.9±4.9
F12 (η, Ni_3Si)	26	9.3	Oxygen	8.3(**VII**)	6.8(III)	5.5(III)	-	-	6.9±1.4
F14 (η, Ni_3Si, $Ni_{31}Si_{12}$)	26	9.3	Oxygen	-	5.2(VIII)	4.7(VIII)	-	-	4.9±0.4
F16 (Ni_2Si)	16	4.7	Oxygen	6.7(V)	7.3(**VII**)	-	-	-	6.8±1.0
	26	9.3	Oxygen	-	-	5.5(VIII)	7.8(V)	-	
F21 (κ,Ni_3Si_2, Ni_2Si)	26	9.3	Oxygen	3.4(VI)	4.2(**VII**)	3.0(VIII)	-	-	3.5±0.6

Note: The Roman numerals in parentheses indicate the type of P-LLD curves defined in Fig. 9.27 for each specimen.

*: volume fraction of Ni(Si) is very low (1.1 % for F6 and 2.9% for F9)

**:The P-LLD types IV and VII which exhibited the linear P-LLD curves prior to the maximum load are in bold letters.

:Oxygen pressure used for most of specimens was 12 psi except for the specimen with '' beside fracture toughness values. The oxygen pressure used for the specimen with the mark, '***' was 15 psi. The level of vacuum used for specimen F9-3rd and 4th specimens was about 6x10-5 and 3x10-6 torr, respectively.

Fracture toughness values of F9 tested in dry oxygen are higher than those tested in vacuum (Table 9.13). Similarly, elongation of intermetallics such as FeAl [89Liu1, 90Liu2, 90Liu[3]], Fe_3Al [90Liu[3]] and Ni_3Si [91Liu] was reported being higher when they were tested in dry oxygen as opposed to test in vacuum. However, this difference in the present work might result from different microstructure of each specimen as well as different test environment. Scatter in fracture toughness values of F9 tested in dry oxygen and vacuum is slightly reduced compared to test in air. The trend of fracture toughness decreasing with increasing specimen number for the bottom to the top of the ingot, i.e., from F9-1st to F9-5th (Table 9.11), is not observed for the specimens tested in vacuum and dry oxygen.

9.3.4 Fractography

9.3.4.1 Fracture behaviour of the specimens tested in air

Fracture surfaces after CNB tests were examined in the SEM. Fractographs showing the overall fracture surfaces at low magnification of all samples are displayed in Fig. H.2 in Appendix H.

9.3.4.1.1 Fracture behaviour of F1

The overall fracture surface of alloy F1 (60 vol. % of Ni(Si) and 40 vol. % of η) is shown in Fig. H.2 (a) in Appendix H. Two typical modes of fracture, particularly associated with the Ni(Si) phase were observed. The pull-out (Fig. 9.30(a)) as well as ductile-type fracture (Fig. 9.30(b)) of the Ni(Si) phase is observed. The highly magnified SEM fractograph in Fig. 9.30(c) shows typical microvoids in the ductile Ni(Si) fracture surface shown in Fig. 9.30(b).

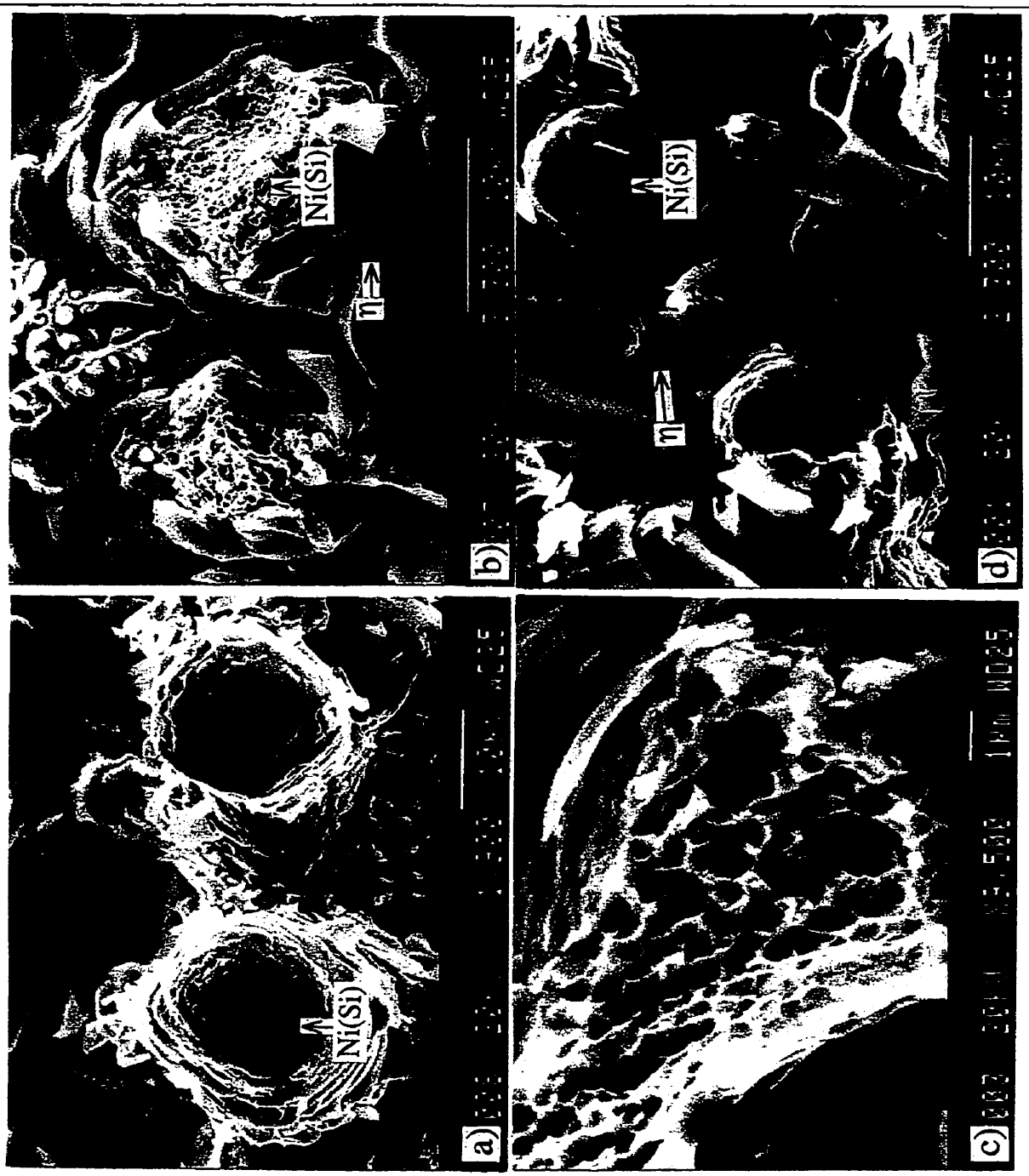

Fig. 9.30 SEM fractographs of F1 showing (a) the pull-out, (b) the ductile fracture, (c) the typical microvoids in the ductile Ni(Si) fracture surface in (b), and (d) smooth fracture surface of the Ni(Si) phase.

A relatively smooth fracture surface of Ni(Si) phase (Fig. 9.30(d)) was also observed in the fracture surface close to the tip of the chevron notch. Compared to the η matrix which developed cracks around the ductile-type fracture of the Ni(Si) phase shown in Fig. 9.30(b)

the η matrix around the smooth fracture surface of Ni(Si) in Fig. 9.30(d) does not develop any cracks. The average CNB fracture toughness value of this in-situ composite is ≈16 MPa $m^{1/2}$ (Table 9.11).

9.3.4.1.2 Fracture behaviour of composites F2 and F3

As already mentioned in section 9.3.1.1, composites F2 and F3 are almost identical in composition and the volume fraction of each microconstituent phase except that F2 was cast and F3 was solidified in the melting crucible. F2 and F3 contain a very fine two phase (η+Ni(Si)) mixture with about 47 vol. % of Ni(Si) (Table 9.10). The significant difference in fracture surfaces of F2 and F3 is the path of crack propagation. The crack propagated through the chevron-notched plane in F2 (Fig. H.2(b)) while in F3 the crack propagated through a preferred path (Fig. H.2(c)). In F2 the crack predominantly propagated in the direction transverse to the fiber-like Ni(Si) phase in the η matrix, cutting through the Ni(Si) (Fig. 9.31(a)). However, two different modes of fracture surface were observed in F3. The crack propagated either through the interface between η and Ni(Si) even though the crack needed to change its directions from the original notched plane (Fig. 9.31(b)), or in the direction transverse to the fiber-like Ni(Si) phase in the η matrix (Fig. 9.31(c)), similarly to F2. When the crack propagated in the transverse direction (Fig. 9.31(a) in F2 and (c) in F3) the fiber-like Ni(Si) phase was pulled out and debonded from the matrix, η. The distribution and shape of Ni(Si) in F3 are more uniform than those in F2. No significant matrix cracking in the η phase was observed. The average CNB fracture toughness values of composites, F2 and F3 are about 13 MPa.$m^{1/2}$ and 10 MPa.$m^{1/2}$, respectively (Table 9.11).

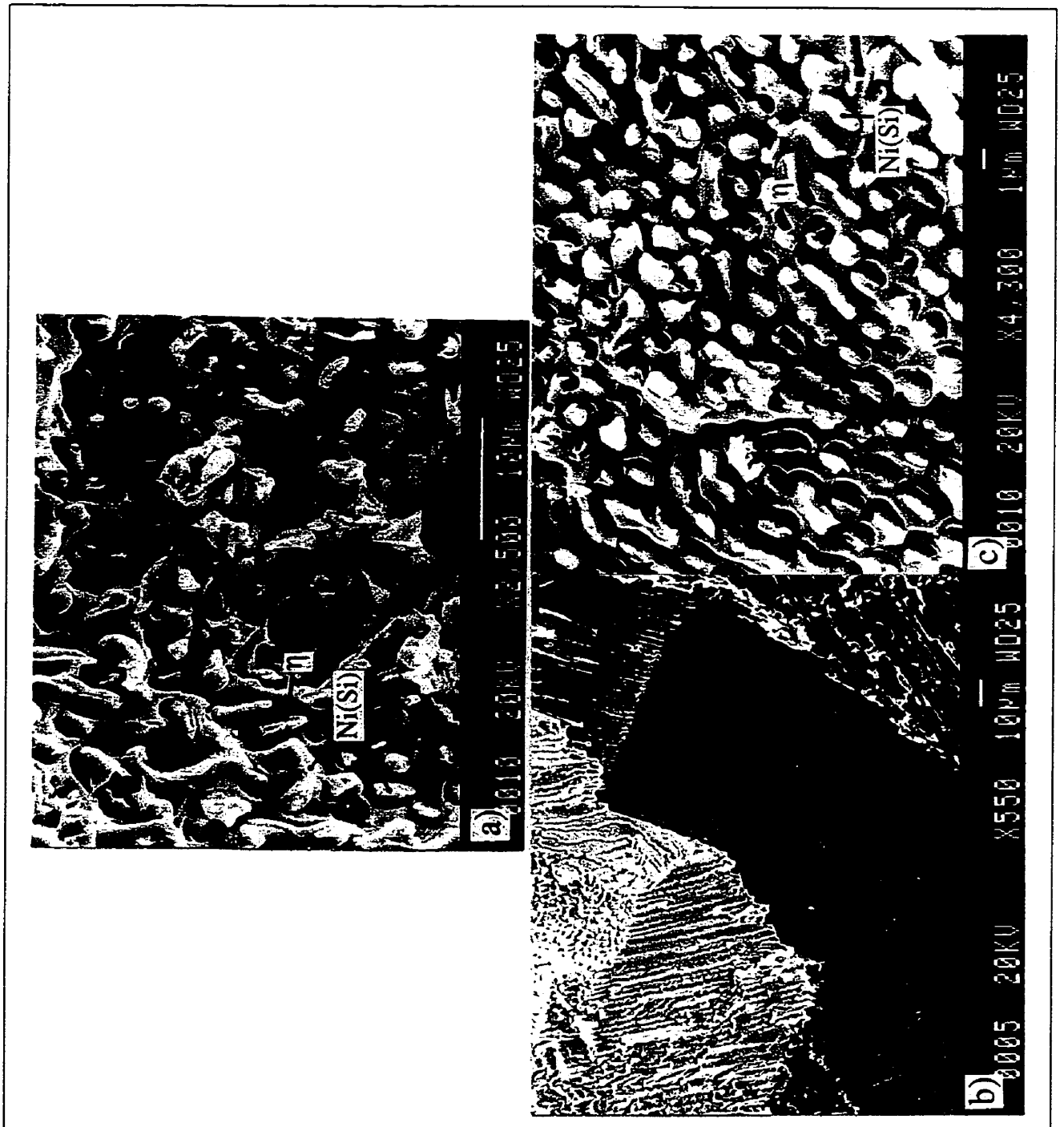

Fig. 9.31 SEM fractographs showing the fracture surfaces (a) in F2, and (b) and (c) in F3.

9.3.4.1.3 Fracture behaviour of F4-F6

SEM fractographs showing the overall fracture surface of in-situ composites F4 and F5 are also presented in Fig. H.2 (d) and (e), respectively, in Appendix H. The fracture surface of the Ni(Si) phase or the area containing Ni(Si) are relatively rough while the fracture surface of

η is very smooth. The η phase shows mostly transgranular cleavage fracture, but the evidence of intergranular fracture of η as a microconstituent phase in F4 was also observed (Fig. 9.32).

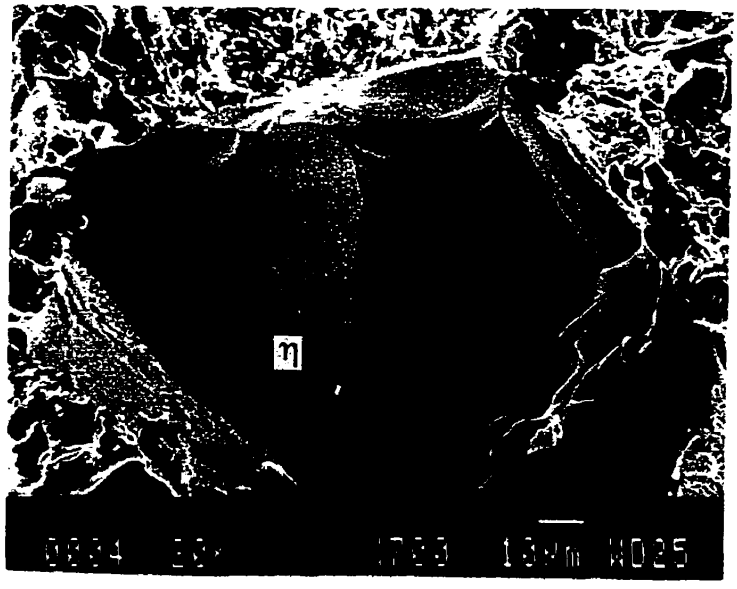

Fig. 9.32 A SEM micrograph showing the evidence of intergranular fracture in the η phase in composite F4.

The fracture surface of near η single phase alloy F6-1st (Appendix H.2 (f)) shows an extremely smooth and flat surface, particularly, in the area from the tip to the middle of the chevron. SEM micrographs showing fracture surface of alloy F6-2nd and F6-3rd are in Fig. H.3 in Appendix H. By comparing the fracture surface, particularly, the chevron tip area of F6-3rd with those of F6-1st and F6-2nd, the higher toughness value of F6-3rd (Table 9.11) than those of F6-1st and F6-2nd might be justified. There are more second phase regions containing Ni(Si) in the fracture surface of F6-3rd compared to the fracture surface of F6-1st and F6-2nd.

9.3.4.1.4 Fracture behaviour of F7 and F8

As already mentioned in section 9.3.2.2, fracture toughness of composite F7 decreases from F7-1st (first specimen from the bottom of the ingot) to F7-5th (fifth specimen from the bottom of the ingot) and this tendency seems to be related to the difference in the microstructure of specimens (Fig. 9.17). The microstructure of the specimen F7-1st consists of finer

(Ni(Si)+Ni_3Si) microconstituent compared to the microstructure at the top of the ingot (Fig. 9.17). Fig. 9.33 shows the SEM fractographs of specimen F7-1st (28MPa.m$^{1/2}$) and F7-5th (17.8 MPa.m$^{1/2}$), having the highest and the lowest fracture toughness values (for S_I=35mm).

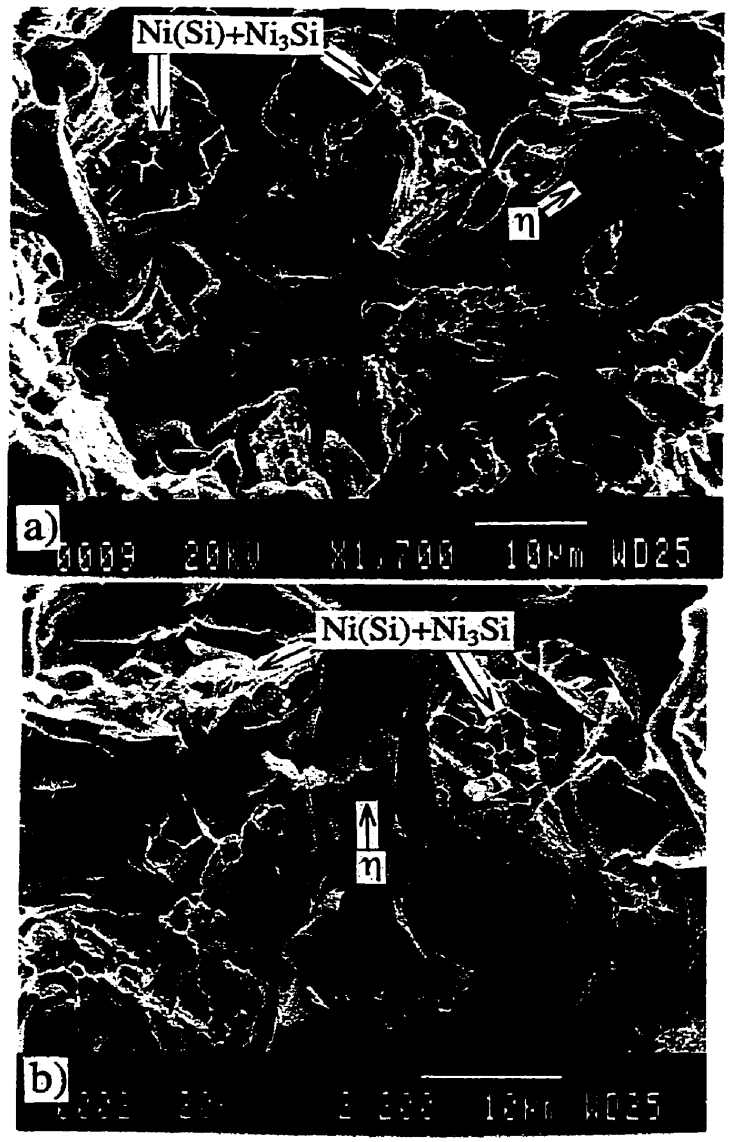

Fig. 9.33 SEM fractographs showing the difference between specimens (a) F7-1st with fracture toughness value of 28 MPa.m$^{1/2}$ and (b) F7-5th with fracture toughness value of 17.8 MPa.m$^{1/2}$. Cracks in the η matrix in F7-1st and slight debonding of the (Ni(Si)+Ni_3Si) microconstituent from the η matrix in F7-5th are noticeable.

The fracture surfaces of F7-1st and F7-5th correspond to the microstructures of the bottom (Fig. 9.17(b)) and the top (Fig. 9.17(a)) of the ingot. Besides the finer (Ni(Si)+Ni_3Si)

microconstituent in the fracture surface of F7-1st (Fig. 9.33(a)), severe cracking in the η matrix is noticeable compared to the uncracked η matrix in F7-5th specimen (Fig. 9.33(b)). The microcracking of the η matrix in F7-1st seems to result from the high crack-propagation resistance in this alloy due to the appropriate distribution of (Ni(Si)+Ni_3Si) microconstituent. In the fracture surface of specimen F7-5th (Fig. 9.33(b)), slight debonding of the (Ni(Si)+Ni_3Si) microconstituent from the η matrix, is observed instead of cracking in the η matrix.

Fracture behaviour of F8 is quite similar to that of F7 as it might be anticipated from its microstructure (Fig. 9.18) which is also similar to that of F7 (Fig. 9.17). However, the volume fraction of the brittle η phase in F8 is higher than that in F7.

9.3.4.1.5 Fracture behaviour of F9

Fracture behaviour of F9, a Ni_3Si based intermetallic in-situ composite is of great interest since its fracture toughness is much higher than expected from the low tensile elongation of Ni_3Si (~0 % in air) [91Liu]. However, as already mentioned in section 9.3.2.2 fracture toughness values (K_{QIvM}) of F9 are in the range of 21.4 MPa.m$^{1/2}$ to 38.7 MPa.m$^{1/2}$ but they show a large scatter.

F9 contains an average of 2.9% volume fraction of Ni(Si). However, as already mentioned in section 9.3.1.4 the volume fraction of Ni(Si) at the bottom is much lower than that at the top of the ingot. In general, intergranular fracture mode is dominant, but transgranular fracture is also observed (Fig. 9.34(a) taken from F9-1st K_{QIvM}=38.7 MPa.m$^{1/2}$). SEM fractographs in Figs. 9.34(b), (c) and (d) reveal step like transgranular fracture of Ni_3Si, indicating that the dislocation movement in Ni_3Si is very restricted to fixed slip systems. Only one or two slip systems were activated during bending test as shown in Fig. 9.34(c) and Fig. 9.34(d). This type of dislocation movement, called 'planar glide' seems to explain the mechanism of the formation of the step like fracture surface shown in Fig. 9.34(b). Fig. 9.34(e) shows transgranular fracture surface and Ni(Si) particles on the Ni_3Si grain boundary facet which seem to be debonded from the other side of the fracture surface. Fig. 9.34(f) shows the fracture surface of the specimen F9-4th (K_{QIvM}=21.4MPa.m$^{1/2}$) containing substantial amount of the fine (Ni(Si)+Ni_3Si) mixture shown in Fig. 9.20(a). Fig. 9.34(g) and (h) show the magnified view of the area containing fine (Ni(Si)+Ni_3Si). The continuous Ni(Si) phase was drawn to failure in a chisel-like ductile mode.

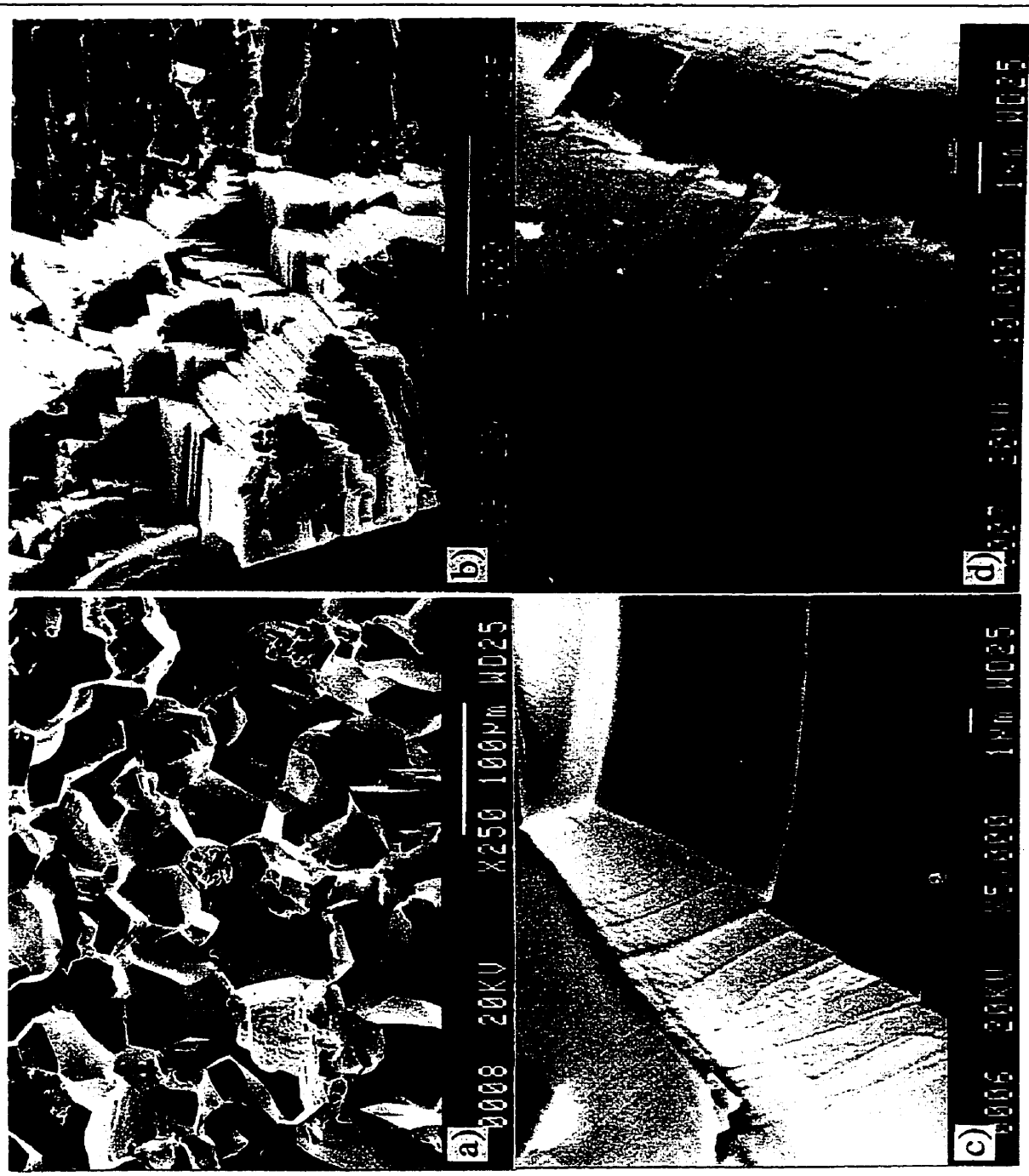

Fig. 9.34 SEM fractographs of alloy F9 showing (a) a mixture of inter- and transgranular fracture taken from F9-1st, (b) a closer view of step like transgranular fracture, (c-d) the formation of the shear steps, (e) transgranular fracture and Ni(Si) particles debonded from the other side of the fracture surface, and (f-h) the area with the fine (Ni(Si)+Ni_3Si) mixture.

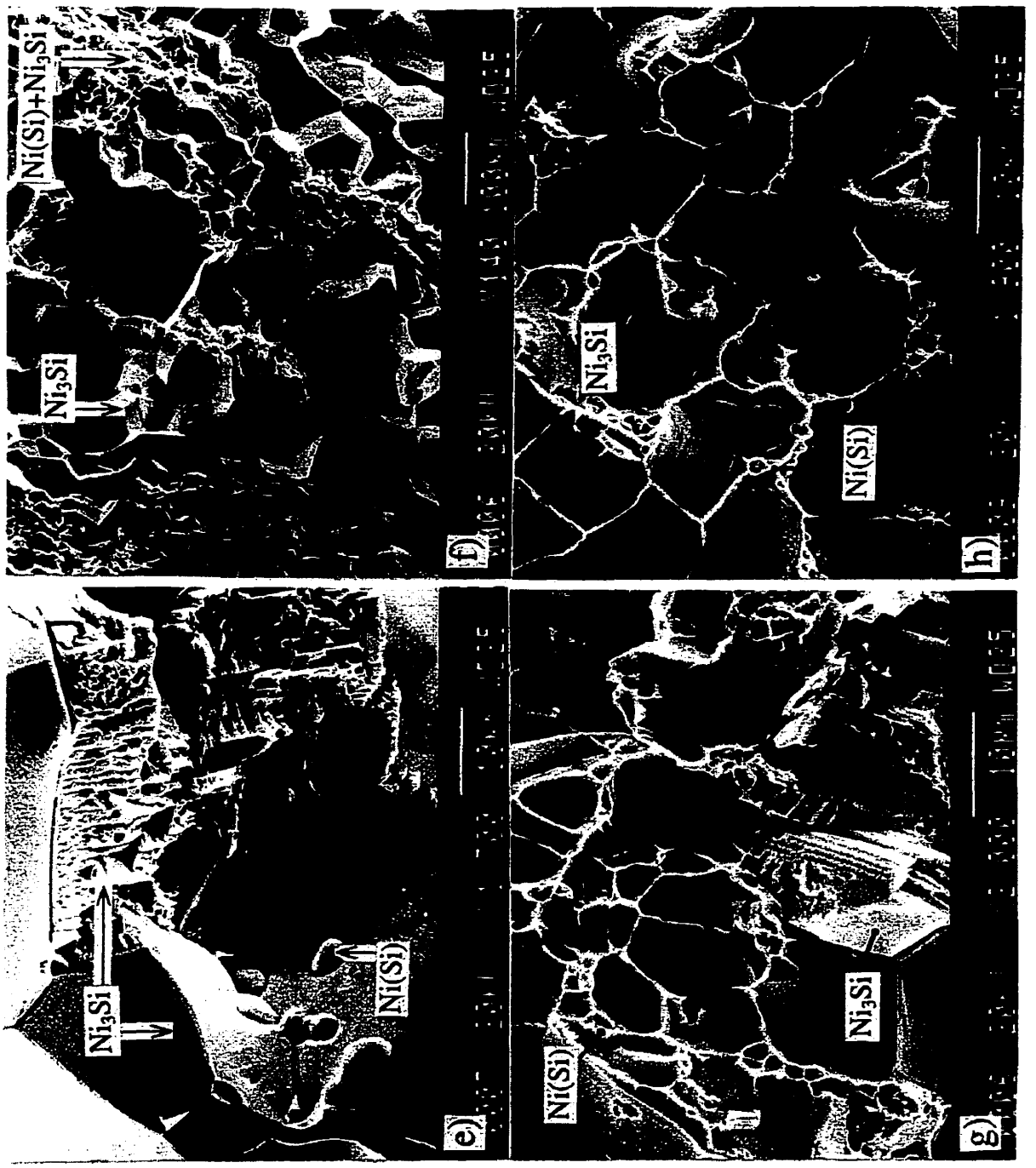

Fig. 9.34 SEM fractographs of alloy F9 showing (a) a mixture of inter- and transgranular fracture taken from F9-1st, (b) a closer view of step like transgranular fracture, (c-d) the formation of the shear steps, (e) transgranular fracture and Ni(Si) particles debonded from the other side of the fracture surface, and (f-h) the area with the fine (Ni(Si)+Ni_3Si) mixture.

One interesting observation on the fracture surface of F9 is the presence of fine precipitates on the grain boundary facet as shown in Figs. 9.35(a) and (b), which are also slightly visible in Fig. 9.34(d). The precipitates were also observed on the transgranular fracture surface as shown in Fig. 9.35(c). The precipitates are distributed a short distance away from another grain boundary similarly to the formation of precipitate free zone (PFZ) (Fig. 9.35(a) and (b)). Based on the peculiar 'glowing' contrast at the edge-on grain boundary plane in Fig. 9.35(a), the precipitates seem to exist also at this grain boundary plane. The correlation between the presence of the fine precipitates and fracture toughness or test environment will be discussed in detail in section 10.2.2.2.

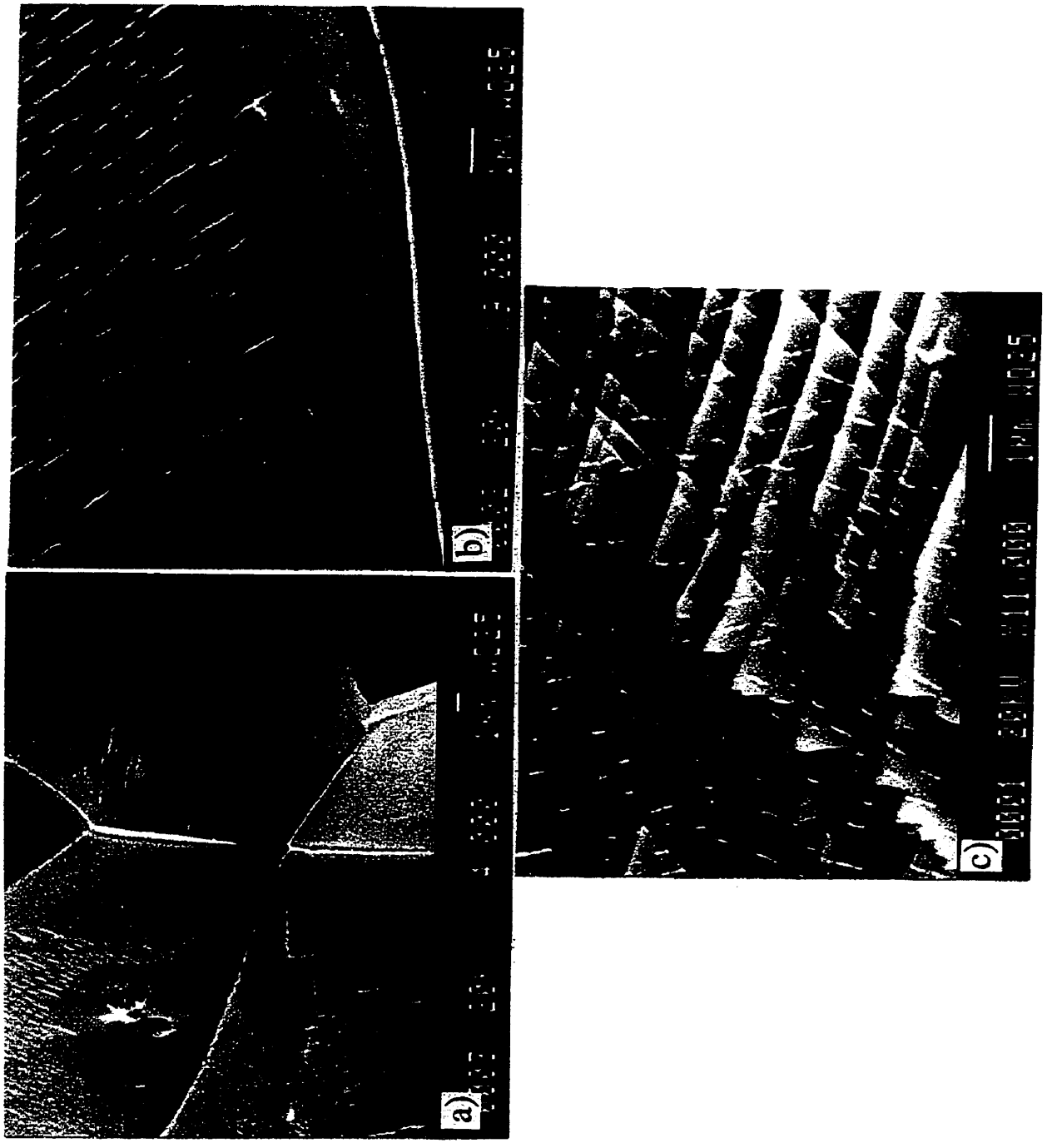

Fig. 9.35 SEM micrographs showing the precipitates observed on the fractured grain boundary facets of F9 (near-single phase Ni_3Si) taken (a) low magnification and (b) high magnification, and (c) on the transgranular fracture surface.

9.3.4.1.6 Fracture behaviour of F10-F15

The fracture behaviour of F10 is almost the same as F9 exhibiting inter- and transgranular fracture of Ni_3Si and ductile failure of Ni(Si) in the fine (Ni(Si)+Ni_3Si) mixture since the microstructure and overall composition of composites, F10 and F9 are similar except the existence of small amount of the η phase as shown in Fig. 9.21(a).

In composites F11-F13, brittle cleavage fracture was observed in the η phase and inter- or transgranular fracture was observed in the Ni_3Si phase existing as a microconstituent phases in these composites. SEM micrographs of inter- and transgranular fracture of Ni_3Si in composites F11 and 12 are shown in Fig. 9.36(a) and (b).

Fig. 9.36(c) and (d) shows the SEM fractographs of F14 and F15 containing fine eutectic mixture of ($Ni_{31}Si_{12}$+η) and (η+Ni_2Si or η+Ni_2Si+ $Ni_{31}Si_{12}$), respectively. A fine two or three phase mixture in F14 and F15 fractured in a brittle manner, exhibiting flat and smooth fracture surfaces.

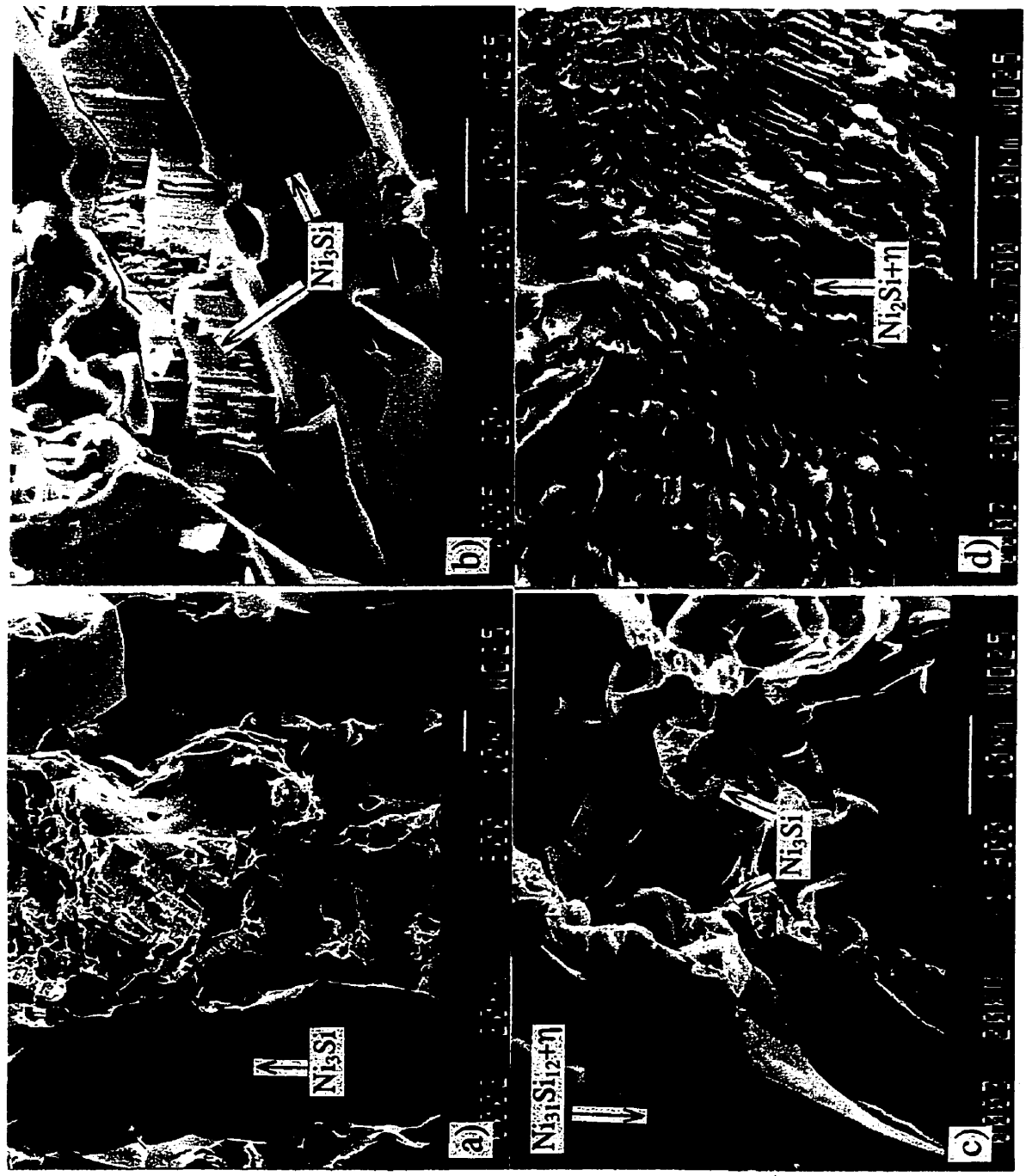

Fig. 9.36 SEM fractographs of (a) F11, (b) F12, (c) F14, and (d) F15.

9.3.4.1.7 Fracture behaviour of F16

The fracture surface of F16, a single phase Ni_2Si, shows two distinctive regions, i.e., rough and smooth (Fig. 9.37(a)). The SEM fractograph of the rough region is shown in Fig. 9.37(b). Numerous ledges and cracks that developed vertically to the fracture surface are seen. The creation of rough fracture surface consisting of ledges seems to be induced by the anisotropic fracture behaviour of Ni_2Si associated with its crystallographic structure. Therefore, the crystallographic orientation of grains with respect to the crack propagation direction seems to result in two different modes of fracture even if F16 consists of Ni_2Si only.

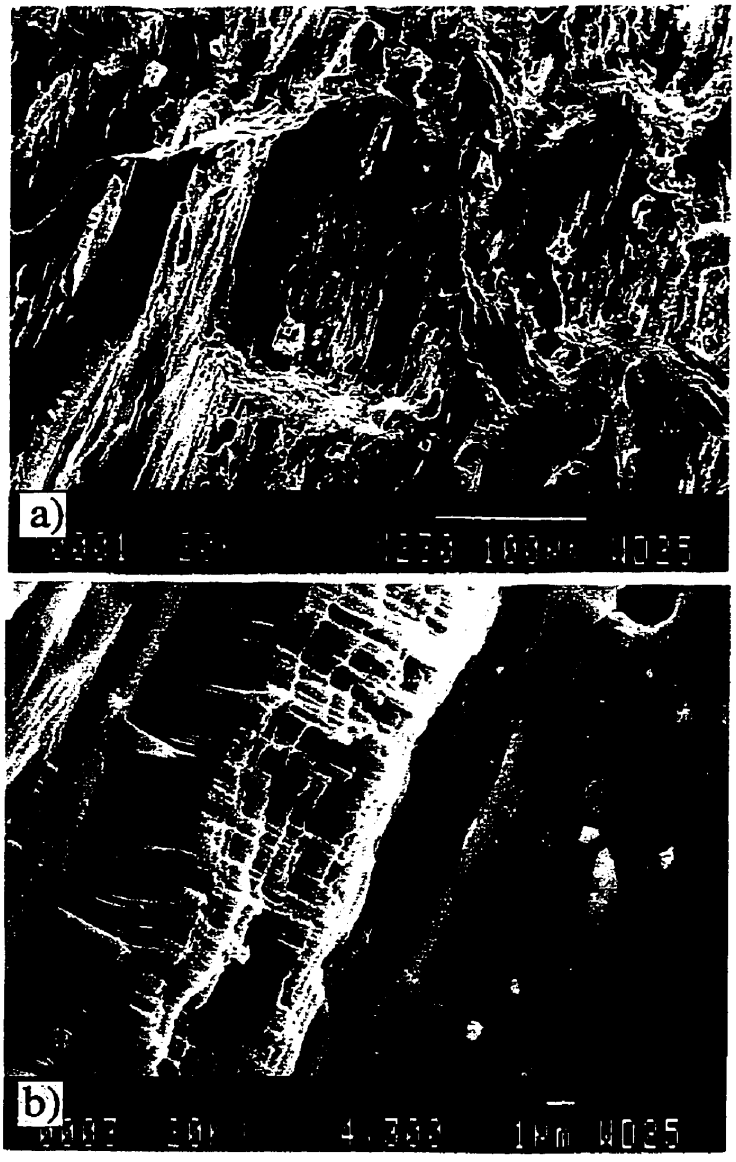

Fig. 9.37 SEM fractographs of Ni_2Si single phase alloy, F16 showing (a) the overall fracture behaviour of Ni_2Si and (b) the magnified view of the rough fracture area in (a).

9.3.4.1.8 Fracture behaviour of F17-F22

All the microconstituent phases in composites F17-F22 showed brittle transgranular fracture as evidenced from their fracture surfaces which are relatively smooth as shown in Fig. H.2(q)-(t) in Appendix H. Only the fracture surface of Ni_2Si exhibited the ledges as already shown in Fig. 9.37. A SEM fractograph of F21 exhibiting brittle cleavage fracture is shown in Fig. 9.38(a). A SEM fractograph of F22 showing brittle cleavage fracture of $MgNi_2$ and many strip-like second phase regions is seen in Fig. H.2(v) in Appendix H. A magnified view of the strip-like second phase region is shown in Fig. 9.38(b).

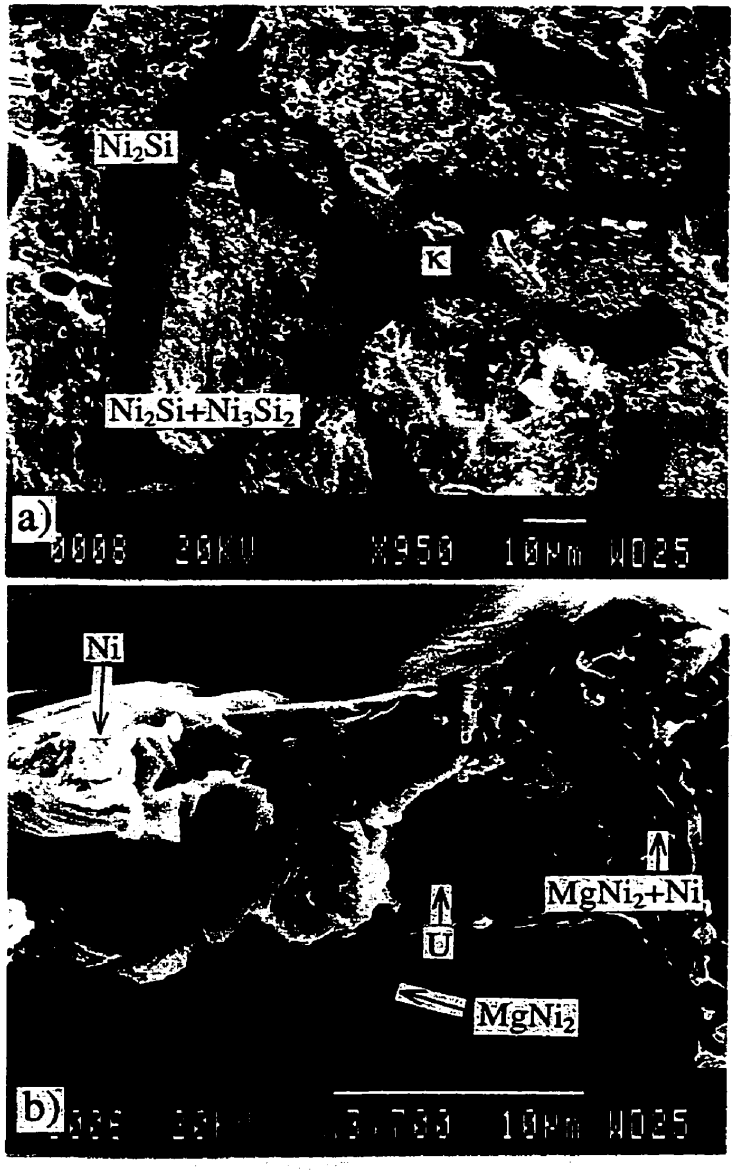

Fig. 9.38 SEM fractographs of (a) F21 showing brittle cleavage fracture and (b) F22 showing the strip-like second phase region in Fig. H.2(v) in Appendix H.

9.3.4.2 Observation of fracture surfaces of the specimens tested in vacuum and dry oxygen

Some of in-situ composites such as F6, F9, F12, F14, F16, and F21 were selected to investigate the effect of test environment on the fracture behaviour and fracture toughness of single phase alloys and composites. The fracture toughness values measured in vacuum or dry oxygen atmosphere are similar to those measured in air except possibly for F9. Similarly, the fracture surfaces of the composites tested in vacuum and dry oxygen did not show significant difference compared to those tested in air. Even if the average fracture toughness value of composite F9 tested in dry oxygen is higher than that tested in air, no recognizable difference in fracture surface between the samples tested in air and dry oxygen was observed.

9.4 Indentation fracture toughness test

9.4.1 Determination of crack systems and crack profiles

Among many of the intermetallic phases existing in the present Ni-Si-Mg ternary phase diagram (Fig. 9.1), the η and κ phases were first selected as standard samples for a systematic study to understand the microindentation fracture behaviour and determine the applicability of the indentation fracture toughness calculations in the literature.

Fig. 9.39 shows the Vickers indentations made at 2000g in the η and κ phases, before and after polishing. Surface lateral cracks are formed around the indentation made in the η phase as shown in Fig. 9.39(a) and sometimes macroscopic chipping occurs (Fig. 9.46(a)). According to Lawn et al. [75Law[4]] and Ogilvy [77Ogi] the lateral cracks are produced in brittle solids and when macroscopic chipping occurs on the surface around an indentation, material is removed by the propagation of cracks during the unloading cycle. They nucleate near the apex of the indentation and grow laterally beneath the surface on unloading of the indenter. Lawn et al. [75Law[4]] suggested that since the lateral system operates only as the indenter is withdrawn from the specimen surface, it is evident that the driving force for propagation must originate from some residual stress field associated with the irreversible deformation zone (indentation impression). Fig. 9.39(b) shows the indentation cracks in the κ phase emanating from only four corners with a small lateral crack (or collapse) along one side of the indentation. Figs. 9.39(c) and (d) show Vickers indentations made at 2000g in the η and κ phases, after polishing. The same indentations made at 2000g before polishing are shown in Fig. 9.39(a) and (b) for the η and κ phases, respectively. The corner cracks are clearly detached from the inverted pyramids suggesting the presence of a Palmqvist crack system for both phases.

As already mentioned in section 7.1, crack systems also can be judged by the relation between the crack length and indentation load, i.e., $W=P/4l$ for the Palmqvist crack system as in Eq.(7.1) and $c=KP^{2/3}$ for the half-penny crack system as in Eq.(7.2). Therefore, the Palmqvist cracks (l) follow a linear dependence on indentation load, while the halfpenny cracks follow a 2/3 power dependence on indentation load.

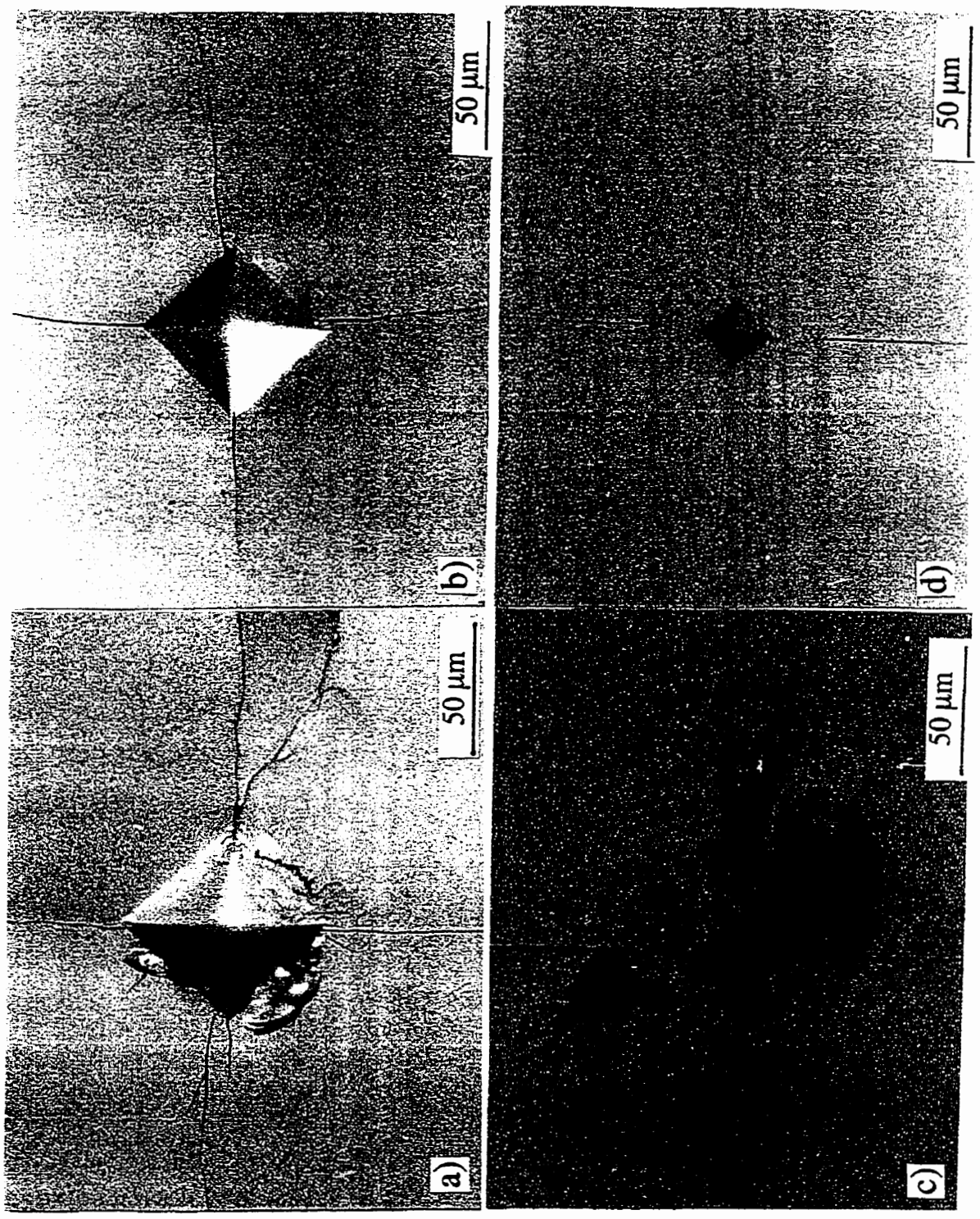

Fig. 9.39 Indentations made at 2000g load (a) in the η phase and (b) in the κ phase before polishing. The same indentations after polishing 7.2µm and 5.9µm from the original indentation surface (c) in the η and (d) in the κ phases, showing the evidence of the Palmqvist crack system.

Table 9.14 shows the parameters defined in Fig. 7.1 and measured in the η and κ phases with various indentation loads for indentation fracture toughness calculations.

Table 9.14 Indentation crack parameters a, *l*, and c (in Fig. 7.1) as a function of the applied load, P for the η and κ phases.

Load, P N (g)	η phase			κ phase		
	a (μm)	*l* (μm)	c=a+*l* (μm)	a (μm)	*l* (μm)	c=a+*l* (μm)
2.942(300)	13.16±0.2	25.56±1.6	38.72±1.5	12.54±0.1	20.73±1.2	33.27±1.2
4.904(500)	17.20±0.1	40.34±4.0	57.54±4.0	16.27±0.1	30.03±2.1	46.30±2.2
9.807(1000)	25.63±0.5	61.93±3.5	87.56±3.3	23.39±0.1	52.30±2.3	75.69±2.2
19.614(2000)	36.87±0.2	115.73±8.2	152.59±8.2	33.69±0.2	88.82±5.5	122.51±5.6

The crack length (*l*) as a function of load (P) is plotted for the η and κ phases in Fig. 9.40 using data from Table 9.14. The relation between the crack length (*l*) and indentation load (P) perfectly satisfies the condition for the Palmqvist crack system, supporting the microstructural observation of detached corner cracks after polishing shown in Fig. 9.39.

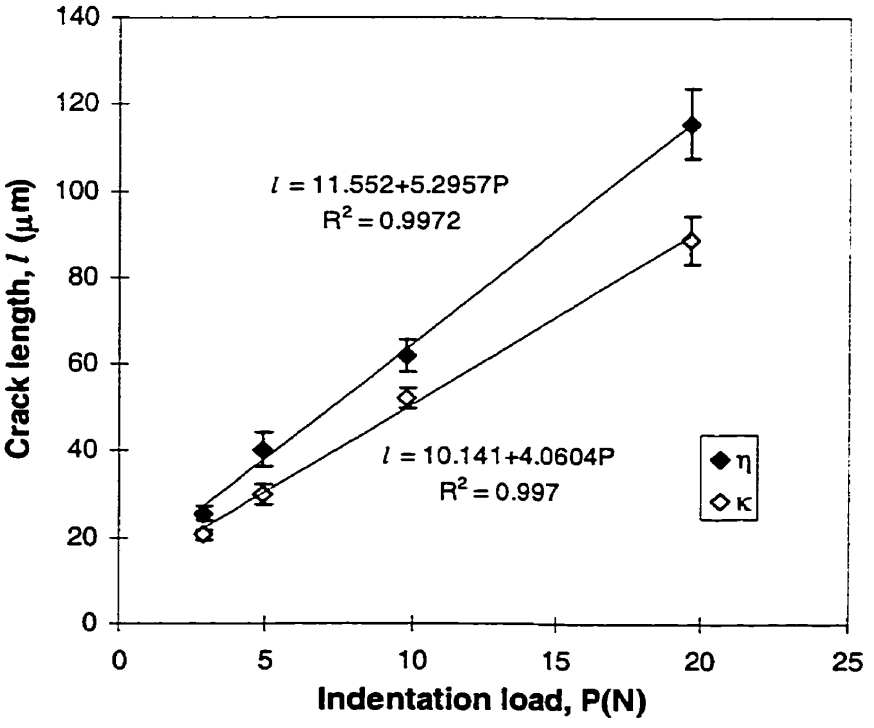

Fig. 9.40 Linear dependence of crack length (*l*) on indentation load (P) for the η and κ phases.

In Fig. 9.41, the crack length, c, as a function of load ($P^{2/3}$) is also plotted to see how the plot fits to satisfy the medium crack system. This graph also indicates that the relation between the crack length, c, and indentation load, P, satisfies the condition for the median crack system. The ambiguity in determining the crack mode by the relationship between the crack length and the load was also argued by Lankford [82Lan] with the analysis of Niihara [83Nii] and Niihara et al. [82Nii].

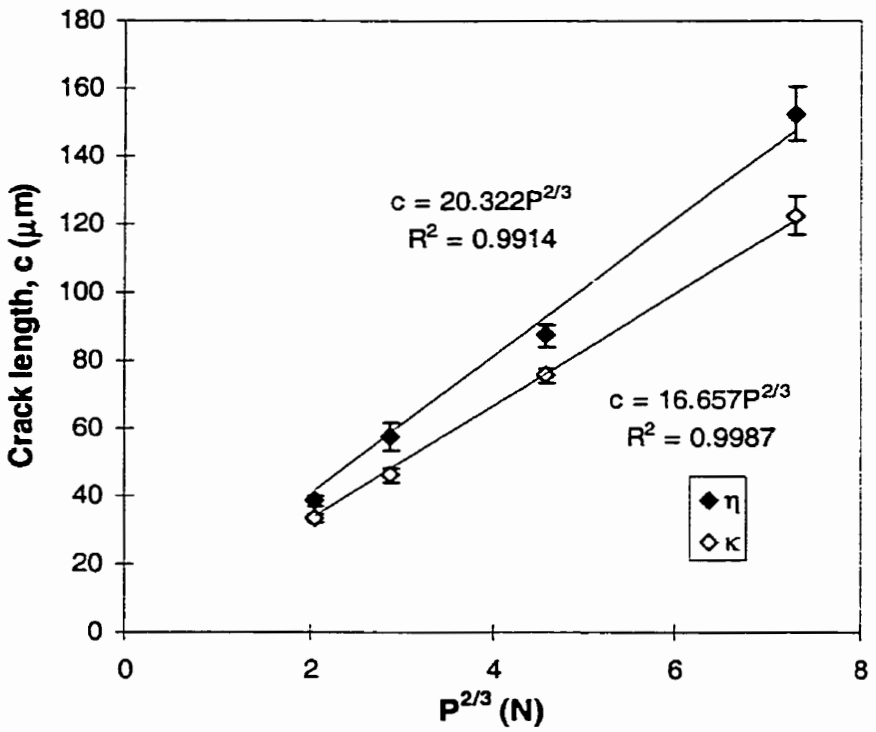

Fig. 9.41 The relationship between indentation crack length, c, and load, P, following a 2/3 power dependence of crack length on indentation load satisfying the half-penny shaped crack system for both the η and κ

As suggested by Shetty et al. [85She[1], 85She[2]] to clearly identify the crack system, the relationship between l vs. P was converted to that between c vs. P for the Palmqvist crack system as shown in Eq. (7.3). Therefore, the relationship between indentation load and crack length for both the Palmqvist and halfpenny cracks can be expressed with respect to c vs. P as shown in Fig. 9.42. Fig. 9.42 shows the experimentally obtained data and the perfect fits

satisfying Eq. (7.2) and Eq. (7.3) for the half-penny shaped and the Palmqvist crack systems for both the η and κ phases. The Palmqvist crack model fits slightly better to the experimental points for the η phase and the median crack model fits slightly better for the κ phase. In deriving the best fit model of Eq. (7.3), *l* and a were obtained from the least square fits for the *l*-P data (Fig. 9.40) and the hardness fit from the relationship between indentation half diagonal, a and load, P in Fig. 9.43, respectively.

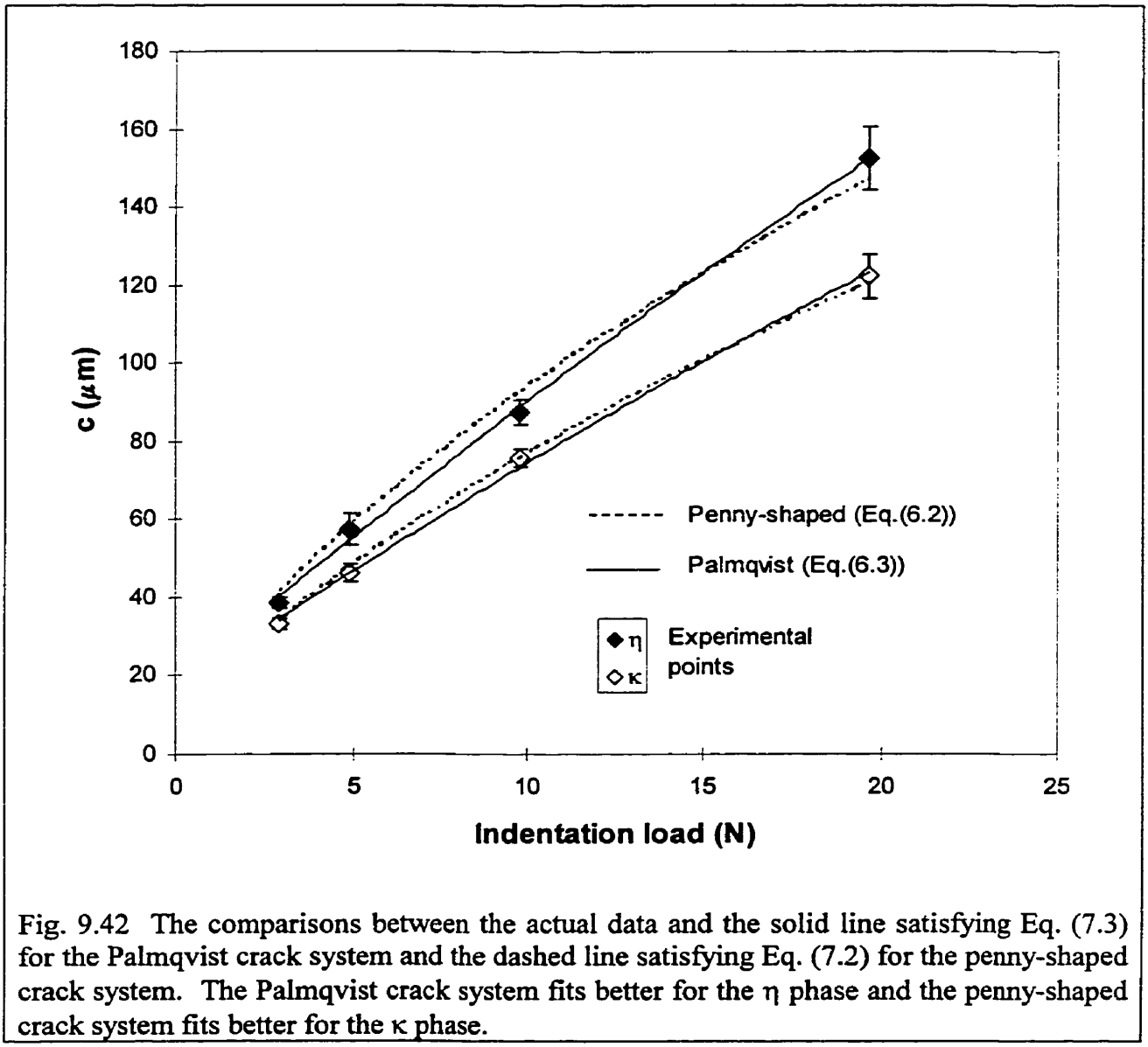

Fig. 9.42 The comparisons between the actual data and the solid line satisfying Eq. (7.3) for the Palmqvist crack system and the dashed line satisfying Eq. (7.2) for the penny-shaped crack system. The Palmqvist crack system fits better for the η phase and the penny-shaped crack system fits better for the κ phase.

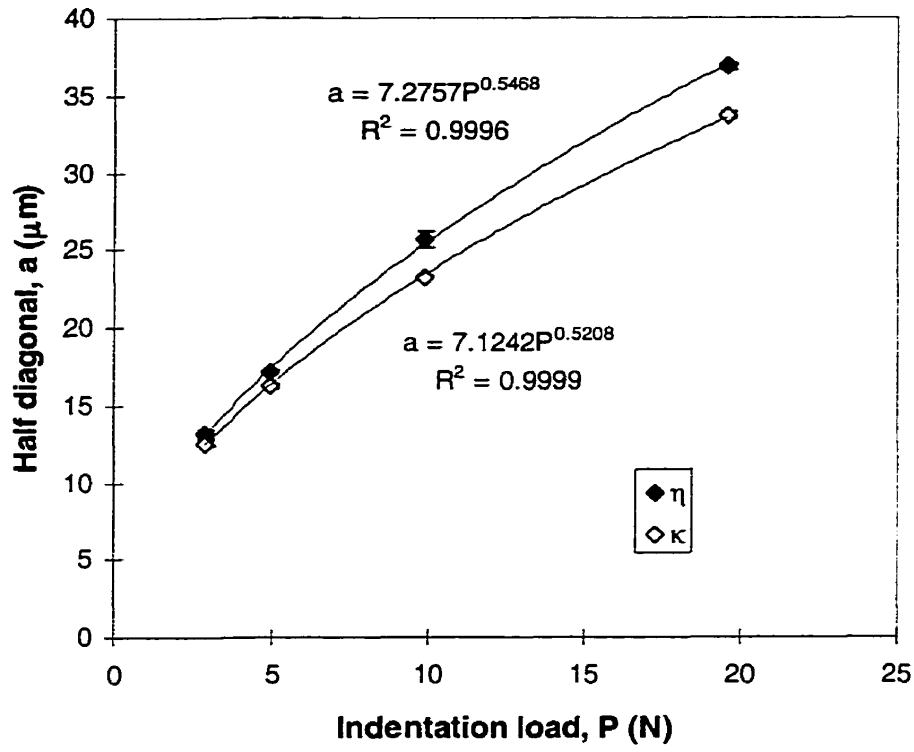

Fig. 9.43 The hardness fit, showing the relationship between indentation half diagonal and load to draw the best fit satisfying Eq. (7.3) for the Palmqvist crack system for both the η and κ phases.

However, there still is an ambiguity in differentiating between the two models with such a little difference between the best fits for the two crack systems and the actual data. Shetty et al. obtained a satisfactorily distinguished crack systems for WC-Co cermets [85She[1]] but found a difficulty in discrimination between the half-penny crack system and the Palmqvist crack system for glass ceramic [85She[2]].

Therefore, serial sectioning method as already mentioned in section 7.1 was applied to determine the crack system through the crack profiles beneath the indentations for the η and κ phases.

Figs. 9.44 and 9.45 show the crack profiles of the η and the κ phases, respectively, at 200g, 500g, and 2000g loads. In the η phases, all the crack profiles show the pseudo halfpenny shaped crack mode (The halfpenny cracks containing a core zone will be called "pseudo halfpenny" rather than halfpenny cracks hereafter in the present work.) between 200g and

2000g with a core zone underneath the indent. In the κ phase, at 200g and 500g loads, the crack modes closely resemble the "kidney shaped" crack types described by Kaliszewski et al. [94Kal] and Pajares [95Paj].

However, it also shows the pseudo half-penny shaped crack system with a core zone at 2000g. To draw the crack profiles, the shape of core region was assumed to be symmetrical and the angle between the two opposite cracks is assumed to be 180°.

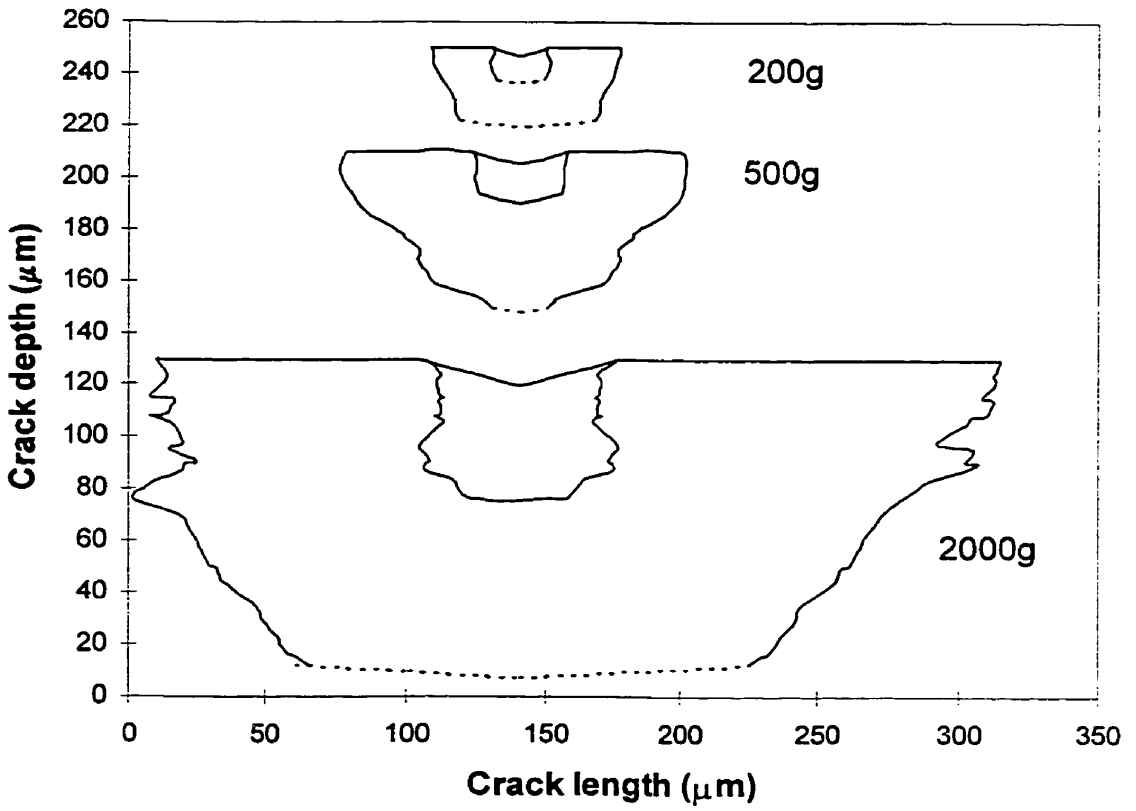

Fig. 9.44 Indentation crack profiles for the η phase at loads of 200g, 500g, and 2000g from the top, showing the pseudo halfpenny shaped crack system with a core. The crack profile plane is along the indent diagonal.

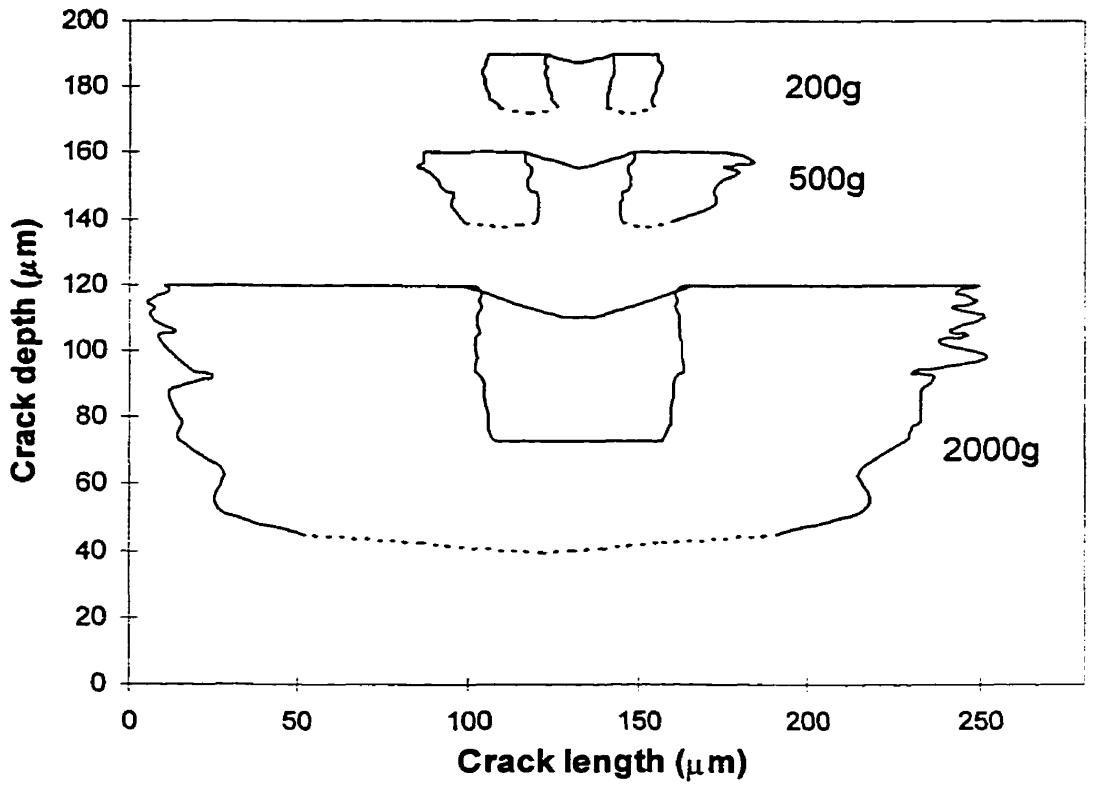

Fig. 9.45 Indentation crack profiles for the κ phase at loads of 200g, 500g, and 2000g from the top, showing kidney-shaped crack system at 200g and 500g, and the pseudo halfpenny shaped crack system at 2000g. The crack profile plane is along the indent diagonal.

Fig. 9.46 shows the crack configurations obtained by serial sectioning of the indentation made at 2000g load in the η phase from the surface to the very deep end at various depths. No cracks are visible in the upper part of the core zone (Fig. 9.46 (b)). In Fig. 9.46(c) at 40 μm depth, besides the main corner cracks, there are also many sub-surface cracks developed in or around the core zone. The corner cracks are likely to connect each other but are still separated from each other. Fig. 9.46(d) at the depth of 54μm shows that the four corner cracks start connecting each other. In Fig. 9.46(e) (60 μm depth) the four corner cracks are completely connected to each other and the crack configuration in and around core zone became simpler. At the end of the crack (Fig. 9.46(f)) mainly four corner cracks exist. As shown in Fig. 9.46 no cracks exist in the upper part of the core zone (Fig. 9.46(b)), but in the lower part of the core zone close to the end of the core, short and thin cracks are observed (Fig. 9.46(c)). Many sub-surface cracks are also developed around the core zone but these

cracks seem to be discrete in length and depth compared to the main corner cracks which extend from the surface to the end of the crack in depth.

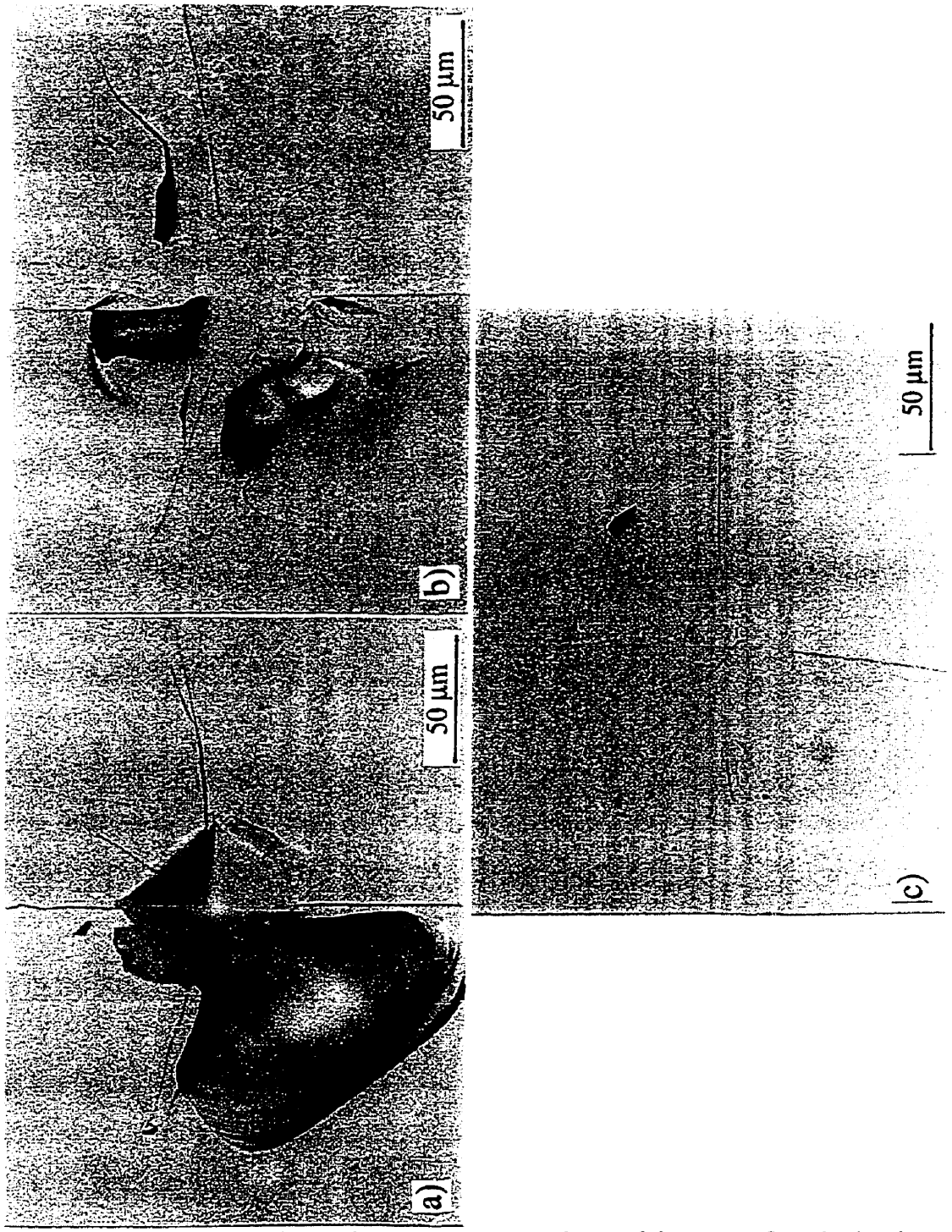

Fig. 9.46 Optical micrographs and electronically enhanced images of optical micrographs of the crack configurations obtained by serial sectioning of (a) an indentation made at 2000g in the η phase on the surface at various depths, (b) 15µm, (c) 40µm, (d) 54µm, (e) 60µm, and (f) 79µm from the original surface.

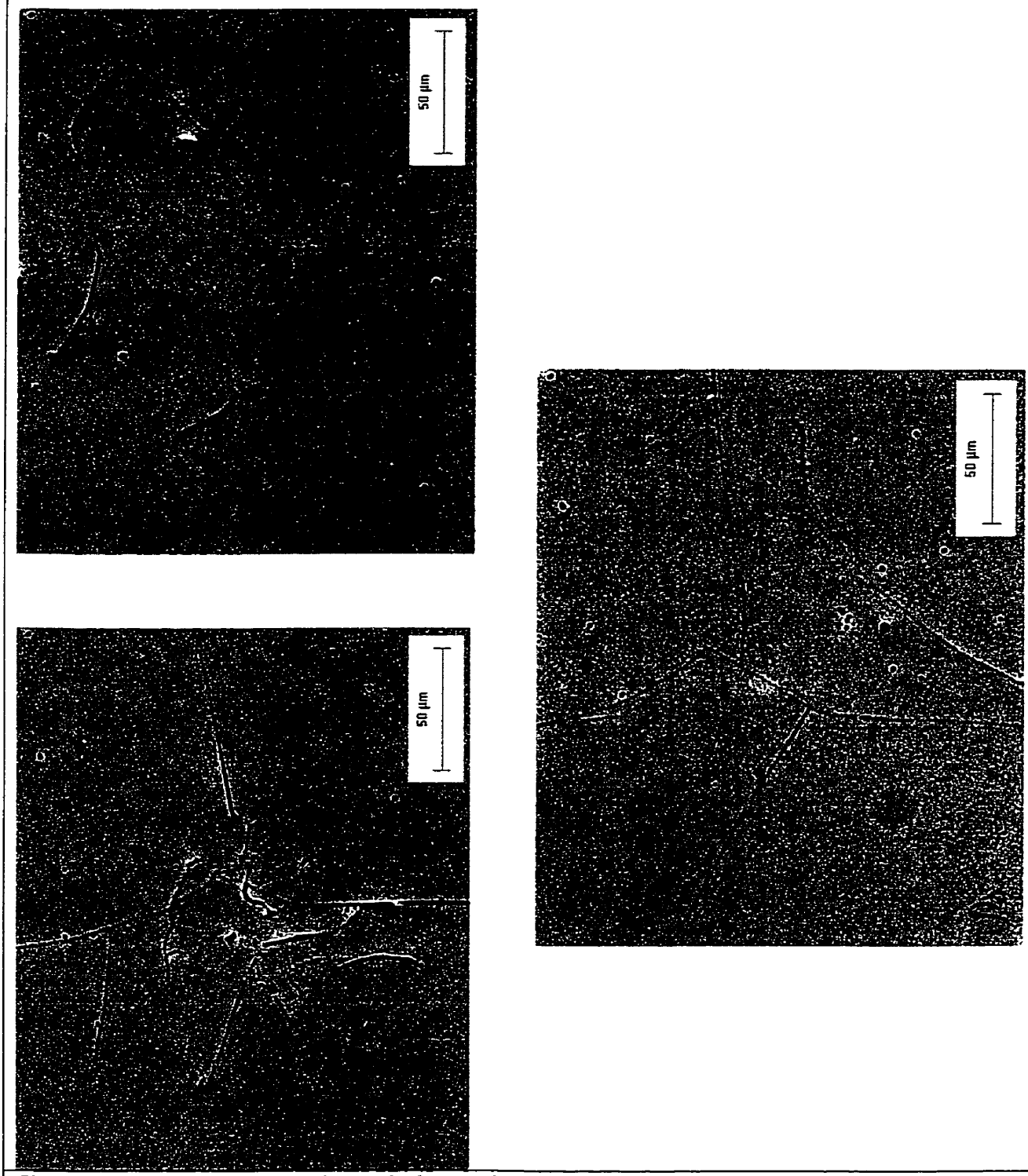

Fig. 9.46 Optical micrographs and electronically enhanced images of optical micrographs of the crack configurations obtained by serial sectioning of (a) an indentation made at 2000g in the η phase on the surface at various depths, (b) 15µm, (c) 40µm, (d) 54µm, (e) 60µm, and (f) 79µm from the original surface.

Fig. 9.47 shows the end of the cracks at various depths made at 200g and 500g in the η phase to show the connection of four corner cracks. Some of the corner cracks changed their shape from being straight to being curved and the position of the two opposite corner cracks also changed. Therefore, they do not connect each other directly at the center. It is possible that at this depth cracking occurred along preferred crystallographic planes but this still needs to be verified.

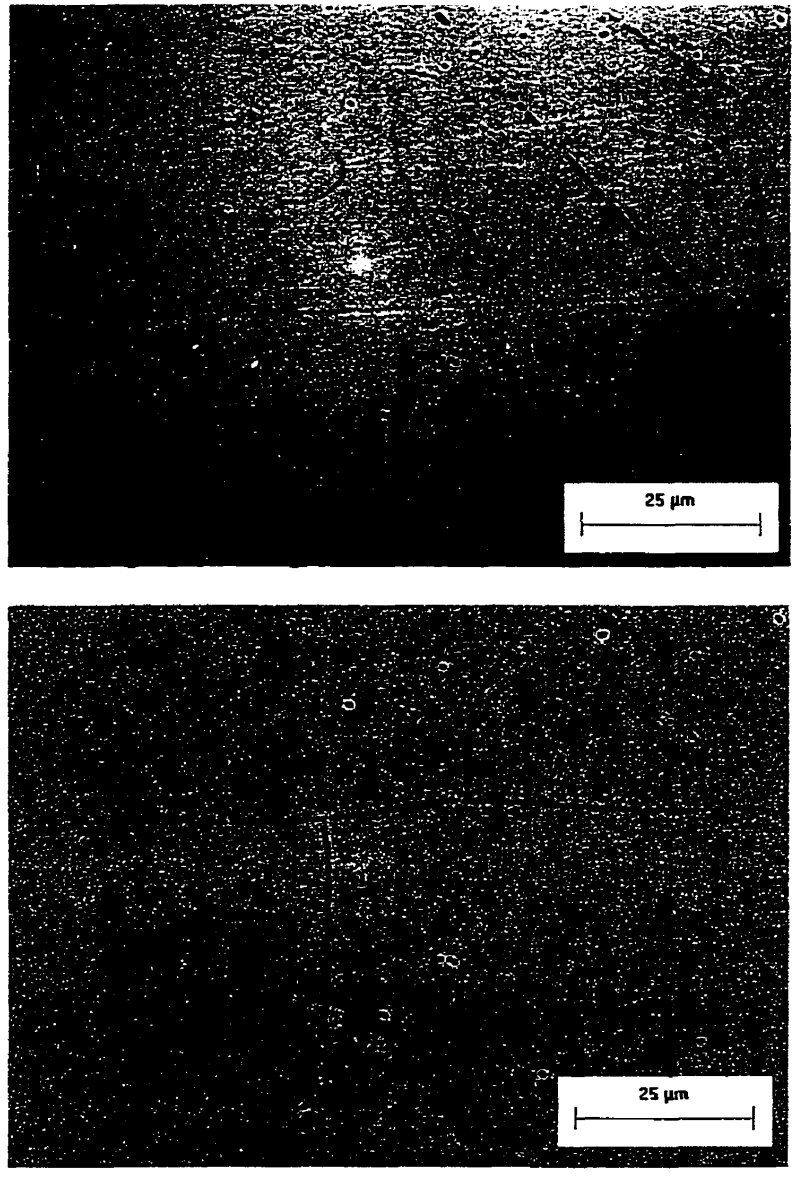

Fig. 9.47 Electronically enhanced images of optical micrographs showing the examples of the connected corner cracks at 25 and 38 μm depth from the primary indentation made at (a) 200g and (b) 500g in the η phase, respectively.

The secondary indentation were also made at 200g in the core of the primary indentation made at 2000g as shown in Fig. 9.48 for the η phase and Fig. 9.49 for the κ phase to see the existence of compressive residual stresses in the core zone just beneath the indentations. The secondary indent in the core region of η (Fig. 9.48 (b)) as compared to that made on the stress free surface (Fig. 9.48(a)) did not develop four corner cracks.

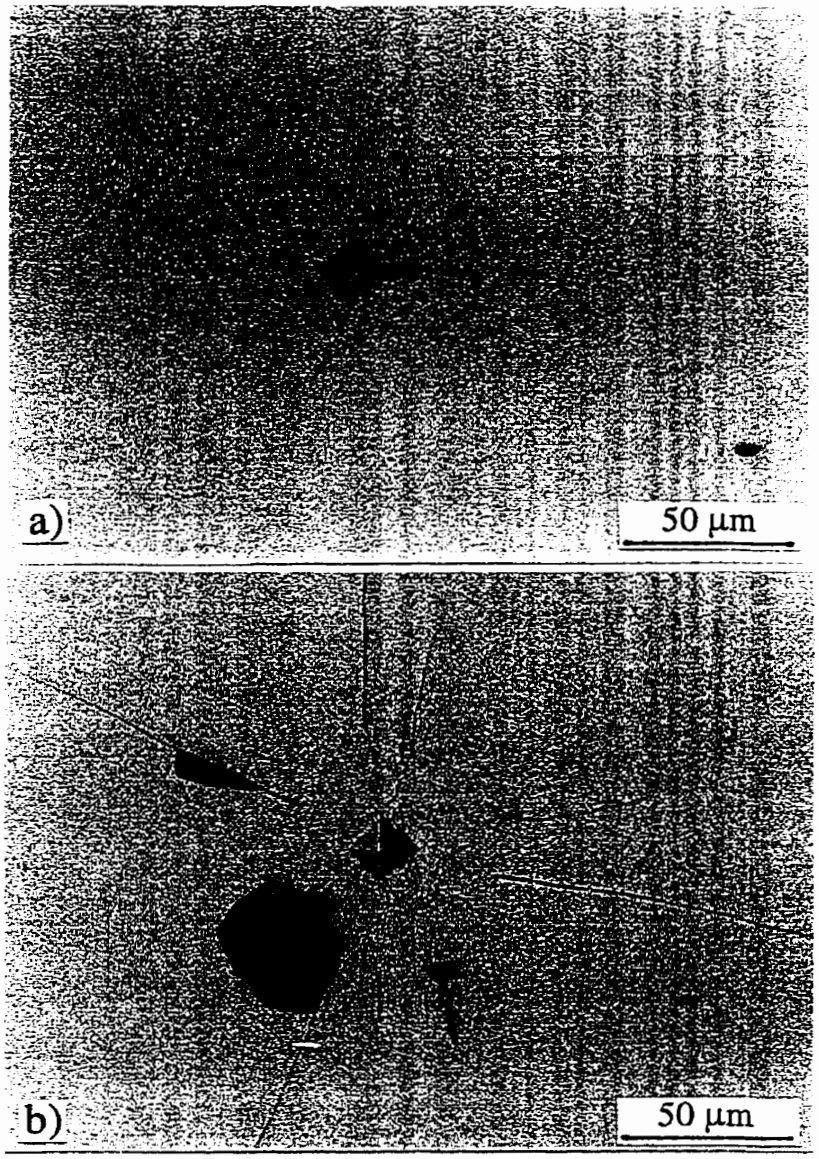

Fig. 9.48 Indentations made at 200g (a) on the stress-free surface and (b) in the core region of the primary indentation made at 2000g in the η phase.

Fig. 9.49 shows the indentations made on the stress free surface and the secondary indents made at various depths in the κ phase. None of the secondary indents developed corner cracks as opposed to the indent made at the stress free surface which developed very clear corner cracks (Fig. 9.49 (a)). The indent made at 12 μm depth (Fig. 9.49 (b)) developed only surface lateral cracks at the edge of the indent and the indent made at 38 μm depth (Fig. 9.49 (d)) shows some short cracks around the indent without any surface lateral cracks. One of these is connected to the pre-existing sub-surface cracks. The indent made at 24 μm depth (Fig. 9.49 (c)) shows the intermediate state between the indent made at 12 μm depth and 38 mμ depth, showing both the surface lateral crack at the edge of and short cracks around it. Vickers hardness values (VHN) measured on the stress free surface and in the core region are compared in Table 9.15. The hardness values just beneath the indentation are much higher than those of the stress free surface for both the η and the κ phases. In the κ phase, VHN measured at 24 μm depth is still higher than that measured on the stress free surface, but lower than that measured at 12 μm depth. However, VHN measured at 38 μm depth from the original surface is lower than that measured on the stress free surface. This depth at 2000g indent is, as shown in the indentation crack profile for the κ phase made at 2000g load in Fig. 9.45, still in the core region but very close to the boundary between the core region and the half-penny cracked region.

Table 9.15 The comparison of the Vickers hardness measured at 200g in the stress free surface and in the core zone.

Phases	Vickers Hardness (VHN) (kg/mm^2)			
η	Stress free surface		Just beneath indentation*	
	841±18		906±12	
κ	Stress free surface	12 μm depth	24 μm depth	38 μm depth
	902±13	1055±44	977±31	817±34

* ; The exact depth from the original surface was not measured. However since the secondary indentations were made just after the primary indentations were removed the depth can be approximated to be about in between 12 μm and 20 μm according to the result of the serial sectioning method.

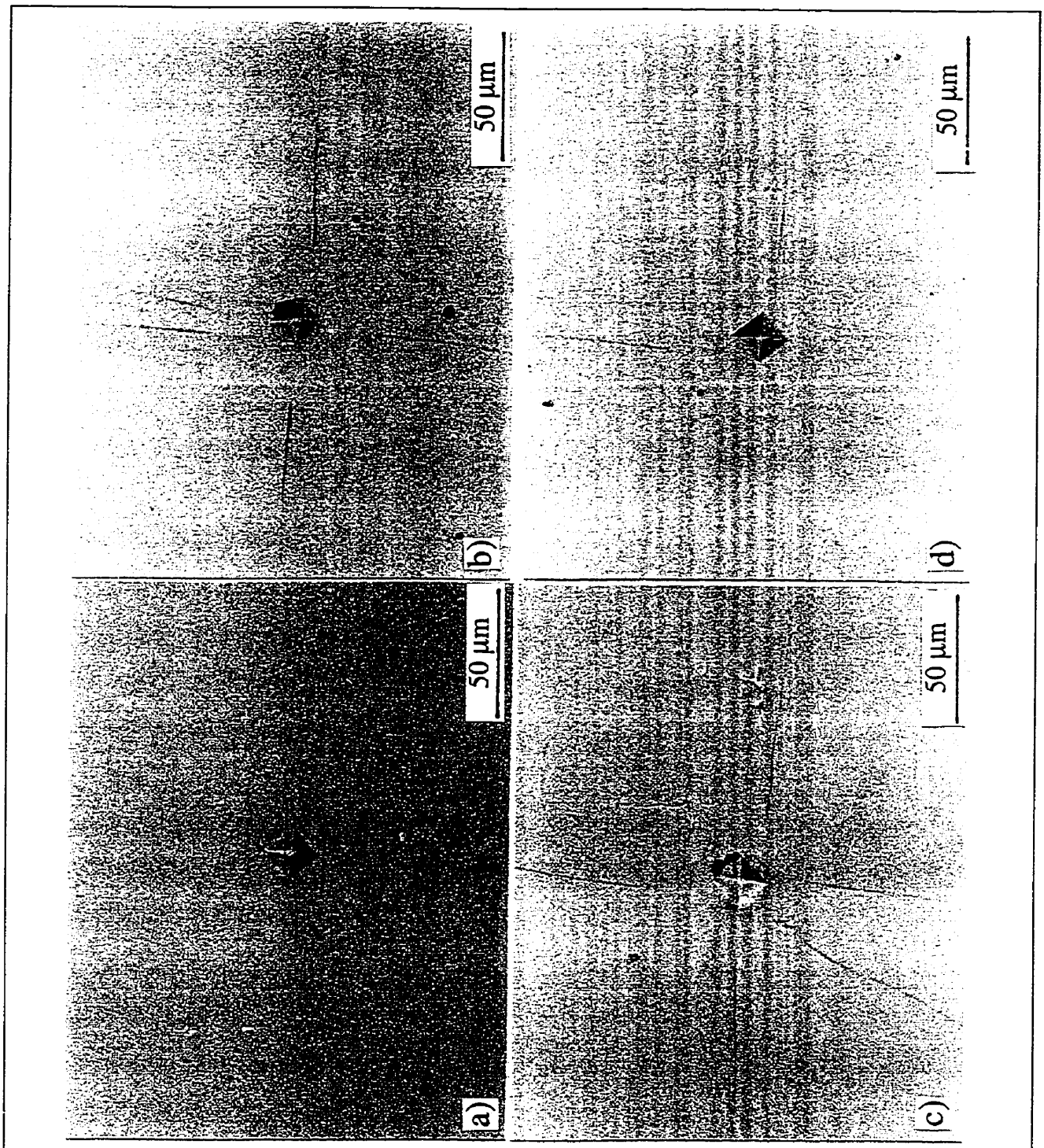

Fig. 9.49 Indentations made in the κ phase at 200g (a) on the stress-free surface and in the core zone of the primary indentation made at 2000g at various depths of (b) 12µm, (c) 24µm, and (d) 38µm from the primary indentation surface.

It is suggested [75Law[2], 89Pon[2], 79Mar] that the median crack depth, D can be substituted by the surface crack length, c, implying that D≈c as mentioned in sections 7.2.2.1 and 7.2.2.2. However, such a substitution is not applicable to the intermetallics used in the present work according to the results of the serial sectioning method. Fig. 9.50 shows the c/D ratio versus load. At low loads, the c/D ratio is close to unity, but with increasing load, the c/D ratio also increases. Comparison of the c/D ratio between the η and κ phases at 2000g load shows an interesting feature. Even if the c values for κ are lower than those for η at 2000g (Table 9.14), implying that κ has higher K_{IC} than η, the c/D ratio at 2000g load is higher for κ than that for η (Fig. 9.50). This implies that the difference of D between κ and η is larger than that of c between the two phases. This means that the higher the toughness of intermetallic phase (e.g. κ versus η) the smaller the crack length and even smaller the crack depth, i.e. higher c/D ratio.

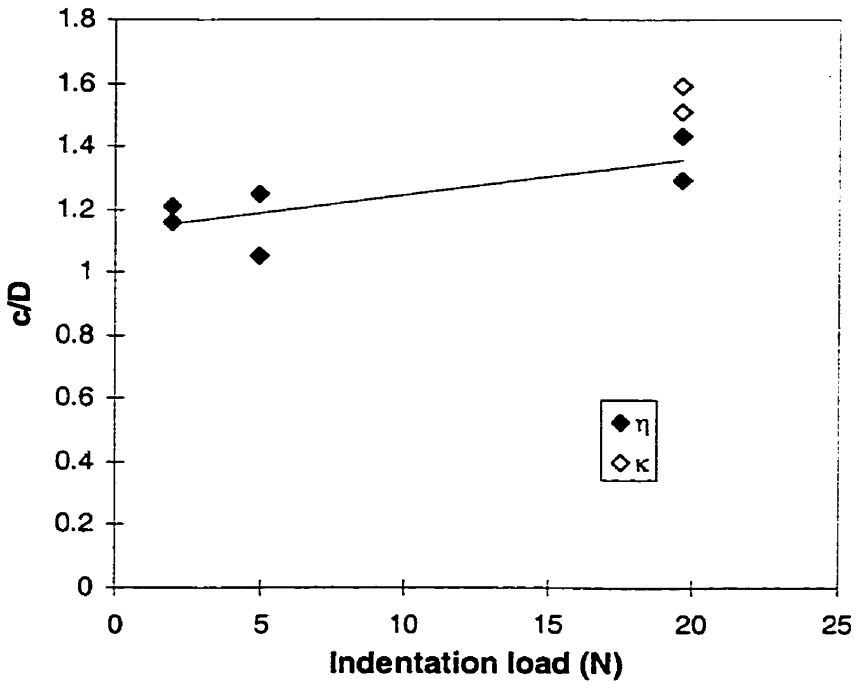

Fig. 9.50 The relationship between the c/D ratio and indentation load.

9.4.2 Indentation fracture toughness calculations

9.4.2.1 Indentation fracture toughness of the η and κ phases

Even though the crack systems for the η and κ phases are determined by a serial sectioning method to be either a type of the pseudo half-penny shaped (with a compressive core zone) or the kidney shaped crack system which closely resembles the Palmqvist crack system, fracture toughness calculations for the η and κ phases will be carried out for both the half-penny shaped and Palmqvist crack systems. These calculations are expected to show whether there is actual difference between the half-penny shaped and Palmqvist crack systems and if it is necessary to distinguish the two crack systems from one another for fracture toughness calculations. In fact, Kaliszewski et al. [94Kal] found that crack length data for a half-penny shaped crack with a core zone (called "pseudo half-penny crack" in this work) follow the half-penny shaped crack relation ($c \sim P^{2/3}$)

According to the results of the serial sectioning method for the determination of crack profile underneath the indentation surface as shown in Fig. 9.44 and 9.45 for the η and κ phases, respectively in this work, the approximation made in Eq. (7.9) for the Lawn and Swain model and Eq. (7.13) for the Lawn and Fuller model i.e., $D \approx c$ does not agree with our results (Fig. 9.50). Therefore, fracture toughness calculations for these models are carried out with only Eq. (7.8) and Eq. (7.12) even if D values are only available for indentations made at 200g, 500g and 2000g for the η phase and 2000g for the κ phase. The indentation parameters, such as 'a' and 'D' values necessary for the indentation fracture toughness calculations using the Lawn and Swain model, and the Lawn and Fuller model are measured from the indentations made for the determination of crack profile underneath the indentation surface as shown in Fig. 9.44 and 9.45 for the η and κ phases, respectively and tabulated in Table 9.16. Note that an indentation provides a set of data having two 'a' and 'D' values each since they could be obtained from two indentation diagonals in an indentation separately.

Table 9.16 Indentation parameters, 'a' and 'D' obtained from the indentations for serial sectioning and used for the calculations for Lawn and Swain's model (Eq. 7.9) and Lawn and Fuller's model (Eq. 7.13). 'c' values are also included for comparison with 'D'.

Load,P	η phase				κ phase			
N (g)	a (μm)	D (μm)	c (μm)	c/D	a (μm)	D (μm)	c=a+*l* (μm)	c/D
1.961	10.35	28	34.03	1.21	-	-	-	-
(200)	10.35	28	32.10	1.15				
4.904	17.49	58	60.62	1.05	-	-	-	-
(500)	16.54	42	52.62	1.25				
19.614	35.81	118	151.10	1.28	33.37	75	113.79	1.52
(2000)	35.77	120	171.17	1.43	33.34	75	119.60	1.59

The critical loads to either propagate a fortuitous flaw as in the Lawn and Evans' model (Eq. 7.18) or generate cracks by dislocation process as in Hagan's model (Eq. 7.19) are 0.147N (15g) for the η phase and in between 0.4903N (50g) and 0.987N (100g) for the κ phase. The κ phase did not initiate corner cracks at 50g but did at 100g, so the critical load for κ is in this range. The 'a' value in $H=P/2a^2$ for the κ phase at 100g was measured from the actual indentations made at 100g load. However, the 'a' values at 15 g for the η and 50g for the κ phase were calculated from the relationship between indentation half diagonal and load shown in Fig. 9.43 since the size of the indentations are too small to measure accurately.

The K_{IC} values calculated from Eq. (7.7) by Shetty et al. [85She[1]] increase with increasing indentation load (Table 9.17). Therefore, the Shetty et al. model [85She[1]] was modified by the present author [98Son[2]] to give load-independent K_{IC} values as also shown in Table 9.17. The derivation of the modified Shetty et al. model will be in the following section 9.4.2.2.

The results of K_{IC} calculations for the η and κ phases using all the indentation fracture toughness equation models described in section 7.2 are listed in Table 9.17. Indentation fracture toughness values (customarily designated K_{IC}) and their standard deviations were calculated from the individual values of indentation crack parameters, a, *l*, and c obtained from each indentation rather than from the average crack geometry parameters in Table 9.14.

As shown in Table 9.17, the K_{IC} values calculated for the η and κ phases in the present work are quite diverse depending on the models used for calculations, regardless of the crack systems. Lawn and Swain model [75Law[3]] yields unreasonably low values of indentation fracture toughness. On the other extreme, Hagan's model [79Hag] gives the highest values

(rather overestimated). The modified Shetty et al. model [75She[1]] as well as Evans and Charles [76Eva] and Lawn and Evans [77Law] models yield the most reasonable values of the indentation fracture toughness being on the order of 1.3-1.8 MPa·$m^{1/2}$ for the η compared to the fracture toughness values of the η obtained by CNB test of 1.7 MPa.$m^{1/2}$.

Table 9.17 Indentation fracture toughness values for the η and κ phases calculated from various equations.

Crack System	Equation model	Indentation load, N (g)	K_{IC} (MPa.$m^{1/2}$)	
			η phase	κ phase
Palm-qvist crack System	Shetty et al. [85She[1]], Eq. (7.7)	2.942 (300)	1.41±0.03	1.65±0.05
		4.904 (500)	1.44±0.08	1.76±0.06
		9.807 (1000)	1.55±0.04	1.85±0.04
		19.614 (2000)	1.58±0.06	1.97±0.07
	Modified Shetty et al. [98Son[2]], Eq. (9.7)	2.942 (300)	1.62±0.05	2.09±0.06
		4.904 (500)	1.51±0.08	2.03±0.07
		9.807 (1000)	1.59±0.04	1.98±0.04
		19.614 (2000)	1.57±0.06	2.04±0.06
		All loads, (average)	1.56±0.07	2.04±0.07
Half-Penny Shaped Crack System	Lawn and Swain [75Law[3]], Eq. (7.8)	1.961 (200)	0.36, 0.36	-
		4.904 (500)	0.37, 0.46	-
		19.614 (2000)	0.51, 0.51	0.69, 0.69
	Lawn and Fuller [75Law[2]], Eq. (7.12)	1.961 (200)	0.96, 0.96	-
		4.904 (500)	0.81, 1.31	-
		19.614 (2000)	1.11, 1.08	2.19
	Evans and Charles [76Eva], Eq. (7.16)	2.942 (300)	1.42±0.09	1.78±0.10
		4.904 (500)	1.30±0.14	1.81±0.13
		9.807 (1000)	1.39±0.08	1.73±0.08
		19.614 (2000)	1.21±0.10	1.68±0.12
		All loads, (average)	1.33±0.13	1.76±0.12
	Lawn and Evans [77Law], Eq. (7.18)	With Pc=0.147 (15) For η	1.76	2.20-2.54
	Hagan [79Hag], Eq. (7.19)	With Pc=0.4903-0.987 (50-100) for κ	3.93	4.91-5.67

9.4.2.2 Modification of the model by Shetty et al.

As already mentioned in the previous section, K_{IC} values calculated from Eq. (7.7) by Shetty et al. increase with increasing indentation load (Table 9.17). Quite opposite variation of K_{IC} values, i.e. decreasing with increasing indentation load, was found in the literature for Mg_2Si [95Bys] and $NbAl_3$ [93Cho]. There was no explanation given as to the origin of such a behaviour. However, in our case, the positive dependence of the indentation load on K_{IC} arises from the two load-dependent variables, H_V and W, in Eq. (7.7). Vickers hardness, H_V, normally decreases with increasing indentation load because of the indentation size effect (ISE) [93Li[2]] which will be discussed in more detail below. In the present work, H_V also decreases with increasing indentation load (the hardness values depending on indentation loads are not given in the present work, but they can be easily calculated with the data of the indentation half-diagonal, a, given in Table 9.14, giving rise to a decrease in K_{IC} values with increasing indentation load according to Eq. (7.7)). However, in this work, the other variable, W, increases K_{IC} with increasing indentation load, as opposed to the effect of H_V on K_{IC} and in our case, the role of W is more predominant than the role of H_V for the K_{IC} behaviour, inducing the positive dependence of the indentation load on K_{IC}.

They can be modified as to obtain more consistent K_{IC} values independent of indentation load. As seen in Fig. 9.40 the *l* versus P relation extrapolated from high loads does not pass through the origin. At l=0 both lines exhibit negative intercepts with load axis, P_o= -2.18139N for the η and P_o= -2.49753N for the κ phases. Such an observation was also reported elsewhere [85She[1], 87Exn] for WC-Co cermets. Shetty et al. [85She[1]] observed an apparent trend in the threshold load for cracking, P_o, with the alloy hardness and fracture toughness. Hard alloys normally exhibited a negative threshold load while the softer alloys showed positive threshold loads. A similar trend was also apparent in the data of Exner et al. [87Exn]. Regarding the non-zero intercept, having positive threshold loads, Shetty et al. [85She[1]] explained that it might be the result of residual compressive stress on the surface which was not adequately prepared leading to a reduced crack size. A tensile stress on the surface will do the reverse, leading to a negative threshold load [89Pon[1]]. However, there is no explanation in the literature by what means the surface tensile stress could be induced, leading to the negative threshold load. Warren and Matzke [83War] noted that in a number of cases, the *l* versus P

plot was found not to pass through the origin in spite of careful sample preparation. In view of the above, W in Eq. (7.1) should be modified to

$$W=(P-P_o)/4l \qquad (9.1)$$

where P_o is a threshold indentation load for cracking.

Also, it has been recognized for quite a long time that Vickers microhardness of many metallic and non-metallic materials becomes greater at lower loads (so-called "indentation size effect" or ISE). This characteristic is believed to be the reason for "indentation size effect" as proposed by Li et al. [93Li^2]. According to Li et al. [93Li^2] when the size of the indentation is reduced the frictional contribution to hardness is increased, resulting in higher hardness values. This also proved to be the case for many intermetallic alloys [93Bys]. The idea of distinguishing between the surface energy contribution and the volume energy contribution effects in microhardness testing resulted in a general equation of the following form [77Fro, 93Bys];

$$P=a_1d+a_2d^2 \qquad (9.2)$$

where P is the load, d is the diagonal length (indentation size), a_1 is the coefficient describing the proportional specimen resistance (the friction between the indenter facets and the test specimen) while a_2 is the coefficient related to the load-independent microhardness. Eq. (9.2) can be rewritten as

$$P/d^2 =a_1/d + a_2 \qquad (9.3)$$

Combining Eq. (9.3) with the standard hardness equation, $H=\phi(p/d^2)$ where ϕ is a constant dependent on the indenter geometry, the equation yields

$$H=\phi(a_1/d+a_2) \qquad (9.4)$$

The above equation shows the inverse dependence of microhardness on the indentation size. Normalizing load in Eq. (9.2) by d gives a linear equation in the form.

$$P/d=a_1 + a_2d \qquad (9.5)$$

This equation yields a slope equal to the a_2-value and an intercept equal to the a_1 value. The linear regression analyses performed according to Eq. (9.5) for both the η and κ phases are shown in Fig. 9.51.

From the fitting equations in Fig. 9.51 the a_2 values corresponding to the slope of the plots, were used to calculate the load-independent microhardness H_o because the a_1 coefficient describes the proportional specimen resistance (the friction between the indenter facets and

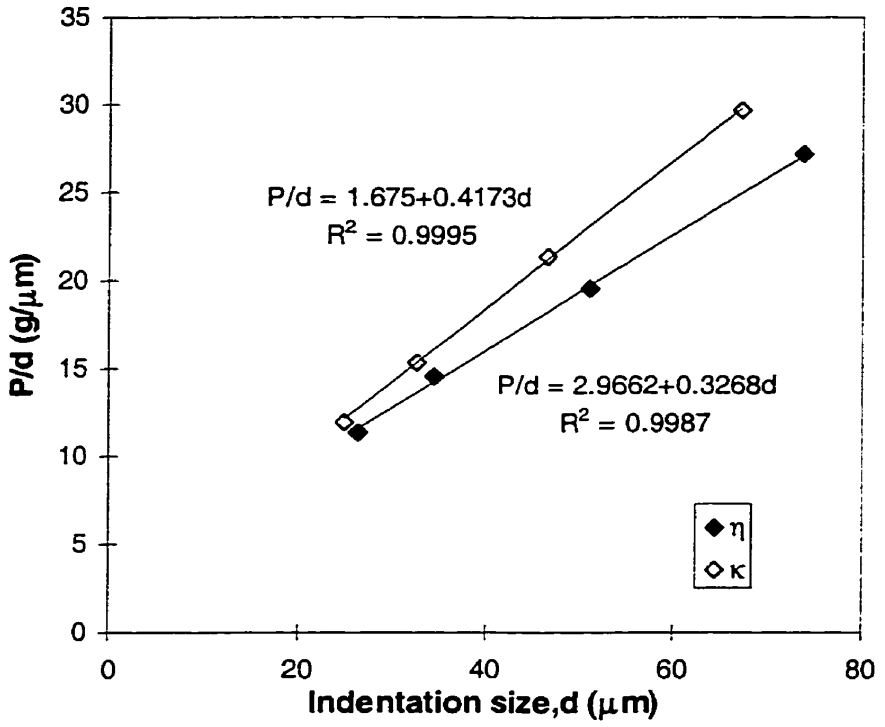

Fig. 9.51 The Vickers indentation results presented by linear regression as P/d versus d. Standard deviations for the load and indentation size are so small that they correspond to the size of phase symbols used.

the test specimen) while the a_2 coefficient is related to the load-independent microhardness as described in [89Pon[1]]. For Vickers test (if d is in μm) H_o is given as [91Li] :

$$H_o=1854.4*a_2 \qquad (9.6)$$

where H_o is in kg/mm^2.

As a result, Eq. (7.7) can be modified to the following equation:

$$K_{IC} =0.0937[H_o(P-P_o)/4l]^{1/2} \qquad (9.7)$$

by substituting H_o (substituted in N/m^2 by conversion from kg/mm^2) for H_V, $(P-P_o)/4l$ (where l is in m) (Eq.(9.1)) for W, and using a_2 values from Fig. 9.51, one obtains K_{IC} in $MPa{\cdot}m^{1/2}$. Using P_o from Fig. 9.40 (P_o = -2.18139N for the η and P_o = -2.49735N for the κ) the fracture toughness values calculated from Eq. (9.7) are given in Table 9.17 in the previous section. The fracture toughness values became quite consistent with varying indentation loads.

9.4.2.3 Indentation fracture toughness of the other phases in the present system

Based on the results of the indentation fracture toughness calculations performed on the η and κ phases, it was found that, at least for the η and κ phases, the selection of equations does not need to be limited only to a certain type of crack systems for indentation fracture toughness calculations.

Therefore, the fracture toughness calculations for the other phases observed in the present work will be performed using the equation models which give the reasonable fracture toughness values similar to that obtained by CNB test (1.7MPa.$m^{1/2}$) for the η phase such as Shetty et al. model, Evans and Charles, and Lawn and Evans models regardless of the type of crack systems. Even if modified Shetty et al. model gives reasonable and load-independent fracture toughness values for the η and κ phases, the use of the equation is omitted since it requires large enough phase area to make indentations at, at least, four different indentation loads for each phase to calculate the threshold indentation load for cracking, P_o from P vs. l relationship curve as shown in Fig. 9.40 and the load-independent microhardness, H_o from P/d vs. d relationship curve as shown in Fig. 9.51.

Table 9.18 shows the indentation parameters, a, l and c used for fracture toughness calculations for several phases. Since the intended phase area for fracture toughness calculations was not large enough in alloys to make indentations at a relatively high load such as 1000g or 2000g, the indentations were made at 100g and 500g. Even lower indentation loads were applied for the Mg_2Ni phase in alloy 43 and the Mg_2NiSi_3 phase in alloy 42. The indentation loads used for fracture toughness calculations for the Mg_2Ni phase in alloy 43 and the Mg_2NiSi_3 phase in alloy 42 are indicated in Table 9.18. Table 9.19 shows the indentation fracture toughness values of several phases calculated using the indentation parameters in Table 9.18.

Comparing the fracture toughness values of the several phases in Table 9.19 with those for the η and κ phases, it is seen that fracture toughness values of ζ are similar to those of η and κ while the other phases in Table 9.19 show even lower fracture toughness values than the η and κ phases.

Table 9.18 Indentation parameters, a, l, and c (in Fig. 7.1) as a function of the applied load, P for the other intermetallic phases.

Phases (alloy no.)	Indentation load, P, N (g)					
	0.9807 (100)			4.904 (500)		
	a (μ)	*l* (μ)	c=a+*l* (μ)	a (μ)	*l* (μ)	c=a+*l* (μ)
ζ (29)	7.02±0.09	10.51±1.36	17.53±1.35	16.68±0.34	34.96±5.68	51.56±5.74
$MgNi_2$ (37)	8.43±0.06	12.72±1.97	21.14±1.95	20.38±0.18	56.04±5.19	76.42±5.14
$Mg(Ni,Si)_2$*(38)	8.3±0.11	13.38±1.10	21.68±1.13	19.80±0.32	50.80±5.27	70.60±5.35
Mg_2Ni(43)	10.56±0.16	11.85±1.51	22.42±1.56	15.54±0.42	14.29±2.67	29.83±2.76
				Indentations made at 1.9614 (200)		
Mg_2SiNi_3 (42)	5.50±0.21	7.01±1.02	12.51±1.07			
	Indentations made at 0.4904 (50)					

*: the phase contains 4.2 at. % Si.

Table 9.19 Indentation fracture toughness values for selected phases observed in the present work.

Equation Model	Indentation load, N (g)	K_{IC} ($MPa.m^{1/2}$)				
		ζ (alloy 29)	$MgNi_2$ (alloy 37)	$Mg(Ni,Si)_2$* (alloy 38)	Mg_2Ni (alloy 43)	Mg_2SiNi_3 (alloy 42)
Shetty et al. [85She[1]] Eq. (7.7)	0.4904	-	-	-	-	1.08±0.10
	0.9807	1.38±0.09	1.05±0.08	1.03±0.05	0.87±0.06	-
	1.9614	-	-	-	1.08±0.11	-
	4.9035	1.60±0.14	1.03±0.05	1.11±0.07	-	-
	Average	1.45±0.15	1.04±0.07	1.06±0.07	0.95±0.14	1.08±0.10
Evans and Charles [76Eva] Eq. (7.16)	0.4904	-	-	-	-	1.30±0.18
	0.9807	1.57±0.18	1.19±0.17	1.13±0.09	1.08±0.12	-
	1.9614	-	-	-	1.42±0.20	-
	4.9035	1.56±0.26	0.86±0.10	0.97±0.12	-	-
	Average	1.56±0.19	1.05±0.22	1.05±0.13	1.22±0.22	1.30±0.18
Lawn and Evans [77Law] Eq. (7.18)		1.98±0.04-2.57±0.04 Pc=0.4904-0.9807 (50-100)	1.18±0.03 Pc=0.2452 (25)	1.38±0.03 Pc=0.2452 (25)	0.82±0.01-1.07±0.03 Pc=0.2452-0.4904 (25-50)	1.09±0.07 Pc=0.1471 (15)

* the phase contains 4.2 % Si.

9.5 Compressive test

9.5.1 Stress-strain curves

The specimens for compressive tests were cut from the broken halves of the already fracture toughness tested chevron-notched specimens from the same alloys. The load-displacement curves for the composites which show yielding were corrected for the machine stiffness according to the procedure described in section 8.4.3 to calculate yield strength. As an example, Fig. 9.52 shows a direct load-displacement and a corrected load-displacement curves with 0.2 % offset lines for the specimen F1-2nd.

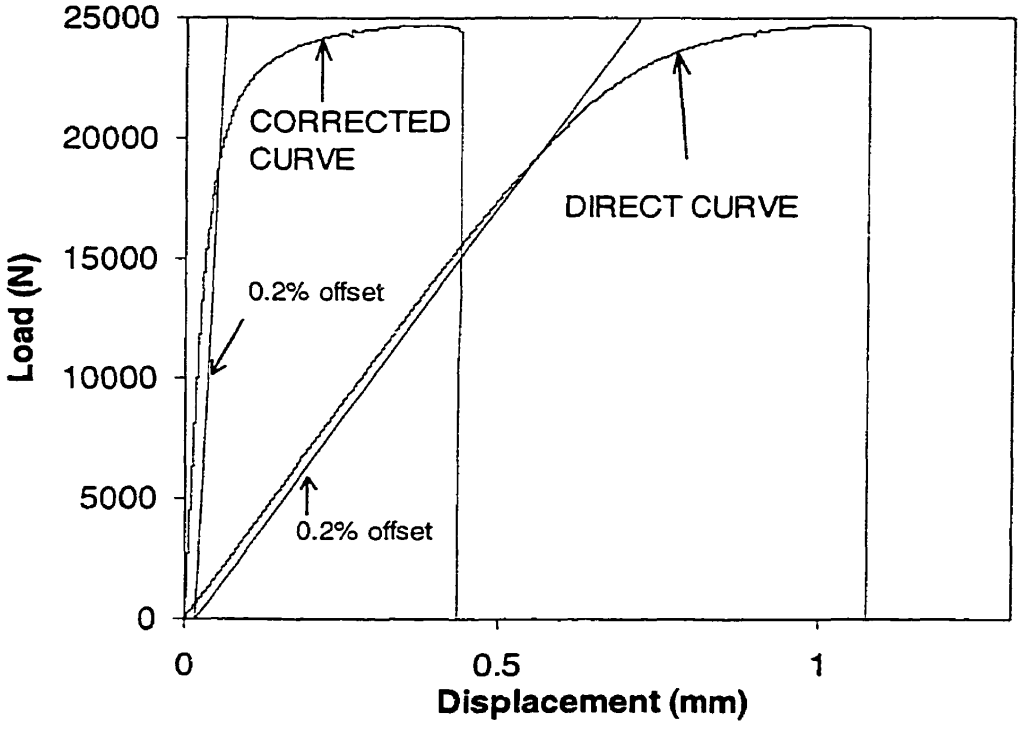

Fig. 9.52 Load-displacement curves showing both the direct and machine stiffness corrected curves for the specimen F1-2nd.

Fig. 9.53 shows the typical stress-strain curves for the composites tested in the present work. The stress-strain curves in Fig. 9.53 were constructed from the corrected load-displacement curves as shown in Fig. 9.52.

The stress-strain curves were then divided into several types based on the shape of the curves similarly to the P-LLD curves for CNB tested specimens (Fig. 9.27).

The specimen representing type E did not fail up to strain 0.11 and the test was discontinued before complete fracture of the specimen. Also, the specimen representing type D in Fig. 9.53 did not fail, but the test was discontinued at the strain shown on the curve D in Fig. 9.53. The little stress drops shown like serrations (encircled) on the stress-strain curves representing types A, E, and F seem to indicate the initiation of microcracks in the samples.

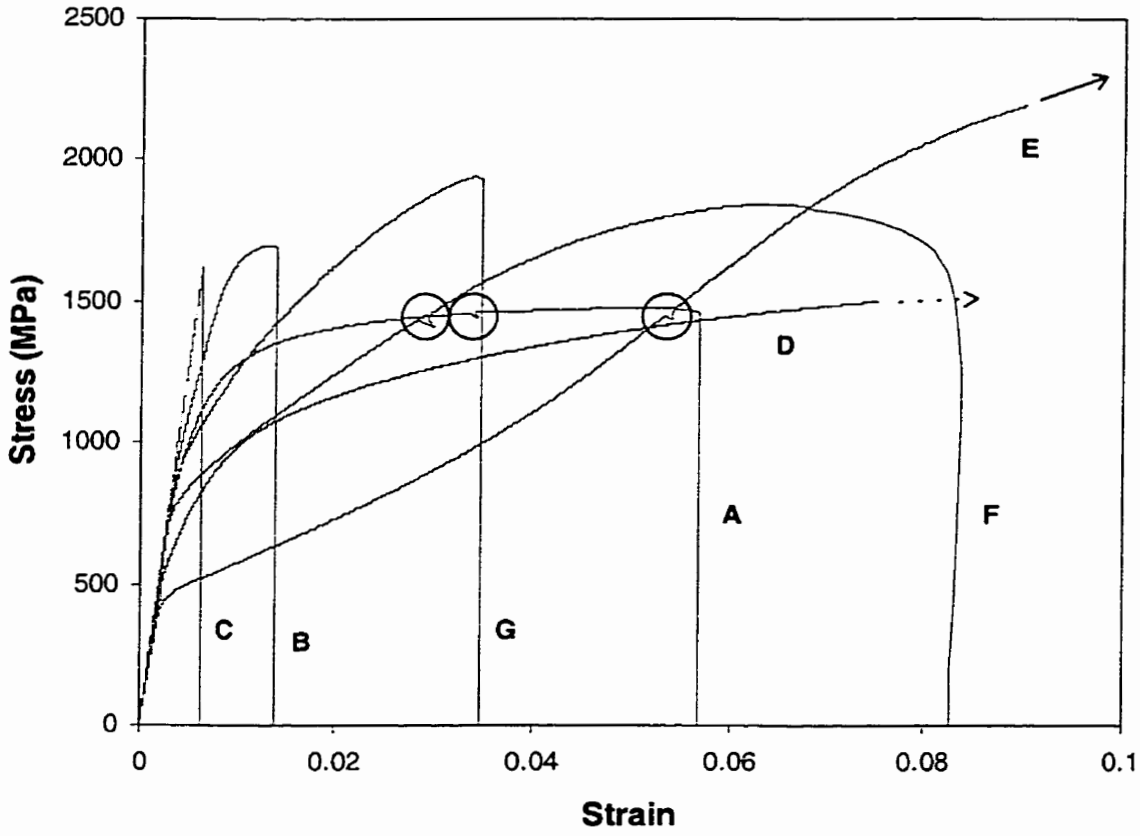

Fig. 9.53 Typical types of stress-strain curves for the composites compression-tested in the present work. Serrations are shown in circles.

9.5.2 Fracture or yield strength of the in-situ composites

In-situ composites F1, F2 and F7-F12 show a yielding on the load-displacement curve while F3-F6, F13-F15, and F18-F22 show only a linear load-displacement curve (or stress-strain curve) type C. Some specimens of F16 and F17 show linear load-displacement curves (type C in Fig. 9.53) and some other specimens of F16 and F17 show non-linear load-displacement curves before fracture (type B).

Fracture strength or yield strength of the in-situ composites was calculated depending on whether the load-displacement curves for the samples showed yielding or linear elastic deformation before fracture. Fracture strength or yield strength as well as the type of stress-strain curve defined in Fig. 9.53 is given in Table 9.20. Yield strength of Ni_3Si reported in the literature is quite diverse. Oliver [89Oli] reported 733MPa (18.9 at. % Si), Liu et al. [96Liu] 677MPa (22.5 at. % Si, in vacuum), Pike et al. [00Pik] 656MPa (18.9 at. % Si), and Takasugi et al. [90Tak[I]] 438MPa (22.0 at. % Si). The average yield strength of Ni_3Si (23.4 at. % Si) in the present work is 502±19MPa.

Yield strength of F1, F2, and F8-F12 was calculated from both the direct and corrected load-displacement curves for comparison and also given in Table 9.20. Yield strength calculated from the direct curves is almost the same as that calculated from the corrected curves.

Table 9.20 Fracture strength or 0.2 % offset yield strength of the in-situ composites obtained from compression tests. Data in parentheses calculated from machine stiffness corrected curves.

Composites No. (Type of stress-strain*)	Fracture strength or 0.2 % offset yield strength (MPa) of the Nth specimen from the bottom of the ingot					
	1st	2nd	3rd	4th	5th	Average
F1 (A)	*1145*** *(1145)****	*1137* *(1134)*	*1084* *(1077)*	*903* *(903)*	*1222* *(1219)*	*1098±120* *(1096±119)*
F2 (B)	*1448* *(1439)*	*1500* *(1488)*	1524***** (1524)	*1463* *(1460)*	- -	*1484±35* *(1478±37)*
F3 (C)	1623	1405	1389	1491	-	1477±107
F4 (C)	1380	1821	1193	1678	1334	1481±259
F5 (C)	1092	779	-	1204	-	1025±220
F6 (C)	498	339	495	-	-	444±91
F7 (D)	*682*	*831*	*809*	*877*	*871*	*814± 79*
F8 (A)	*1103* *(1099)*	*1105* *(1105)*	*1101* *(1101)*	*1113* *(1104)*	*1028* *(1020)*	*1090±35* *(1086±37)*
F9 (E)	*482* *(482)*	*522* *(521)*	*514* *(514)*	*490* *(490)*	- -	*502±19* *(502±19)*
F10 (F)	*711* *(709)*	*663* *(662)*	*701* *(700)*	*713* *(711)*	*711* *(711)*	*700±21* *(699±21)*
F11 (F)	*882* *(882)*	- -	*897* *(897)*	*878* *(877)*	- -	*886±10* *(885±10)*
F12 (G)	*1054* *(1054)*	*1149* *(1145)*	*1175* *(1175)*	*1159* *(1159)*	*1104* *(1102)*	*1128±49* *(1127±49)*
F13 (C)	1406	1215	1162	1526	1157	1293±165
F14 (C)	2083	1921	1649	1815	1356	1765±278
F15 (C)	1746	1882	1714	-	1379	1680±214
F16 (B-C)	458*****(B)	*537* (B)	*464* (B)	704*****(B)	596 (C)	552±102
F17 (B-C)	810 (C)	1014 (C)	*1185* (B)	*1223* (B)	*1128* (B)	1072±166
F18 (C)	1382	1482	1216	1414	1435	1386±102
F19 (C)	2258	1781	1793	2003	1339	1835±338
F20 (C)	1789	1761	1611	-	1487	1662±140
F21 (C)	1689	1309	1400	1784	1764	1589±220
F22 (C)	-	351	459	-	-	405±76

*: the designations of the type of stress-strain curves corresponds to the designations in Fig. 9.53.

**: the numbers in italic letter are yield strength while the numbers in regular are fracture strength.

***: the numbers in parentheses represent the yield strength calculated from machine stiffness corrected load-displacement curves.

****: the specimens show a little amount of yielding behaviour, but it is within 0.2 % deformation. Therefore, the numbers indicate either fracture strength or maximum compressive strength of the specimens.

9.5.3 Deformation behaviour during compression

None of the in-situ composites F7 and F9 fail during compression tests. One of the specimens of F10 was not loaded to fracture intentionally in order to investigate its deformation and fracture behaviour. As a consequence, it was possible to investigate the initiation of crack, crack propagation, and deformation mechanisms, of in-situ composites F7, F9, and F10 by examining the surface of compression-tested specimens.

Fig. 9.54 shows the microstructures on the polished side surface of compression-tested specimens F7, F9, and F10 after 7.2%, 3.5%, and 7.9% plastic strain which may also include the strain component due to microcracking (calculated from corrected load-displacement curves), respectively. For F7, cracks mostly developed in the η phase separating the Ni(Si)+Ni_3Si microconstituents (Fig. 9.54(a)). Slip bands are observed in the Ni(Si)+Ni_3Si microconstituent. Cracks developed in the η phases are blunted at the interface between the η and the Ni(Si) or (Ni(Si)+Ni_3Si) microconstituents (Fig. 9.54(b)). This microstructure also shows that some of slip bands in the Ni(Si)+Ni_3Si microconstituents are connected to the end of microcracks, therefore, the slip bands seem to be induced by the stress concentration at the microcrack tips. Fig. 9.54(c) shows the side surface of compression-tested specimens of composite F9 containing mostly Ni_3Si. Cracks which started at the grain boundary and slip bands aligned in one direction in each grain (planar glide) are observed. In Fig. 9.54(d) for F10 also containing mostly Ni_3Si, planar slip deformation is observed.

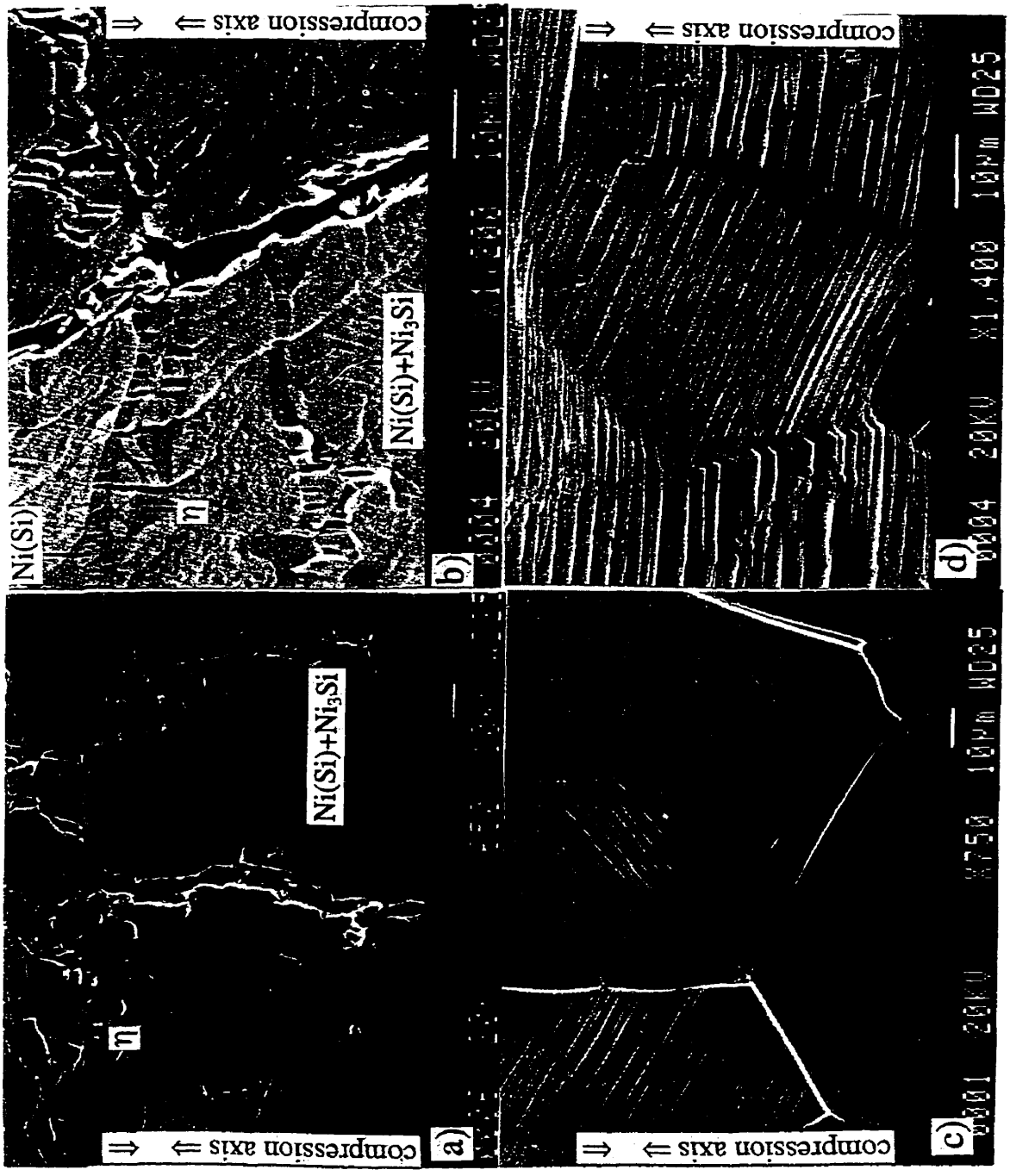

Fig. 9.54 Microstructures of the surface of composites (a-b) F7, (c) F9, and (d) F10 after 7.2%, 3.5%, and 7.9% compressive plastic strain including the plastic deformation component and displacement due to microcracking.

10. Discussion

10.1 Intermetallic phases in the Ni-Si-Mg system

The ternary phase region in the equilibrium phase diagram containing alloys 38-40 conform to the phase transformation sequence based on the binary Mg-Ni phase diagram [90Mas] as for example alloy 38 in Fig. 9.6(a). Any ternary alloy in this region contains only two phases: $MgNi_2$-type ternary intermediate phase (i.e. $Mg(Ni,Si)_2$) and Mg_2Ni. This is like a quasi-binary phase region existing in the ternary phase diagram. This was also observed in the equilibrium phase region with alloy 1 as already reported in the previous paper [98Son[1]].

The $MgNi_2$ Laves phase in the Ni-Mg binary alloy system is observed to accommodate up to about 11 at. % Si at room temperature, forming a ternary intermediate phase (Fig. 9.1). From the shape of the ternary $Mg(Ni,Si)_2$ phase region, which is elongated along the constant Mg content line, it can be invoked that the Ni atoms in the $MgNi_2$ phase are replaced by the Si atoms, forming the $Mg(Ni,Si)_2$ stoichiometry. The solid solubility of the third element in the $MgNi_2$ phase was also observed in the Mg-Ni-Zn (up to 14 at. % Zn) and Mg-Ni-Cu (up to 26 at. % Cu) systems [53Lie]. In the Mg-Ni-Zn system, a single phase in the homogeneity range from $Mg(Ni_{0.7}Zn_{0.3})_2$ to $Mg(Ni_{0.18}Zn_{0.82})_2$ exists along the constant Mg content of 33.3 at. % which corresponds to $MgCu_2$-type ternary phase. Its homogeneity range is similar to the entire region extending from the Mg_2SiNi_3 to the ω through the ν phase region in the present system along the constant Mg content of about 33 at. % (Fig. 9.1). However, comparing the x-ray diffraction spectra of the $MgCu_2$ phase which has the same structure and lattice parameters [85Vil] as the ternary $MgCu_2$-type phase in the Mg-Ni-Zn system, with the present Mg_2SiNi_3, ν, or ω phases no crystallographic relationship between the ternary $MgCu_2$-type phase and the Mg_2SiNi_3, ν, or ω phase in the present Mg-Si-Ni system could be established.

Similarly, it has been observed that Mg is soluble in the Ni_3Si up to about 1 at. % and the Si content in Ni_3Si is decreasing with increasing Mg content in Ni_3Si as implied by the shape of the Ni_3Si phase region with Mg in Fig. 9.1.

The ternary phase with an approximate composition of 34.0 at. % Mg, 16.0 at. % Si and 50.0 at. % Ni, located just above the ternary intermediate $Mg(Ni,Si)_2$ phase has been reported by Noreus et al. [85Nor] to be the Mg_2SiNi_3 compound in a hexagonal symmetry with the lattice parameters, a = 0.50044nm and c = 1.10894nm. A small discontinuity between the $Mg(Ni,Si)_2$ and the Mg_2SiNi_3 phase regions, about 4 at. % Si wide, along the same Mg content, is observed in the present work (Fig. 9.1). Because of the similar composition and contrast between these two phases, XRD was used to discriminate between them. The XRD spectrum from alloy 32 was indexed mostly by the standard diffraction spectra from η [96Song, 98Son[1]] and Mg_2SiNi_3 [85Nor], but not by the diffraction spectra from $MgNi_2$, confirming that alloy 32 consists of mainly η and Mg_2SiNi_3 (fraction of $Mg(Ni,Si)_2$ is negligible). However, the diffraction spectrum from alloy 40 containing mainly Mg_2Ni and $Mg(Ni,Si)_2$ was indexed by the Mg_2Ni and $MgNi_2$ diffraction spectra, indicating that $Mg(Ni,Si)_2$ containing 11 at. % Si is based on the $MgNi_2$-type phase rather than Mg_2SiNi_3. This also confirms the solubility limit of Si in this phase after homogenization and slow cooling.

The Mg_2SiNi_3 phase has the same type of stoichiometry as some ternary Laves phases like Mg_2Cu_3Si, and Mg_2Cu_3Al derived from the binary $MgZn_2$ and $MgCu_2$ Laves phases [95Wes], respectively. However, XRD spectrum as well as the number of atoms in a unit cell of the hexagonal Mg_2SiNi_3, do not match any of the binary $MgZn_2$, $MgCu_2$ as well as $MgNi_2$-type Laves phases. That means Mg_2SiNi_3 is not a ternary Laves phase derived from the binary Laves phases.

The stoichiometries of the intermetallic phases observed in the present work were calculated for the center of the phase region except for the μ phase. The stoichiometry of the μ phase was calculated for the right-hand portion where most of the data points are located in its phase region. The $Mg_{34}Si_{15}Ni_{51}$composition corresponding to the center of the Mg_2SiNi_3 phase field is quite close to the stoichiometric composition of the Mg_2SiNi_3 phase ($Mg_{33.33}Si_{16.66}Ni_{49.98}$). The stoichiometry of the η phase is about $Mg_{5.80}Si_{6.96}Ni_{16.24}$ ($Mg_{20}Si_{24}Ni_{56}$) close to the prototypical stoichiometry, $Mg_6Si_7Ni_{16}$ ($Mg_{20.67}Si_{24.14}Ni_{55.17}$) for this type of phase such as $Mg_6Si_7Cu_{16}$ [85Vil, 98Son[1]]. A good agreement in the stoichiometries between the above two phases in the present work and the corresponding phases reported previously in the literature [85Nor, 85Vil, 98Son[1]] indicates that the accuracy of EDS analysis used in the present work

was very satisfactory. Table 10.1 lists the compositions and the suggested stoichiometries of the phases. The stoichiometry for the μ and ω phases was already suggested as $Mg(Si_{0.48}Ni_{0.52})_7$ and $(Mg_{0.52}Ni_{0.48})_7Si_4$ in section 9.2.2 and in section 9.2.2.1, respectively.

Table 10.1 The approximate compositions and their corresponding stoichiometries at the centers of their respective phase fields of the ternary intermetallic phases observed in the present work.

Phases	Approximate composition (at. %)	Suggested stoichiometry
η	$Mg_{20}Si_{24}Ni_{56}$ ($Mg_{5.80}Si_{6.96}Ni_{16.24}$)	$Mg_6Si_7Ni_{16}$
κ	$Mg_8Si_{41}Ni_{51}$ ($Mg_2Si_{10.25}Ni_{12.75}$)	$Mg_2Si_{10}Ni_{13}$
ζ	$Mg_{15}Si_{35}Ni_{50}$ ($Mg_3Si_7Ni_{10}$)	$Mg_3Si_7Ni_{10}$
ν	$Mg_{33}Si_{30}Ni_{37}$ ($Mg_{11}Si_{10}Ni_{12.33}$)	$Mg_{11}Si_{10}Ni_{12}$
ω	$Mg_{33}Si_{37}Ni_{30}$ ($Mg_{11}Si_{12.33}Ni_{10}$)	$(Mg_{0.52}Ni_{0.48})_7Si_4$
μ	$Mg_{13}Si_{41.5}Ni_{45.5}$ ($Mg_2Si_{6.38}Ni_7$)	$Mg(Si_{0.48}Ni_{0.52})_7$
τ	$Mg_{10}Si_{50}Ni_{40}$ ($MgSi_5Ni_4$)	$MgSi_5Ni_4$
Mg_2SiNi_3	$Mg_{34}Si_{15}Ni_{51}$ ($Mg_{2.04}Si_{0.90}Ni_{3.06}$)	Mg_2SiNi_3

Interestingly, it has been found that some of the phases observed in the present system are very similar in composition (stoichiometry) to phases observed in other ternary systems such as Ni-Si-Mn [64Kuz] and Ni-Mg-Cu[72Kom] which have the same two elements in common with the present ternary Ni-Si-Mg system. Particularly, the Ni-rich section of the present ternary Ni-Si-Mg phase diagram is quite similar to the Ni-rich section of the ternary Ni-Si-Mn phase diagram. As already mentioned in the previous paper [98Son[1]], the η phase in the present work, belonging to the structure type of $Mn_{23}Th_6$ (also called $Mg_6Ni_7Cu_{16}$) is the same type as the $Mn_6Si_7Ni_{16}$ phase (designated as T phase in [64Kuz]). In addition, the ζ and μ phases (Table 10.1) in the present work have similar compositions to a phase with a composition of $Mn_{15}Si_{35}Ni_{50}$ (designated as p phase in [64Kuz]) and another phase with a composition of $Mn_{15}Si_{40}Ni_{45}$ (designated as ν phase in [64Kuz]), respectively, in the Ni-Si-Mn system, if Mn is considered as corresponding to Mg. The ω phase (Table 10.1) has the same composition as a phase with a composition of $Mg_{33.3}Cu_{36.7}Ni_{30.0}$ (designated as

$Mg(Ni_{0.45}Cu_{0.55})_2$ in Ref. [72Kom]) in the Ni-Mg-Cu system [72Kom], if Cu is considered as corresponding to Si.

10.2 CNB fracture toughness

10.2.1 The validity of CNB fracture toughness test

10.2.1.1 Determination by the shape of load-load line displacement (P-LLD) curves

The validity of CNB fracture toughness test can be first determined by the shape of the P-LLD curves as already mentioned in Chapter 6 (Fig. 6.2) because the initially linear P-LLD curve may be indicative of overloading during the test. Therefore, if the P-LLD curve exhibits a linear behaviour prior to the maximum load as, shown in Fig. 6.2 (type III and IV), the test should be treated as suspicious, i.e. possibly invalid. The same validity criterion of the CNB test by the shape of the P-LLD curve is also mentioned in ASTM provisional test method, PS 70-97 [97AST] for the determination of the CNB fracture toughness of advanced ceramics.

In general, the P-LLD curves of 4pt bend-tested CNB specimens in the present work showed the stable crack growth region either in a smooth or a serrated shape. Only some of the P-LLD curves defined as either type IV or type VII (Fig. 9.27) showed the linear P-LLD curve prior to the maximum load (Table 9.11 and 9.13). In general, the linear P-LLD curve prior to the maximum load is more likely to occur for the specimens of in-situ composites which have low fracture toughness values or for the specimens tested with short span, i.e., S_1=16mm. However, no considerable difference in fracture toughness values between the samples which exhibited the stable crack growth region and the samples which exhibited the linear P-LLD curve was observed (Table 9.11 and 9.13). No significant difference in fracture toughness values between the samples which showed the evidence of non-linearity in the P-LLD curve and the samples which showed the linear P-LLD curves was also reported by Withey et al. [91Wit] and Chuck et al. [84Chu] for silicon carbide (SiC) and SiC reinforced with titanium diboride (SiC/TiB_2) and soda lime glass, respectively. Therefore, it could be concluded that all fracture toughness values of the CNB specimens calculated from the maximum load in the

linear P-LLD curves might be valid. Therefore, the fracture toughness values obtained in this work should be considered valid provided that they conform to the size requirement validity criterion as shown below regardless of whether the P-LLD curves shows the stable crack growth region or not.

10.2.1.2 Determination by the size requirement

The validity of CNB fracture toughness tests exhibiting an initial stable crack growth region can also be determined by the size of specimens. Since there is no standard test method in ASTM for CNB specimens for metallic materials, there is no size requirement available for the determination of validity of CNB tests in ASTM. However, in ASTM E1304-89 [89AST[1]], the plane-strain fracture toughness determined by using *chevron-notched bar* and *rod* specimens in tension for metallic material, in order for a test result to be considered valid, it is required that the thickness of the specimen, B, equals or exceeds 1.25 $(K_{QIvM}/\sigma_{YS})^2$, i.e., $B \geq 1.25\ (K_{QIvM}/\sigma_{YS})^2$, where σ_{YS} is the 0.2 % offset yield strength. Therefore, the validity of CNB tests in the present work will be assessed by the size requirement as in ASTM E 1304-89.

The required thickness, B of individual specimen was calculated based on the K_{QIvM} and the compressive yield stress of individual specimen from Table 9.11 and Table 9.20, respectively, and tabulated in Table I.1 in Appendix I. The thickness, B of most of the tested specimens far exceeds the thickness required for the test result to be considered valid. However, the size requirement was not satisfied for five out of nine specimens of in-situ composite F9. The specimens with actual size (B) smaller than the size required in ASTM E 1304-89 are marked by bold letters (Table I.1 in Appendix I). Regarding the validity of the test results obtained from the 5 specimens which did not satisfy the size requirement, it is still difficult to conclude that the test results are really invalid. All the P-LLD curves of the specimens F9 are defined as type I in Fig. 9.27. Considering the shape of the maximum load region defined as type I no extensive plasticity is expected to occur in this type P-LLD curve. Load drops suddenly by unstable crack propagation as soon as the load reaches the maximum.

10.2.2 Fracture behaviour of Ni_3Si

10.2.2.1 Scatter in fracture toughness values

A certain trend could be found in the fracture toughness values of a near-single phase Ni_3Si alloy F9 tested in air (Table 9.11 and Fig. 10.1). Fracture toughness of the specimen taken from the bottom of the ingot is the highest one and subsequently, the fracture toughness gradually decreases with increasing the specimen number, i.e. from F9-1st to F9-5th (Fig. 10.1). This behaviour is observed for specimens tested in air with S_1=16mm and S_1=35mm except the specimen F9-5th tested with S_1=35mm having anomaly high fracture toughness which, as mentioned earlier, seems to arise from the abnormal crack initiation at the chevron tip (Fig. H.1 in Appendix H). However, no such a trend is observed for the specimens tested in dry oxygen and vacuum (Fig. 10.1).

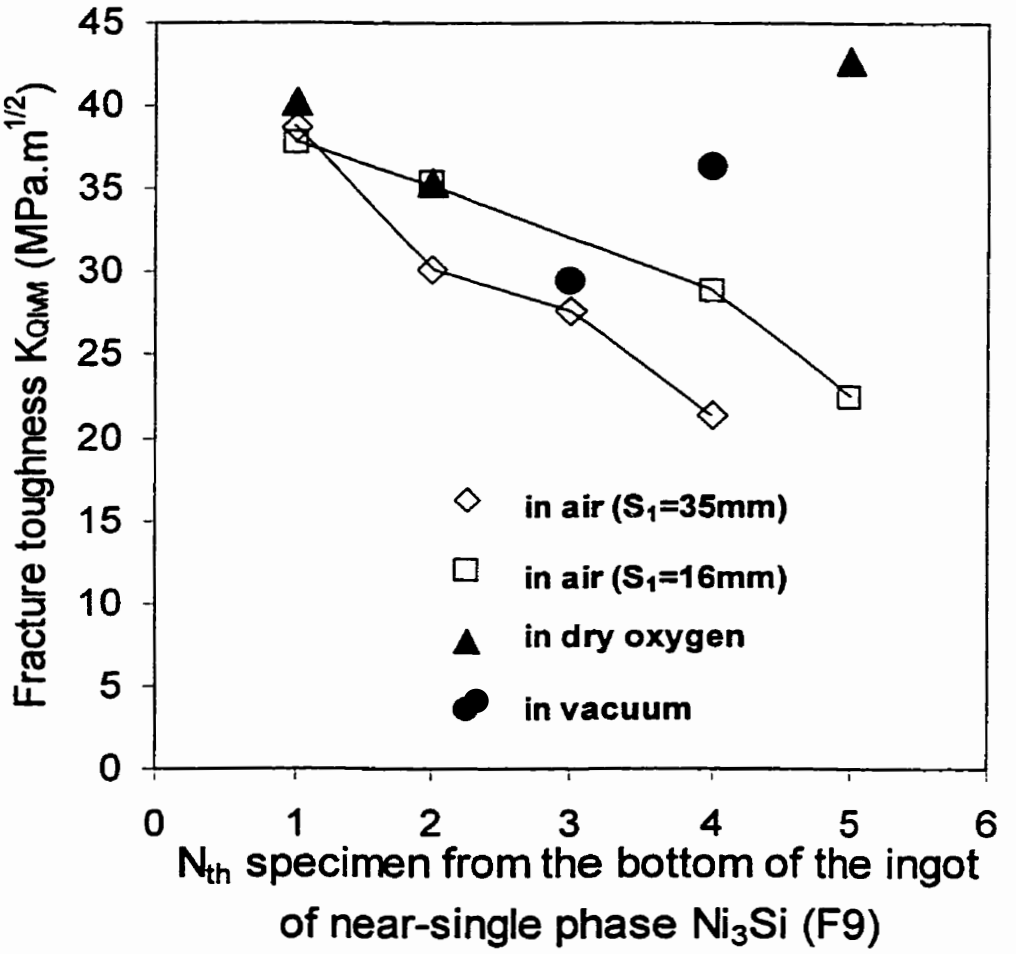

Fig. 10.1 Fracture toughness of a near-single phase Ni_3Si (F9) tested in air, vacuum, and dry oxygen.

One of possible reasons giving rise to a decrease in fracture toughness vs. the distance from the bottom of the ingot in alloy F9 could be the microstructural differences in the top and bottom of the ingot (Fig. 9.20). Therefore, an attempt to characterize the microstructure of the specimens, particularly associated with the volume fractions of Ni(Si), fine (Ni(Si)+Ni_3Si) mixture, and fine-grained Ni_3Si was carried out. To measure the volume fraction of Ni(Si) phase, fine (Ni(Si)+Ni_3Si) mixture, and fine-grained Ni_3Si on the fracture surface of each specimen would desirable, but unfortunately, preliminary trials showed that it was practically impossible. Therefore, these measurements were done on the specimen removed from the ingot which was directly in contact with CNB specimen. Table 10.2 shows the volume fraction of Ni(Si), fine (Ni(Si)+Ni_3Si) mixture, and fine-grained Ni_3Si measured for each specimen with corresponding fracture toughness values. The volume fraction of Ni(Si) changes only slightly. However, one can see that the volume fraction of fine (Ni(Si)+Ni_3Si) mixture or/and fine-grained Ni_3Si increases substantially as the specimen number increases from F9-1st to F9-5th, i.e., from the bottom to the top of the ingot. The increase in the volume fraction of fine (Ni(Si)+Ni_3Si) mixture is more pronounced for the specimens with S_1=16mm while the increase in the volume fraction of fine-grained Ni_3Si is more pronounced for the specimens with S_1=35mm. Fracture toughness dependence on the volume fraction of fine (Ni(Si)+Ni_3Si) mixture and fine-grained Ni_3Si in F9 as shown in Table 10.2 is plotted in Fig. 10.2.

Table 10.2 Volume fraction of the Ni(Si), fine (Ni(Si)+Ni_3Si) mixture, and fine-grained Ni_3Si in the specimens of composite F9 tested with S_1=16mm and 35mm.

Speci-mens	Vol. of Ni(Si)		vol. of (Ni(Si)+Ni_3Si)		vol. of fine grained Ni_3Si		K_{QIvM} (MPa.m$^{1/2}$)	
	16mm	35mm	16mm	35mm	16mm	35mm	16mm	35mm
F9-1st (bottom)	1.1±0.9	0.9±0.9	3.3	1.1	5.1	6.6	37.8	38.7
F9-2nd	2.5±1.0	3.1±0.3	14.9	8.4	1.7	26.8	35.4	30.1
F9-3rd	4.0±2.0	2.4±0.8	16.1	7.9	6.3	42.5	-	27.7
F9-4th	3.1±1.4	3.0±0.2	10.6	5.5	41.9	50.3	28.9	21.4
F9-5th (top)	4.0±1.9	3.4±1.5	18.3	12.3	18.1	37.0	22.5	-

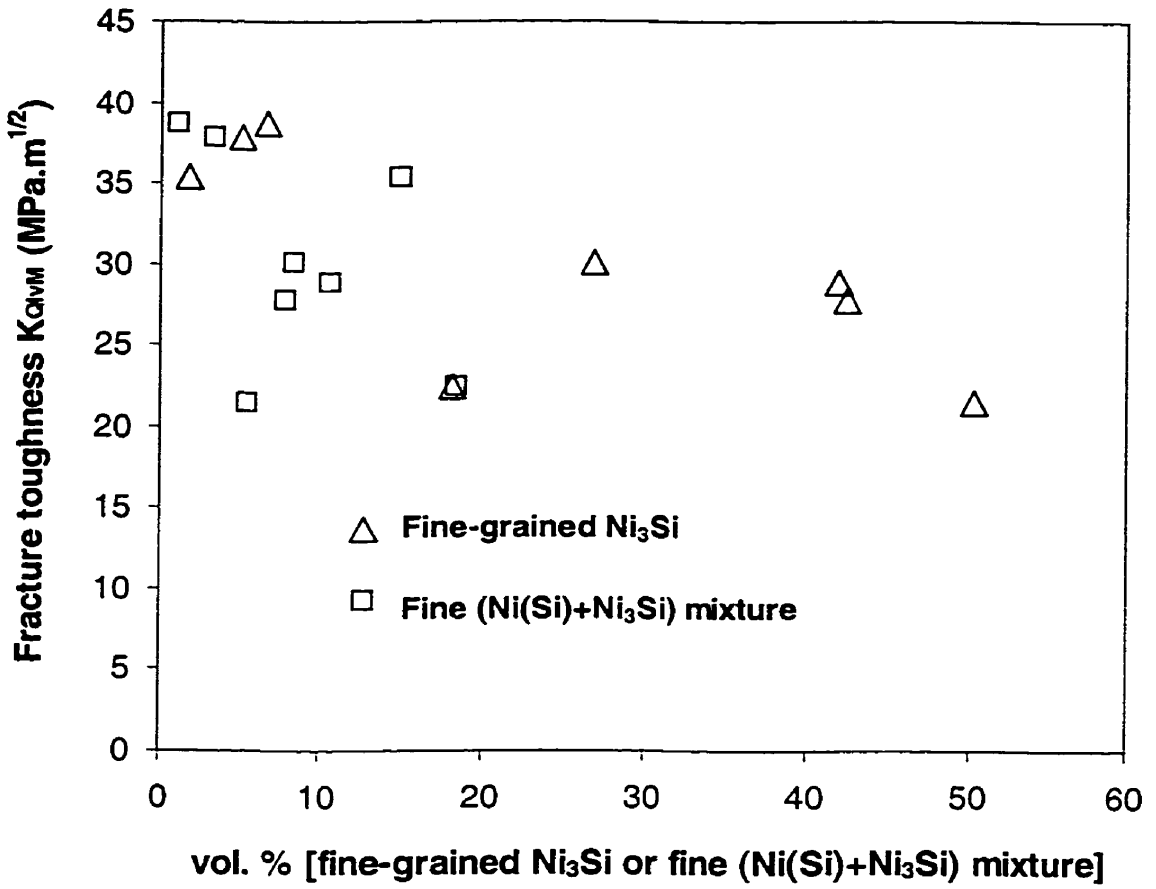

Fig. 10.2 Fracture toughness dependence of Ni_3Si based alloy on the volume fraction of the fine (Ni(Si)+Ni_3Si) mixture and fine-grained Ni_3Si in F9. Data from Table 10.2.

A decreasing trend is observed between fracture toughness and both the volume fraction of fine-grained Ni_3Si and volume fraction of fine (Ni(Si)+Ni_3Si) mixture. Therefore, a substantial decrease in fracture toughness of Ni_3Si-based composite F9 seems to be related to the substantial increase in the volume fraction of these two microstructural constituents. However, no satisfactory correlation between fracture toughness and any one of the above two microstructural constituents can be established. On the other hand, a relatively high linear correlation coefficient is obtained when fracture toughness is correlated with the total volume fraction of (fine (Ni(Si)+Ni_3Si) mixture + fine-grained Ni_3Si) as shown by one of the linear regression lines in Fig. 10.3. Since fracture toughness of F9 decreases more rapidly with increasing volume fraction of the fine (Ni(Si)+Ni_3Si) mixture rather than with increasing volume fraction of the fine-grained Ni_3Si (Fig. 10.2), it was attempted to apply a weight factor

between the fine (Ni(Si)+Ni_3Si) mixture and the fine-grained Ni_3Si. Weight factors from 0.1 to 1.0 for the volume fraction of the fine-grained Ni_3Si were tested. The highest correlation coefficient is obtained when the weight factor for the volume fraction of fine-grained Ni_3Si is half of that for the volume fraction of fine (Ni(Si)+Ni_3Si) mixture, i.e., the effect of fine (Ni(Si)+Ni_3Si) mixture on fracture toughness is assumed to be twice as strong as that of the fine-grained Ni_3Si (Fig. 10.3). Note that the increase in the volume fraction of fine (Ni(Si)+Ni_3Si) mixture implies that the area fraction of the Ni(Si) and Ni_3Si interface boundary increases.

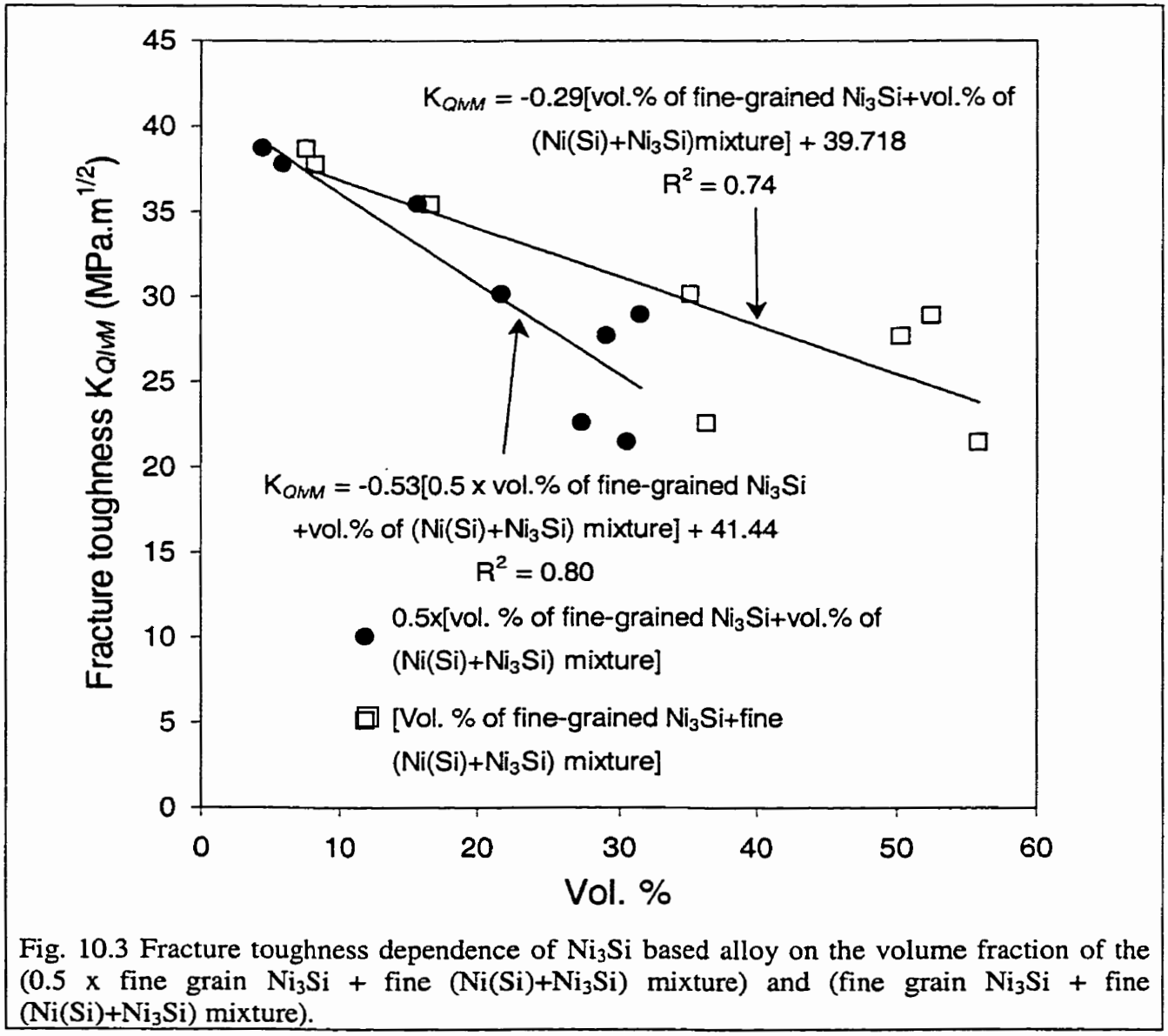

Fig. 10.3 Fracture toughness dependence of Ni_3Si based alloy on the volume fraction of the (0.5 x fine grain Ni_3Si + fine (Ni(Si)+Ni_3Si) mixture) and (fine grain Ni_3Si + fine (Ni(Si)+Ni_3Si) mixture).

The above results in Fig. 10.3 can be supported by the fracture surface observation of composite F9. Fracture surfaces of composite F9, which exhibits the highest and lowest fracture toughness values tested with S_1=35mm and S_1=16mm in air, and in dry oxygen or vacuum, are compared in Fig. H.4 in Appendix H. In general, fracture surfaces (Fig. H.4 (a), (c), and (e)) of specimens which exhibit the highest fracture toughness values in each test condition contains less of the fine (Ni(Si)+Ni_3Si) mixture and the fine-grained Ni_3Si than those of the specimens (Fig. H.4 (b), (d), and (f)) which have the lowest fracture toughness values. According to the general composite rule-of-mixtures, fracture toughness values would be expected to increase with increasing volume fraction of more ductile fine (Ni(Si)+Ni_3Si) mixture, as opposed to the behaviour in Fig. 10.2. Therefore, the detrimental effect of higher volume fraction of the fine (Ni(Si)+Ni_3Si) mixture on toughness must be discussed from the standpoint of environmental embrittlement. In this regard, it is suspected that the environmental effect at the interfaces between Ni(Si) and Ni_3Si in the fine mixture might be responsible for such a detrimental trend. A different mode of fracture of Ni_3Si tied up in the fine (Ni(Si)+Ni_3Si) mixture (Fig. 9.34) may support the above argument. This mode of fracture shows transgranular cleavage fracture (Fig. 9.34(h)) whereas that in the single-phase Ni_3Si shows either step-like transgranular (Fig. 9.34(b) and (e)) or intergranular fracture.

Comparing the highest fracture toughness values of the first specimens from the bottom of the ingot (F9-1st) tested in air (S_1=16mm and S_1=35mm) and dry oxygen (Fig. 10.1), one can find that they are rather close to each other. The difference in the microstructural variables (i.e., vol. % of Ni(Si), fine (Ni(Si)+Ni_3Si) mixture or fine-grained Ni_3Si) is almost non-existent for the specimens taken from the bottom of the ingot (F9-1st) because they have very low volume fractions of such microstructural variables, i.e., this specimen is a single-phase Ni_3Si. Therefore, the comparison of fracture toughness values between the first specimens (F9-1st) tested in air and dry oxygen should only reflect the environmental effect on a single phase Ni_3Si. Even the CNB specimens tested in the present work in dry oxygen also showed predominantly intergranular fracture (Fig. H.4(e) in Appendix H) same as those tested in air. Liu et al [91Liu] also observed that the elimination of the environmental effect by testing in dry oxygen did not lead to extensive tensile ductility (they observed only ~7.5%) and a complete suppression of intergranular fracture.

Therefore, it could be concluded that a single-phase Ni_3Si does not seem to be very sensitive to the test environment and intergranular fracture of Ni_3Si is primarily caused by a weak grain boundary cohesion, i.e., an intrinsic factor. Subsequently, the decrease in the fracture toughness related to increasing volume fraction of fine-grained Ni_3Si might be mainly caused by the increase in the fraction of weak grain boundary areas since smaller grains of Ni_3Si lead to the larger total grain boundary area.

10.2.2.2 Presence of fine precipitates

Fine precipitates were observed on the fractured grain boundary facets and also on transgranular cleavage fracture surface of F9 (near-single phase Ni_3Si) (Fig. 9.35). The identity of the precipitates is not obvious at the present moment, however, if one considers the reaction of active metal with the water vapour in air (e.g. $Si+2H_2O \rightarrow SiO_2+4H$ in case of Ni_3Si) and the generation and movement of atomic hydrogen postulated as the cause of the environmental embrittlement in Ni_3Si and many other intermetallics (section 3.1.3), the precipitates are possibly either a silica (SiO_2) or a hydride formed during crack propagation. However, based on the precipitate-like appearance, they are more likely to be a hydride such as NiH or Ni_2H [97Vil] precipitated through the formation of nuclei. If silica (SiO_2) was formed based on the above reaction, the surface product would be a continuous film covering the fracture surface rather than precipitates.

The following factors indicate that the precipitates are formed during crack propagation, ruling out the possibility of pre-existing precipitates. First, the precipitates are not distributed uniformly throughout entire area of the fracture surface. There are plenty of precipitates on some fractured grain boundary facets but there is none on other grain boundary facets in the same specimen. In general, if present, the precipitates are mostly observed on the grain boundary facets only in the chevron section extending from the apex to the middle of the chevron. The precipitates are rarely observed in the chevron section located between the middle to the root of the chevron. Second, the precipitates were not observed at all in some of the fractured specimens as will be shown in Table 10.3. Since all the CNB specimens were cut out from the homogenized ingot, individual specimens should not have any different microstructural characteristics such as varying densities of precipitates. Third, the precipitates observed on the transgranular fracture surface do not appear as they were pre-existing within

the grain. They are aligned in one direction rather than distributed randomly on the fracture surface and also do not seem to be embedded within the grain.

The possibility that the precipitates were formed after fracture toughness test due to the long-term exposure of fracture surface to air can also be ruled out of hand. Examination of the fracture surface of F9 several days after the testing and re-examination a year after the fracture toughness test was done, shows the same distribution of precipitates existing only in the section of the fracture surface extending from the apex to the middle of the chevron.

Assuming that the precipitates are formed during crack propagation as argued above, an attempt was made to investigate the correlation between the fracture toughness, test environment and the presence or amount of precipitates in specimens F9. Quantification of the probability of the precipitate presence on the fracture surface for each specimen F9 was done for 15 randomly selected grain boundary facets present in the the chevron section extending from the apex to, approximately, the middle of the chevron. This is consistent with the CNB fracture toughness calculated from the maximum load which is determined when the crack is propagating from the appex to the one third of chevron section. The specimens tested in vacuum and dry oxygen are also included. The results are shown in Table 10.3. It must be kept in mind that even if the number of grain boundary facets with precipitates observed in the 2nd specimen (7/15) is the same as that in the 3rd specimen (7/15) tested with S_t=35mm in air (Table 10.3), it does not mean that actual amount of precipitates in the 2nd specimen is the same as that in the 3rd specimen. Fig. 10.4 shows the probability of the precipitate presence plotted vs. fracture toughness. An interesting result can be seen in Table 10.3 and Fig. 10.4. The probability of the presence of precipitates strongly depends on fracture toughness values. It increases with increasing fracture toughness values under the same test environment. However, this does not imply that fracture toughness increases due to the formation of fine precipitates. As already discussed, the large scatter in fracture toughness values in a near-single phase Ni_3Si is related to the vol. % of fine-grained Ni_3Si and the fine (Ni(Si)+Ni_3Si) mixture (Fig. 10.2 and 10.3). Therefore, higher probability of presence of precipitates simply reflects the higher stress intensity factor at the crack tip experienced by the specimens with higher fracture toughness values. In other words, the formation of the precipitates was easier when the stress intensity factor at the crack tip was higher.

Interestingly, the threshold level of fracture toughness to form precipitates (see arrows in Fig. 10.4) is lower for the specimens tested in air, higher for the specimens tested in dry oxygen, and intermediate for the specimens tested in vacuum. In other words, the formation of the precipitates is found to be the easiest for the specimens tested in air and most difficult for the specimens tested in dry oxygen. Even for the specimens with the lowest fracture toughness values, the precipitates were observed when the test was conducted in air (Table 10.3). However, for the specimen tested in dry oxygen such as F9-2nd, the precipitates were not observed even in specimens rendering relatively high fracture toughness values.

Table 10.3 The probability of presence of the precipitates on the fracture surface of F9 as quantified to investigate correlation between the amount of the precipitates and fracture toughness, testing environments, or the location of specimen taken from the ingot.

Test Condition	N_{th} specimen from Bottom	Fracture toughness (K_{QivM})	Number of grain facets with precipitates out of 15 arbitrarily selected grain facets in chevron notch tip* and probability of the presence of precipitates**
in air with S_I= 35mm	1st	38.7	12 (80%)
	2nd	30.1	7 (47%)
	3rd	27.7	7 (47%)
	4th	21.4	3 (20%)
in air with S_I= 16mm	1st	37.8	13 (87%)
	2nd	35.4	5 (33%)
	4th	28.9	2 (13%)
	5th	22.5	1 (7%)
In dry oxygen with S_I=26mm	1st	40.3	4 (27%)
	2nd	35.4	0 (0%)
	5th	42.7	12 (80%)
in vacuum with S_I=26mm	3rd	29.4	0 (80%)
	4th	36.3	12 (80%)

*: 'Chevron notch tip' indicates the region approximately from the apex to the middle section of the chevron.

**: Probability of presence of the precipitates in parentheses calculated from the number of grain facets with precipitates out of 15 arbitrarily selected grain facets

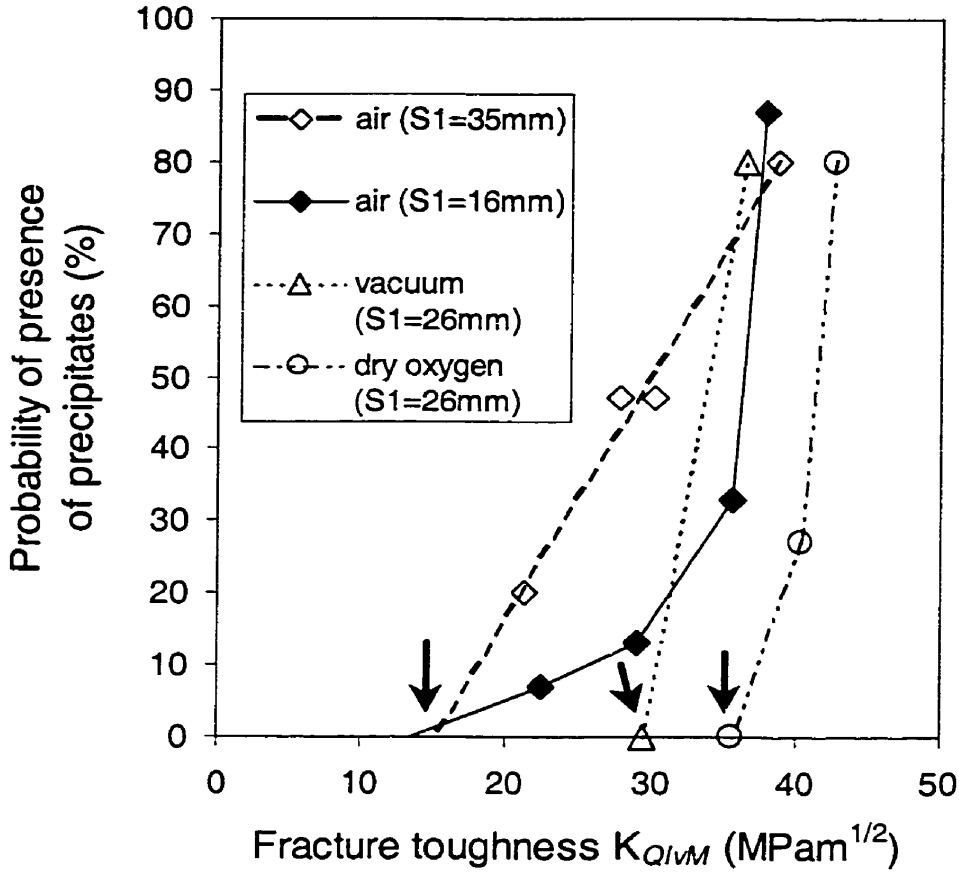

Fig. 10.4 The relationship between the probability of the presence of the precipitates and fracture toughness of specimens F9. Arrows show the threshold value of fracture toughness to form precipitates.

As a conclusion drawn from various aspects of formation of the precipitates observed in the present work, generation of hydrogen by the reaction at the crack tip (e.g. $Si+2H_2O \rightarrow SiO_2+4H$ in case of Ni_3Si) may not necessarily induce or enhance environmental embrittlement in intermetallics. Even if generation of atomic hydrogen occurs, resulting in the formation of the precipitates, a single phase Ni_3Si does not seem to be environmentally sensitive. If Ni_3Si were sensitive to hydrogen, its fracture toughness should decrease as the probability of presence of the precipitates increases since the higher probability of presence of the precipitates implies the occurrence of more hydrogen generation at the crack tip (if one assumes that the formation of the precipitates results from the generation of atomic hydrogen). Therefore, the generation of hydrogen through the above reaction will probably occur regardless of environmental sensitivity of intermetallics whenever moisture-active

elements such as Si in Ni_3Si or Al in Ni_3Al are present and additionally, the stress intensity at the crack tip is high enough. The ability of precipitate formation (expected to be a hydride), however, might depend on whether hydride forming elements are present in the intermetallic systems under consideration and also on the rate of crack propagation (slower rate may enhance formation of hydrides).

10.2.3 Toughening of in-situ composites

10.2.3.1 Rule-of-mixtures (ROM)-like relationship for fracture toughness

The applicability of rule-of-mixture (ROM)-like relationship between fracture toughness and volume fraction of toughening phases was tested for the in-situ composites containing the brittle η matrix phase and the toughening phases either Ni(Si) or Ni_3Si. Fig. 10.5 shows the dependence of fracture toughness on the volume fraction of the Ni(Si) and Ni_3Si. Composites F9-F11 also contain small fraction of Ni(Si) in addition to the majority phase Ni_3Si (Fig. 10.5) but the toughening effect of Ni(Si) can be ignored since its volume fraction is negligibly small. The two sets of upper and lower bound of ROM lines in Fig. 10.5 for composites reinforced with either Ni_3Si or Ni(Si) were constructed by arbitrarily replacing E with K in Eq. 5.40 for the upper bound and in Eq. 5.41 for the lower bound, by analogy to the upper and lower bound of ROM lines in Fig. 5.16. Therefore, the equations representing the upper and lower bound of ROM lines in Fig. 10.5 become

$$K_{QIvM} = V_{(Ni(Si)orNi_3Si)}K_{(Ni(Si)orNi_3Si)} + V_{(\eta)}K_{(\eta)} \quad (V_{(\eta)} = 1 - V_{(Ni(Si)orNi_3Si)}) \text{ (upper)} \quad (10.1)$$

and

$$K_{QIvM} = \frac{K_{(\eta)}K_{(Ni(Si)orNi_3Si)}}{V_{(Ni(Si)orNi_3Si)}K_{(\eta)} + (V_{(\eta)})K_{(Ni(Si)orNi_3Si)}}, \qquad \text{(lower)} \qquad (10.2)$$

The upper bound of ROM lines in Fig. 10.5 is the same as the straight ROM line constructed by Davidson et al. [96Dav] shown in Fig. 5.18(b) and (c).

The fracture toughness of a single-phase η in Fig. 10.5 was taken as 1.7 $MPa.m^{1/2}$ which is the fracture toughness value of the specimens F6-1st and F6-2nd (Table 9.11). The fracture toughness of 100 vol. % Ni(Si) or Ni is not available in the literature. Therefore, fracture toughness of Ni(Si) was assumed to be 100$MPa.m^{1/2}$ based on Fig. 3 in [98ASM] showing the characteristic range of fracture toughness for Ni–base alloys.

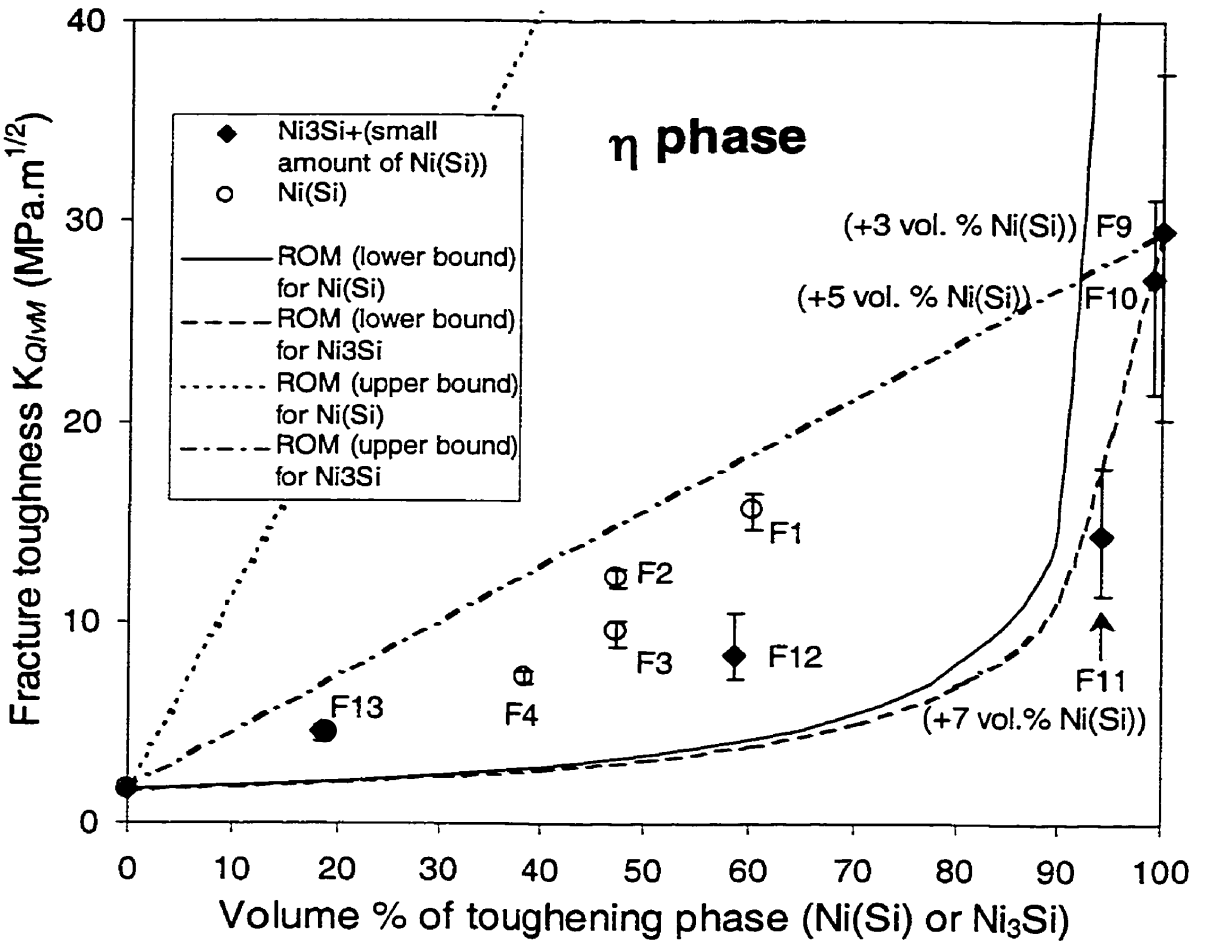

Fig. 10.5 Dependence of fracture toughness on the volume fraction of the Ni(Si) and Ni_3Si (or Ni_3Si+(small volume fraction of Ni(Si)) phases for the composites containing the brittle η phase. The upper and lower bound of ROM lines were calculated based on Eq. (10.1) and Eq. (10.2), respectively.

The fracture toughness of a single phase Ni_3Si in air was assumed to be 30 MPa.m$^{1/2}$, which is the average fracture toughness of F9 (Table 9.11). As opposed to the predictions showing something similar to a near-synergistic effect, as illustrated in Fig. 5.17, the trend of the fracture toughness values with increasing volume fraction of the toughening Ni(Si) or Ni_3Si phases in the present in-situ composites, falls much below the upper bound of ROM line. All the fracture toughness values are located slightly above or very close to the lower bound of ROM lines. The dependence of fracture toughness values on the volume fraction of toughening phases in Fig. 10.5 is quite similar to that in Fig. 5.18 for V-V_3Si, Nb(Cr,Ti)-Cr_2Nb, Nb(Si)-Nb_5Si_3, and Nb(Cr,Ti)-Cr_2Nb systems also established based on the

experimental results. Even if the composites fabricated in the present work might not behave ideally as predicted in the models in terms of microstructural parameters such as cohesive strength between the toughening phase and the matrix, and the alignment of the toughening phase, etc., the predictions made by the models are quite far away from the actual trend obtained from the experiments. It must be mentioned, however, that comparing the fracture toughness value of composite F1 toughened by 60.7 vol. % Ni(Si) with that of composite F12 toughened by similar vol. % Ni_3Si (58.7%) the toughening effect induced by Ni(Si) seems to be larger than that of Ni_3Si.

10.2.3.2 Fracture behaviour of toughened composites

Fracture behaviour of composites containing toughening phase (or microconstituent) in a brittle matrix was able to be interpreted by considering the fracture behaviour of lead/glass fiber composite and the derivation of the equation for crack bridging model by Ashby et al. [89Ash] in section 5.3.1.1. For in-situ composite F1 containing ductile Ni(Si) in the brittle η matrix when the ductile phase, Ni(Si) was pulled out (Fig. 9.30(a)) or when the ductile phase fractured in a brittle manner (Fig. 9.30(d)), the microcracking of the brittle matrix, η, was not observed. In other words, when there is no evidence of ductile phase stretching, that enhances the effect of crack bridging, the matrix remains uncracked and the energy absorption by the ductile phase is minimal. The complete pull-out of Ni(Si) from the η phase (Fig. 9.30(a)) is due to the weak interface between the Ni(Si) and η phases and the brittle fracture of ductile Ni(Si) phase (Fig. 9.30(d)) is due to the excessive plastic constraint in the Ni(Si) by the brittle matrix as for the case shown in Fig. 5.10(a). However, when the η matrix fractured, the ductile failure of Ni(Si) occurred without the excessive constraint in the Ni(Si) phase as shown in Fig. 9.30(b). This is the similar case to the one shown in Fig. 5.10(d) and in this case the energy absorption by the ductile phase is enhanced. However, fracture toughness values of the specimens F1 are close to one another since all the fracture mechanisms described above, i.e., ductile phase pull out, brittle fracture and ductile failure of ductile phase accompanying matrix cracking, were co-operating simultaneously in the same specimen during fracture. If the mechanism of ductile phase stretching without much constraint were prevailing, then higher fracture toughness would be expected.

10.2.4 Fracture toughness vs. yield strength (fracture strength)

Fig. 10.6 shows the relation between the yield strength and fracture toughness. Yield strength for the composites which exhibited a fracture without yielding during compression tests, is approximated by their fracture strength. In general, within a given class of material, when yield strength increases fracture toughness decreases or vice versa [90Cou, 99Dow]. For the composites which exhibited a yield during compression tests, the relationship between the yield strength and fracture toughness falls broadly into a scatter band between lines A and B in Fig. 10.6. Depending on the microconstituent phases and microstructural features such as refinement and distribution of toughening phases in the composites the relationship between the yield strength and fracture toughness varies within the band between lines A and B.

One interesting result is observed for F16 and F17 containing mostly Ni_2Si. Some of the F16 and F17 specimens exhibited yielding during compression test as shown by their stress-strain curves defined as the type 'B' in Table 9.20. Note that the yielding in composites F16 and F17 is induced by twining rather than slip deformation. These alloys bring the yield strength-fracture toughness relationship line close to the origin of the co-ordinate axes as shown by line C. To confirm twinning behaviour in Ni_2Si, alloy 24 from [96Son, 98Son[1]] and alloy F16 were etched using the solution reported in [90Tak[2]] after Knoop indentations had been made. Fig. 10.7(a) shows annealing twins observed in alloy 24 after homogenization at 1000°C for 200h. Figs. 10.7(b) and (c) clearly show the deformation mechanism in Ni_2Si by revealing deformation twins, rather than slip lines around the Knoop indentation. The twin bands manifested by the change in contrast compared to the untwinned area due to the lattice reorientation are clearly shown in Fig. 10.7(b) and (c). Therefore, the conclusion can be drawn that if the plasticity of an intermetallic alloy is a result of twinning both its fracture toughness and yield strength are probably rather low.

The relationship between the fracture strength and fracture toughness for the composites F3, F4, F13-F15, F18-F21 also falls in the scatter band between line A and B as the data points for the composites are located at the highest yield strength region in Fig. 10.6. This might indicate that the fracture strength of the composites obtained by compression tests is indeed very close to the theoretical yield strength of the composites. However, for some brittle composites which fractured before yielding (e.g., F5, F6, F13-F15, F18-F21 and F22), the

fracture toughness might be independent of the fracture strength as approximated by a horizontal line indicated as line D.

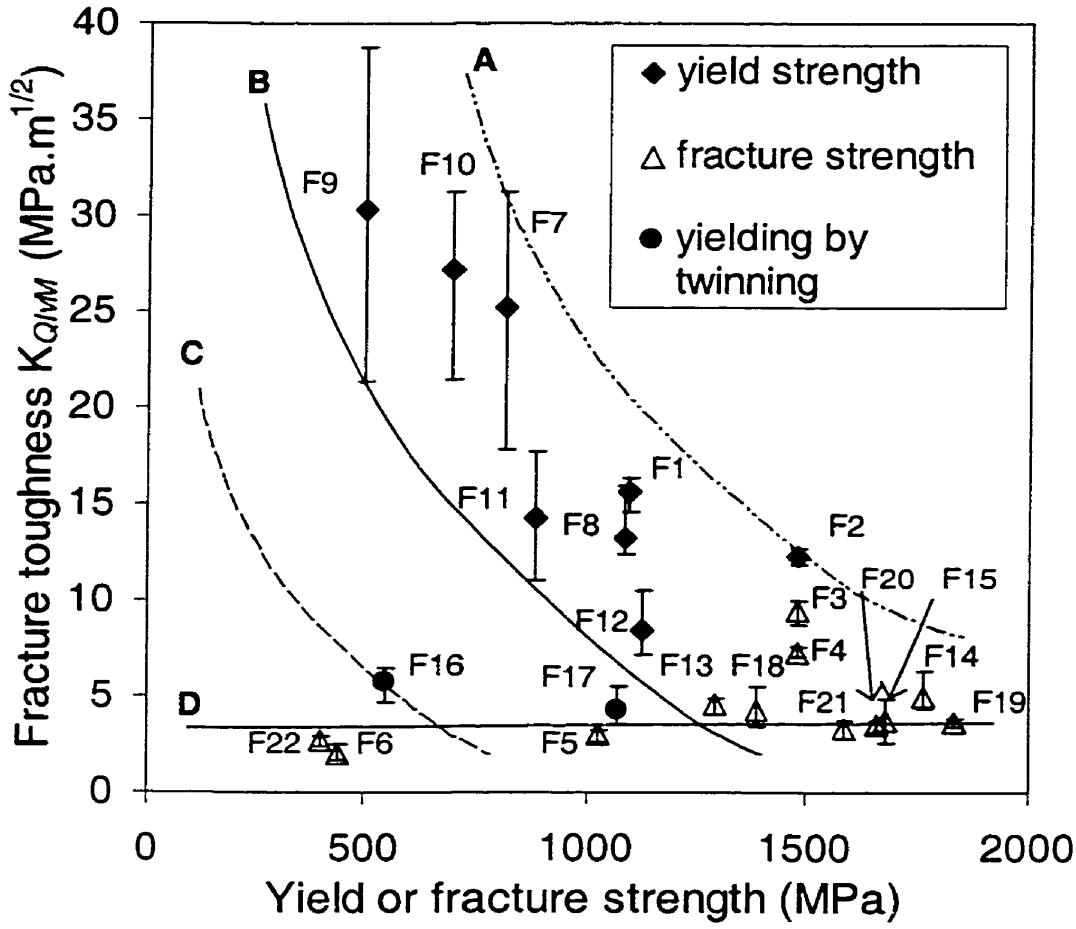

Fig. 10.6 The relation between the average yield strength and fracture toughness of the composites investigated in the present work.

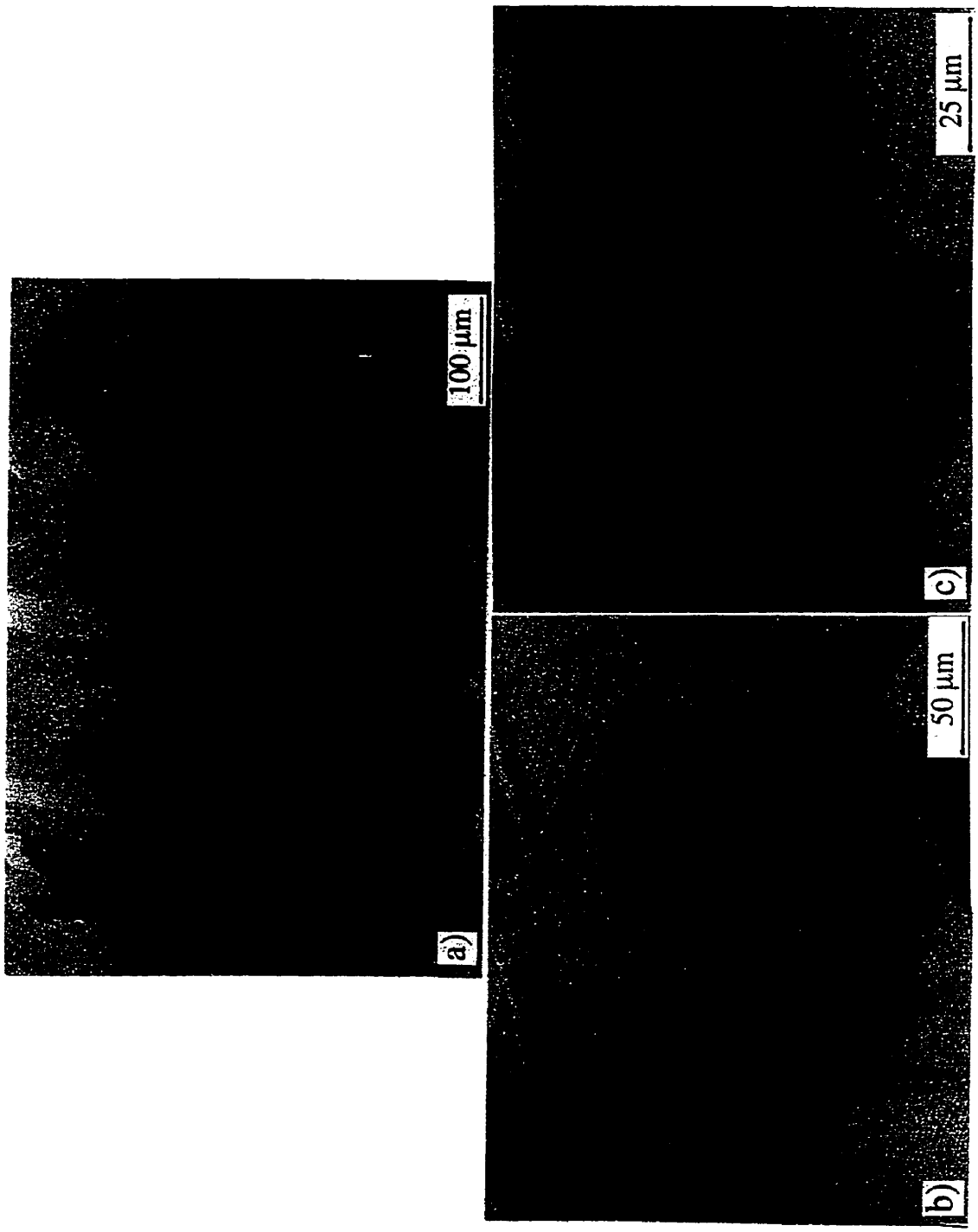

Fig. 10.7 Optical micrographs showing (a) the annealing twins observed in a single phase Ni_2Si alloy 24 and (b-c) the deformation twins developed by a Knoop indentation in a single phase Ni_2Si alloy F16.

10.2.5 Fracture toughness versus density

Fig. 10.8 shows the graphical representation of the fracture toughness vs. density of the alloys investigated in the present study (Table 9.10). This plot is solely made for the selection purposes of the composites with the best combination of high fracture toughness and low density and does not imply any fundamental relationship between these two material parameters. The rate of fracture toughness increment with increasing the density of composites in the present work is low for the low-density composites with densities up to about 7.5 g/cm^3 while it increases rapidly only for the composites with high-density which is the manifestation of the increase in the fracture toughness values with increasing the volume fraction of the toughening phase as shown in Fig. 10.5. However, it is noticeable that fracture toughness of composite F2 (microstructure in Fig. 9.15(b)) is twice higher than that of composites F16 having the density even higher than that of F2.

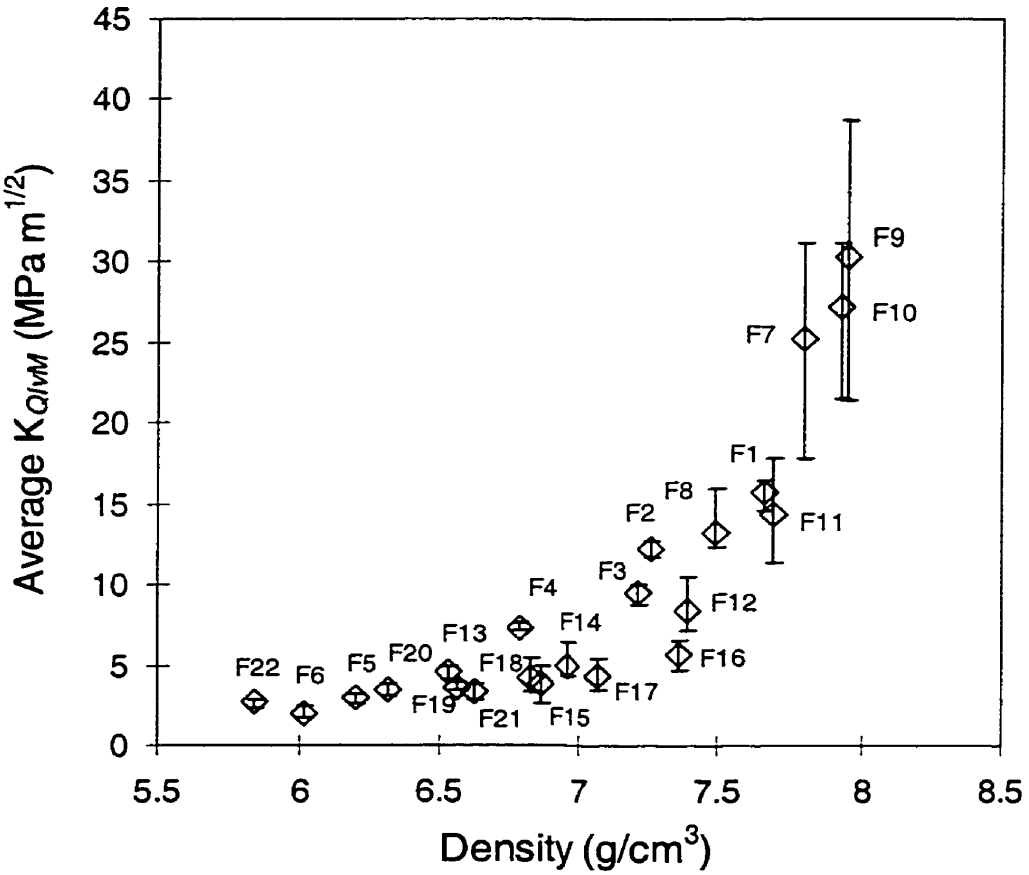

Fig. 10.8 The dependence of average fracture toughness values on the density of the investigated composites in the present study.

10.2.6 Design of intermetallic composites

On the basis of fracture toughness, yield strength, porosity and density of composites investigated in the present work, some of the in-situ composites such as F1, F2, F7, F8, and F11 seem to be promising candidates for further development as structural materials. Their properties are summarized in Table 10.4. These composites have very high yield strength (900-1500MPa) and quite high fracture toughness (12-16MPa.$m^{1/2}$) even if their microstructures were not optimized. By optimization of microstructure, the fracture toughness of the composites is expected to increase without loss in high yield strength. Specially for alloy F2 with the lowest density, it seems to be desirable to improve fracture toughness probably through making the interface Ni(Si)/η stronger, e.g., by boron doping because during fracture pull out is a prevailing mechanism of fracture (Fig. 9.31).

Table 10.4 Description of promising composites F1, F2, F8, and F11 for development of structural alloys.

Composites	Volume % of Phases		K_{IvM}* (MPa.$m^{1/2}$)	Porosity (%)	Yield strength (MPa)	Density (g/cm^3)
F1	Ni(Si)	60.7	15.6±0.7	0.09	1096±119	7.66
	η	39.3				
F2	η	52.6	12.1±0.3	0.06	1478±37	7.26
	Ni(Si)	47.4				
	Ni_3Si	Negligible				
F7	Ni_3Si	49.8	22.1±4.6	0.25	814±79	7.80
	Ni(Si)	34.6				
	η	15.6				
F8	Ni(Si)	62.4 (Ni(Si)	13.2±1.5	0.15	1086±37	7.49
	Ni_3Si	+Ni_3Si)				
	η	37.6				
F11	Ni_3Si	86.9	14.3±3.2	1.36	885±10	7.69
	Ni(Si)	7.2				
	η	5.1				
	$Ni_{31}Si_{12}$	0.8				

*: K_{IvM} values in this table are only for the specimens tested with S_1=35mm.

10.3 Indentation fracture toughness

10.3.1 Indentation microcracking pattern

Determination of the crack mode by simply polishing away the indented surface can be erroneous due to the existence of the core zone just beneath the indentation. The crack geometry including the core zone underneath the indentation was profiled by the serial sectioning method. Another way to determine the crack mode by the relationship between the crack length and indentation load also does not give a satisfactory result even if the method suggested by Shetty et al. [85She[1]] is used.

The test sample surface polishing on the SiC paper, followed by a finishing lapping with alumina powder does not seem to cause a residual stress on the surface. Such a conclusion can be drawn on the basis of the indent crack profiles along the depth as shown in Fig. 9.44 and 9.45, compared to Fig. 4 in [85She[1]] which shows the crack profile with reduced surface crack length relative to the subsurface crack extension due to the existence of surface compressive residual stress.

The existence of the core zone in which no cracks develop can be clearly seen in Figs. 9.44 and 9.45, and the residual compressive stress in the core zone was also confirmed by the secondary indentation which does not initiate four corner cracks (Fig 9.48 and 9.49). Along with the secondary indentation without developing four corner cracks, the higher hardness just beneath the primary indentation (Table 9.15) also indicates the existence of the residual compressive stress in the core zone.

The existence of the core zone and the corresponding stress field does not change the characteristic of the half-penny crack system, still exhibiting the 2/3 power dependence of crack length (c) on indentation load as seen in Fig. 9.41 and as also mentioned in [94Kal] and [95Paj]. This allows the use of equations from the literature for the penny-shaped crack system. However, it must be pointed out that the indentation fracture toughness can also be calculated on the basis of a Palmqvist crack system using Shetty et al. [85She[1]] model or its modified form for the indentation size effect (ISE) as shown in the present work (see section 9.4.2.2). They give similar values of the indentation fracture toughness as those calculated

from the equation based on the half-penny crack model by Evans and Charles [76Eva] and Lawn and Evans [77Law].

10.3.2 Indentation fracture toughness vs. CNB fracture toughness

An attempt was made to compare the two different fracture toughness measurement methods, i.e., indentation fracture toughness and chevron-notched bend (CNB) test. Comparing the fracture toughness values in the range of 1.3-1.8 MPa.$m^{1/2}$ (Table 9.17) for the η phase with 1.7 MPa.$m^{1/2}$ obtained from bulk CNB specimens containing only the η phase (F6-1st and F6-2nd tested in air (Table 9.11) and F6-1st tested in dry oxygen (Table 9.13), the indentation fracture toughness values are in a good agreement with those obtained on the bulk materials. However, it seems that indentation fracture toughness gives more conservative value.

Unfortunately, indentation fracture toughness values of $MgNi_2$ phase being in the range of 1.0-1.2 MPa.$m^{1/2}$ (Table 9.19) can not be directly compared to that of 2.7 MPa.$m^{1/2}$ (Table 9.11) obtained from bulk CNB specimens (F22) since the bulk CNB specimens contains 3.5 vol. % second phases including 2.1 vol. % of ductile Ni(Si) phase (Table 9.10). However, the above indentation fracture toughness values of single $MgNi_2$ phase seem to be quite reasonable in comparison to the fracture toughness of near single phase F22.

11. Summary and conclusions

The ternary Ni-Si-Mg phase diagram was established. The microstructural evolution of alloys and crystallographic structure and melting temperature of the intermetallic phases discovered in the present work were investigated. Based on the microstructural evolution of the alloys in the Ni-Si-Mg system, intermetallic in-situ composites in the Ni-rich region were fabricated to investigate the fracture behaviour and fracture toughness of composites. Environmental effect on fracture toughness and the composite rule-of-mixture-like relationship between fracture toughness and volume fraction of toughening phases were investigated. Indentation microcracking pattern and indentation fracture toughness of binary and ternary intermetallic phases were studied. Finally, a comparison of the fracture toughness by indentation and CNB methods was carried out. The following conclusions can be drawn from the present study.

11.1 Phase equilibria in the Ni-Si-Mg system

1. Quantitative analysis of alloys and their microconstituent phases containing both heavy and light elements by energy dispersive x-ray spectroscopy (EDS) using standard spectrum files created from intermetallic compounds containing the same heavy and light element provides more accurate results than using standards created from pure elements.
2. The phase equilibria in the ternary Ni-Si-Mg system were established. Four new ternary intermetallic phases ν, ω, μ, and τ, a ternary intermediate phase $Mg(Ni,Si)_2$ based on the $MgNi_2$ binary phase, three ternary intermetallic phases η, κ, and ζ previously reported by the present authors [98Son[1]], as well as the previously reported ternary phase [85Nor], Mg_2SiNi_3, were observed.
3. The volume of the hexagonal unit cell of $Mg(Ni,Si)_2$ which accommodates up to about 11 at. % Si at room temperature by replacing the Ni atoms, increases with increasing Si content, by the increase in lattice parameter, 'c' with an almost constant 'a'.
4. The previously reported $MgNi_6Si_6$ [81Buc] phase was not observed at the corresponding composition in the present work. The x-ray diffraction peaks determined to arise from the μ phase were indexed based on the crystallographic symmetry reported for the $MgNi_6Si_6$

phase. The hexagonal symmetry with the lattice parameters, a = 0.4948nm and c = 0.3738nm reported for the $MgNi_6Si_6$ phase (Cu_7Tb type) fits well to the phase designated as μ ($Mg(Si_{0.48},Ni_{0.52})_7$).

5. Most probably, the lattice structure of the ω phase ($(Mg_{0.52}Ni_{0.48})_7Si_4$) is a hexagonal structure of the Ag_7Te_4-type with the lattice parameters, a ≈ 1.3511nm c ≈ 0.8267nm.

11.2 Fracture behaviour, toughness, and yielding strength of the in-situ intermetallic composites

1. Most of P-LLD curves of the CNB specimens in the present work exhibit the stable crack growth region prior to the maximum load satisfying the requirement for the test considered to be valid. However, it was found that the specimens which have low fracture toughness and were tested with short support span (S_1) are more probable to have linear P-LLD curve. Fracture toughness, however, was not affected whether the P-LLD curves showed the linearity or stable crack growth region prior to the maximum load.
2. The ratio of the support span to the specimen width (S_1/W) does not seem to affect when fracture toughness values are lower or equal to 12 $MPa.m^{1/2}$. However, it is not clear whether or not the lower span length, S_1 affects the fracture toughness values in the higher range.
3. The highest average CNB fracture toughness, ≈ 31 $MPam^{1/2}$ was obtained for a near single phase Ni_3Si alloy containing about 3 vol. % of the Ni(Si) phase even if intergranular fracture in the Ni_3Si occurred.
4. No environmental effects (air, oxygen, and vacuum) were observed for most of the alloys in the present work.
5. Fracture toughness of near-single phase Ni_3Si decreases linearly with increasing fraction of fine (Ni(Si)+Ni_3Si) mixture and fine-grained Ni_3Si. The decrease in fracture toughness associated with fine (Ni(Si)+Ni_3Si) mixture might be related to the environmental effect of H on the interfaces between Ni(Si) and Ni_3Si in the mixture. However, the decrease in fracture toughness associated with fine-grained Ni_3Si might be mainly related to the increase in the fraction of inherently weak Ni_3Si grain boundary area.

6. Fine precipitates were observed on the fractured grain boundary facets and transgranular fracture surface of near-single phase Ni_3Si. Based on their precipitate-like appearance, they are probably hydrides formed during crack propagation. The formation of the precipitates is easier for the specimens tested in air than for those tested in vacuum or dry oxygen. In the same test environment, the formation of the precipitates is easier for the specimens, which have higher fracture toughness values (experiencing a higher stress intensity factor).
7. The fracture toughness values plotted against the volume fraction of the toughening phases, Ni_3Si (or Ni_3Si+(Ni(Si)) and Ni(Si) seems to follow close to the lower bound of composite rule of mixture. This result is different from that predicted by models in the literature, but similar to the results obtained by experiments in the literature.
8. The fracture toughness values of the selected composites calculated by determining the work-of-fracture (K_{wof}) are about 1.5 times higher than the fracture toughness values determined by the maximum load (K_{QIvM}).
9. Some of the composites can be promising candidates for the development of structural materials. They have very high yield strength (900-1500MPa) and quite high fracture toughness (12-16 $MPa.m^{1/2}$) with the densities in the range of 7.26-7.80g/cm^3. In particular, a cast alloy (F2) consisting of about 47 vol.% Ni(Si) and 53 vol.% η phases (Table 9.10) in a eutectic mixture shows fracture toughness of 12 $MPa.m^{1/2}$, yield strength of 1478MPa, and a density of 7.26g/cm^3.

11.3 Indentation fracture toughness test

1. The determination of crack systems (Palmqvist or half-penny) by simply polishing away the indented surface can be erroneous because of the existence of the core zone containing compressive stresses.
2. The crack length, *l* versus load, P plot does not pass through the origin despite that according to the crack profiles obtained by serial sectioning method, there is no evidence of surface residual stress as required by the indentation cracking models.
3. Crack profiles determined by a serial sectioning method show the pseudo half-penny shaped crack systems for the η phase in the 200g to 2000g range of loads. However, the κ phase develops either the "kidney shaped" or Palmqvist crack system at lower loads, 200g

and 500g, but also shows the pseudo half-penny shaped crack system at 2000g load. All the pseudo half-penny shaped cracks analyzed in the present work consist of core zone just beneath the indentations. That is why they are not typical half-penny (median) cracks and are called the "pseudo half-penny" cracks.

4. A residual compressive stress exists in the core zone which is manifested in a high hardness and the absence of corner cracks if a secondary indentation is made in the core zone. However, the hardness measured in the core zone close to the boundary between the core region and the cracked region yields lower hardness than that measured on the stress free surface.
5. The modification of the Shetty et al. [85She[1]] model for fracture toughness is proposed. It takes into account the indentation size effect (ISE) and yields results of K_{IC} independent of indentation loads as opposed to the original model which gives K_{IC} values dependent on loads.
6. The K_{IC} values calculated for the η and κ phases in the present work are quite diverse depending on the models used for calculations, regardless of the crack systems. However, comparing the indentation fracture toughness with the CNB fracture toughness on the bulk materials for the η phase, Shetty et al. model [85She[1]] as well as modified Shetty et al. model, Evans and Charles [76Eva], and Lawn and Evans [77Law] models yield the most reasonable values. Those equation models yield the indentation fracture toughness values 1.3-1.8 $MPa \cdot m^{1/2}$ for the η phase and 1.8-2.5 $MPa \cdot m^{1/2}$ for the κ phase.
7. Comparing the fracture toughness values obtained by indentation method with those obtained by bulk CNB specimens for the near η single phase alloy, the indentation fracture toughness values (~1.3-1.8 $MPa \cdot m^{1/2}$) are in a good agreement with those obtained from CNB test on bulk materials (1.7$MPa.m^{1/2}$).

References

34Tim: S.P. Timoshenko, and J.N. Goodier, in "Theory of Elasticity", McGraw-Hill, New York, 1934.

36Lav: F. Laves and H. Witte, Metallwirtsch, vol.15, p.840, 1936.

50Low: R. Lowrie, Trans. Metall. Soc., A.I.M.E., vol.194, p.1093, 1950.

53Lie: K.H. Lieser, and H. Witte, Z. Metallkunde, vol. 43, pp. 396-401, 1953.

59Dwi: A.E. Dwight, and P.A. Beck, Trans. AIME, vol.215, p.976-979, 1959.

60Pau: L. Pauling, The Nature of The Chemical Bond and The Structure of Molecules and Crystals, 3rd Ed., Cornell University Press, p. 403, 1960.

64Kuz: Yu.B. Kuz'ma, E.I. Gladyshevskii, and E.E. Cherkashin, Russian Journal of Inorganic Chemistry, vol. 9, no. 8, pp. 1028-1031, 1964.

64Sai: G.S. Saini, L.D. Calvert, and J.B. Taylor, Can. J.Chem., vol.42(7), p.1511-1517, 1964.

65Van: J.H.N. Van Vucht, and K.H. Buschow, J. Less-Common Met., vol.10, p.98-107, 1965.

66Van: J.H.N. Van Vucht, J. Less-Common Met., vol.11, p.308-322, 1966.

65Mor: J.B. Moran, Trans. Metall. Soc. of AIME, vol. 233, p. 1473-1482, 1965.

65Ram[1]: A. Raman, and K. Schubert, Z. Metallkunde, vol. 56, p.99-104, 1965.

65Ram2: A. Raman, and K. Schubert, Z. Metallkunde, vol. 56, p.40-43, 1965.

66Ima: R.M. Imamov, and Z.G. Pinsker, Soviet Physics-Crystallography, vol.11, no.2, pp. 182-188, 1966.

66Ram: A. Raman, Z. Metallkunde, vol.57, p.535-540, 1966.

66Tat: H.G. Tattersall, and G. Tappin, J. Mater. Sci., vol. 1, p.296-301, 1966.

67Coo: G.A. Cooper, and A. Kelly, J. Mech. Phys. Solids, vol.15, p.279-297, 1967.

68Hut: J.W. Hutchinson, J. Mech. Phys. Solids, vol. 16, p.13-31, 1968.

68Ric: J.R. Rice and G.R. Rosengren, J. Mech. Phys. Solids, vol. 16, p.1-13, 1968.

69Exn: H.E. Exner, Trans., AIME, vol. 245, no.4, p.677-683, 1969.

70Coo: G.A. Cooper, J. Mech. Phys. Solids, vol.18, p.179-187, 1970.

70Tho: P.H. Thornton, R.G. Davies, and T.L. Johnston, Metall. Trans., vol. 1, p. 207-218, 1970.

71Fra: K. Frank and K. Schubert, Acta Crystallogr. B, vol. 27(5), p.916-920, 1971.

71Sim: G. Simmons and H. Wang, in Single Crystal Elastic Constants and Calculated Aggregate Properties, A Handbook, 2nd ed., MIT Press, Cambridge, MA, p.215, 1971.

71Wil: K.J. Williams, J. Inst. Metals, vol.99, p.310-315, 1971.

71Ger: W.W. Gerberich, J. Mech. Phys. Solids, vol.19, p.71-87, 1971.

72Hin: P. Hing, and G.W. Groves, J. Mater. Sci., vol.1, p.427-434, 1972.

72Kom: Y. Komura, A. Nakaue, and M. Mitarai, *Acta Crystallographica*, vol. B28, p.727-732, 1972.

72Poo: L.P. Pook, Int. J. Frac., vol.8, p.103-108, 1972.

73Tak: S. Takeuchi, and E. Kuramoto, Acta metall. vol.21, p.415-425, 1973.

75Blu: J.I. Bluhm, Engineering Fracture Mechanics, vol. 7, p.593-604, 1975.

75Law[1]: B.R. Lawn, and T. Wilshaw, in "Fracture of Brittle Solids", Cambridge Univ. Press, 1975.

75Law[2]: B.R. Lawn and E.R. Fuller, J. Mater. Sci., vol. 10, p.2016-2024, 1975.

75Law[3]: B.R. Lawn and M.V. Swain, J. Mater. Sci., vol. 10, p.113-122, 1975.

75Law[4]: B.R. Lawn, J. Mater. Sci., vol. 10, p.1236-1239, 1975.

75Ros: L.R.F. Rose, Mech. Mater. vol.6, p.11, 1975.

76Eva: A. G. Evans and E.A. Charles, J. Am. Ceram. Soc., vol. 59, p. 371-372, 1976.

76Kur: E. Kuramoto, and D.E. Pope, Philos. Mag., vol.33, p.625, 1976.

76Sra[1]:J.E. Srawley, Int. J. Fracture Mech., vol. 12, p.475-476, 1976.

76Sra[2]:J.E. Srawley and B. Gross, in "Cracks and Fracture", p.559-579, ASTM STP, no. 601, American Society for Testing and Materials, Philidelphia, Pa, 1976

77Blu: J.I. Bluhm, in Fracture 1977, ed. D.M.R. Taplin, vol.3, p.409-417, University of Waterloo Press, Waterloo, Ont. Ca., 1977.

77Fro: F. Frohlich, P. Grau, and W. Grellmann, Phys. Status Sol. A, vol. 42, p. 79-89, 1977.

77Law: B.R. Lawn and A.G. Evans, J. Mater. Sci., vol.12, p.2195-2199, 1977.

77Ogi: I.M. Ogilvy, C.M. Perrott, and J.W. Suiter, Wear, vol.43, p.239-252, 1977.

77Wes: J.H. Westbrook, Metall. Trans., 8A, p.1327-1360, 1977.

78Aok: K. Aoki, and O. Izumi, J. Mater. Sci., vol.13, p. 2313-2320, 1978.

78Cul: B.D. Cullity, in Elements of x-ray diffraction, 2nd ed., Addison-Wesley Publishing Company, Inc., p.352-358, 1978.

78SPD: Selected Powder Diffraction Data Search Manual, JCPDS, International Center for Diffraction Data, 1601 Parklane, Swarthmore, PA 19081, USA, 1978.

79Aok[1]: K. Aoki, and O. Izumi, J. Japan Inst. Metals, vol.43, p.1190, 1979.

79Aok[2]: K. Aoki, and O. Izumi, Acta metall. vol.27, p.807-816, 1979.

79Bar: L.M. Barker, Inter. J. Frac. vol.15, no.6, p.515-536, 1979.

79Eva: A.G. Evans, in "Fracture mechanics applied to brittle materials", STP 678, (ed. S.W. Freiman), Philadelphia, PA, ASTM, p.112-135, 1979.

79Hag: J.T. Hagan, J. Mater. Sci., vol. 14, p.2975-2980, 1979.

79Liu: C.T. Liu, and H. Inouye, Metall. Trans. A, 10A, p.1515-1525, 1979.

79Mar: R.H. Marion, in Fracture Mechanics Applied to Brittle Materials, STP 678, ed., S.W. Freiman, ASTM, Philadelphia, PA, p.103, 1979.

80Cot: B. Cotterell and J.R. Rice: Int. J. Fracture, vol. 16, p.155-69, 1980.

80Mun[1]: D. Munz, R.T. Bubsey and J.L. Shannon, Journal of Testing and Evaluation, vol.8, no.3, p.103-107, 1980.

80Mun[2]: D.G. Munz, J.L. Shannon, Jr., and R.T. Bubsey, Int. J. Frac., vol. 16, p.R137-R141, 1980.

80Mun[3]: D. Munz, R.T. Bubsey, and J.L. Shannon, Jr., J.Am. Ceram. Soc., vol.63, no.5-6, p.300-305, 1980.

81Buc: W. Buchholz, and H-U. Schuster, *anorg. allg. Chem.*, vol. 482, pp. 40-48, 1981.

81Krs: V.V. Krstic, P.S. Nicholson, and R.G. Hoagland, J.Am. Ceram. Soc., vol. 64, p.499-504, 1981.

81Por: D.A. Porter, and K.E. Easterling, in Phase Transformations in Metals and Alloys, Van Nostrand Reinhold Company, p. 27, 1981.

81Sei: A. Seibold, Z. Metallkunde, vol. 72, p. 712-719, 1981.

81Shi: T.T. Shih, Journal of Testing and Evaluation, vol.9, no.1, p.50-55, 1981.

82Lan: J. Lankford, J. Mater. Sci. Lett., vol.1, p.493-495, 1982.

82Nii: K. Niihara, R. Morena, and D.P.H. Hasselman, J. Mater. Sci. Lett., vol.1, p.13-16, 1982.

83Bar: L.M. Barker, Engineering Fracture Mechanics, vol. 17, p.289-312, 1983.

83Krs: V.D. Krstic, Philosophical Magazine A, vol. 48, no.5, p.695-708, 1983.

83Mun: D.Munz, "Fracture Mechanics of Ceramics" R.C. Bradt, A.G. Evans, D.P.H. Hasselman, and F.F.Lange, eds., Plenum Press, vol. 6, p.1-25, 1983.

83Nii: K. Niihara, Journal of Materials Science Letters, vol. 2, p.221-223, 1983.

83Tak: T. Takasugi, and O. Izumi, Acta Metall., vol.31, p.1187-1202, 1983.

83War: R. Warren and H. Matzke, in Proceedings of the International Conference on the Science of Hard Materials, Jackson, Wyoming, Plenum, New York, p. 563, 1983.

84Chu: L. Chuck, E.R. Fuller, Jr., and S.W. Freiman, in "Chevron-Notched Specimens: Testing and Stress Analysis", ASTM STP 855, J.H. Underwood, S.W. Freiman, and F.I. Baratta, eds., American Society for Testing andMaterials, Philadelphia, p.167-175, 1984.

84Hul: D. Hull and D.J. Bacon, in "Introduction to Dislocations", 3rd edition, Pergamon Press, p.212, 1984.

84Liu[1]: C.T. Liu, and J.O. Stiegler, Ductile Intermetallic Compounds, Science, vol. 226, p.636-642, 1984.

84Liu[2]: C.T. Liu, International Metals Reviews, vol.29, p.168-194, 1984.

84Mey: M.A. Meyers and K.K. Chawla, in Mechanical Metallurgy (Principles and Applications), p.561-563, Prentice-Hall, Inc., Englewoo Cliffs, New Jersey, 1984.

84Och: S. Ochiai, Y. Oya, and T. Suzuki, Acta Metall. vol. 32, p.289-298, 1984.

84Pop: D.P. Pope, and S.S. Ezz, Int. Metals Rev. vol.29, p.136-167, 1984.

84Sch: E.M. Schulson, International Metals Reviews, vol. 29, p.195-209, 1984.

84Tau: A.I. Taub, S.C. Huang, and K.M. Chang, Metall. Trans. A, vol.15A, p.399-402, 1984.

84Wu[1]: S-X. Wu, Engineering Fracture Mechanics, vol. 19, no.2, p.221-232, 1984.

84Wu[2]: S-X. Wu, in "Chevron-Notched Specimens: Testing and Stress Analysis", ASTM STP 855, J.H. Underwood, S.W. Freiman, and F.I. Baratte, eds., American Society for Testing and Materials, Philadelphia, p.176-193, 1984.

85Liu: C.T. Liu, C.L. White, and J.A. Horton, Acta Metall., vol.33, p.213-219, 1985.

85Nor: D. Noreus, L. Eriksson, L. Gothe, and P.-E. Werner, *J. Less-Common Met.,* 1985, vol. 107, pp. 345-349.

85Rit: R.O. Ritchie and A.W. Thompson, Metall. Trans. A, vol. 16A, p.233-248, 1985.

85She[1]: D.K. Shetty, I.G. Wright, P.N. Mincer, and A.M. Clauer, J. Mater. Sci., vol.20, p.1873-1882, 1985.

85She[2]: D.K. Shetty, A.R. Rosenfield, and W.H. Duekworth, J.Am.Ceram.Soc., vol.68, no. 10, p.C282-C284, 1985.

85Sur: S. Suresh, Metall. Trans. A, vol. 16A, p. 249-260, 1985.

85Tak: T. Takasugi and O. Izumi, Acta metall. vol.33, p.1247-1258, 1985.

85Vil: P. Villars, and L.D. Calvert, *Pearson's Handbook of Crystallographic Data for Intermetallic Phases*, vol. 1, ASM, 1985.

85Wer: P.-E. Werner, L. Eriksson, and M. Westdahl, *J. Appl. Cryst.*, vol. 18, pp. 367-370, 1985.

86Eva: A.G. Evans, and R.M. McMeeking, Acta Metall., vol.34, p.2435-2441, 1986.

86Oli: W.C. Oliver, and C.L. White, "High-Temperature Ordered Intermetallic Alloys II" edited by N.S. Stoloff, C.C. Koch, C.T. Liu, and O. Izumi, vol. 81, p.241-246, Proc. MRS Symp., 1986.

86Tak: T. Takasugi and O. Izumi, Acta Metall. vol.34, no.4, p.607-618, 1986.

87Exn: E.L. Exner, J.R. Pickens, and J. Gurland, J. Metallugical Trans. A, vol. 9A, p.736-738, 1987.

87Ezz: S.S. Ezz, D.P. Pope, and V.Paidar, Acta metall., vol.35, p.1879-1885, 1987.

87Fle: R.L. Fleisher, Journal of Materials Science, vol. 22, p.2281-2288, 1987.

87Him: G. Himsolt, D. Munz, and T.Fett, J. Am. Ceram. Soc., vol.70, no.6, p.c133-c135, 1987.

87Rit: R.O. Ritchie, in Mechanical Behaviour of Materials-V, eds., M.G. Yan, S.H. Zhang, and Z.M. Zheng, Pergamon Press, vol.2, p. 1399, 1987.

87Pam: P. K. Brindley, in High-Temperature Ordered Intermetallic Alloys II, MRS, vol. 81, p.419-424, 1987.

87Ros: L.R.F. Rose, J. Mech.Phys. Solids, vol.35, p.383-405, 1987.

88Ant: D.L. Anton, in High Temperature/High Performance Composites, MRS, vol. 120, p.57-64, 1988.

88Bud: B. Budiansky, J.C. Amazigo, and A.G. Evans, J. Mech. Phys. Solids, vol. 36, p.167-187, 1988.

88Ell: C.K. Elliott, G.R. Odette, G.E. Lucas and J.W. Sheckherd, in High Temperature/ Performance Composites, eds., F.D. Lemkey, S.C. Fishman, A.G. Evans, and J.R. Strife, MRS, Pittsburgh, Pennsylvania, vol. 120, p.95-101, 1988.

88Izu: O. Izu and T. Takasugi, J. Mater. Res., vol.3, no.3, p.426-440, 1988.

88Kum: K.S. Kumar, and J.R. Pickens, Scripta Met., vol. 22, p. 1015-1018, 1988.

88Mas: N. Masahashi, T. Takasugi, and O. Izumi, Acta Metall., vol. 36, p.1823-1836, 1988.

89Ash: M.F. Ashby, F.J. Blunt, and M. Bannister, Acta Metall., vol. 37, p.1847-57, 1989.

89AST[1]: ASTM standard E 1304-89.

89AST[2]: ASTM standard E9-89a.

89Cao: H.C. Cao, B.J. Dalgleish, H.E. Deve, C. Elliott, A.G. Evans, R. Mehrabian, and G.R. Odette, Acta Metall., vol. 37, p.2969-2977, 1989.

89Eva: A.G. Evans and D.B. Marshall, Acta Metall., vol. 37, p.2567-2583, 1989.

89Fle: R.L. Fleisher, and A.I. Taub, JOM, sep. P.8-11, 1989.

89Fli: B.D. Flinn, M. Ruhle, and A.G. Evans, Acta Metall., vol. 37, p.3001-3006, 1989.

89Gho: A. Ghosh, M.G. Jenkins, K.W. White, A.S. Kobayashi, and R.C. Bradt, in "Ceramic Materials & Components for Engines", V.J. Tennery, ed., The American Ceramic Society, Westerville, OH., p.592-600, 1989.

89Izu: Osamu Izumi, Materials Transactions, JIM, vol.30, no.9, p.627-638, 1989.

89Liu: C.T. Liu, E.H. Lee, and C.G. McKamey, Scripta Metallurgica, vol. 23, p.875-880, 1989.

89Liv: D. Livingston, E.L. Hall, and E.F. Koch, in High Temperature Ordered Intermetallic Alloys III, vol. 133, eds., C.T. Liu, A.I. Taub, N.S. Stoloff, and C.C. Koch, MRS, Pittsburgh, p. 243-248, 1989.

89Mab: H. Mabuchi, K. Hirukawa, and Y. Nakayama, Scripta Metall., vol. 23, p. 1761-1766, 1989.

89Mat: P.A. Mataga, Acta Metall., vol. 37, p.3349-3359, 1989.

89Ode: G.R. Odette, H.E. Deve, C.K. Elliott, Hasegawa and G.E. Lucas, in Interfaces in Metal-Ceramic Composites, eds., R.Y. Lin, R.J. Arsenault, G.P. Martins and S.G. Fishman, Warrendale, PA, MMMs, p.443, 1989.

89Ohb: Y. Ohba and N. Sakuma, Acta. Metall., vol. 37, p. 2377-2384, 1989.

89Oli: W.C. Oliver, "High-Temperature Ordered Intermetallic Alloys III", vol. 133, eds:C.T.Liu, A.I.Taub, N.S. Stoloff, and C.C. Koch, p.397-402, 1988.

89Pon[1]: C.B. Ponton, R.D. Rawlings, Materials Science and Technology, vol.5, p961-976, 1989.

89Pon[2]: C.B. Ponton, R.D. Rawlings, Materials Science and Technology, vol.5, p865-871, 1989.

89Sch: J.H. Schneibel, and W.D. Ponter, in High Temperature Ordered Intermetallic Alloys III, eds., C.T.Liu, A.I. Taub, N.S. Stoloff, and C.C. Koch, MRS Symp. Proc., vo. 133, MRS, Pittsburgh, p. 335-340, 1989.

89Sun: J. Sung, and P.S. Nicholson, J. Am. Ceram. Soc., vol.72, no.6, p.1033-1036, 1989.

89Suz: T.Suzuki, Y.Mishima, and S. Miura, Int. Iron Steel Inst. Japan, vol.29, p.1, 1989.

89Tak: T. Takasugi, S. Watanabe, O. Izumi, and N.K. Fat-Halla, Acta metall. vol. 37, no.12, p.3425-3436, 1989.

89Tau: A.I. Taub and C.L. Briant, Metall. Trans. A, vol. 20A, p.2025-2032, 1989.

90AST: ASTM Standard E 399-90.

90Cha[1]: K.S. Chan, Metall. Tarans. A, vol. 21A, p. 69-80, 1990.

90Cha[2]: K.S. Chan, Metall. Tarans. A, vol. 21A, p. 2687-2699, 1990.

90Cou: T.H. Courtney, in Mechanical Behaviour Of Materials, McGraw-Hill, Inc., 1990.

90Eva: A.G. Evans, J. Am. Ceram. Soc., vol.73, p.187-206, 1990.

90Dev: H.E. Deve, A.G. Evans, G.R. Odette, R. Mehrabian, M.L. Emiliani, and R.J. Hecht, Acta Metall. Mater., vol. 38, p. 1491-1502, 1990.

90Kim: Y.-W. Kim, and F.H. Froes, in "High-Temperature Aluminides and Intermetallics", S.H. Whang, C.T. Liu, D. Pope, and J.O. Stiegler, eds., TMS-AIME, Warrendale, PA, p.465-492, 1990.

90Liu[1]: C.T. Liu, J.O. Stiegler, and F.H. Froes, in Metals Handbook, 10th ed., ASM Int., vol.2, p.913-941, 1990.

90Liu[2]:C.T.Liu, and E.P. George, Scripta Metallurgica et Mat., vol. 24, p. 1285-1290, 1990.

90Liu[3]:C.T.Liu, C.G. Mckamey, and E.H. Lee, Scripta Metallurgica et Mat., vol.24, p.385-390, 1990.

90Liv: J.D. Livingston and E.L. Hall, J. Mater. Res., vol.5, p.5-8, 1990.

90Mas: T.B. Massalski, P.R. Subramanian, H. Okamoto, and L. Kacprzak, *Binary Alloy Phase Diagrams*, 2nd ed., ed. T.B. Massalski, ASM International, Material Park, OH, 1990.

90Met: Metals Handbook®, Tenth Edition, vol.2, ASM International, 1990.

90Pow: W.O. Powers, and J.A. Wert, Met. Trans., 21A, p. 145-151, 1990.

90Sch: E.E. Schmid, K.V. Oldenburg, and G. Frommeyer, Z. Metallkd., vol. 81, p. 809-15, 1990.

90Tak[1]:T.Takasugi, M. Nagashima, and O. Izumi, Acta Metall. Mater. vol.38, no.5, p.747-755, 1990.

90Tak2: T.Takasugi, D.Shindo, O.Izumi, and M. Hirabayashi, Acta metall. Mater., vol.38, no.5, p.739-745, 1990.

90Wit: P.A. Withey and P. Bowen, International Journal of Fracture, vol. 46, p. R55-R59, 1990.

91Bow: A.F. Bower and M. Ortiz, J. Mech. Phys. Solids, vol. 39, p.815-858, 1991.

91Cal: W.D. Callister, Jr., *Materials Science and Engineering*, 2nd ed., John Wiley & Sons, Inc., 1991.

91Cao: H.C. Cao, and A.G. Evans, Acta Metall., vol. 39, p.2997-3005, 1991.

91Cha: K.S. Chan, Metall. Trans. A, vol. 22A, p.2021-2029, 1991.

91Gla: J.C. Glandus, T. Rouxel, and Q. Tai, Ceramics International, vol. 17, p. 129-135, 1991.

91Li: H. Li, and R.C. Bradt, Mater. Sci. Eng., vol. A142, p.51-61, 1991.

91Liu: C.T.Liu, and W.C. Oliver, Scripta Metallurgica et Mat. vol.25, p.1933-1937, 1991.

91Liv: J.D. Livingston, and E.L. Hall, *High Temperature Ordered Intermetallic Alloys IV,* vol.213, MRS, eds.,L.A. Johnson, D.E. Pope, and J.D. Stiegler, pp. 443-448. 1991.

91Nas: P. Nash, Phase Diagrams of Binary Nickel Alloys (Monograph Series on Alloy Phase Diagram), ASM International, Materials Park, OH, 1991.

91Tak[1]: T. Takasugi, and A. Yoshida, J. Mat. Sci., vol. 26, p.3517-3525, 1991.

91Tak[2]: T. Takasugi, H. Suenaga, and O. Izumi, J. Mater. Sci, vol. 26, p.1179-1186, 1991.

91Vir: I.S. Virk, and R.A. Varin, Scripta Metall., vol. 25, p.1381-1386, 1991.

91Wit: P.A. Withey and P. Bowen, in "Mechanical Behaviour of Materials VI", M. Jono, and T. Inoue, eds., p.153-158, 1991.

92Cha: K.S. Chan, Metall. Trans. A, vol. 23A, p. 183-199, 1992.

92Jen: M.G. Jenkins, M.K. Ferber, A. Ghosh, J.T. Peussa, and J.A. Salem, in "Chevron-Notch Fracture Test Experience:Metals and Non-Metal", ASTM STP 1172, K.R. Brown and F.I. Baratta, eds., American Society for Testing and Materials, Philadelphia, p.159-177, 1992.

92Liu: Y. Liu, J.D. Livingston, and S.M. Allen, Metal. Trans. A, vol. 23A, p.3303-3308, 1992.

92Liv: J.D. Livingston, Phys. Status Solidi A, vol. 131, p. 415-23, 1992.

92Mer: I. Merkel, and U. Messerschmidt, Materials Science and Engineering, vol. A151, p.131-135, 1992.

92Mur: L. Murugesh, K.T. Venkateswara Rao, L.C. Edjonche, and R.O. Ritchie, in Intermetallic Matrix Composite II, eds., D.B. Miracle, D.L. Anton, and J.A. Graves, Pittsburgh, Pennsylvania, MRS, vol. 273, p.433-438, 1992.

92Rav: K.S. Ravichandran, Acta metall. mater., vol. 40, no.5, p. 1009-1022, 1992.

92Ric: D.W. Richerson, in Modern Ceramic Engineering, 2nd ed., M.Dekker, New York, p.168, 1992.

92Sal: J.A. Salem, J.L. Shannon, Jr., and M.G. Jenkins, in "Chevron-Notch Fracture Test Experience:Metals and Non-Metals", ASTM STP 1172, K.R. Brown and F.I. Baratta, eds., American Society for Testing and Materials, Philadelphia, p.9-25, 1992.

92Sob: W.O. Soboyejo, D.S. Schartz, S.M.L. Sastry, Metall. Trans. A, vol. 23A, p.2039-2059, 1992.

92Tve: V. Tvegarrd, Int. J. Mech. Sci., vol.34, p.635-49, 1992.

92Vir: I.S. Virk and R.A. Varin, Metallurgical TransactionsA, vol. 23A, p.617-625, 1992.

93Ant: D.L. Anton and D.M. Shah, in High Temperature Ordered Intermetallic Alloys V, eds., I. Baker, R. Darolia, J.D. Whittenberger, and M.H. Yoo, Mat. Res. Soc., Pittsburgh, Pennsylvania, vol. 288, p.141-150, 1993.

93Ash: M.F. Ashby, Acta metall. mater., vol. 41, no. 5, p.1313-1335, 1993.

93Bys: J. Bystrzycki, and R.A. Varin, Scripta Metallurgica et Materialia, vol.29, p.605-609, 1993.

93Cha[1]: K.S. Chan, Metall. Trans. A, vol. 24A, p.569-583, 1993.

93Cha[2]: K.S. Chan, M.Y. He, and J.W. Hutchinson, Mat. Sci. Eng., vol. A167, p.57-64, 1993.

93Cho: S.R. Choi, J.A. Salem, and M.G. Hebsur, Journal of Materials Science, vol. 28, no. 1-3, p.155-160, 1993.

93Chu: F. Chu, and D. P. Pope, Scripta Metallurgica et Materialia, vol.28, p.331-336, 1993.

93Ebr: F. Ebrahimi, D.T. Hoelzer, and J.R. Castillo-Gomez, Materials Science and Engineering, vol. A. 171, p.35-45, 1993.

93Haz: P.M. Hazzledine and P. Pirouz, Scripta Metal et Mater., vol. 28, p. 1277-1282, 1993.

93He: M.Y. He, F.E. Heredia, D.J. Wissuchek, M.C. Shaw, and A.G. Evans, Acta Metall. Mater., vol. 41, p.1223-1228, 1993.

93Her: F.E. Heredia, M.Y. He, G.E. Luca, A.G. Evans, H.E. Deve, and D. Konitzer, Acta Metall. Mater., vol. 41, p.505-511, 1993.

93Li[1]: G.H. Li, H.S. Gill, and R.A. Varin, Metall. Trans. A, vol. 24A, p.2383-2391, 1993.

93Li[2]: H. Li, A. Ghosh, Y.H. Han, and R.C. Bradt, J. Mater. Res., vol. 8, p.1028-1032, 1993.

93Liu: C.T. Liu and N.S. Stoloff, in Diffusion in ordered alloys, eds., B. Fultz, R.W. Chan, and D. Gupta, p.223-246, 1993.

93Sha: M.C. Shaw, D.B. Marshall, M.S. Dadkhah, and A.G. Evans, Acta Metall. Mater., vol. 41, p.3311-3322, 1993.

93Sob[1]: W.O. Soboyejo, K.T.V. Rao, S.M.L. Sastry, and R.O. Ritchie, Metall. Trans. A, vol. 24A, p.585, 1993.

93Sob[2]: W.O. Soboyejo, and S.M.L. Sastry, Materials Science and Engineering, vol. A171, p.95-104, 1993.

93Str: M.J. Strum and G.A. Henshall, High Temperature Ordered Intermetallic Alloys V, vol. 288, eds., I. Baker, R. Darolia, J.D. Whittenberger, M.H. Yoo, p.1093-1098.

93Tak: W. Takahashi, H. Anada, and Y. Sida, *The Sumitomo Search* (Special Issue for New Material), no.52, 1993, pp. 89-100.

93Ulv: J.H. Ulvensoen, G. Rorvik, T. Kyvik, K. Pettersen, and L. L'Estrade, Structural Intermetallics, Proceedings of the First International Symposium on Structural Intermetallics, eds., R. Darolia, J.J. Lewandowski, C.T. Liu, P.L. Martin, D.B. Miracle, M.V. Nathal, p.707-713, 1993.

93Var: R.A. Varin, G. Li, and H.G. Gill, Processing and Fabrication of Advanced Materials For High Temperature Applications-II, eds., V.A. Ravi and T.S. Strivatsan, The Minerals, Metals, and Materials Society, p.127-140, 1993.

93Xia: L. Xiao and R. Abbaschian: Metall. Trans. A, vol. 24A, p. 403-15, 1993.

93Yoo: M.H. Yoo, S.L. Sass, C.L. Fu, M.J. Mills, D.M. Dimiduk, and E.P. George, Acta Metall. Mater. vol. 41, no.4, p.987-1002, 1993.

94Cha[1]: K.S. Chan, in High Temperature Ordered Intermetallic Alloys VI, eds., J. Horton I. Baker, S. Hanada, R.D. Noebe, and D.S. Schwartz, MRS, Pittsburgh, Pennsylvania, vol. 364, p.469-480, 1994.

94Cha[2]: K.S. Chan, Metall. Trans. A, vol. 25A, p.299-308, 1994.

94Che: Z. Chen, I.P. Jones, N. Saurders, and C.J. Small, Scripta Metallurgica et Materialia, vol.30, no.11, p.1403-1408, 1994.

94Dra: G.W. Dransmann, R.W. Steinbrech, A. Pajares, A. Dominguez-Rodriguez, and A.H. Heure, J. Am. Ceram. Soc., vol. 77, no.5, p.1194-1201, 1994.

94Kal: M.S. Kaliszewski, G. Behrens, A.H. Heuer, M.C. Shaw, D.B. Marshall, G.W. Dransmann, R.W. Steinbrech, A. Pajares, F. Guiberteau, F.L. Cumbrera, and A. Dominguez-Rodriguez, J. Am. Ceramic. Soc., vol.77, no.5, p.1185-1193, 1994.

94Li: G.H. Li, and R.A. Varin, Material Science and Engineering, vol. A183, p.145-155, 1994.

94Liu: Y. Liu, J.D. Livingston, and S.M. Allen, Metallurgical and Materials Transactions A, vol. 26A, p. 1441-1447, 1995.

94Noe: R.D. Noebe, NASA Technical Memorandum 106534, Cleveland, Ohio, April, 1994.

94Ven: K.T. Venkateswara Rao, G.R. Odette, and R.O. Ritchie, Acta metall. mater., vol.42, no.3, p.893-911, 1994.

94Wan: X.J. Wan, J.H. Zhu, and K.L. Jing, Scripta Metal. Mater., vol.31, no.6, p.677-681,1994.

95And: T.L. Anderson, Fracture Mechanics, CRC Press, 2nd edition, 1995.

95Bys: J. Bystrzycki, K.J. Kurzydlowski, and R.A. Varin, Advances in Science and Technology, vol.9, p.393-400, 1995.

95Cha[1]: K.S. Chan, in " High-Temperature Ordered Intermetallic Alloys VI", ed. J. Horton, vol. 364, MRS, p. 469-480, 1995.

95Cha[2]: K.S. Chan, Metall. Trans. A, vol. 26A, p.1407-1418, 1995.

95Cha3: K.S. Chan, and Y-M, Kim, Acta. Met. et. Mat., vol.43, no.2, p.439-451, 1995.

95Geo: E.P. Geo, C.T.Liu, H. Lin, D.P. Pope, Mater. Sci. Eng. A, vol. 192/193, p.277-288, 1995.

95Hor: J.A. Horton and J.M. Schneibel, In "High Temperature Ordered Intermetallic Alloys VI", J. Horton, I. Baker, S. Hanada, R.D. Noebe, and D.S. Schwartz, eds., MRS, vol. 363, p.1107-1110, 1995.

95Liu: Y. Liu, J.D. Livingston, and S.M. Allen, *Metallurgical and Material Transactions A*, 1995, vol. 26A, pp. 1441-1447.

95Men: M.G. Mendiratta, R. Goetz, D.M. Dimiduk, and J. Lewandowski, Metall. Mater. Trans. A, vol. 26A, p.1767-76, 1995.

95Nak: M. Nakamura, in Intermetallic Compounds Principles and Properties, vol.2 eds., J.H. Westbrook, and R.L. Fleisher, John Wiley & Sons, Chichester, p.885, 1995.

95Paj: A. Pajares, F. Guiberteau, R.W. Steinbrech and A. Dominguez-Rodriguez, Acta Metall. Mater., vol. 43, no.10, p.3649-3659, 1995.

95Var: R.A. Varin and G.H. Li, Materials Science and Engineering, A192/193, p.59-68, 1995.

95Wes[1]: J.H. Westbrook, in Intermetallic Compounds, Principles and Practice, vol. 1-Principles, eds., J.H. Westbrook, and R.L. Fleisher, p.14, 1995.

95Wes[2]: J.H. Westbrook, in Intermetallic Compounds, Principles and Practice, vol. 1-Principles, eds., J.H. Westbrook, and R.L. Fleisher, p.107-109, 1995.

96Ask: D.R. Askeland, *The Science and Engineering of Materials*, 3rd ed., Chapman & Hall, pp. 823-833, 1996.

96Ben: C.D. Ben, L. Murugesh, K.T.V. Rao, and R.O. Ritchie, Intermetallics, vol. 4, p.23, 1996.

96Cha: K.S. Chan, Metallurgical and Materials Transactions A, vol. 27A, p.2518-2531, 1996.

96Dav: D.L. Davidson, K.S. Chan, and D.L. Anton, Metallurgical and Materials Transactions A, p.3007-3018, 1996.

96Dee: S.C. Deevi, and V.K. Sikka, Intermetallics, vol.4, p.357-375, 1996.

96Her: R.W. Hertzberg, in Deformation and Fracture Mechanics of Engineering Materials, 4th edition, John Wiley & Sons, 1996.

96Liu: C.T. Liu, E.P. George, and W.C. Oliver, Intermetallics, vol.4, p.77-83, 1996.

96Son: Y.K. Song, MASc Thesis, University of Waterloo, 1996.

96Sun: X. Sun, and J.A. Yeomans, J. Mater. Sci. Technol., vol. 12, p.124, 1996.

97AST: ASTM standard PS 70-97.

97Geo: E.P. George and C.T. Liu, Proceedings of The Second International Symposium on Structural Intermetallics, eds. M.V. Nathal et al., Pennsylvania, TMS, p.693-702, 1997.

97Van: S. Van Dyck, L.Delaey, L. Froyen, and L. Buekenhout, Intermetalllics, vol.5, p.137-145, 1997.

97Vil: P. Villars, Pearson's Handbook Desk Edition (Crystallographic Data for Intermetallic Phases), Materials Park, OH, 1997.

97Wil: J.C. Williams, Proceedings of The Second International Symposium on Structural Intermetallics, eds. M.V. Nathal et al., Pennsylvania, TMS, p.3, 1997.

98Abd: M. Abdellaoui, D. Cracco, A. Percheron-Guegan, *Journal of Alloys and Compounds,* 1998, vol. 268, pp. 233-240.

98ASM: Metalls Handbook® Desk Edition (2nd edition), eds., J.R. Davis and Associates, ASM international, 1998.

98Cra: D. Cracco, and A. Percheron-Guegan, *Journal of Alloys and Compounds*, 1998, vol. 268, pp. 248-255.

98Kim: Y. Kimura, D. Pope, D. Luzzi, in Interstitial and Substitutional Solute Effects in Intermetallics, eds., I. Baker, R.D. Noebe, and E.P. George, The Minerals, Metals, & Materials Society, p.295-309, 1998.

98Lia: G. Liang, S. Boily, J. Huot, A. Van Neste, R. Schulz, Journal of Alloys and compounds, vol.267, p.302-306, 1998.

98Noh: S. Nohara, N. Fujita, S.G. Zhang, H. Inoue, C. Iwakura, Journal of Alloys and Compounds, vol.267, p.76-78, 1998.

98Son[1]: Y.K. Song, and R.A. Varin, *Intermetallics*, vol. 6, pp. 43-59, 1998.

98Son[2]: Y.K. Song, and R.A. Varin, Intermetallics, vol.6, p.379-393, 1998.

98Tak: T. Takasugi, in Interstitial and Substitutional Solute Effects in Intermetallics, eds., I. Baker, R.D. Noebe, and E.P. George, The Minerals, Metals, & Materials Society, p. 279-293, 1998.

98Tes: P. Tessier, H. Enoki, M. Bououdina, E. Akiba, Journal of Alloys and Compounds, vol.268, p.285-289, 1998.

99Dow: N.E. Dowling, in Mechanical Behaviour Of Materials, 2nd edition, Prentice-Hall, Inc., 1999.

99Loc: I.E. Locci, S. V. Raj, J.D. Whittenberger, J.A. Salem, D.J. Keller, High-Temperature Ordered Intermetallic Alloys VIII, vol. 552, p.KK8.1.1-KK8.1.6, 1999.

99Sch: R.B. Schwarz, MRS Bulletin, Nov., p.40-44, 1999.

99Tak: T. Takasugi and S. Hanada, "High-Temperature Ordered Intermetallic Alloys VIII" edited by E.P. George, M.J. Mills, and M. Yamaguchi, vol. 552, p.KK6.5.1-KK6.5.6.

99Zbr: L. Zbroniec, PhD Thesis, University of Waterloo, 1999.

00Jan: J.S.C Jang, S.K. Wong, P.Y. Lee, Materials Science and Engineering, A281, p.17-22, 2000

00Pik: L.M. Pike and C.T. Liu, Scripta mater., vol. 42, p. 265-270, 2000.

Appendix A

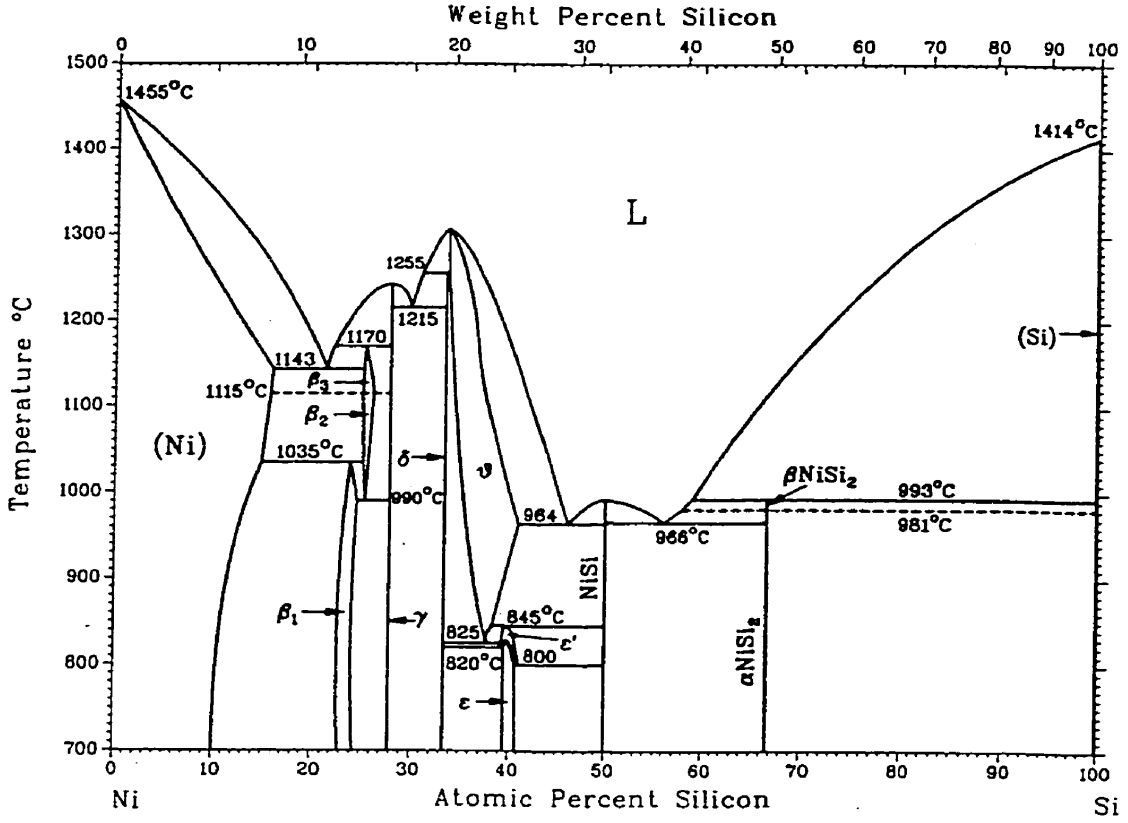

Special Points of the Ni-Si System

Reaction		Composition, at.% Si		Temperature, °C	Reaction type
L ↔ (Ni) + β_3	21.4	15.8	25	1143	Eutectic
β_2 ↔ β_3		...		~1115	Polymorphic
(Ni) + β_2 ↔ β_1	14.7	25.1	23.7	1035	Peritectoid
β_2 ↔ β_1 + γ	25.2	24.5	27.9	990	Eutectoid
L + γ ↔ β_3	22	27.9	25.2	1170	Peritectic
L ↔ γ		27.9		1242	Congruent
L ↔ γ + δ	29.8	27.9	33.3	1215	Eutectic
L + θ ↔ δ	30.8	33.4	33.3	1255	Peritectic
L ↔ θ		~33.5		1306	Congruent
θ ↔ δ + ε'	37.8	33.3	39.2	825	Eutectoid
ε' ↔ δ + ε	39.2	33.3	39.5	820	Eutectoid
ε' ↔ ε + NiSi	41	40.7	50	800	Eutectoid
θ + NiSi ↔ ε'	38.5	50	40	845	Peritectoid
ε ↔ ε'		40		~830	Polymorphic
L ↔ θ + NiSi	46	41	50	964	Eutectic
L ↔ NiSi		50		992	Congruent
L ↔ NiSi + $\alpha NiSi_2$	56.2	50	66.7	966	Eutectic
L + (Si) ↔ $\beta NiSi_2$	59	~100	66.7	993	Peritectic
$\beta NiSi_2$ ↔ $\alpha NiSi_2$		66.7		981	Polymorphic

Fig. A.1 The Ni-Si binary phase diagram [90Mas].

(a)

Ni-Si Crystal Structure Data

Phase	Composition, at.% Si	Pearson symbol	Space group	Struktur-bericht designation	Prototype
(Ni)	0 to 15.8	*cF*4	$Fm\bar{3}m$	*A*1	Cu
β_1 (Ni_4Si)	22.8 to 24.5	*cP*4	$Pm\bar{3}m$	$L1_2$	$AuCu_3$
β_2 (Ni_3Si)	~24.5 to 25.5	*mC*16	...	...	$GePt_3$
β_3 (Ni_3Si)	~24.5 to 25.5	*mC*16	...	...	$GePt_3$
γ ($Ni_{31}Si_{12}$)	27.9	*hP*14	...	...	...
θ (Ni_2Si)	33.4 to 41	*hP*6	...	...	...
δ (Ni_2Si)	33.3	*oP*12	...	...	...
ε(Ni_3Si_2)	39 to 41	*oP*80	...	...	...
NiSi	50	*oP*8	*Pnma*	*B*31	MnP
$\beta NiSi_2$	66.7	?	...	...	?
$\alpha NiSi_2$	66.7	*cF*12	$Fm\bar{3}m$	*C*1	CaF_2
(Si)	~100	*cF*8	$Fd\bar{3}m$	*A*4	C(diamond)

(b)

Ni-Si Crystal Structure Data

Phase	Composition, at.% Si	Pearson symbol	Space group	Strukturbericht designation	Prototype
(Ni)	0 to 15.8	*cF*4	$Fm\bar{3}m$	*A*1	Cu
β_1(Ni_3Si)	22.8 to 24.5	*cP*4	$Pm\bar{3}m$	$L1_2$	$AuCu_3$
β_2 (Ni_3Si)	~24.5 to 25.5	*mC*16	...	...	($GePt_3$?)
β_3 (Ni_3Si)	~24.5 to 25.5	*mC*16	...	...	($GePt_3$?)
γ ($Ni_{31}Si_{12}$)	27.9	*hP*43	*P*321	...	$Ni_{31}Si_{12}$
θ (Ni_2Si)	33.4 to 41	*hP*6	$P6_3/m$	...	Ni_2Si
δ (Ni_2Si)	33.3	*oP*12	*Pnma*	*C*23	Co_2Si
ε (Ni_3Si_2)	39 to 41	*oP*80	...	...	...
ε' (Ni_3Si_2)	39 to 41	...	...	...	...
NiSi	50	*oP*8	*Pnma*	*B*31	MnP
ζ' ($NiSi_2$)	66.67	...	...	...	...
ζ ($NiSi_2$)	66.67	*cF*12	$Fm\bar{3}m$	*C*1	CaF_2
(Si)	~100	*cF*8	$Fd\bar{3}m$	*A*4	C(diamond)

Fig. A.1.1 Ni-Si crystal structural data from (a)[90Mas] and (b)[91Nas].

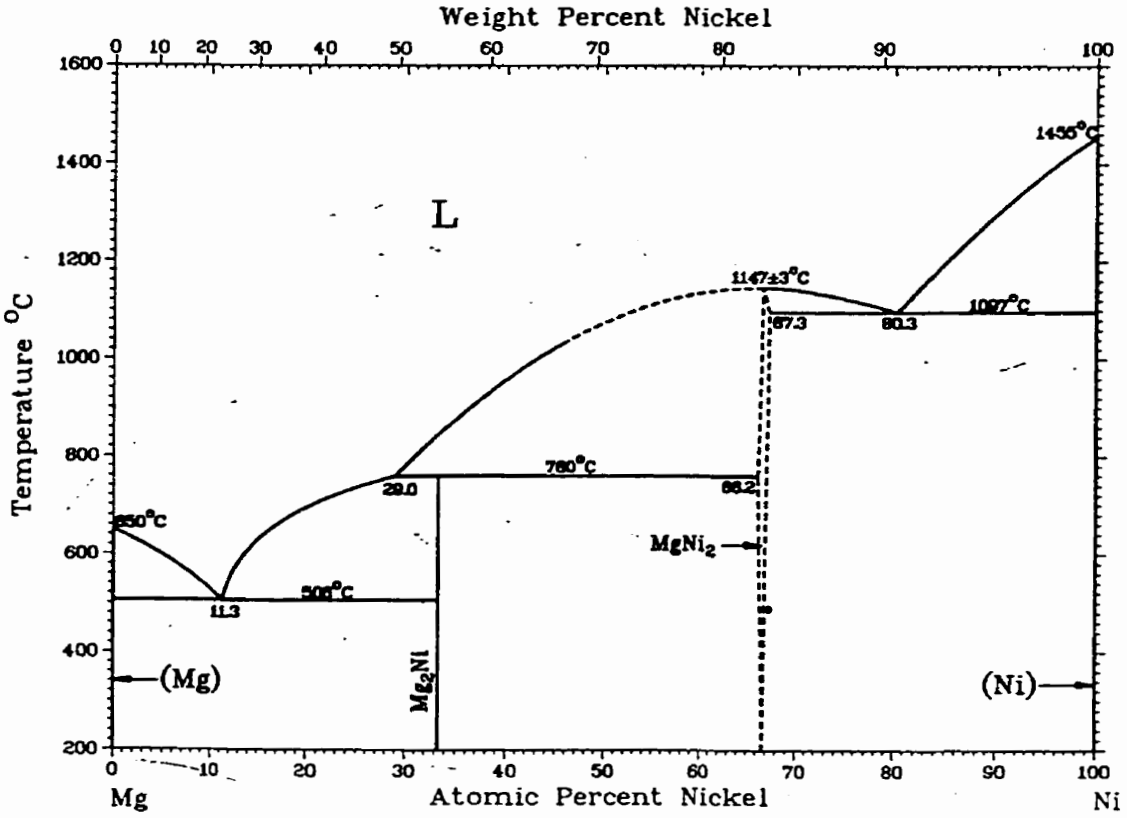

Special Points of the Mg-Ni System

Reaction		Composition, at.% Ni		Temperature, °C	Reaction type
L ↔ Mg		0		650	Melting
L ↔ (Mg) + Mg_2Ni	11.3	0	33.3	506	Eutectic
L + $MgNi_2$ ↔ Mg_2Ni	29	66.2	33.3	760	Peritectic
L ↔ $MgNi_2$		66.7		1147 ± 3	Congruent
L ↔ $MgNi_2$ + (Ni)	80.3	67.3	100	1097	Eutectic
L ↔ Ni		100		1455	Melting

Fig. A.2 The Mg-Ni binary phase diagram [90Mas].

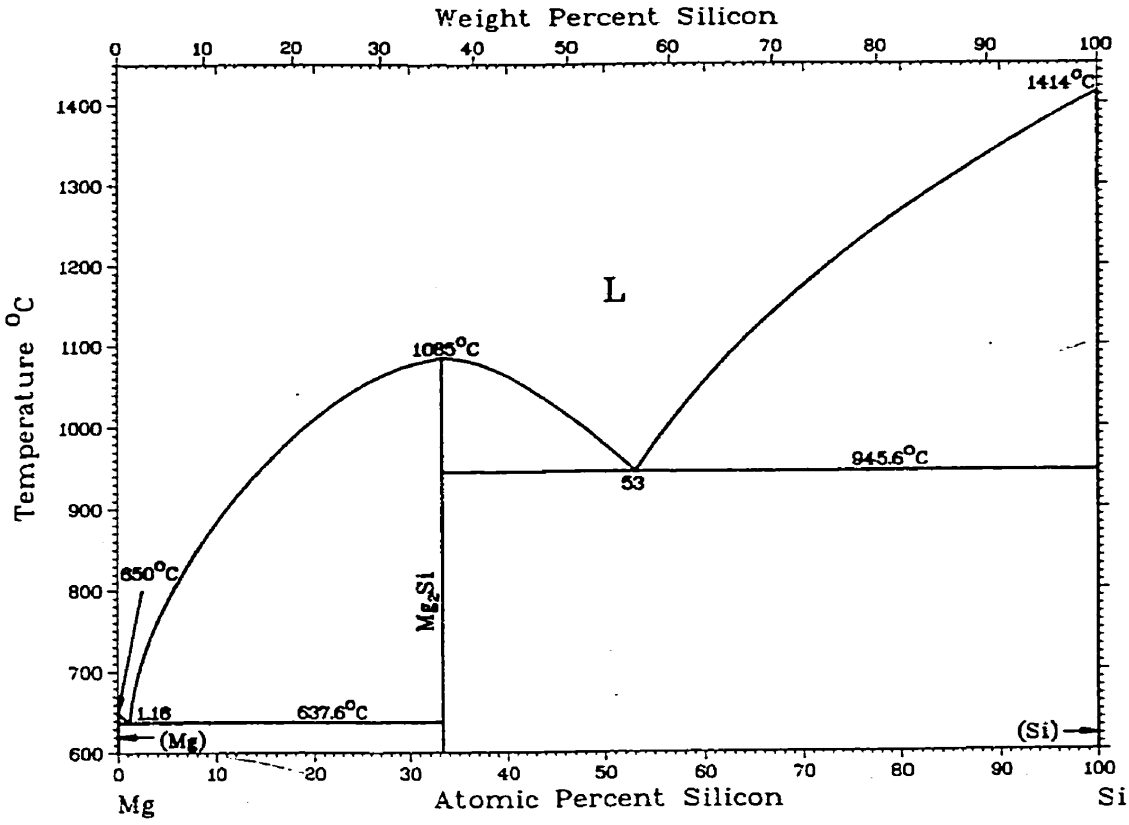

Special Points of the Mg-Si System

Reaction	Composition, at.% Si			Temperature, °C	Reaction type
L ↔ Mg		0		650	Melting
L ↔ (Mg) + Mg_2Si	1.16	~0	33.3	637.6	Eutectic
L ↔ Mg_2Si		33.3		1085	Congruent
L ↔ Mg_2Si + (Si)	53	33.3	~100	945.6	Eutectic
L ↔ Si		100		1414	Melting

Fig. A.3 The Mg-Si binary phase diagram [90Mas].

Appendix B

Table B.1 The initial composition and overall composition of the homogenized alloys fabricated for microstructural observation.

Alloy No.	Initial composition – mixture of raw elements (at. %)			Composition of alloys (homogenized) (at. %)			Melting Temp. / time
	Mg	Si	Ni	Mg	Si	Ni	
1	17.0	3.0	80.5	18.5±1.5	2.8±0.2	78.7±1.5	1350°C / 15min.
2	15.0	21.0	63.7	5.5±1.4	16.0±0.8	78.5±2.2	failed*
3	8.5	22.0	69.5	8.4±0.8	22.2±0.6	69.4±1.2	1350°C / 15min.
4	25.0	21.0	54.0	11.3±0.6	25.7±0.3	63.0±0.4	1350°C / 15min.
5	20.2	23.4	56.4	11.2±0.3	25.5±0.2	63.3±0.4	1350°C / 5min.
6	5.3	31.3	63.4	4.0±0.2	29.4±0.4	66.6±0.6	1400°C / 15min.
7	8.0	28.0	64.0	7.7±0.5	27.9±0.2	64.4±0.5	1350°C / 15min.
8	12.0	27.5	60.5	10.2±0.6	28.1±0.3	61.7±0.5	1350°C / 15min.
9	29.0	20.8	50.2	16.4±1.5	26.7±0.5	56.9±1.2	1320°C / 10min.
10	33.4	20.7	45.9	17.3±1.1	25.5±0.5	57.2±0.6	1350°C / 10min.
11	24.0	25.0	51.0	8.4±0.9	30.1±0.2	61.54±0.7	1420°C / 15min.
12	24.0	25.0	51.0	13.2±0.6	28.1±0.4	58.7±0.4	1320-40°C/ 30min.
13	23.5	23.3	53.2	19.2±0.3	26.5±0.4	54.4±0.2	1300°C / 10min.
14	5.3	31.3	63.4	3.5±0.5	32.4±0.4	64.1±0.2	1350°C / 35min.
15	3.5	32.4	64.1	4.1±1.4	32.1±0.5	63.8±1.1	1350°C / 10min.
16	18.0	29.5	52.5	14.1±1.1	31.91±0.6	54.04±0.5	1350°C / 15min.
17	11.0	34.5	54.5	9.5±0.5	37.9±0.7	52.6±0.6	1350°C / 15min.
18	3.7	39.1	57.3	3.0±0.8	40.3±0.7	56.7±0.6	1350°C / 15min.
19	31.7	20.1	48.2	19.1±0.4	23.5±0.5	57.5±0.6	1300°C / 10min.
20	29.0	20.8	50.7	20.9±0.3	24.1±0.3	55.0±0.3	1320°C / 10min.
21	10.2	39.4	50.4	8.7±0.4	40.3±0.2	51.0±0.6	1350°C / 5min.
22	-	25.0	75.0	-	25.2±0.4	74.8±0.4	1400°C / 15min.
23	-	29.5	70.5	-	29.5±0.5	70.5±0.7	1420°C / 15min.

Table B.1 continued

24	-	33.5	66.5	-	33.5±0.4	66.5±0.4	1420°C / 10min.
25	6.5	36.0	57.5	6.1±0.7	37.4±0.4	56.6±0.8	1350°C / 15min.
26	3.5	38.0	58.5	3.43±0.8	37.9±0.4	58.6±0.5	1350°C / 15min.
27	6.6	44.5	48.9	6.3±0.5	44.7±0.2	49.0±0.7	1350°C / 15min.
28	2.0	46.2	51.8	1.8±0.5	46.5±0.6	51.7±0.7	1350°C / 15min.
29	29.0	28.5	42.5	21.7±0.9	31.4±1.3	46.9±2.2	1300°C / 10min.
30	41.0	21.0	38.0	23.7±0.9	26.9±0.8	49.4±0.1	1200°C / 5min.
31	45.0	19.0	36.0	25.8±1.2	25.6±0.5	48.6±1.5	1200°C / 10min.
32	39.0	17.0	44.0	26.6±0.6	19.1±1.2	54.3±0.9	1200°C / 5min.
33	34.0	13.0	53.0	25.3±0.1	14.9±0.8	59.8±0.7	1300°C / 5min.
34	32.0	13.0	55.0	24.7±0.8	13.9±1.1	61.5±1.3	failed*
35	43.0	9.0	48.0	27.0±0.6	11.5±0.7	61.4±0.4	1300°C / 5min.
36	33.6	3.5	62.9	33.5±0.4	3.8±0.5	62.7±0.2	1250°C / 10min.
37	32.7	-	67.3	32.3±0.9	-	67.6±0.9	1200°C / 15min.
38	40.0	3.5	56.5	36.2±1.1	3.7±0.2	60.2±0.9	1250°C / 5min.
39	45.0	3.3	52.7	44.8±1.4	3.0±0.3	52.2±1.2	1300°C / 10min.
40	66.0	2.0	32.0	60.1±0.2	1.8±0.3	38.1±0.3	1200°C / 10min.
41	56.0	7.0	37.0	50.5±1.9	7.1±1.2	42.4±0.7	1200°C / 10min.
42**	36.0	20.0	44.0	40.4±1.1	10.5±0.8	49.1±0.5	Failed
43**	67.0	-	33.0	77.9±0.2	-	22.1±0.3	1200°C / 15min.
44**	82.0	1.5	16.5	79.6±3.6	2.6±0.9	17.8±2.8	1080°C / 15min.
45**	80.0	4.0	16.0	80.9±2.0	2.3±0.4	16.8±1.7	1120°C / 5min.
46**	91.0	1.0	8.0	88.5±2.0	2.2±0.3	9.4±1.6	1080°C / 15min.
47***	60.0	18.0	22.0	76.7±2.9	12.25±1.2	11.08±2.0	1080°C / 10min.
48***	55.0	29.0	16.0	64.8±1.5	24.5±0.4	10.7±1.9	1200°C / 15min.
49***	48.0	29.5	22.5	49.5±0.9	31.4±0.7	19.1±1.6	1200°C / 10min.
50	48.0	24.0	28.0	33.7±0.6	30.8±0.2	35.6±0.8	1200°C / 10min.
51	36.0	30.0	34.0	32.6±0.8	31.7±1.3	35.7±1.0	1200°C / 15min.
52	44.0	30.0	26.0	31.2±0.1	36.0±0.1	32.8±0.2	1200°C / 5min.
53	48.0	33.0	19.0	40.4±1.2	39.9±0.6	19.7±0.7	1200°C / 10min.

Table B.1 continued

54***	38.0	48.0	14.0	42.0±0.6	49.5±0.7	8.5±0.4	1200°C / 15min.

*: failed in measuring temperature.

**: Ingots of alloys such as 42-46 are not homogeneous throughout the whole ingot exhibiting different composition, usually, at the top and bottom. Therefore, the compositions of homogenized alloys, 42-46 are not representative of the entire ingot.

***: Mg content in this alloy increased and Ni content decreased after melting. This behaviour is not understood at this moment, but it seems to arise from insufficient mixing of molten metal during melting causing inhomogeneous composition through out the whole ingot. Therefore, there might be some portion of the ingot enriched with Ni.

Appendix C

C.1 Lattice parameter calculations using the Nelson-Riley function

The results of extrapolations of measured lattice parameters against the Nelson-Riley function for the determination of the lattice parameters, a and c for both the $MgNi_2$ (alloy 37) and the $(Mg,Si)Ni_2$ (alloys 36 and 40).

Table C.1.1 Diffraction peaks, Nelson-Riley function, and a′ calculated for each *hk0* peak and c′ calculated for each *00l* peak.

Alloy No	2θ	*(hk0)*	f(θ)*	a′	2θ	*(00l)*	f(θ)	c′
37 ($MgNi_2$)	21.33	1 0 0	10.40620	0.48100	22.50	0 0 4	9.83501	1.58144
	37.31	1 1 0	5.56368	0.48205	45.98	0 0 8	4.28182	1.57910
	67.26	3 0 0	2.43324	0.48224	71.89	0 0 12	2.16106	1.57593
	79.49	2 2 0	1.77684	0.48230				
36 ($Mg(Ni,Si)_2$ with 3.7 at. % Si)	21.36	1 0 0	10.39375	0.48046	22.40	0 0 4	9.87688	1.58765
	37.40	1 1 0	5.54687	0.48087	45.74	0 0 8	4.31130	1.58694
	67.27	3 0 0	2.43231	0.48215	71.82	0 0 12	2.16515	1.57733
	79.53	2 2 0	1.77495	0.48210				
40 ($Mg(Ni,Si)_2$ with 11.1 at. % Si)	21.30	1 0 0	10.42237	0.48169	22.44	0 0 4	9.85802	1.58485
	37.34	1 1 0	5.55813	0.48166	45.80	0 0 8	4.30390	1.58497
	67.20	3 0 0	2.43667	0.48259	71.80	0 0 12	2.16626	1.57771
	79.38	2 2 0	1.78202	0.48289				

*: f(θ): Nelson-Riley function, $\left(\frac{\cos^2\theta}{\sin\theta}+\frac{\cos^2\theta}{\theta}\right)$

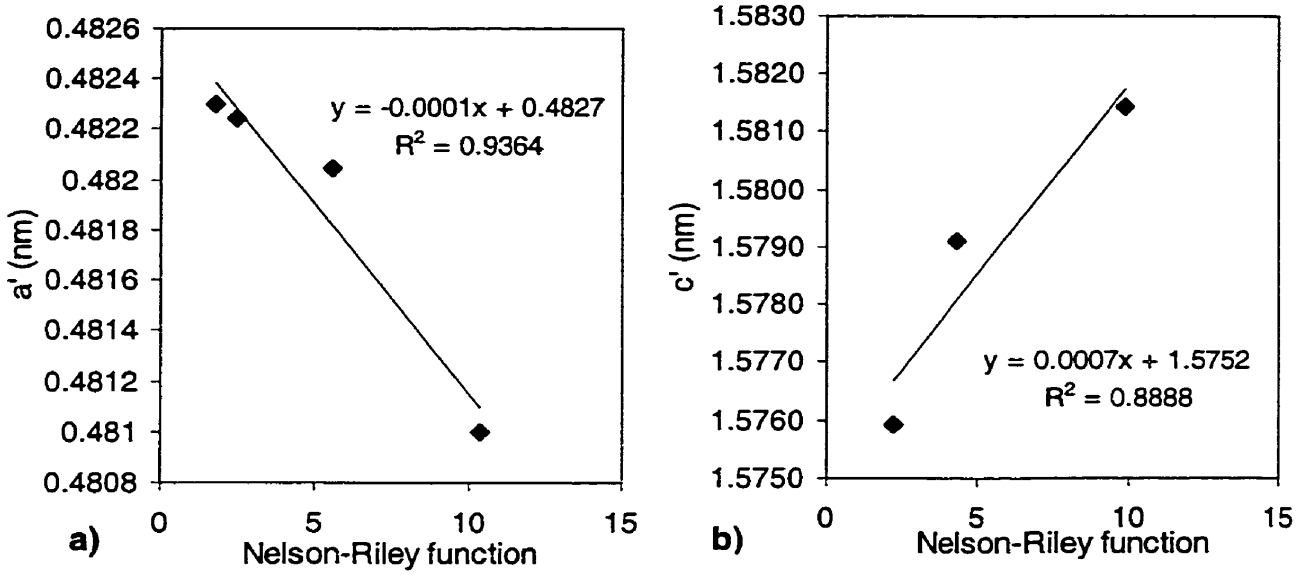

Fig. C.1.1 The results of extrapolations of measured lattice parameters against the Nelson-Riley function for the determination of the lattice parameters, a and c for the $MgNi_2$ phase in alloy 37.

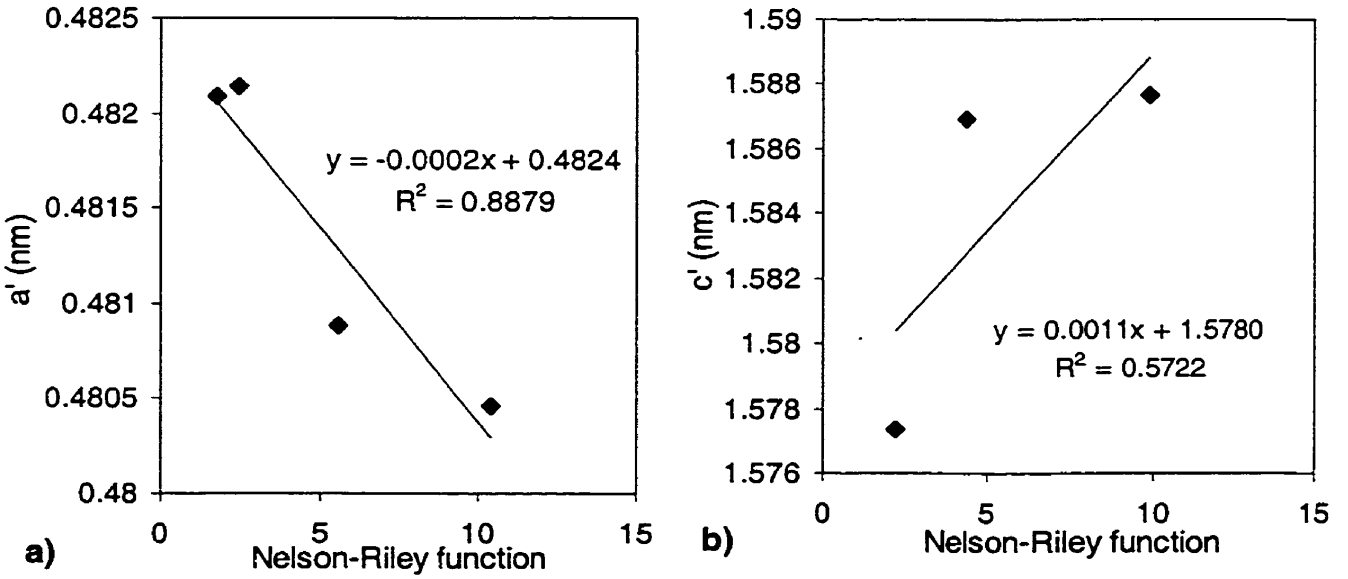

Fig. C.1.2 The results of extrapolations of measured lattice parameters against the Nelson-Riley function for the determination of the lattice parameters, a and c for the $(Mg,Si)Ni_2$ phase with 3.7 at. % Si in alloys 36.

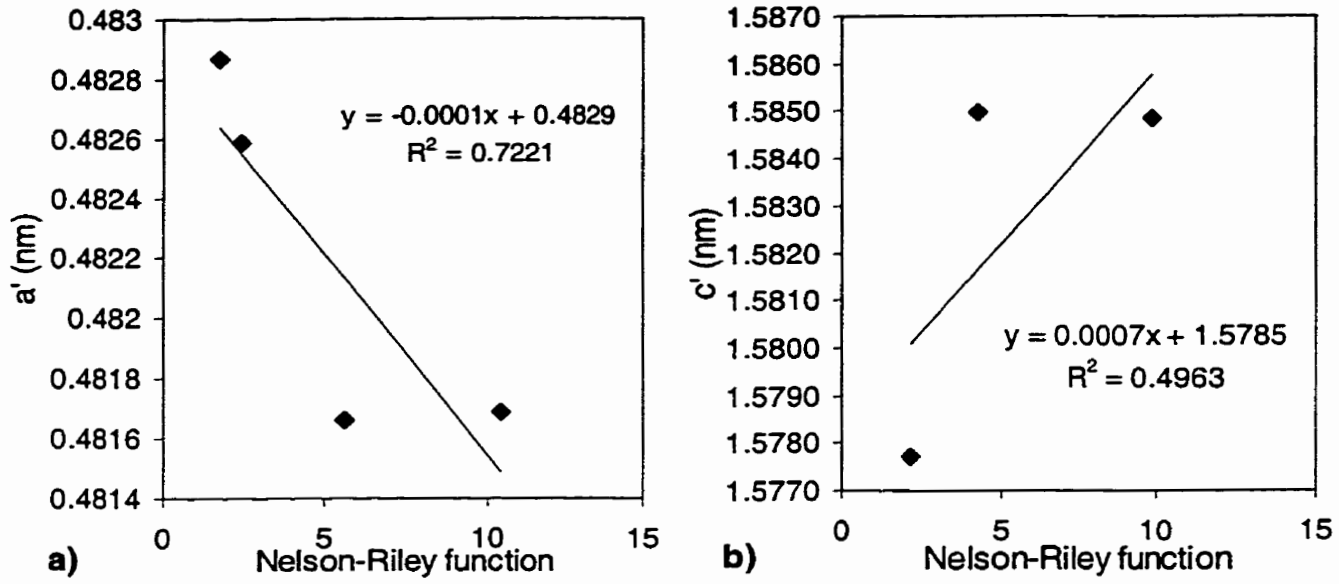

Fig. C.1.3 The results of extrapolations of measured lattice parameters against the Nelson-Riley function for the determination of the lattice parameters, a and c for the $(Mg,Si)Ni_2$ phase with 11.1 at. % Si in alloys 40.

C.2 Estimation of the accuracy in lattice parameter calculations

This is calculated based on the step size 0.05° in 2θ and under the assumption that the maximum deviation induced by the step size of 0.05° in 2θ from a theoretical x-ray diffraction peak position is 0.025° in 2θ (i.e. half of the step size), i.e. a theoretical peak at 2θ=20.025° would be detected as either at 2θ=20.00° or 2θ=20.05°.

C.2.1 Deviation of lattice spacing d

The maximum deviation of lattice spacing d values induced by the step size of 0.05° in 2θ was calculated at various diffraction angles from 20° to 80° in 2θ for the same λ (0.15418nm) using the Bragg's equation, $\lambda=2d\sin\theta$. The result of the calculation is tabulated in Table C.2.1 and plotted in Fig. C.2.1. Δd values are substantially decreasing with increasing diffraction angle.

Table C.2.1 The maximum possible deviation of lattice spacing d values induced by the step size of 0.05° in 2θ at various diffraction angles.

Theoretical peak position (2θ)	Observed (or deviated) peak position (2θ)	d_{th} for theoretical peak (nm)	$d_{obs.}$ for observed peak (nm)	Δd (nm), $\lvert d_{th}-d_{obs.} \rvert$
20.0	20.025	0.443944	0.443395	0.000549
30.0	30.025	0.297853	0.297611	0.000242
40.0	40.025	0.225396	0.225261	0.000135
50.0	50.025	0.182410	0.182325	0.000085
60.0	60.025	0.154180	0.154122	0.000058
70.0	70.025	0.134402	0.134360	0.000042
80.0	80.025	0.119931	0.119900	0.000031

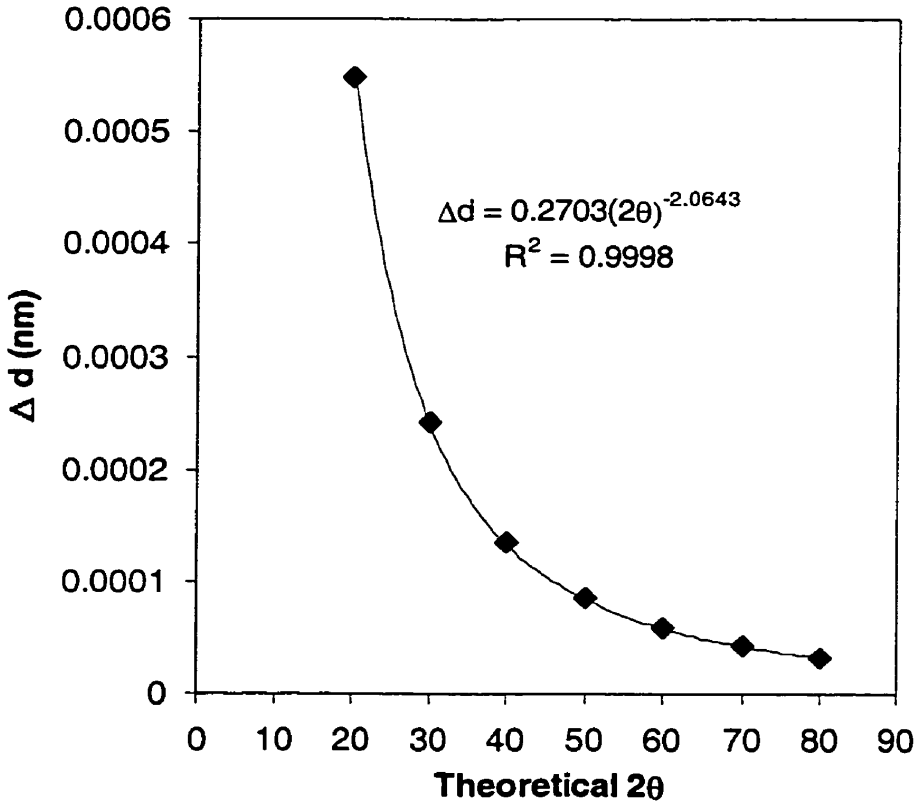

Fig. C.2.1 The maximum possible deviation of lattice spacing d values induced by the step size of 0.05° in 2θ at various diffraction angles.

C.2.2 Deviation of lattice parameters

This is calculated based on the diffraction peaks from alloy 37 ($MgNi_2$) used for the lattice parameter calculations using the Nelson-Riley function as an example. The deviation in lattice parameters 'a' and 'c' were calculated separately based on the hexagonal symmetry using the peaks indexed with *hk*0 (e.g. (100), (110), (300), and (220)) and those indexed with 00*l* (e.g. (004), (008), and (00$\underline{12}$)), respectively.

The maximum possible deviation in 'a' and 'c' values calculated using the following equation [78Cul] are listed in Table C.2.2 and Table C.2.3, respectively, and plotted in Fig. C.2.2.

$$\frac{1}{d^2} = \frac{4}{3}\left(\frac{h^2 + hk + k^2}{a^2}\right) + \frac{l^2}{c^2}$$

Table C.2.2 The maximum possible deviation of lattice parameter 'a'.

hkl	Observed 2θ*	Theoretical 2θ**	$a_{obs.}$ calculated from observed peak (nm)	a_{th} calculated from theoretical peak (nm)	Δa (nm), $\lvert a_{obs.} - a_{th} \rvert$
100	21.33	21.355	0.480994	0.480438	0.000557
110	37.31	37.335	0.482010	0.481699	0.000311
300	67.25	67.275	0.482249	0.482091	0.000158
220	79.49	79.515	0.482286	0.482159	0.000126

*: observed peaks are taken as an example from alloy 37 ($MgNi_2$).
**: theoretical peaks are calculated by adding 0.025 to the observed peaks assuming that observed peaks are deviated 0.025° in 2θ from the theoretical peaks.

Table C.2.3 The maximum possible deviation of lattice parameter 'c'.

hkl	Observed 2θ*	Theoretical 2θ**	$c_{obs.}$ calculated from observed peak (nm)	c_{th} calculated from theoretical peak (nm)	Δc (nm), $\lvert c_{obs.} - c_{th} \rvert$
004	22.49	22.515	1.581295	1.579562	0.001733
008	45.98	46.005	1.579024	1.578212	0.000812
00$\underline{12}$	71.89	71.915	1.575923	1.575449	0.000474

*: observed peaks are taken as an example from alloy 37 ($MgNi_2$).
**: theoretical peaks are calculated by adding 0.025 to the observed peaks assuming that observed peaks are deviated 0.025° in 2θ from the theoretical peaks.

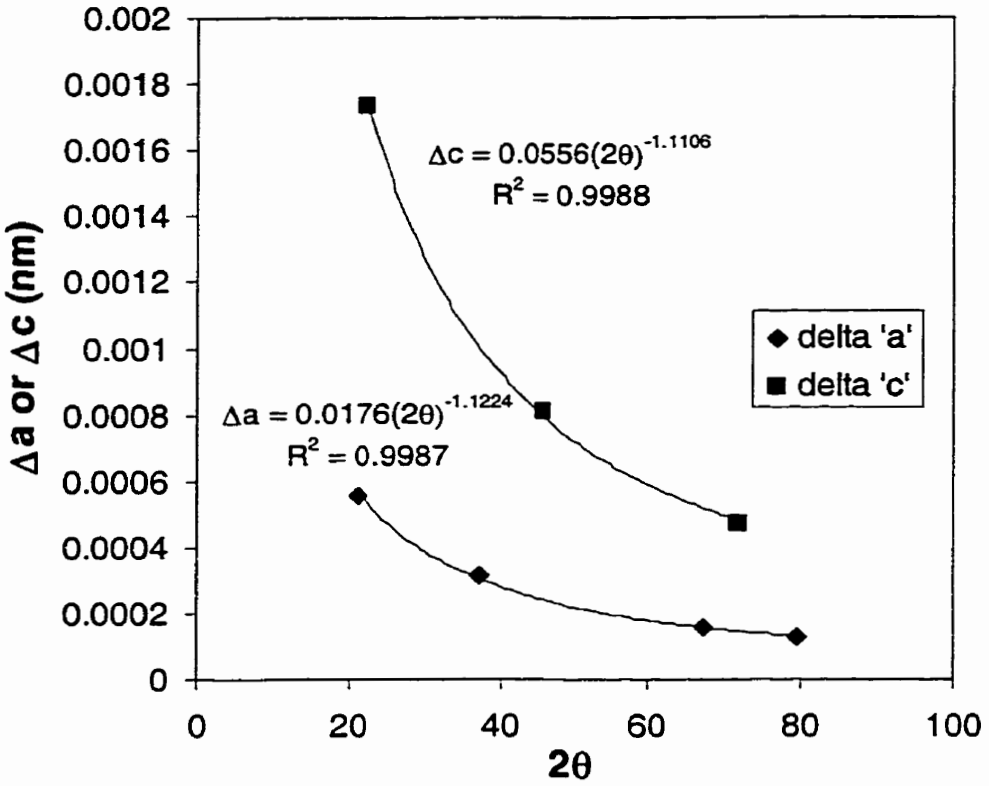

Fig. C.2.2 The maximum possible deviation of lattice parameters of 'a' and 'c'.

Appendix D

Table D.1 Overall composition, homogenization temperature, time and the identified phases.

Alloy no.	Overall composition of alloys (at. %) Mg	Si	Ni	Phases	Homogenization temp. / time
27	6.3±0.5	44.7±0.2	49.0±0.7	NiSi, κ, μ	780°C/200h
28	1.8±0.5	46.5±0.6	51.7±0.7	NiSi, Ni_3Si_2, κ	780°C/200h
29	21.7±0.9	31.4±1.3	46.9±2.2	η, ζ, ν	850°C/200h
30	23.7±0.9	26.9±0.8	49.4±0.1	η, ζ, ν	850°C/100h
31	25.8±1.2	25.6±0.5	48.6±1.5	η, ζ, ν	700°C/100h
32	26.6±0.6	19.1±1.2	54.3±0.9	η, Mg_2SiNi_3, $Mg(Ni,Si)_2$	850°C/200h
33	25.3±0.1	14.9±0.8	59.8±0.7	η, Ni(Si), $Mg(Ni,Si)_2$, U	850°C/200h
34	24.7±0.8	13.9±1.1	61.5±1.3	η, Ni(Si), $Mg(Ni,Si)_2$, U	850°C/100h
35	27.0±0.6	11.5±0.7	61.4±0.4	η, Ni(Si), $Mg(Ni,Si)_2$, U	900°C/100h
36	33.5±0.4	3.8±0.5	62.7±0.2	$Mg(Ni,Si)_2$, U	700°C/100h
37	32.3±0.9	-	67.6±0.9	Ni, $MgNi_2$, U	900°C/100h
38	36.2±1.1	3.7±0.2	60.2±0.9	$MgNi_2$, $Mg(Ni,Si)_2$, Mg_2Ni	850°C/100h
39	44.8±1.4	3.0±0.3	52.2±1.2	$MgNi_2$, $Mg(Ni,Si)_2$, Mg_2Ni	700°C/100h
40	60.1±0.2	1.8±0.3	38.1±0.3	$MgNi_2$, $Mg(Ni,Si)_2$, Mg_2Ni, Mg_2SiNi_3	700°C/100h
41	50.5±1.9	7.1±1.2	42.4±0.7	$Mg(Ni,Si)_2$, Mg_2Ni, Mg_2SiNi_3	600°C/300h
42	40.4±1.1	10.5±0.8	49.1±0.5	$Mg(Ni,Si)_2$, Mg_2Ni, Mg_2SiNi_3	700°C/200h
43	77.9±0.2	-	22.1±0.3	Mg, Mg_2Ni	480°C/100h
44	79.6±3.6	2.6±0.9	17.8±2.8	Mg, Mg_2Ni, Mg_2SiNi_3	480°C/200h

Table D.1 continued

45	80.9±2.0	2.3±0.4	16.8±1.7	Mg, Mg_2Ni, Mg_2SiNi_3	480°C/400h
46	88.5±2.0	2.2±0.3	9.4±1.6	Mg, Mg_2Ni, Mg_2SiNi_3	480°C/200h
47	76.7±2.9	12.3±1.2	11.1±2.0	Mg, Mg_2Si, ν	480°C/100h
48	64.8±1.5	24.5±0.4	10.7±1.9	Mg, Mg_2Si, ν	480°C/100h
49	49.5±0.9	31.4±0.7	19.1±1.6	Mg_2Si, ν, ω	800°C/200h
50	33.7±0.6	30.8±0.2	35.6±0.8	ν, ω	800°C/200h
51	32.6±0.8	31.7±1.3	35.7±1.0	ν, ω	780°C/200h
52	31.2±0.1	36.0±0.1	32.8±0.2	ν, ω, μ, [τ]*	750°C/500h
53	40.4±1.2	39.9±0.6	19.7±0.7	Mg_2Si, Si, ω	750°C/200h
54	42.0±0.6	49.5±0.7	8.5±0.4	Mg_2Si, Si, ω	750°C/100h

Note: "U" stands for unidentified phases.

*: The phase considered as a non-equilibrium phase is in the brackets.

Appendix E

Table E.1 X-ray diffraction peaks which are determined to arise solely from the ν phase in alloys 47 and 48.

Alloy 47			Alloy 48		
Diffraction angle (obs.-2θ°)	$d_{obs.}$, interplanar spacing (nm)	Intensity ($I/I_{0\ obs.}$)	Diffraction angle (obs.-2θ°)	$d_{obs.}$, interplanar spacing (nm)	Intensity ($I/I_{0\ obs.}$)
20.886	0.4253	23.6	20.753	0.4280	18.4
23.347	0.3810	15.2	23.516	0.3783	12.8
23.946	0.3716	24.4	23.881	0.3726	19.4
26.471	0.3367	6.9	26.408	0.3375	7.7
32.318	0.2770	4.6	32.426	(0.2761)	2.3
34.023	(0.2635)	4.1	33.772	0.2654	4.6
34.049	(0.2633)	4.9	34.076	0.2631	4.4
41.339	0.2184	26.2	41.458	0.2178	24.9
42.416	0.2131	7.4	42.167	0.2143	10.1
43.818	0.2066	89.1	43.685	0.2072	58.2
44.133	0.2052	100.0	43.885	0.2063	100.0
45.730	0.1984	3.7	45.632	0.1988	5.63
48.915	0.1862	25.3	48.803	0.1866	20.8
52.467	0.1744	4.5	52.793	0.1734	6.5
54.036	(0.1697)	2.4	53.796	0.1704	3.2
56.263	0.1635	12.2	56.189	0.1637	6.9
73.067	0.1295	4.4	73.001	0.1296	22.2
76.660	0.1243	12.4	76.953	0.1239	21.9

Table E.2 X-ray diffraction from alloy 26 after quenching from 900°C.

Diffraction angle (obs.-2θ°)	$d_{obs.}$, interplanar spacing (nm)	Intensity ($I/I_{0\ obs.}$)	Interplanar spacing (nm)	
			κ[98Son[1]]	θ-Ni_2Si [78SPD]
15.050	0.5882	10.1	0.5842	
17.523	0.5057	15.0	0.5032	
26.929	0.3308	16.7		0.330
30.700	0.2910	6.2	0.2903	
31.699	0.2821	6.1	0.2817	
32.474	0.2755	11.4		0.274
34.396	0.2605	5.3	0.2600	
35.589	0.2521	6.5	0.2515	
42.342	0.2133	13.1	0.2159	
42.783	0.2112	31.7	0.2112	
43.877	0.2062	15.0	0.2012	
45.917*	0.1975	100.0	0.1985	0.197
47.622*	0.1908	79.3	0.1903	0.190
48.483	0.1876	17.1	0.1838	
50.350	0.1811	6.7	0.1808	
51.098	0.1786	6.2	0.1787	
52.732	0.1735	5.8	0.1730	
53.564	0.1710	8.6	0.1709	
68.314	0.1372	17.7		0.137

*: the peaks are diffracted from both the κ and the θ-Ni_2Si.

Appendix F

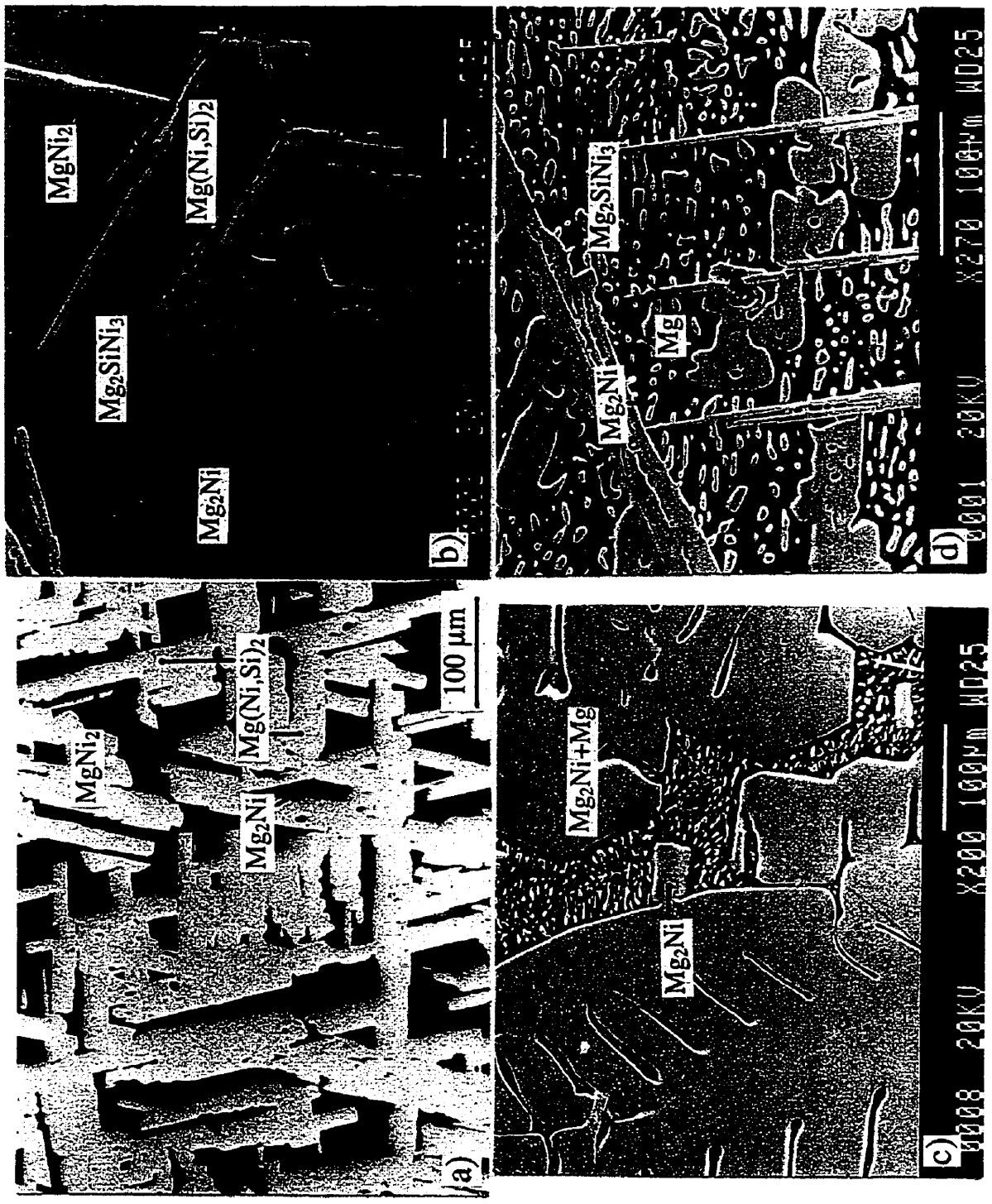

Fig. F.1 Homogenized microstructures of alloys (a)39, (b)40, (c)43, (d)45, (e)47, and (f)53.

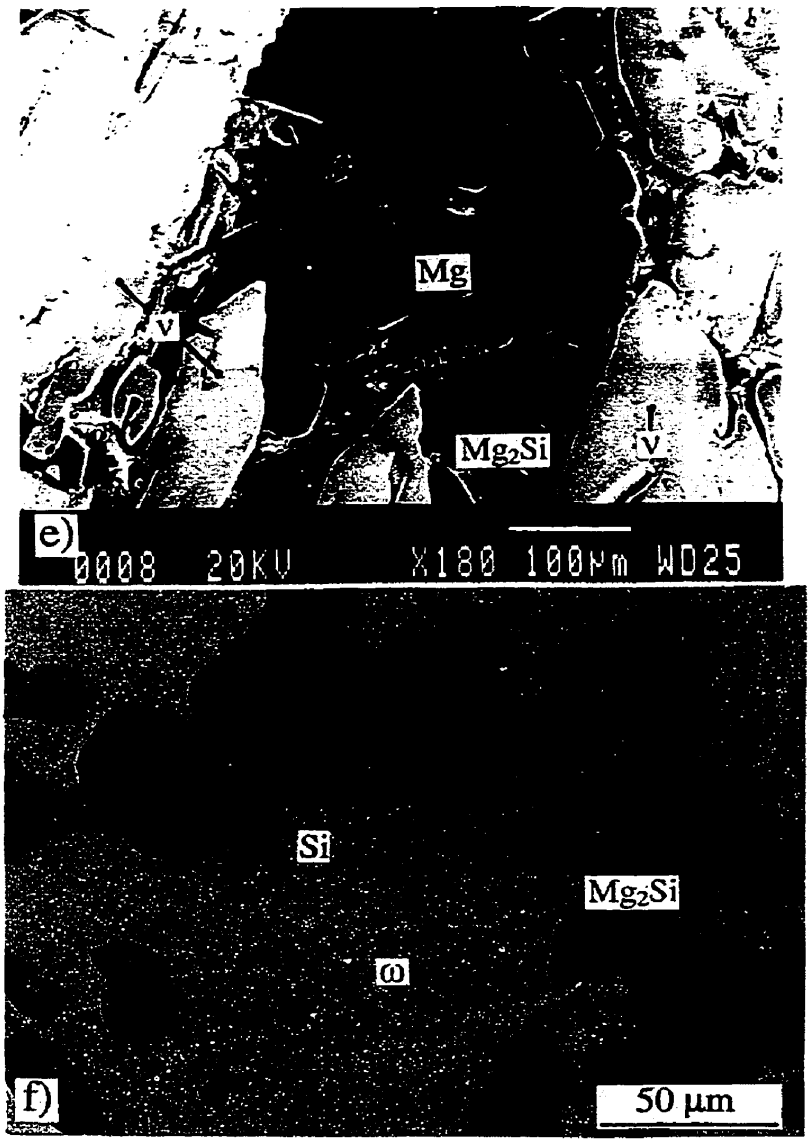

Fig. F.1 Homogenized microstructures of alloys (a)39, (b)40, (c)43, (d)45, (e)47, and (f)53.

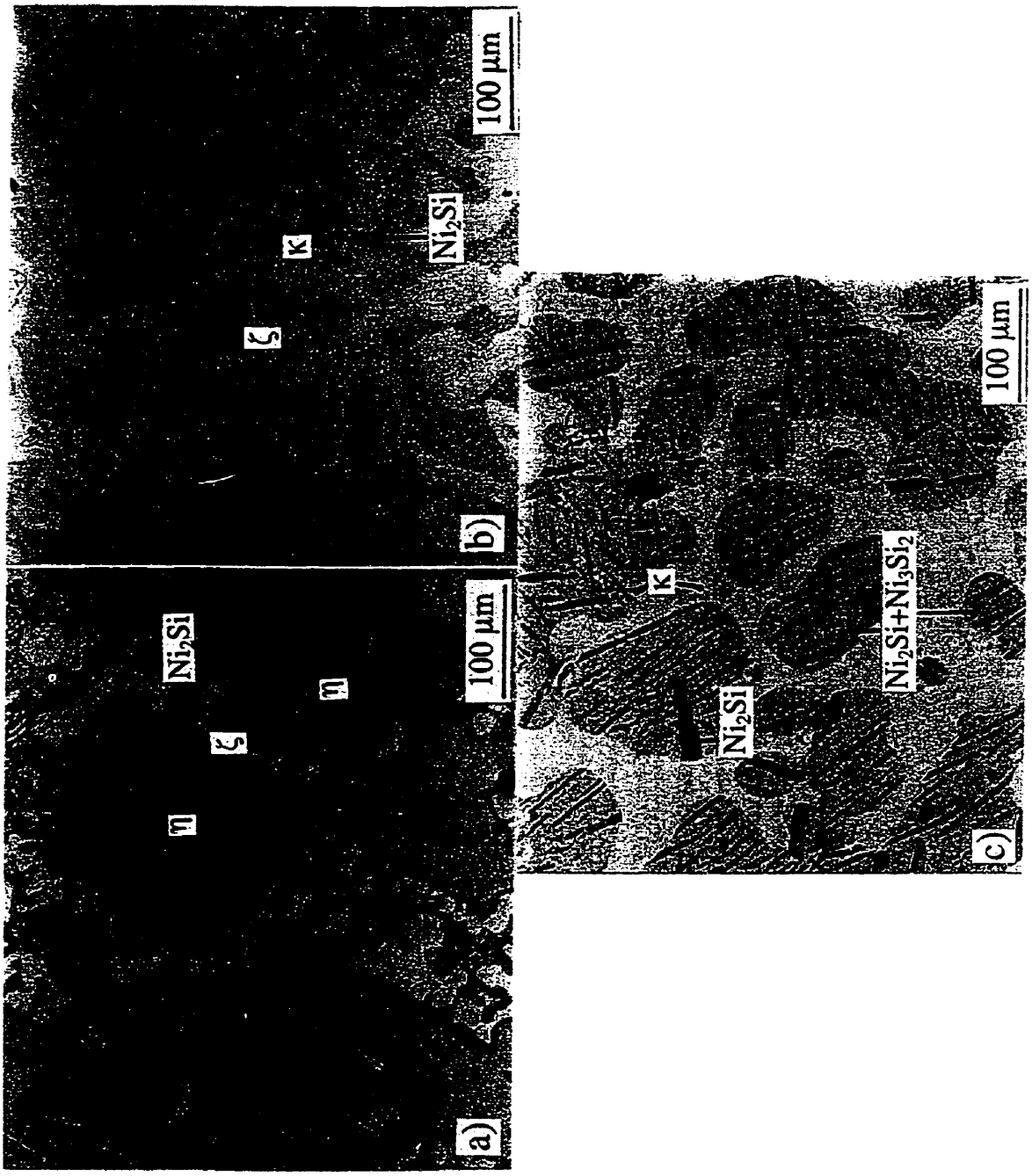

Fig. F.2 Homogenized microstructures of alloys (a)16, (b) 25, and (c) 26.

Appendix G

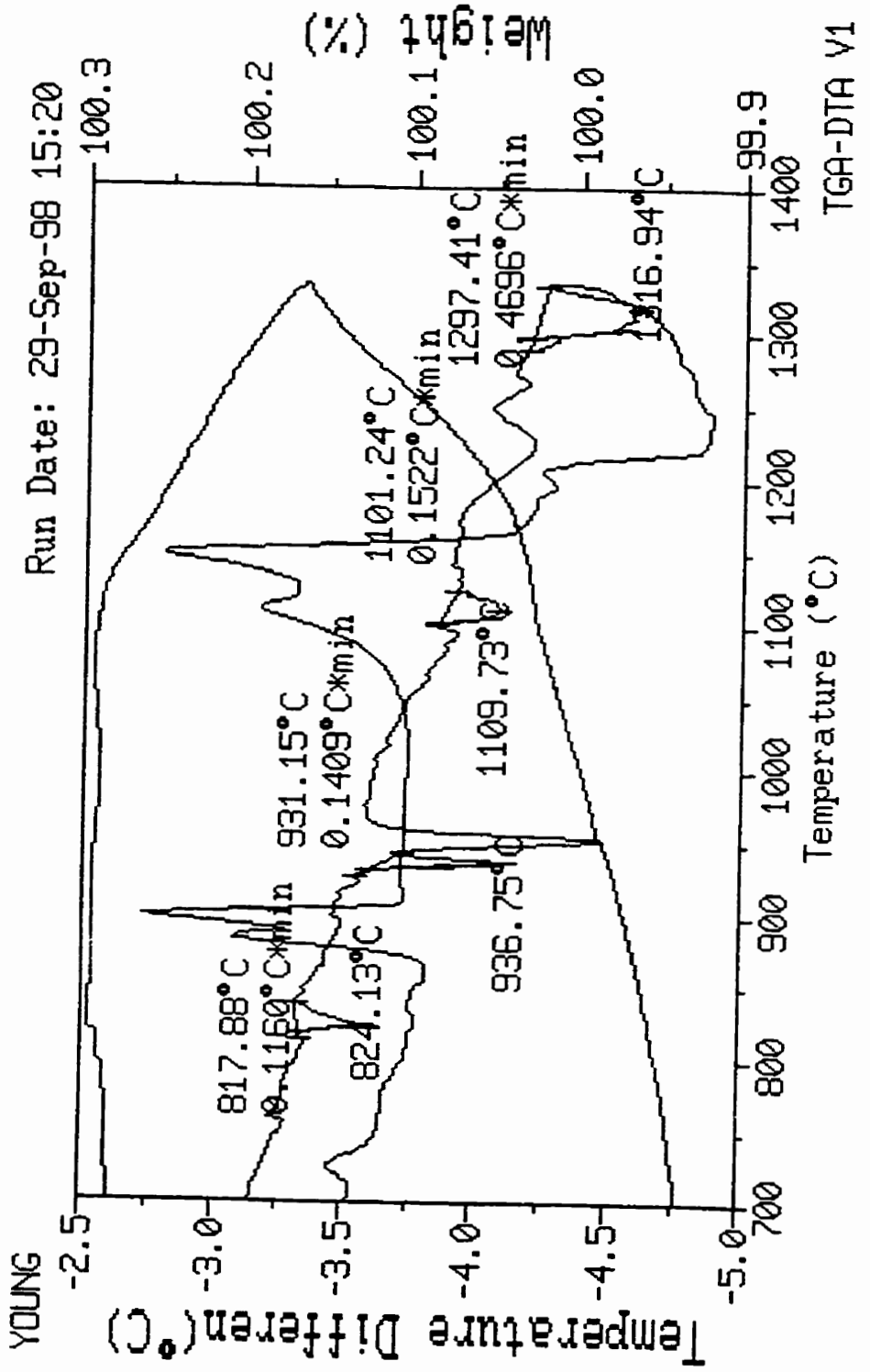

Fig. G.1 DTA and TGA result of alloy 16

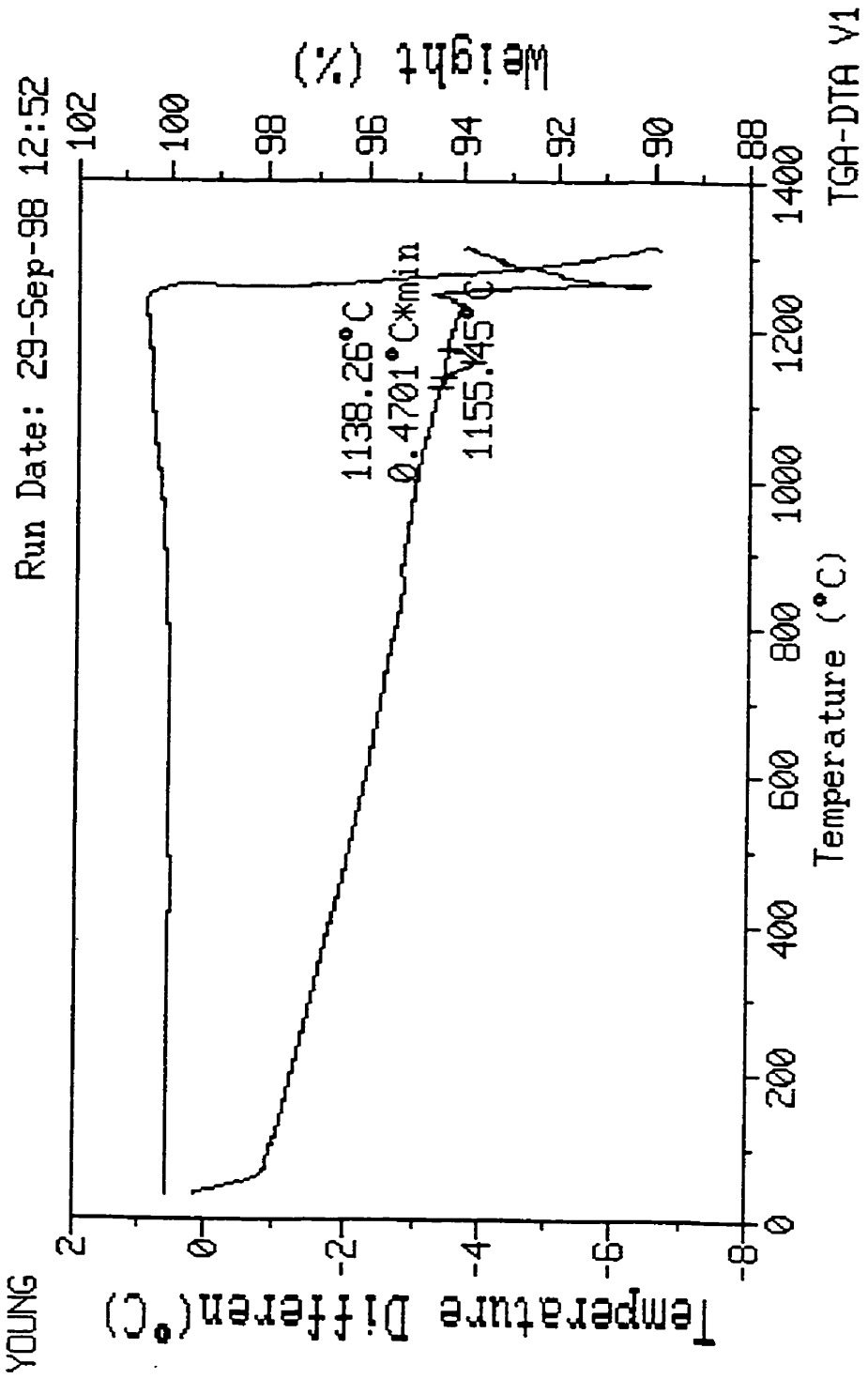

Fig. G.2 DTA and TGA result of alloy 32.

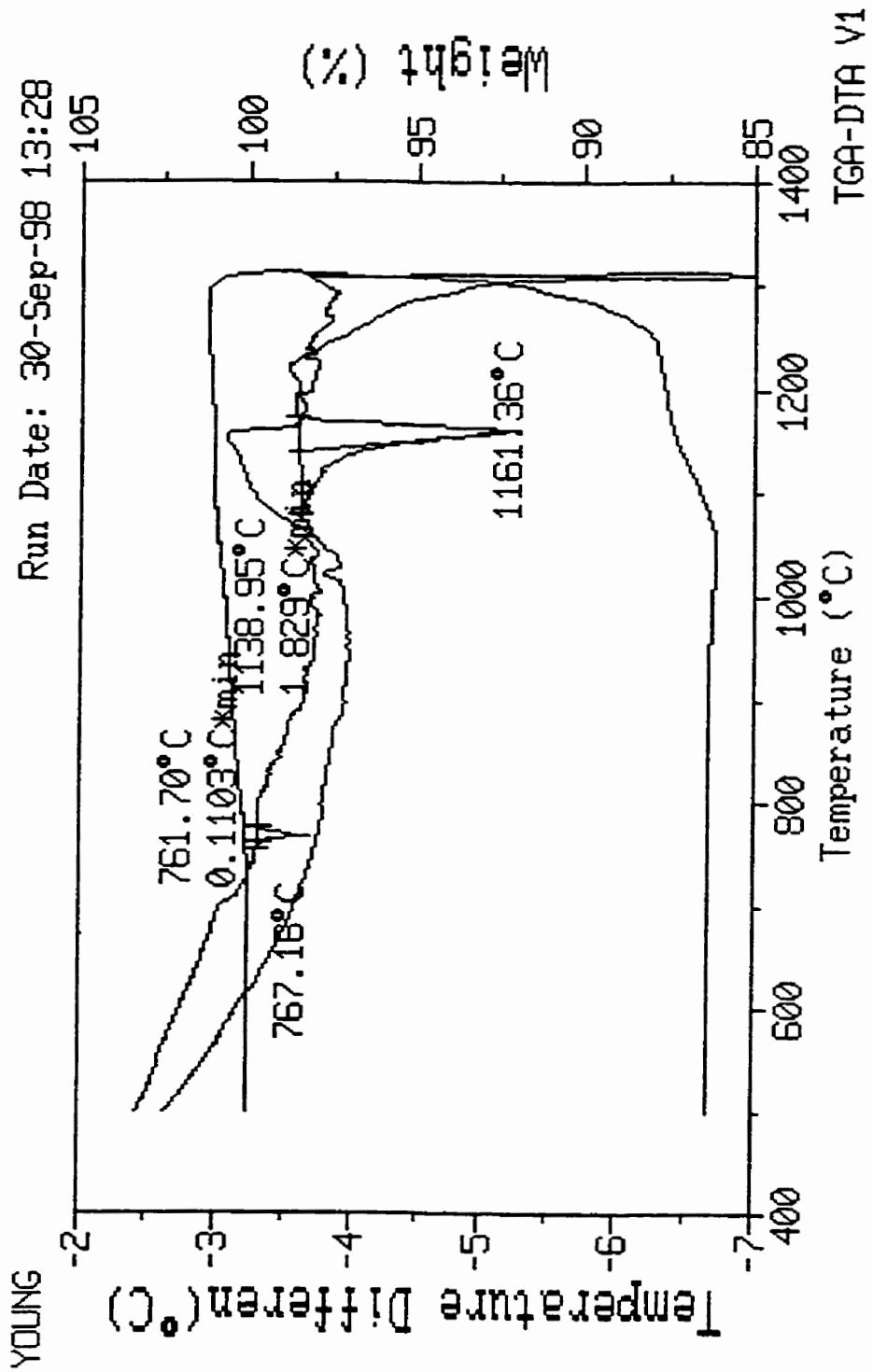

Fig. G.3 DTA and TGA result of alloy 38.

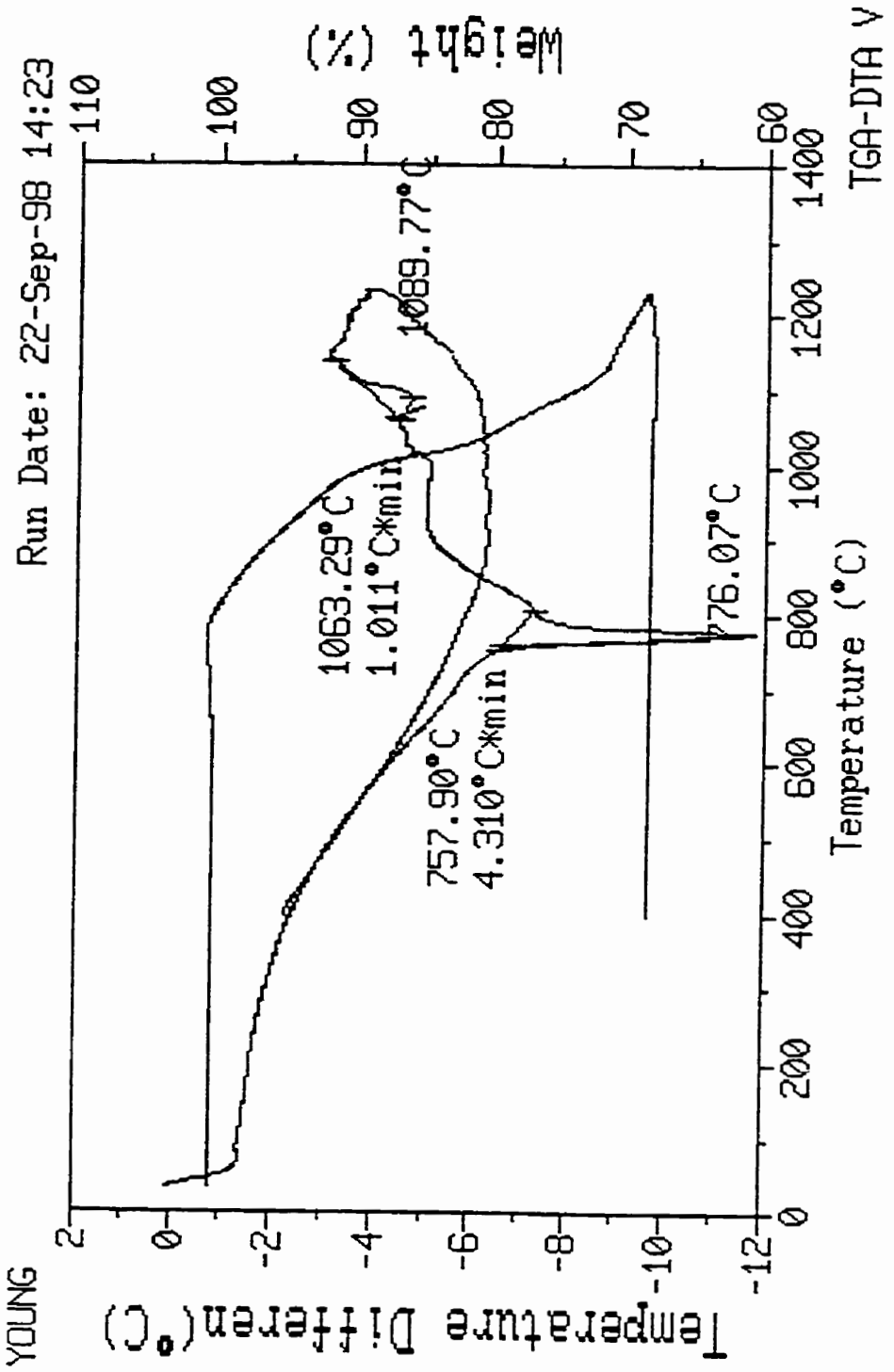

Fig. G.4 DTA and TGA result of alloy 40.

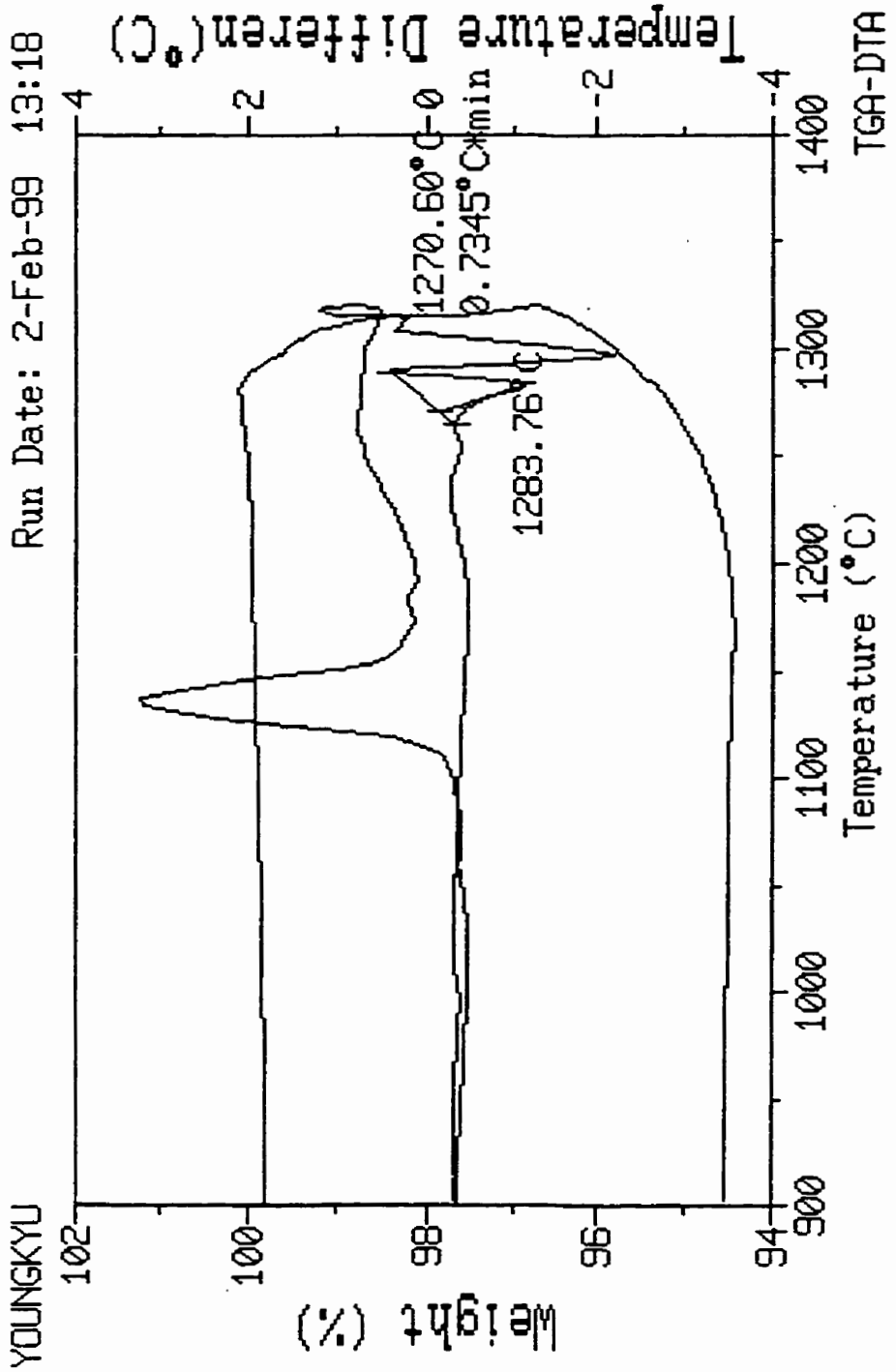

Fig. G.5 DTA and TGA result of single η phase alloy (alloy 20).

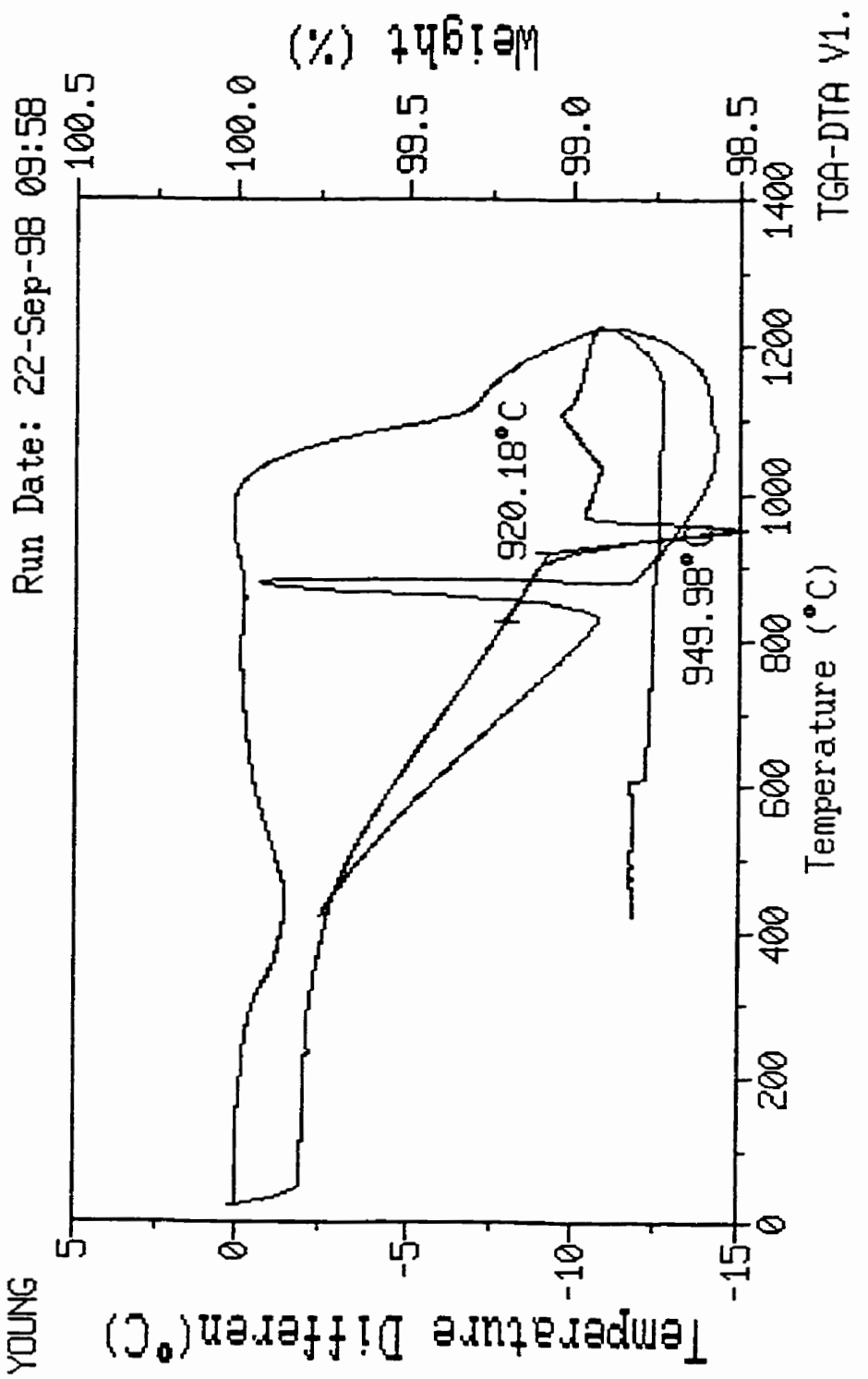

Fig. G.6 DTA and TGA result of single κ phase alloy (alloy 21).

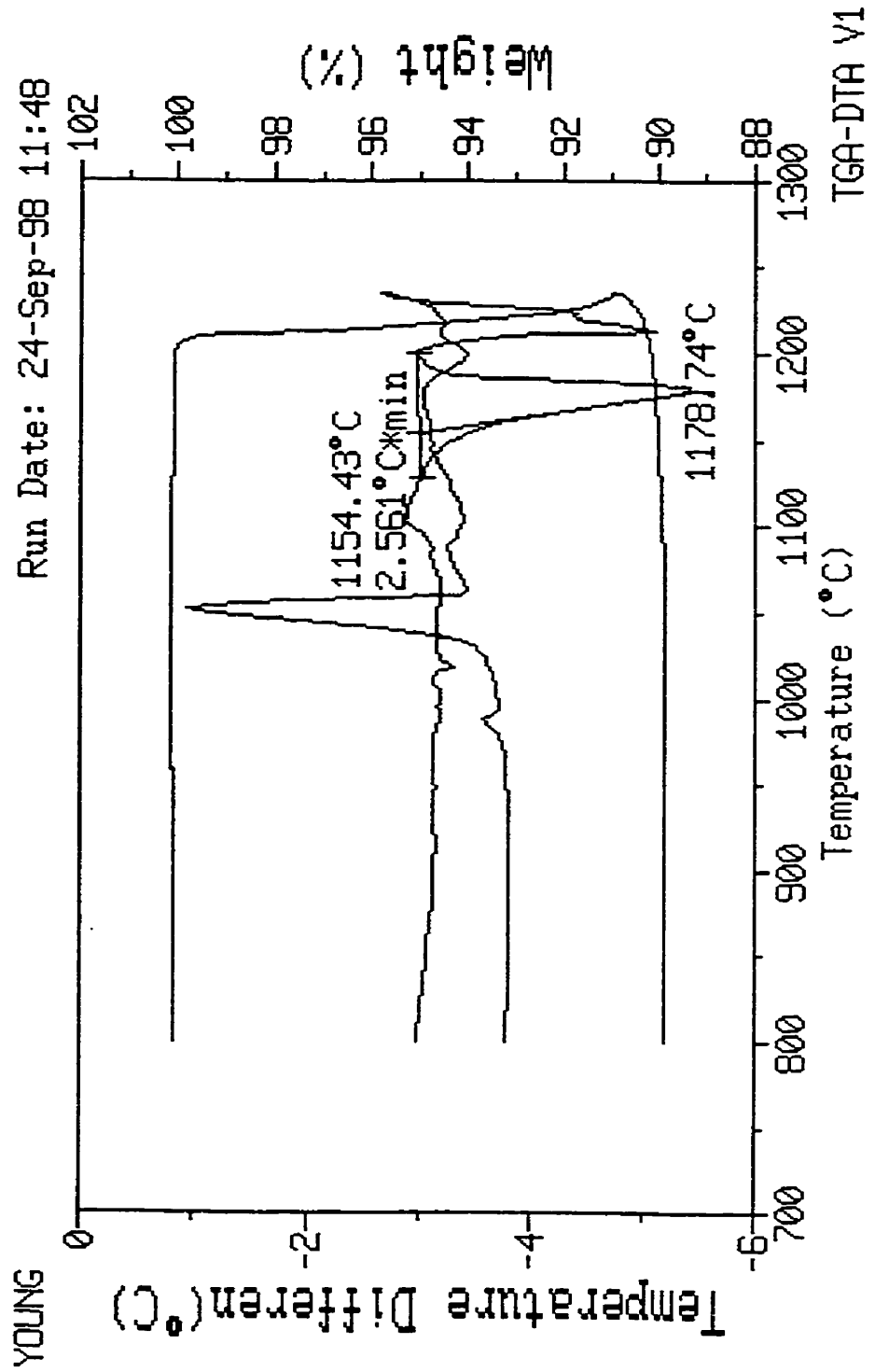

Fig. G.7 DTA and TGA result of alloy 37.

Appendix H

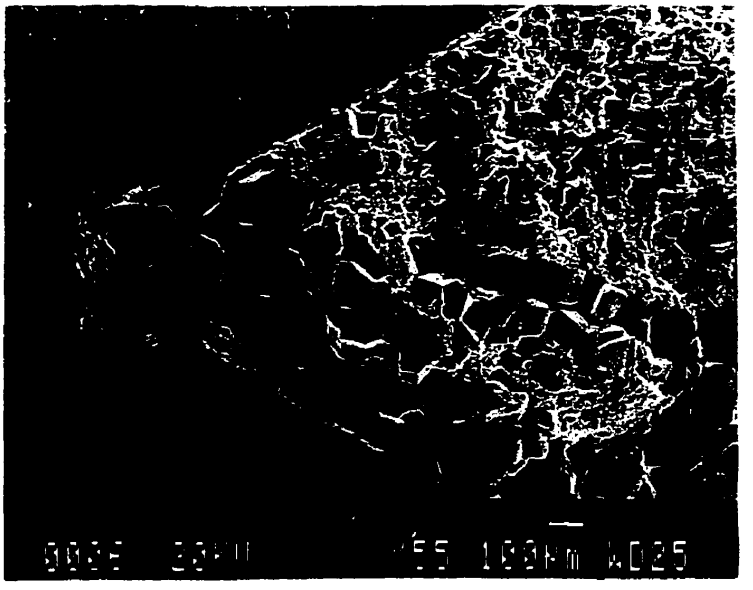

Fig. H.1 A SEM fractograph of F9-5th tested with S_1=35mm shows the evidence of abnormal crack initiation. The crack did not start from the tip of the chevron.

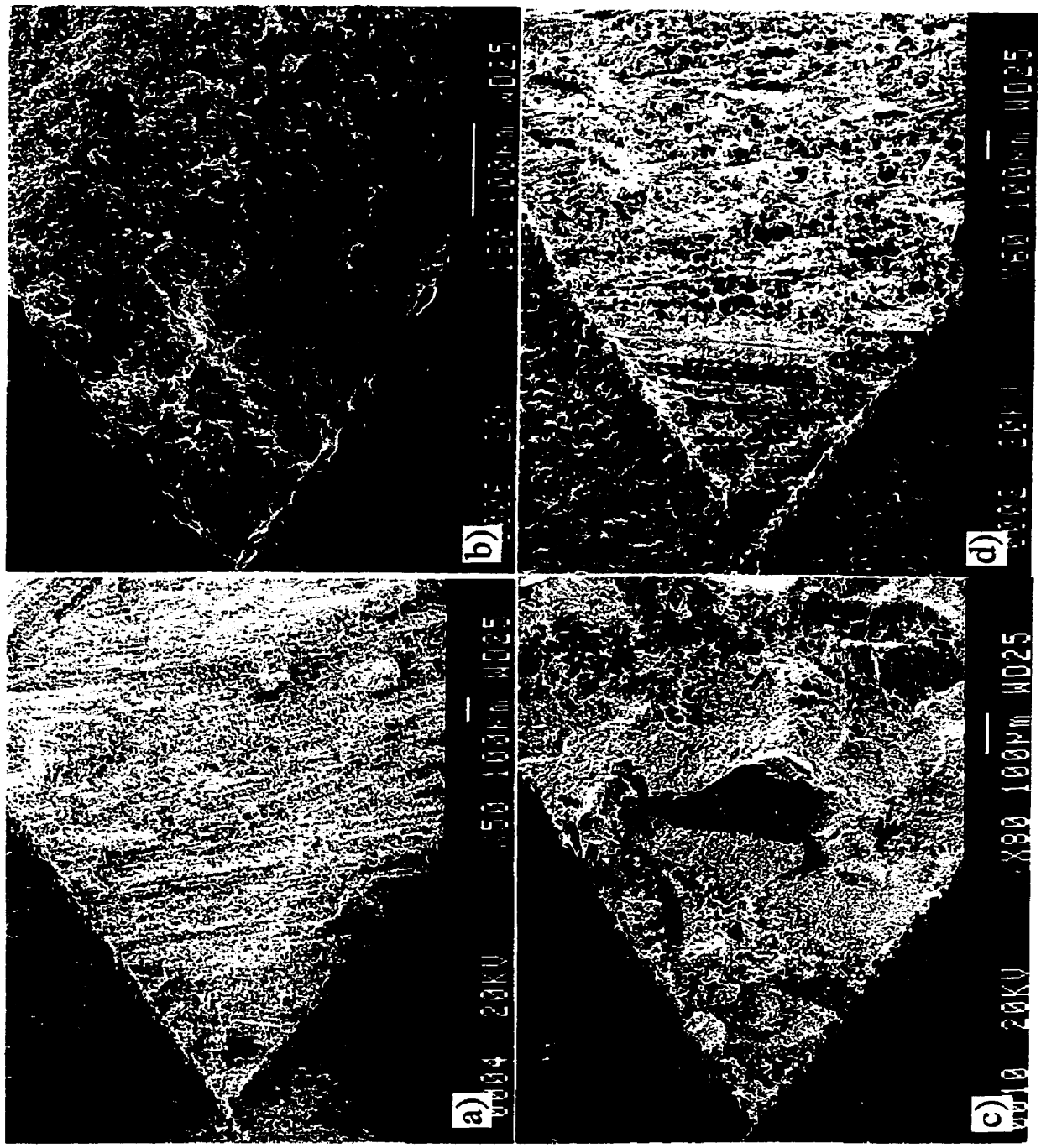

Fig. H.2 SEM micrographs showing overall fracture surfaces of composites (a) F1-1st, (b) F2-3rd, (c) F3-3rd, and (d) F4-1st tested in air.

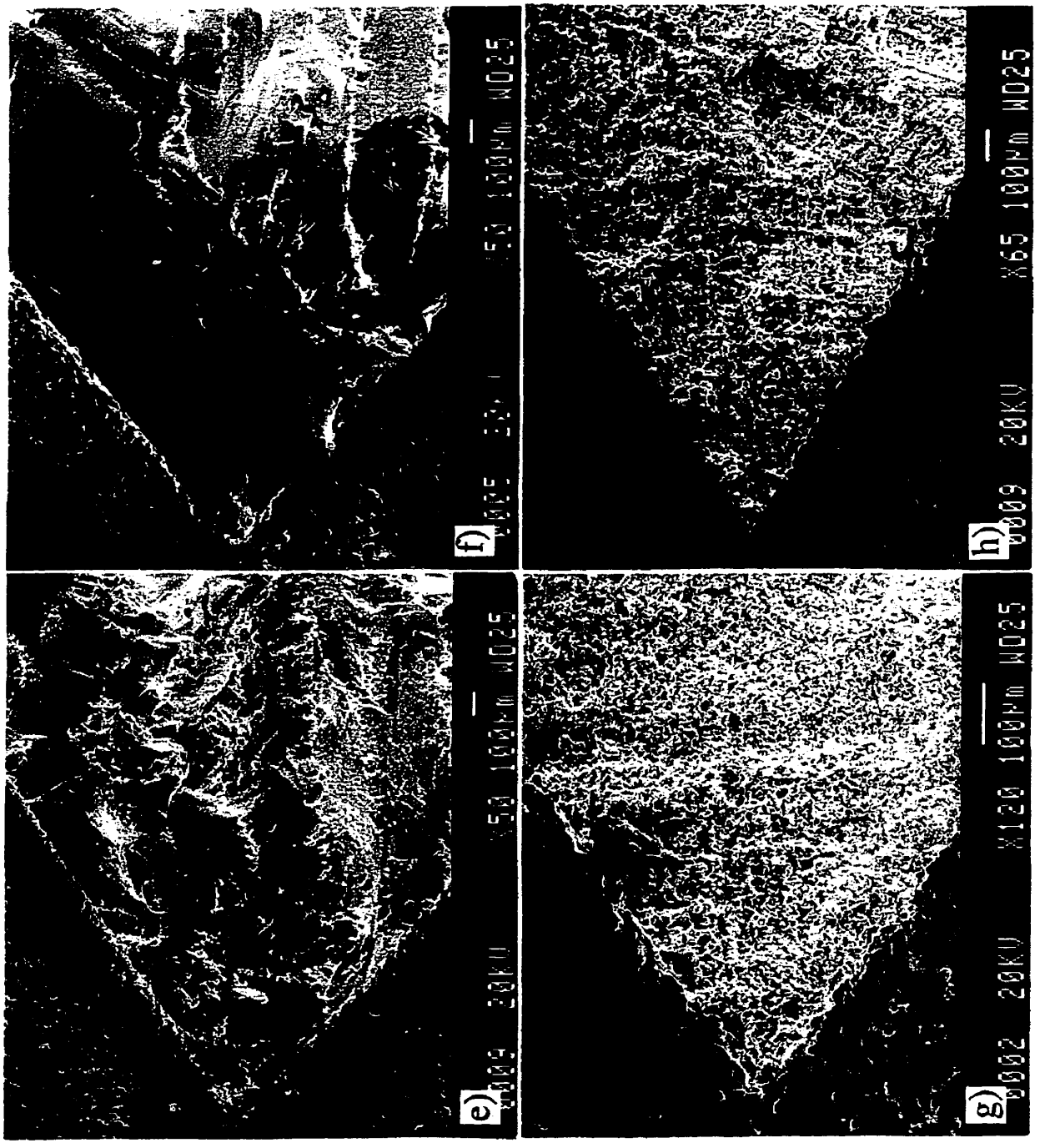

Fig. H.2 SEM micrographs showing overall fracture surfaces of composites (e) F5-2nd, (f) F6-1st, (g) F7-1st, and (h) F8-1st tested in air.

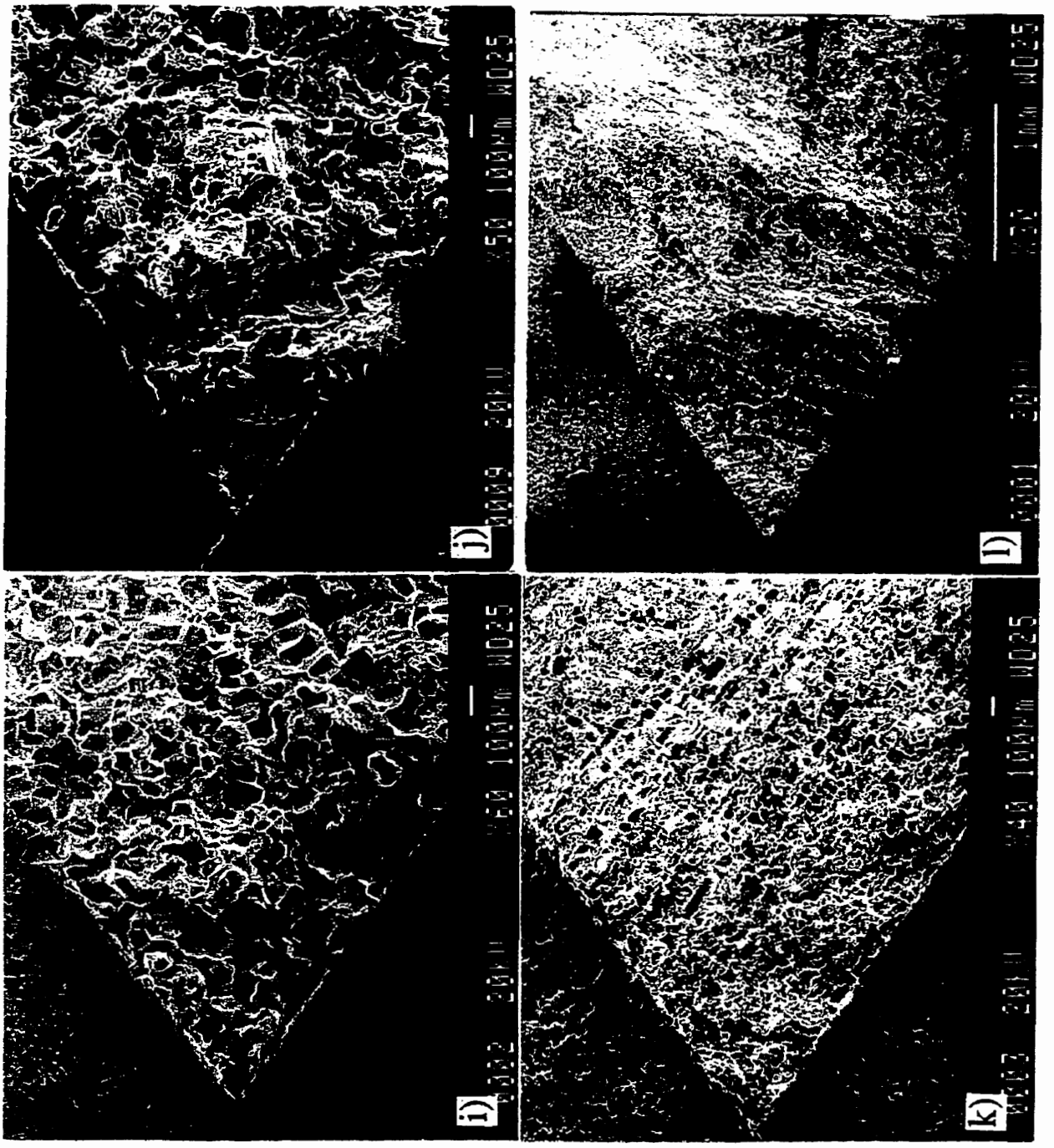

Fig. H.2 SEM micrographs showing overall fracture surfaces of composites (i) F9-1st, (j) F10-1st, (k) F11-2nd, and (l) F12-1st tested in air.

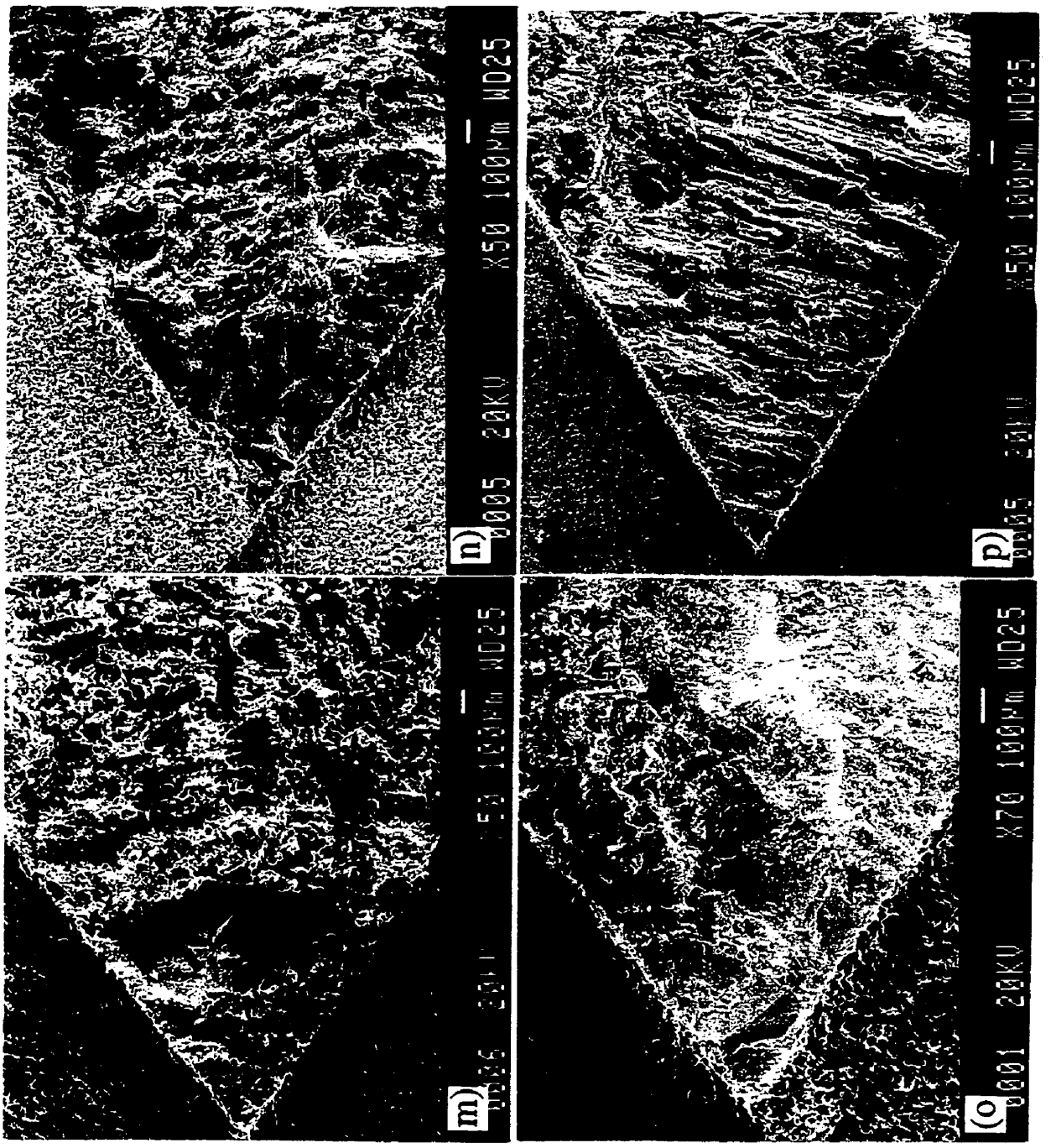

Fig. H.2 SEM micrographs showing overall fracture surfaces of composites (m) F13-1st, n) F14-3rd, (o) F15-3rd, and (p) F16-5th tested in air.

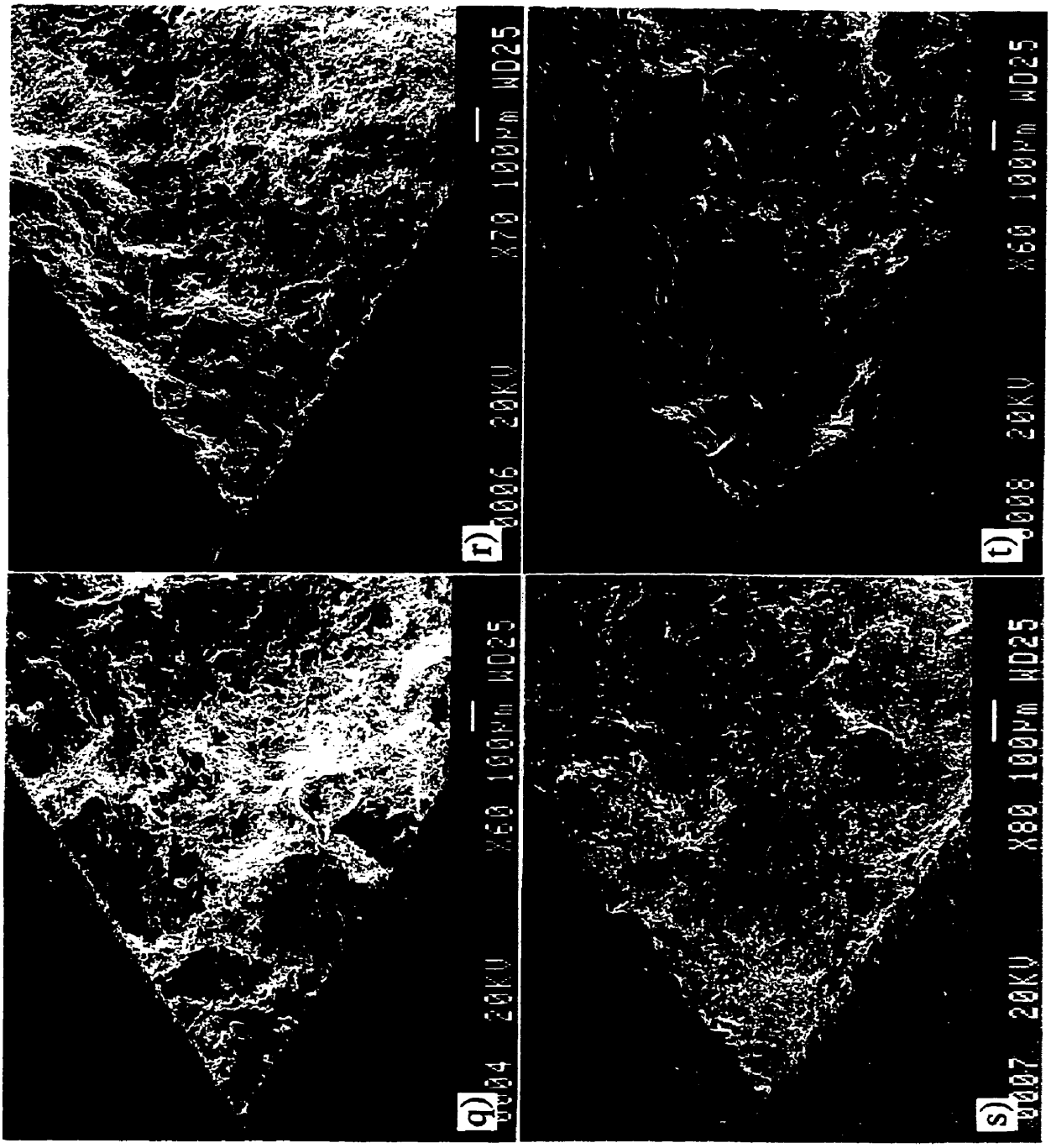

Fig. H.2 SEM micrographs showing overall fracture surfaces of composites (q) F17-1st, (r) F18-1st, (s) F19-3rd, and (t) F20-4th tested in air.

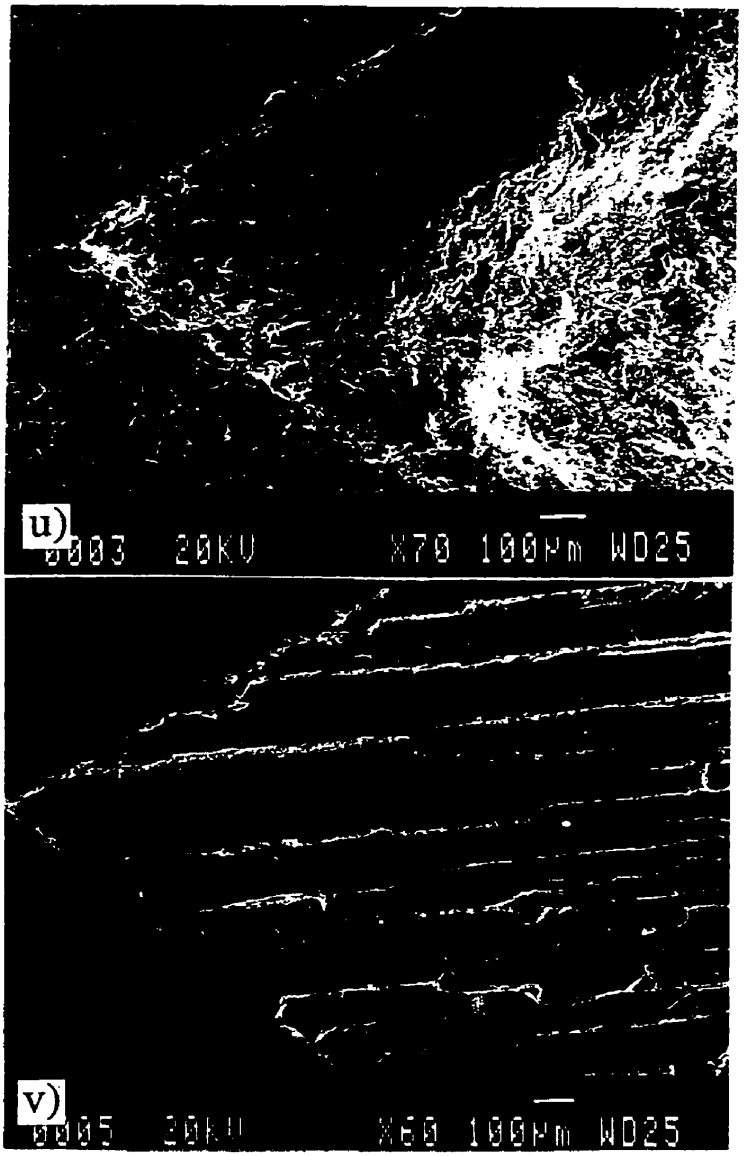

Fig. H.2 SEM micrographs showing overall fracture surfaces of composites (u) F21-3rd and (v) F22-1st tested in air.

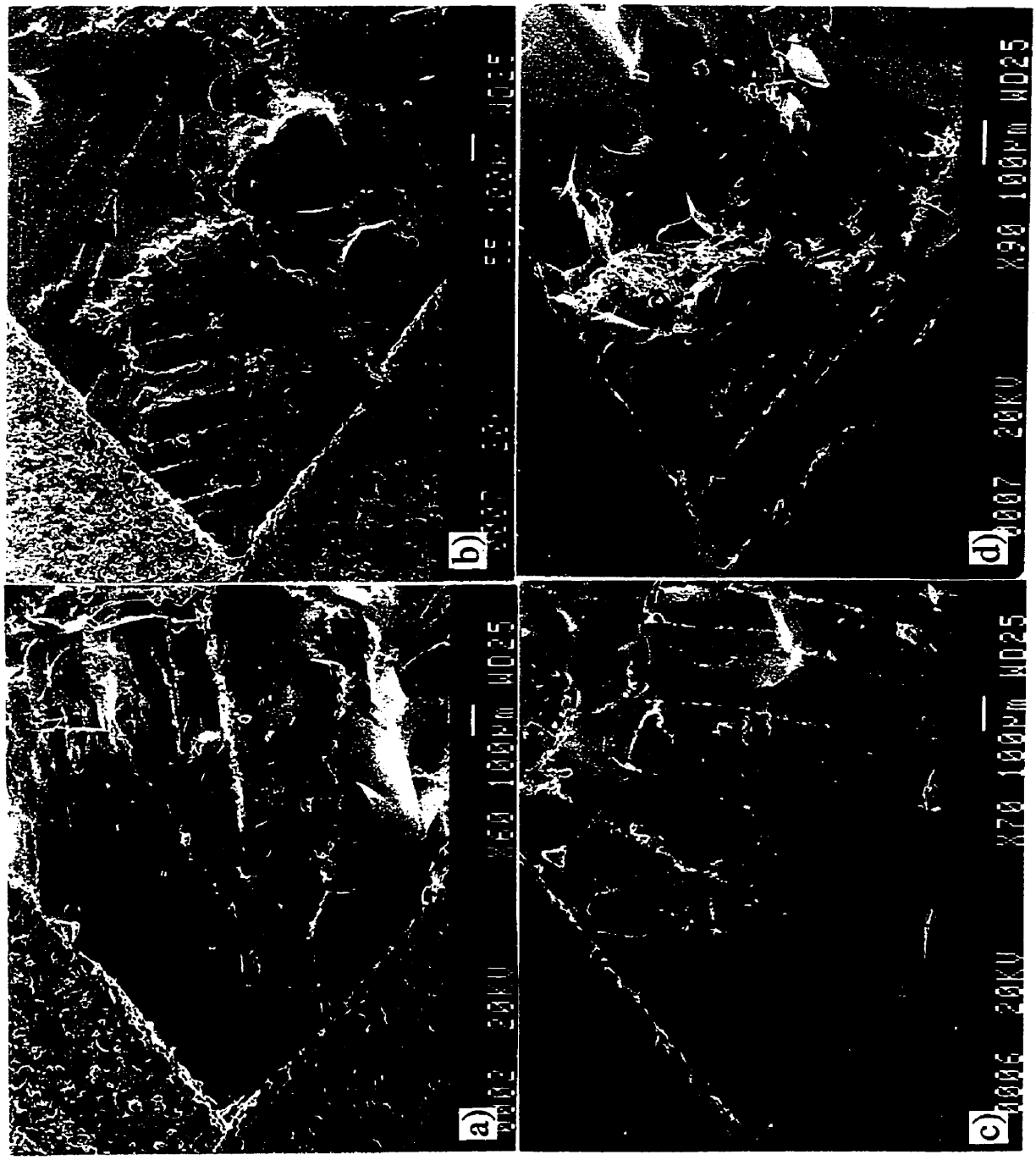

Fig. H.3 SEM micrographs showing overall fracture surfaces of CNB tested composites of (a) F6-2nd (1.7MPa.m$^{1/2}$) and (b) F6-3rd (2.5MPa.m$^{1/2}$) tested in air, and (c) F6-1st (1.7MPa.m$^{1/2}$) and (d) F6-2nd (3.0MPa.m$^{1/2}$) tested in dry oxygen.

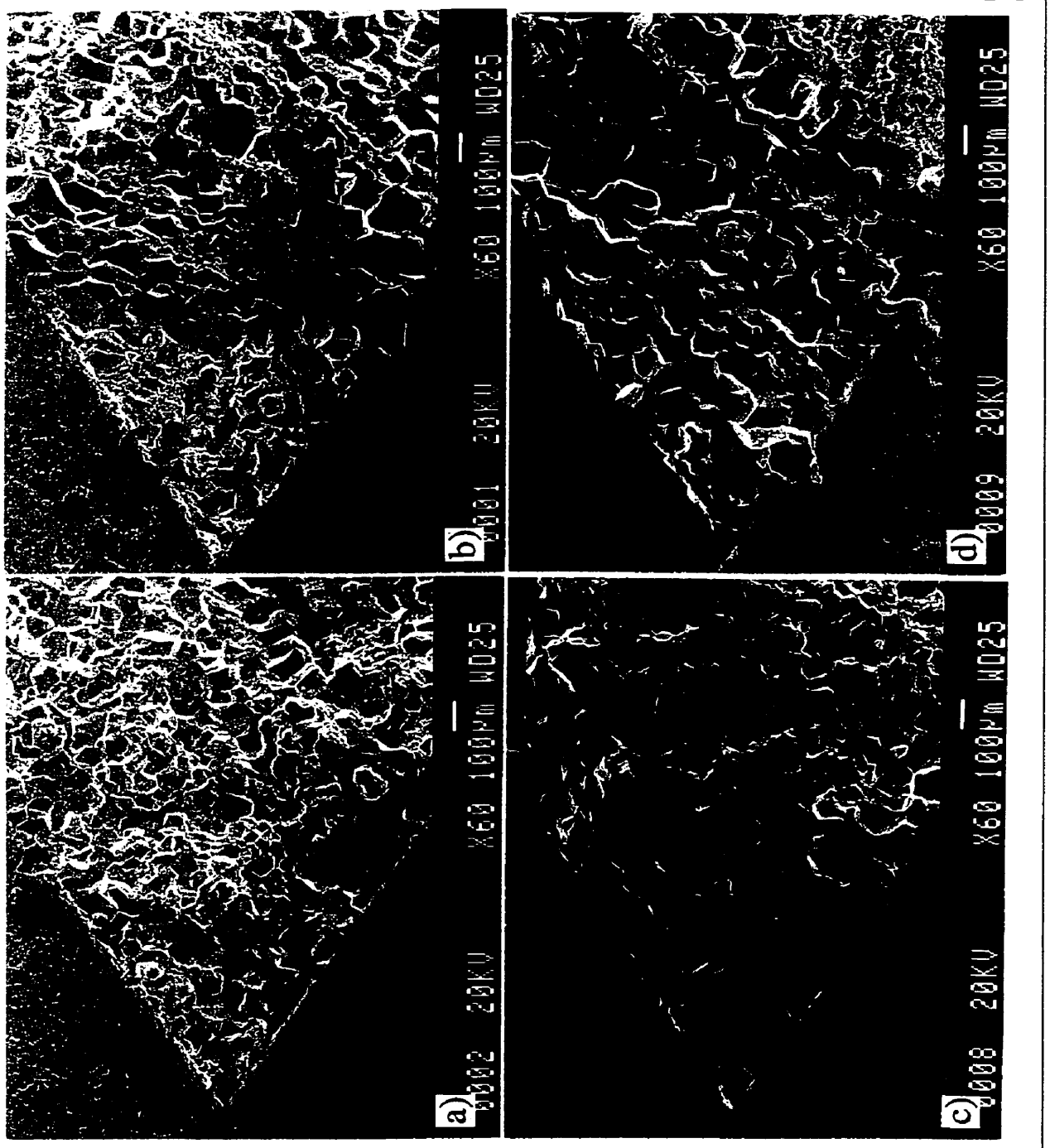

Fig. H.4 SEM micrographs showing overall fracture surfaces of composites (a) F9-1st (38.7MPa.m$^{1/2}$) and (b) F9-4th (21.4MPa.m$^{1/2}$) tested in air with S_1=35mm, and (c) F9-1st (37.8 MPa.m$^{1/2}$) and (d) F9-5th (22.5MPa.m$^{1/2}$) tested in air with S1=16mm.

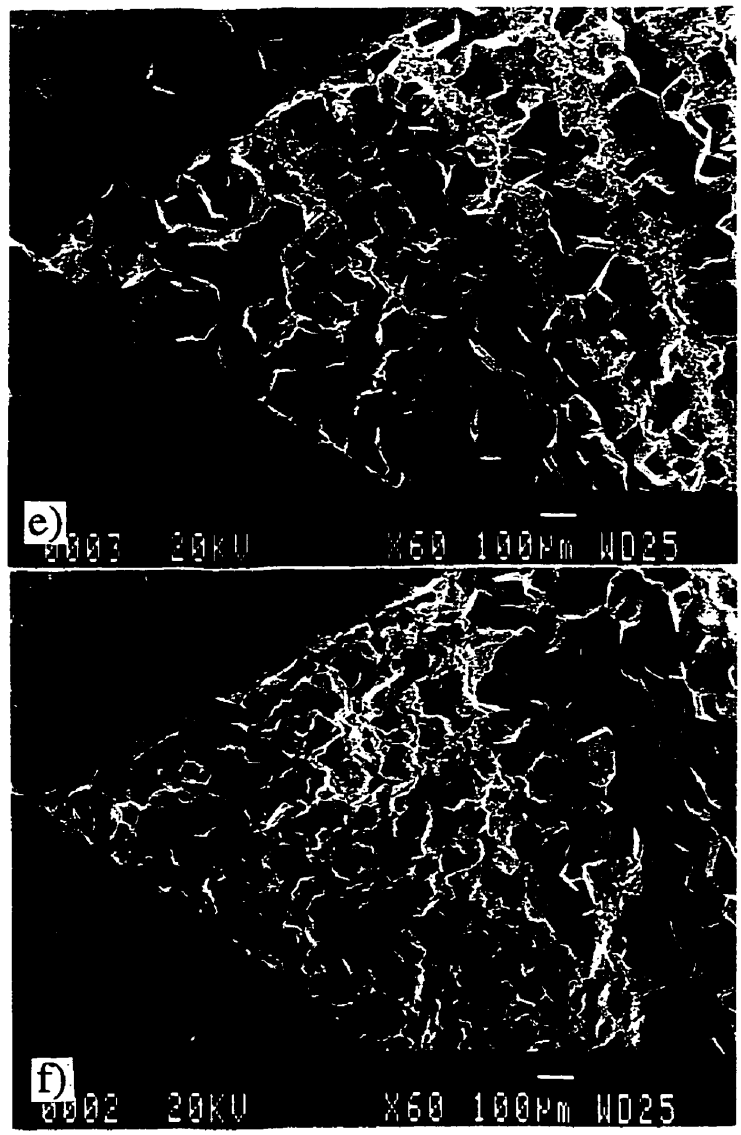

Fig. H.4 SEM micrographs showing overall fracture surfaces of composites (e) F9-5th (42.7 MPa.m$^{1/2}$) tested in dry oxygen and (f) F9-3rd (29.4 MPa.m$^{1/2}$) tested in vacuum.

Appendix I

Table I.1 The geometry, fracture toughness (K_{QIvM}) and compressive yield strength (σ_y) (or fracture strength, σ_f) of each CNB specimen tested in air and the size required based on ASTM E1304-89, i.e., $B \geq 1.25 (K_{QIvM}/\sigma_{YS})^2$ in order for a test result to be considered valid.

Specimen No.	S1 (mm) at S2=4.7	B (mm)	W (mm)	α_0	α_1	K_{QIvM} (MPa.m$^{1/2}$)	σ_y or σ_f (MPa)	required size, B (mm)
F1-1st	35	3.98	4.42	0.331	0.973	15.8	*1145**	0.24
F1-2nd		4.10	4.42	0.268	0.991	14.6	*1134*	0.21
F1-3rd		4.06	4.42	0.260	0.983	16.4	*1079*	0.29
F1-4th		4.08	4.42	0.244	0.976	15.3	*903*	0.36
F1-5th		4.10	4.40	0.221	0.976	16.1	*1219*	0.22
F2-1st	35	4.12	5.14	0.286	0.999	12.4	*1439*	0.09
F2-2nd		4.04	5.14	0.331	0.995	12.0	*1488*	0.08
F2-3rd		4.00	5.14	0.301	0.985	12.0	*1524*	0.08
F2-4th		4.02	5.14	0.294	0.989	11.8	*1460*	0.08
F2-1st	16	4.14	5.16	0.311	0.989	12.3	1439	0.09
F2-2nd		4.06	5.18	0.342	0.995	12.2	1488	0.08
F2-3rd		4.00	5.18	0.332	0.991	12.6	1524	0.09
F2-4th		4.06	5.16	0.332	0.995	12.7	1460	0.09
F3-1st	32	4.26	4.58	0.243	0.999	9.9	1623	0.05
F3-2nd		4.00	4.58	0.248	0.994	9.2	1405	0.05
F3-3rd		4.02	4.58	0.255	0.990	10.0	1389	0.06
F3-4th		3.96	4.56	0.337	0.994	8.7	1491	0.04
F4-1st	35	3.48	4.76	0.344	0.989	7.1	1380	0.03
F4-2nd		4.06	4.78	0.309	0.983	7.6	1821	0.02
F4-3rd		4.12	4.78	0.311	0.996	7.4	1193	0.05
F4-4th		4.14	4.78	0.291	0.983	7.3	1678	0.02
F4-5th		4.12	4.76	0.304	0.994	7.1	1334	0.04
F5-1st	25	3.90	3.96	0.211	0.974	3.2	1092	0.01
F5-2nd		3.96	3.96	0.212	0.996	2.6	779	0.01
F5-3rd		3.90	3.96	0.246	0.993	3.1	1025(A)**	0.01
F5-4th		3.96	4.00	0.204	0.973	2.9	1204	<0.01
F6-1st	22	3.72	4.08	0.300	0.985	1.7	498	0.01
F6-2nd		3.76	3.98	0.278	0.983	1.7	339	0.03
F6-3rd		3.76	4.02	0.391	0.999	2.5	495	0.03

Table I.1 continued

Specimen No.	S1 (mm) at S2=4.7	B (mm)	W (mm)	α_0	α_1	$K_{Q/M}$ (MPa.m$^{1/2}$)	σ_y or σ_f (MPa)	required size, B (mm)
F7-1st	35	4.22	5.28	0.296	0.990	28.0	*682*	2.11
F7-2nd		4.26	5.42	0.306	0.988	23.4	*831*	0.99
F7-3rd		4.08	5.40	0.333	0.956	19.0	*809*	0.69
F7-5th		3.64	5.34	0.359	0.984	17.8	*871*	0.52
F7-1st	16	4.24	5.30	0.286	0.994	28.8	*682*	2.23
F7-2nd		4.28	5.44	0.280	0.987	26.5	*831*	1.27
F7-3rd		4.08	5.38	0.321	0.986	26.7	*809*	1.36
F7-4th		4.12	5.36	0.285	0.982	31.2	*877*	1.58
F7-5th		3.70	5.32	0.362	0.969	25.1	*871*	1.04
F8-1st	35	3.58	4.72	0.270	0.991	15.9	*1099*	0.26
F8-2nd		3.94	4.72	0.233	0.977	12.7	*1105*	0.17
F8-3rd		4.04	4.72	0.252	0.989	12.4	*1101*	0.16
F8-4th		3.92	4.70	0.260	0.996	12.6	*1104*	0.16
F8-5th		3.50	4.70	0.290	0.988	12.4	*1020*	0.18
F9-1st	35	**4.22**	**4.94**	**0.270**	**0.984**	**38.7**	***482***	**8.06*** **
F9-2nd		**3.86**	**4.94**	**0.290**	**0.999**	**30.1**	***521***	**4.17**
F9-3rd		4.02	4.94	0.259	0.985	27.7	*514*	3.63
F9-4th		4.06	4.96	0.278	0.979	21.4	*490*	2.38
F9-5th		**4.04**	**4.96**	**0.251**	**0.987**	**35.1**	***502(A)***	**6.11**
F9-1st	16	**4.30**	**4.98**	**0.243**	**0.983**	**37.8**	***482***	**7.69**
F9-2nd		**3.90**	**5.00**	**0.296**	**0.999**	**35.4**	***521***	**5.77**
F9-4th		4.08	4.96	0.251	0.983	28.9	*490*	3.95
F9-5th		3.86	5.00	0.319	0.992	22.5	*502(A)*	2.64
F10-1st	35	3.90	5.12	0.368	0.972	29.7	*709*	2.19
F10-2nd		4.08	5.14	0.278	0.947	27.2	*662*	2.11
F10-3rd		3.96	5.16	0.356	0.977	21.5	*700*	1.18
F10-4th		4.06	5.18	0.304	0.981	31.2	*711*	2.41
F10-5th		4.42	5.18	0.269	0.965	26.2	*711*	1.70
F11-1st	35	4.34	4.96	0.240	0.982	17.7	*882*	0.50
F11-3rd		4.00	4.96	0.306	0.980	14.0	*897*	0.30
F11-4th		3.72	4.96	0.374	0.980	11.3	*877*	0.21

Table I.1 continued

Specimen No.	S1 (mm) at S2=4.7	B (mm)	W (mm)	α_0	α_1	$K_{Q/vM}$ (MPa.m$^{1/2}$)	σ_y or σ_f (MPa)	required size, B (mm)
F12-1st	35	3.98	4.66	0.268	0.997	10.5	*1054*	0.12
F12-2nd		3.96	4.66	0.285	0.980	9.0	*1145*	0.08
F12-3rd		3.98	4.68	0.266	0.995	7.2	*1175*	0.05
F12-4th		4.00	4.68	0.280	0.999	7.7	*1159*	0.06
F12-5th		3.94	4.68	0.248	0.999	7.4	*1102*	0.06
F13-1st	35	3.98	4.66	0.315	0.999	4.8	1406	0.01
F13-2nd		3.98	4.66	0.309	0.999	4.7	1215	0.02
F13-3rd		3.96	4.64	0.309	0.998	4.1	1162	0.02
F13-4th		3.98	4.62	0.286	0.996	4.6	1526	0.01
F13-5th		3.98	4.60	0.272	0.999	4.9	1157	0.02
F14-1st	35	4.14	5.08	0.295	0.990	4.8	2083	<0.01
F14-2nd		4.10	5.16	0.372	0.999	4.4	1921	<0.01
F14-3rd		4.42	5.20	0.307	0.989	5.0	1649	0.01
F14-4th		4.20	5.16	0.335	0.999	4.7	1815	<0.01
F14-5th		4.12	5.24	0.334	0.999	4.4	1356	0.01
F14-1st	16	4.14	5.08	0.125	0.980	6.4	2083	0.01
F14-2nd		4.12	5.14	0.247	0.988	4.9	1921	<0.01
F14-3rd		4.38	5.14	0.211	0.992	5.0	1649	0.01
F14-4th		4.20	5.20	0.231	0.985	5.1	1815	<0.01
F14-5th		4.14	5.26	0.245	0.989	5.0	1356	0.02
F15-1st	16	3.96	4.90	0.284	0.999	2.6	1746	<0.01
F15-2nd		4.02	4.92	0.321	0.999	4.6	1882	<0.01
F15-3rd		4.12	4.82	0.256	0.972	4.9	1714	0.01
F15-5th		4.10	4.64	0.341	0.999	2.9	1379	<0.01
F16-1st	35	4.26	5.16	0.267	0.993	4.7	458	0.13
F16-2nd		4.00	5.16	0.266	0.991	5.1	*537*	0.11
F16-3rd		4.18	5.16	0.246	0.999	6.1	*464*	0.21
F16-4th		3.96	5.18	0.282	0.983	6.3	704	0.10
F16-5th		3.96	5.18	0.273	0.985	6.5	596	0.15

Table I.1 continued

Specimen No.	S1 (mm) at S2=4.7	B (mm)	W (mm)	α_0	α_1	K_{QivM} (MPa.m$^{1/2}$)	σ_y or σ_f (MPa)	Required size, B (mm)
F17-1st	35	4.30	5.34	0.198	0.959	5.5	810	0.06
F17-2nd		4.20	5.34	0.202	0.959	3.7	1014	0.02
F17-3rd		4.22	5.34	0.222	0.976	4.4	1185	0.02
F17-4th		4.22	5.34	0.243	0.995	3.5	1223	0.01
F17-5th		3.96	5.34	0.253	0.976	4.2	1128	0.02
F18-1st	35	3.80	5.10	0.309	0.974	5.4	1382	0.02
F18-2nd		3.84	5.10	0.311	0.999	3.3	1482	<0.01
F18-3rd		3.82	5.10	0.314	0.988	3.4	1216	<0.01
F18-4th		4.08	5.14	0.245	0.999	4.6	1414	0.01
F18-5th		3.76	5.14	0.340	0.994	4.1	1435	0.01
F18-2nd	16	3.84	5.08	0.325	0.983	5.0	1482	0.01
F18-3rd		3.84	5.12	0.310	0.979	4.0	1216	0.01
F18-4th		4.08	5.12	0.250	0.988	3.5	1414	<0.01
F18-5th		3.78	5.12	0.308	0.999	4.6	1435	0.01
F19-1st	35	3.86	5.08	0.322	0.996	3.5	2258	<0.01
F19-2nd		4.00	5.14	0.323	0.995	3.4	1781	<0.01
F19-3rd		3.84	5.16	0.338	0.989	3.9	1793	<0.01
F19-4th		4.00	5.20	0.333	0.984	3.6	2003	<0.01
F19-5th		4.16	5.24	0.317	0.967	3.7	1339	<0.01
F20-1st	35	3.91	4.93	0.338	0.997	3.1	1789	<0.01
F20-2nd		3.98	4.92	0.358	0.999	3.1	1761	<0.01
F20-3rd		4.02	4.90	0.325	0.991	3.8	1611	<0.01
F20-4th		3.98	4.88	0.314	0.985	3.8	1662(A)	<0.01
F20-5th		3.89	4.91	0.347	0.999	3.7	1487	<0.01
F21-1st	32	4.02	5.34	0.376	0.999	3.0	1689	<0.01
F21-2nd		4.02	5.32	0.350	0.996	2.8	1309	<0.01
F21-3rd		3.78	5.16	0.399	0.999	3.6	1400	<0.01
F21-4th		3.88	5.20	0.321	0.974	3.4	1784	<0.01
F21-5th		4.00	5.24	0.358	0.997	3.8	1764	<0.01
F22-2nd	22	3.64	4.44	0.359	0.976	2.4	351	0.05
F22-3rd		3.98	4.04	0.255	0.986	2.9	459	0.05

*: the number in italic is a yield strength.
**: (A) indicates the average value of yield or fracture strength.
***: the actual specimen size (B) is smaller than that required in ASTM E 1304-89.